



NTNU – Trondheim
Norwegian University of
Science and Technology

Experimental Validation and Design Review of Wave Loads on Large-Diameter Monopiles

Joakim Fürst Frimann-Dahl

Marine Technology

Submission date: June 2015

Supervisor: Jørgen Ranum Krokstad, IMT

Norwegian University of Science and Technology
Department of Marine Technology



NTNU Trondheim
Norwegian University of Science and Technology
Department of Marine Technology

MASTER THESIS, SPRING 2015

Stud. tech. Joakim Fürst Frimann-Dahl

Experimental Validation and Design Review of Wave Loads on Large-Diameter Monopiles

The background for this project is related to the development of offshore wind parks at Dogger Bank outside the coast of England. Stable, strong winds and shallow water depths make this a well-suited site for bottom-fixed turbines. One of the main challenges for the industry is to drive down cost without compromising on safety. Design loads are of high importance for the total cost and a balanced trade-off securing sufficient conservatism is strived for. Methods for computing extreme loads are not well established in the industry, in particular for shallow water and highly dynamic turbines. A trend to reduce the cost of energy has been to increase turbine dimensions, making the structures more inertia dominated. The thesis will address challenges related to the modeling of environmental ULS loads, especially for large-diameter inertia-dominated turbines on shallow and intermediate water depths (20-45 m). It will focus on available tools, models and theories for such calculations, and includes the following tasks:

1. Review design challenges related to large column-based foundations.
2. Review how ULS wave loads and slamming loads are estimated according to standards, especially DNV's OS-J101 and RP-C205, with emphasis on new design challenges.
3. Perform model tests of a flexible bottom-fixed pile supporting a large turbine. The objective is to investigate forces/moments and slamming loads on the structure in an irregular sea state using statistical data from the Dogger Bank metocean report.
4. Validate theoretical models of distributed higher-order loads in the surface zone and slamming loads by means of deterministic and stochastic comparisons with model tests.
5. Based on load statistics and magnitudes, discuss how the different load types should be considered in structural design.

The work scope may prove to be more extensive than initially anticipated. Subject to approval from the supervisor, topics may be left out from the list above or reduced in extent.

In the thesis the candidate shall present his personal contribution to the resolution of problems within the scope of the thesis work. Theories and conclusions should be based

on mathematical derivations and/or logic reasoning identifying the various steps in the deduction. The candidate should utilize the existing possibilities for obtaining relevant literature.

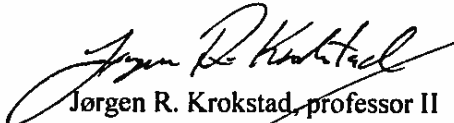
The thesis should be organized in a rational manner to give a clear exposition of results, assessments and conclusions, and the text should be brief and to the point. Telegraphic language should be avoided. The following elements must be included: A text defining the work scope, preface, summary, list of contents, list of symbols and acronyms, main body, conclusions with recommendations for further work, references and (optional) appendices. All figures, tables and equations shall be numerated.

The original contribution of the candidate and material taken from other sources shall be clearly defined. Work from other sources shall be properly referenced using an acknowledged referencing system.

The report shall be submitted in two copies in bound volumes, signed by the candidate. If needed, additional material shall be delivered in a separate folder.

According to the present rules NTNU has the ownership of the thesis. Any use of it has to be approved by NTNU (or an external partner when this applies). The department has the right to use the thesis as if an NTNU employee carried out the work, if nothing else has been agreed in advance.

Deadline: June 10, 2015


Jørgen R. Krokstad, professor II
Supervisor

Preface

This thesis concludes my Master of Science in Technology degree at the Norwegian University of Science and Technology (NTNU). The work has been performed at the Department of Marine Technology during the spring semester of 2015, and the experimental tests were executed in the small wave flume at MARINTEK, from the middle of April until May. Working with the thesis, and especially conducting experiments in the tank, has been demanding and time-consuming.

Having the opportunity to perform model testing as part of my thesis was a great way to complete my time at NTNU, and it has been truly fulfilling to gain insight into the offshore wind industry. Thus, I am grateful to my supervisor for providing the thematics.

Acknowledgements

Many people have been of great help during the thesis work. My supervisor, professor II Jørgen Ranum Krokstad has shown great dedication and willingness to teach through our weekly guidance meetings. Loup Suja-Thauvin has been my partner in the model testing. He is big-hearted and talented, and I am lucky to have had the chance to collaborate with him this year.

Statkraft AS funded the experiments, so no testing could have been performed without them. I would also like to thank MARINTEK employees Torgeir Jensen, Trygve Kristiansen and Torgeir Wahl for helping in the setup and instrumentation of the experimental tests.

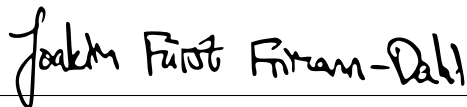
Lene Eliassen and Erin Bachynski have helped me in post-processing, and professor Dag Myrhaug provided guidance with non-linear wave theories. I am astounded by their never-ending willingness to help.

Professor Marilena Greco and Claudio Lugni supplied valuable study material in slamming, and they have been a great help in interpreting the experimental structural responses.

My office mates have brightened the days and acted as sparring partners in academic discussions. Thanks for all the laughs.

I could not have finished this thesis without the love and support of my family, Iben F. Frimann-Dahl, Hedda B. Fürst and Claus Frimann-Dahl. Finally, I am truly grateful to Ingrid B. Hauan for her endless backing and for keeping my motivation up.

Trondheim, June 10, 2015



Joakim Fürst Frimann-Dahl

Summary

The objective of the thesis work was to explore challenges related to ULS wave loading on offshore wind turbines, with special emphasis on large-diameter inertia-dominated monopile foundations.

Experimental studies testing ULS loads on a 6.9-m diameter pile in eight different three-hour sea states were performed in two water depths. The wave conditions were set to represent those at location 2 of Creyke Beck B at Dogger Bank, with specified sea state return periods up to 1000 years. The tested structure was a rigid smooth-surfaced bottom-fixed pile with a flexible rotational base stiffness. Wave elevation, pile-top acceleration, shear force and moment time realizations were measured. In addition, the runs were video-taped for deterministic studies.

A numerical model was developed in MATLAB, considering an idealized single degree-of-freedom rotational system with a rigid pile and flexible base stiffness. The program includes two general force models generating the Morison or the FNV excitation forces. The Morison model includes the option of running either shallow, intermediate or deep water, with or without Wheeler stretching. In addition, an impulsive force term is included, aimed at evaluating the impact of an individual spilling breaker. The FNV model is expanded to include the finite-depth vertical kinematic distribution and dispersion relation. This is inconsistent with the assumption of deep water in the derivation of the FNV formulae.

The model tests were shown to give less than a 1 % deviation in H_s for repeated sea states. The agreement in H_s between the calibration tests and tests with the model was within a -3 % to 3 % range for all sea states, whilst the discrepancy in nominal and effective H_s varied between a 12 % reduction to a 3 % increase for the calibrated waves. The greatest decrease in H_s occurred for the roughest sea state, indicating a large amount of breaking waves.

Throughout the tests an excessive first-mode motion was observed. The pile was almost constantly oscillating at its eigenfrequency, even in between large wave groups. The cause is thought to have been a combination of self-excitation from radiated waves reflecting off the wavemaker, the conservative mode shape and the low (but realistic) damping level.

Generally, the longer moment arm, i.e. the greatest water depth, generated the largest loads. The relative difference was smaller for $T_p = 15$ s than for $T_p = 11.25$ s, indicating the effect of increased wave non-linearity causing higher loads.

The largest response moments for almost every sea state were a result of a

breaking wave impacting the structure. However, uncertainty remains regarding the excitation mechanism, as to whether it is caused by the impulse load or ringing induced by non-linear wave components.

The feasibility of the metocean conditions are questioned, due to the large amount of breaking for the roughest sea states. There is reason to believe that shallow-water effects at Dogger Bank are not properly considered. The relative propagation distance for an unstable energy-dissipating breaking wave before impacting a turbine could be significantly larger in real life than in the wave flume.

The FNV force gave the most conservative response moment values, the finite-depth version more so than the one for deep water. The Morison force gave unconservative responses for the roughest sea states. The FNV formulae implementation was validated, yet uncertainty regarding the linearity of the measured input waves still remains.

Sammendrag

Målet med avhandlingen var å utforske utfordringer knyttet til ULS-laster fra bølger på offshore vindturbiner, med spesielt fokus på bunnfaste, tregheitsdominerte monopælfundamenter med stor diameter.

Eksperimentelle tester av ULS-laster ble utført på en sylindrisk konstruksjon med diameter 6,9 m for åtte forskjellige tre-timers sjøtilstander på to vanddyp. Bølgeforholdene skulle være representative for lokasjon 2 av Creyke Beck B på Doggerbank, med spesifiserte returperioder opptil 1000 år. Modellen var en stiv, bunnfast konstruksjon med glatt overflate, festet med en fleksibel rotasjonsfjær. Overflateheving-, sylindertoppakselerasjon-, skjærkraft- og momentrealisasjoner ble målt. I tillegg ble kjøringene tatt opp på video for bruk i deterministiske studier.

En numerisk MATLAB-modell ble utviklet med utgangspunkt i et idealisert rotasjonssystem med én frihetsgrad. Den besto av en stiv, hul sylinder med toppmasse og rotasjonsfjær, spesifisert av de testede modellegenskapene. Programmet inkluderer to kraftmodeller for beregning av eksitasjonskraften fra enten Morison eller FNV. Med Morison-modellen har brukeren muligheten til å kjøre med enten grunt, mellomdypt eller dypt vann, med eller uten Wheeler-strekking. I tillegg kan man legge til en impuls kraft som skal utgjøre slagkraften fra en brytende bølge. FNV-modellen er utvidet til å omfatte endelig vanddyp i beregningen av bølgekinematikk som avtar vertikalt og dispersasjonsrelasjonen. Dette motstrider antakelsen om dypt vann i utledningene av FNV-formlene.

I modellforsøkene ble det vist mindre enn 1 % avvik i signifikant bølgehøyde H_s for gjentatte kjøringene av sjøtilstander. Sammenligninger av H_s for bølgekalibreringstestene og kjøringene med modellen installert ga overensstemmelse innenfor et intervall på -3 % til 3 % for alle sjøtilstander, mens avviket i nominell og effektiv H_s varierte mellom en 12 % reduksjon til en 3 % økning av signifikant bølgehøyde i kalibreringen. Den største reduksjonen i H_s oppsto i den groveste sjøtilstanden, noe som indikerer mye bølgebryting.

En frekvent førstemodebevegelse ble observert i alle kjøringene. Konstruksjonen var nesten konstant eksitert og oscillerte med egenfrekvensen, selv mellom store bølgegrupper. Årsaken antas å ha vært en kombinasjon av selv-eksitering fra radierte bølger som reflekteres i bølgemaskinen, den konservative førstemodeformen og det lave (men realistiske) dempingsnivået.

Den lengste momentarmen, dvs. den største vanddybden, resulterte generelt i de største bølgelastene. Den relative forskjellen var mindre for $T_p = 15$ s enn for

$T_p = 11.25$ s, noe som indikerer at økningen i bølgens ulinearitet resulterer i større laster.

For nesten hver sjøtilstand oppsto den største momentresponsen ved virkningen av en brytende bølge. Det er dog knyttet usikkerhet til eksitasjonsmekanismen som genererer disse lastene. Enten er de forårsaket av impulslasten fra bølgen eller så er de grunnet ringing induisert av ikke-lineære bølgekomponenter.

Det ble observert og målt mye bølgebrytning for de største sjøtilstandene. Derfor settes det spørsmålsteget ved om forholdene beskrevet av metocean-rapporten er realistiske. Det er grunn til å tro at den ikke tar tilstrekkelig hensyn til gruntvannseffekter på Doggerbank. I tillegg kan den relative avstanden en ustabil, energidissiperende, brytende bølge må propagere før den når en vindturbin være vesentlig større for det virkelige Doggerbank enn i bølgetanken. Store brytende bølger beveget seg ofte fra den ene enden til den andre før den brøt ved modellen.

FNV-kraften ga de mest konservative responsmomentresultatene, og versjonen for endelig vanndyb var mer konservativ enn den for dypt vann. Morison-modellen var ukonservativ for de groveste sjøtilstandene. Implementeringen av FNV-formlene ble validert, men det er knyttet usikkerhet til lineariteten av bølgene som benyttes i beregningene av kreftene.

Contents

1. Introduction	1
2. Design Challenges for Large-Diameter Monopiles	3
2.1. Upscaling offshore wind turbines	4
2.2. Dynamic response of offshore wind turbines	7
2.3. Standard regulations in the design of offshore wind turbines	8
2.3.1. Ultimate limit states (ULS)	9
2.3.2. Fatigue limit states (FLS)	10
2.3.3. Accidental limit states (ALS)	10
2.3.4. Serviceability limit states (SLS)	11
2.3.5. Transient loads	12
3. Wave Loads	13
3.1. Wave load components on an offshore structure	13
3.2. Slender structures	18
3.3. Large-volume structures	19
3.4. Non-linear forces on a structure	20
3.5. Wave kinematics	22
3.5.1. Linear wave theory	22
3.5.2. Non-linear wave theories	25
3.5.3. The validity of wave theories	31
3.5.4. Kinematics in irregular waves	34
3.6. Ringing	37
3.6.1. The FNV model	40
3.6.2. Selecting force model	42
4. Slamming	47
4.1. Fundamentals of slamming	47
4.2. Slamming loads from waves	50
5. Model Testing of a Pile with a Flexible Rotational Spring	63
5.1. Principles of model testing	63
5.2. A discussion on the model roughness	65
5.3. Irregular sea	69
5.4. Wavemaker theory	73
5.5. MATLAB implementation	75
5.6. Dogger Bank site characteristics	77
5.6.1. Contour plot for location 2 of Creyke Beck B	78
5.7. Experimental setup	82
5.7.1. Testing facility and model setup	82

5.7.2. Instrumentation	87
5.8. Selecting waves for testing	91
5.8.1. Regular time series	92
5.8.2. Irregular time series	92
5.8.3. Test matrix	95
5.8.4. Regular wave regimes	97
5.9. System testing	100
5.9.1. Model wave radiation and tank reflections	100
5.9.2. Testing the force gauges	101
5.9.3. Testing the accelerometers	104
6. Numerical Model	105
6.1. Objective and assumptions	105
6.2. Implementation of the load models	107
6.3. Program testing	110
7. Results and Discussions	115
7.1. Decay test	115
7.2. Regular wave post-processing	122
7.3. Irregular wave post-processing	132
7.3.1. Comments on the execution of the irregular test program . .	143
7.4. Special, bi-chromatic wave tests	146
7.4.1. Special wave post-processing	148
7.5. Repeatability	150
7.6. Checking the results of the wave calibration	152
7.7. Stochastic analysis	153
7.8. Response from breaking wave events	157
7.9. Results from the numerical program	169
8. Conclusions	177
9. Further Work	181
A. Regular Wave Realizations	I
B. Moment Gumbel Plots	III
C. Moment Gumbel Plots for the Numerical Program	V
D. Validation of the FNV implementation	VII
E. MATLAB routines	XI

List of Figures

2.1.	Interaction between 6P and the 2 nd tower mode.	6
2.2.	A DAF for different damping levels	8
2.3.	Behavior of the distributions of environmental load mechanisms. . .	11
3.1.	The phase angle between a harmonic load and the response for different damping levels.	15
3.2.	The response of an inertia-dominated SDOF system in time.	16
3.3.	Relative importance of inertia, drag and diffraction wave forces. . .	17
3.4.	Relative magnitude of drag and inertia forces for slender structures.	17
3.5.	The general shape of the Morison equation terms.	19
3.6.	Force contributions in an inertia-dominated system.	19
3.7.	z-dependence illustrated for linear waves in shallow, intermediate and deep water.	25
3.8.	A 2 nd -order Stokes surface profile.	28
3.9.	Validity ranges for different wave theories.	32
3.10.	Wheeler stretching	35
3.11.	A typical ringing event.	38
3.12.	Illustrating the secondary load cycle.	39
3.13.	Simulation of the FNV bending moment at the point of maximum utilization.	43
4.1.	The Wagner wetted length	48
4.2.	Ringing from breaking and non-breaking waves.	51
4.3.	The impact area for a plunging breaker.	53
4.4.	Different types of breaking waves.	53
4.5.	The slamming coefficient as a function of submergence.	55
4.6.	The resulting load, with and without the slamming load component.	56
4.7.	The impact of a breaking wave.	58
4.8.	Comparison of the slamming coefficient (C_s) time histories for two impact force models.	60
4.9.	Force development for a breaking wave. A comparison of the Wienke and Goda force models.	61
4.10.	Slamming load composition	61
5.1.	Froude scaling of dimensional parameters.	64
5.2.	C_D variation with Re.	66
5.3.	C_D and C_M variation with Re and roughness ($KC = 20$).	68
5.4.	The frequency and depth-dependent ϕ parameter of the TMA spec- trum, given as a function of ω	71

5.5.	The Biésel transfer function	74
5.6.	Flow chart for generating and post-processing the regular waves. . .	75
5.7.	Flow chart for generating and post-processing the irregular waves. . .	76
5.8.	The Dogger Bank Creyke Beck locations.	77
5.9.	Metocean data locations at Dogger Bank.	78
5.10.	Dogger Bank topography	81
5.11.	A bird's eye view of the model tank setup.	82
5.12.	A side view of the model tank setup.	82
5.13.	Contents of the tank pit.	83
5.14.	The top mass and the accelerometers.	84
5.15.	The parabolic beach	85
5.16.	Comparing mechanical transfer functions.	86
5.17.	The wavemaker	87
5.18.	Checking the force/moment transducer calibration and the base stiffness, using a pulley system.	89
5.19.	Force gauges in the front of the pile (upstream).	90
5.20.	The camera placements	91
5.21.	The regular wave batches	92
5.22.	Contour plot for extreme waves with return periods 10, 50, 100, 1 000 and 10 000 years for location 2, Creyke Beck B.	94
5.23.	Irregular H_s , T_p points shown in the contour plot for Creyke Beck B, location 2.	95
5.24.	An illustration of the wavemaker reflection of the radiated waves from the flexible model during a decay test.	100
5.25.	The wave elevation at wave gauge 8 during a decay test in water depth $h=20.9$ m.	101
5.26.	Measurements for each of the operative force gauges, exemplified for a specific seed at $h = 30$ m.	102
5.27.	Model scale force gauge measurements plotted with the wave eleva- tion at wave gauge 7.	103
5.28.	The realization for force gauge 2 at $h=20.9$ m.	103
6.1.	The SDOF model	105
6.2.	Comparing the measured decays with the numerical calculations. . .	107
6.3.	Flow chart for the numerical model.	110
6.4.	Comparing the absolute value of the transfer function $ H(\omega) $ with the numerical model output.	111
6.5.	Zooming in on the measured transfer function values.	111
6.6.	Moment spectrum with a low-pass ideal filter with a cut-off fre- quency at $1.5 \cdot f^{(1)}$	112

6.7.	Illustrating the relative FNV contributions order of magnitude for a large force event at $h=20.9$ m.	113
6.8.	Seed-averaged top-of-pile acceleration spectra compared.	113
7.1.	The decay test in x-direction in the form of a M_y time series.	115
7.2.	Moment spectrum cut-outs from the decay test giving the first and second mode eigenfrequencies, respectively.	116
7.3.	Decay test in the x-direction (tank longitudinal), showing time series of M_y [Nm]. The oscillation maxima are marked.	117
7.4.	Decay test in the y-direction (tank transverse), showing time series of a_y [m/s^2]. The oscillation maxima are marked.	117
7.5.	Logarithmic decay plotted against mean amplitudes for decay tests in x-direction.	119
7.6.	Logarithmic decay plotted against mean amplitudes for decay tests in y-direction.	120
7.7.	An eigenperiod regular wave realization at $h = 20.9$ m.	122
7.8.	Showing the moment build-up for the eigenfrequency waves.	123
7.9.	No moment build-up to the long 10-s regular waves.	123
7.10.	The nominal and effective wave heights of the regular tests at $h = 20.9$ m.	125
7.11.	The nominal and effective wave periods of the regular tests at $h = 20.9$ m.	125
7.12.	The nominal and effective wave heights of the regular tests at $h = 30$ m.	127
7.13.	The nominal and effective wave periods of the regular tests at $h = 30$ m.	127
7.14.	Showing non-linear features of steep waves at shallower water (b), compared with less steep regular waves (a).	129
7.15.	Plots to determine the theoretical regular wave regimes, as from tables 5.14 and 5.15.	129
7.16.	Data for categorizing the measured regular wave series.	130
7.17.	Effect of water depth on higher-harmonic response moment contributions.	130
7.18.	Effect of steepness on higher-harmonic response moment contributions.	131
7.19.	Effect of the wave period on higher-harmonic response moment contributions.	131
7.20.	Wave gauge measurement comparisons.	132
7.21.	Measured H_s for the different wave gauges shows wave breaking along the tank.	133

7.22. Comparing effective H_s values for different steepness irregular sea states.	134
7.23. Comparing effective T_p values for different steepness irregular sea states.	134
7.24. Averaged wave spectrum	135
7.25. Longitudinal sloshing	136
7.26. Illustrations of the wave gauge eigenfrequencies.	136
7.27. Comparing force and moment spectra	137
7.28. Realistic bending moment spectrum	138
7.29. Comparing averaged max. moments as a function of measured H_s for $T_p=11.25$ s.	140
7.30. Comparing averaged max. moments as a function of measured H_s for $T_p=15$ s.	140
7.31. A low-pass and high-pass filter applied on a moment time series, for the largest moment of a sea state.	141
7.32. The wave elevation and moment time series corresponding to the event in figure 7.31.	142
7.33. The resulting low-pass and high-pass contributions of the moment spectrum after applying the ideal fifth-order Butterworth filter. . .	143
7.34. Comparing piston stroke spectra	144
7.35. Application of the 3-Hz filter	144
7.36. Effects of the high-frequency filter on the wavemaker stroke.	145
7.37. Applying a high-frequency filter had little effect on the resulting wave elevations.	145
7.38. A special wave run with and without the eigenfrequency component. The wave periods are $T=3.94$ s and $T=10$ s, at $h=30$ m. The steepness of the 10-s extreme wave is twice the steepness of the other 10-s waves.	147
7.39. The eigenfrequency waves are generated before the 10-s waves. . . .	148
7.40. Comparing wave elevations with and without the eigenfrequency component.	149
7.41. Comparing moment spectra with and without the eigenfrequency component.	149
7.42. Comparing moment time series with and without the eigenfrequency component.	150
7.43. Comparing wave elevations in a repeated test of $H_s=7.69$ m, $T_p=11.25$ s. The measured H_s were 7.23 m and 7.28 m, corresponding to a difference of 0.7 %.	151

7.44. Comparing bending moments in a repeated test of $H_s=7.69$ m, $T_p=11.25$ s. The measured maximum moments were 32.1 Nm and 29.0 Nm, corresponding to a difference of 10.0 %.	151
7.45. Comparing the measured wave elevations from the model tests and wave calibration runs for a given sea state seed.	153
7.46. Linear Gumbel fits of the maximum moments for each seed, exemplified for two different sea states at $h = 30$ m.	155
7.47. The cumulative distribution for the measured moments.	156
7.48. Comparing the stabilization of moment maxima quantiles.	157
7.49. Idealized ringing and slamming events.	158
7.50. Incoming breaking wave wall	160
7.51. Wave breaker impact	160
7.52. Water run-up and spray is observed	160
7.53. Incoming breaking wave wall, viewed from behind the structure	161
7.54. Wave breaker impact, viewed from behind the structure	161
7.55. Water run-up and spray is observed from behind the structure	161
7.56. Full scale wave elevation and response moment of the slamming event.	162
7.57. Full scale wave elevation and response moment of the slamming event.	163
7.58. Full scale slamming event wave elevations at wave gauges 5 and 7.	164
7.59. Dynamic response of an undamped single degree-of-freedom system due to a rectangular impulse.	165
7.60. Shock spectra for three different impulse shapes of equal area as a function of the ratio between the impulse duration and the first natural period of the system.	166
7.61. Wavelet analysis around the breaker event of figure 7.56.	168
7.62. Realizations of response moments are exemplified, comparing the measured moment with the deep-water FNV and the deep-water Morison with Wheeler stretching and slamming ($H_s=9.04$ m, $T_p=11.25$ s, $h=30$ m).	169
7.63. Inertia dominance for the entire sea state seed	170
7.64. Inertia dominance, with focus on the breaking wave event	170
7.65. Illustrating the effect of self-excitation	171
7.66. Gumbel plots comparing the response moments from the numerical program with measured data ($H_s=6.71$ m, $T_p=11.25$ s, $h=20.9$ m).	172
7.67. Gumbel plots comparing the response moments from the numerical program with the measured data ($H_s=9.04$ m, $T_p=11.25$ s, $h=30$ m).	172
7.68. Gumbel plots for the finite-depth version of the FNV, with and without a 0.8 factor applied on the cut-off frequencies.	174
7.69. Comparing the measured shear force with the numerical Morison excitation force.	175

List of Figures

A.1. Regular wave realizations at $h = 20.9$ m.	I
A.2. Regular wave realizations at $h = 30$ m.	II
B.1. Gumbel plots for the maximum response moments in each seed, $h = 20.9$ m.	III
B.2. Gumbel plots for the maximum response moments in each seed, $h = 30$ m.	IV
C.1. Comparing numerical model output with measured data. Gumbel regression lines for the maximum response moments in each seed, $h = 20.9$ m.	V
C.2. Comparing numerical model output with measured data. Gumbel regression lines for the maximum response moments in each seed, $h = 30$ m.	VI
D.1. First-order free-surface elevation ζ_1	VII
D.2. F_1	VIII
D.3. F_2	VIII
D.4. $F_3^{(1)}$	IX
D.5. $F_3^{(2)}$	IX

List of Tables

3.1. Validity ranges of different wave theories	33
4.1. A comparison of slamming coefficients and curling factors	59
5.1. Approximate C_D and C_M values in model and full scale.	68
5.2. Parameters used in the calculations of the LoNoWe H_s distribution and the conditional lognormal T_p distribution.	79
5.3. H_s , T_p values in the southern point for the three largest 50-year storms originating in the northern point.	81
5.4. Model test parameters	84
5.5. Testing the force and moment transducer.	87
5.6. Testing the force and moment transducer.	88
5.7. Vertical full scale pressure gauge positions.	89
5.8. The test matrix for regular waves.	96
5.9. The test matrix for irregular waves.	97
5.10. Full-scale theoretical regular wave heights at $h = 20.9$ m.	98
5.11. Full-scale theoretical regular wave heights at $h = 30$ m.	98
5.12. Theoretical regular wave Ursell numbers at $h = 20.9$ m.	98
5.13. Theoretical regular wave Ursell numbers at $h = 30$ m.	99
5.14. Theoretical regular wave regimes for $h = 20.9$ m.	99
5.15. Theoretical regular wave regimes for $h = 30$ m.	99
6.1. Model test parameters	106
7.1. Eigenperiods at the two water depths.	118
7.2. Linear and non-linear damping coefficients for each decay test.	120
7.3. Resulting effective wave periods and wave heights for each nominal steepness at $h=20.9$ m.	124
7.4. Resulting effective wave periods and wave heights for each nominal steepness at $h=30$ m.	126
7.5. Measured regular wave regimes for $h = 20.9$ m.	128
7.6. Measured regular wave regimes for $h = 30$ m.	128
7.7. Effective H_s , T_p values at $h=20.9$ m, considering all 20 seeds of each sea state.	139
7.8. Effective H_s , T_p values at $h=30$ m, considering all 20 seeds of each sea state.	139
7.9. Maximum loads for each sea state at $h=20.9$ m.	139
7.10. Maximum loads for each sea state at $h=30$ m.	139
7.11. The test matrix for special waves.	147

7.12. Seed-averaged percentage values for the significant wave height and peak period for all sea states at $h = 20.9$ m.	152
7.13. Seed-averaged percentage values for the significant wave height and peak period for all sea states at $h = 30$ m.	152

Nomenclature

$1P$	Rotational frequency	F_0	Harmonic force amplitude
$3P$	Blade passing frequency	F_D	Morison drag force
α	Steepness-dependent wave celerity parameter	F_I	Impulse force
ϵ	Wave steepness parameter	F_M	Morison inertia force
γ	JONSWAP peakedness parameter	F_N	Froude number
γ_m	Material factor	f_s	Sampling frequency
γ_f	Load factor	FLS	Fatigue limit states
Λ	Logarithmic decrement	H_b	Maximum wave height before breaking
λ	Scaling factor	H_s	Significant wave height
λ	Wavelength	HAT	Highest astronomical tide
λ_c	Breaking wave curling factor	I	Moment of inertia
μ	Dispersion/shallow water parameter	k_θ	Rotational stiffness
ω	Circular wave frequency	KC	Keulegan-Carpenter number
$\omega_{N/2}$	Nyquist frequency	LAT	Lowest astronomical tide
ϕ	TMA redistribution factor	m_n^ω	Spectral moments
ϕ_I	Incident wave potential	OWT	Offshore wind turbine
ϕ_s	Linear scatter potential	p_1	Linear damping coefficient
ψ	Higher-order scatter potential	p_2	Non-linear damping coefficient
σ	JONSWAP constant	P_a	Atmospheric pressure
ξ	Damping ratio	R	Stokes convergence parameter
ζ	Instantaneous free surface elevation	Re	Reynolds number
ζ_A	Wave amplitude	S	Wave steepness
ALS	Accidental limit states	S	Wavemaker stroke
C	Phase velocity	s	Wave penetration factor
c	Wetted surface length	$SDOF$	Single degree-of-freedom
c_θ	Rotational damping	SLS	Serviceability limit states
C_A	Added mass coefficient	t_d	Impulse duration
C_D	Drag coefficient	T_p	Spectral peak period
C_g	Group velocity	u_0	Static response
C_M	Inertia coefficient	U_r	Ursell parameter
C_p	Pressure coefficient	ULS	Ultimate limit states
C_s	Slamming coefficient	x_c	Characteristic environmental load effect
DAF	Dynamic amplification factor	X_k	Complex wave component
		y_c	Characteristic capacity
		z_s	Wheeler stretching vertical coordinate

1 | Introduction

After the installation of the first operative offshore wind turbine at the beginning of the 1990s, the technological development has been considerable and the industry has grown immensely. A main driver has been to bring down costs without compromising on safety, inducing a tendency to increase turbine dimensions, intuitively causing the structural loads to increase. The upscaling of these turbine loads has proven to be a non-trivial task, and some of the related challenges will be presented in this thesis.

Since 2008, the United Kingdom has been leading in the offshore wind field, having an installed capacity equivalent to that of the rest of the world combined [RenewableUK, 2015]. With an annual electricity production of over 13 TWh, British wind power supplies an equivalent of approximately 3.1 million residences.

The proposed wind farm at Dogger Bank outside the East coast of England and Statkraft's involvement in the project acts as the backdrop of this thesis work. The site boasts great wind conditions and shallow water depths, making it a well-suited location for a wind farm of monopile-foundation turbines.

In order to avoid over-conservatism in turbine design, and thus to reduce project costs, understanding the physical mechanisms inducing the largest loads is vital. Shallow water depths and strong winds introduce complex wave kinematics, of which models to accurately estimate forces are not well established. As turbine dimensions increase it is important to document the effect on loads and responses in order to maintain structural integrity and safety in turbine operation.

Compared to many other offshore structures, bottom-fixed wind turbines are very sensitive to dynamically amplified response, due to its relatively large and highly placed top mass. Thus, ringing, a not fully understood burst-like transient response phenomenon, is a concern in the industry. A major motivation of this thesis has been to explore the occurrence of ringing in experiments and to capture the phenomenon numerically.

The main objective of the work has been to perform experimental studies of wave loads in extreme sea states, in order to investigate how the largest response loads on an idling wind turbine develop. Deterministic and stochastic validation of theoretical higher-order wave load models has been a main part of the thesis scope.

Most bottom-fixed offshore wind turbines are placed in shallow-water regions where the possibility of breaking-wave impact may be significant for design. In

many of the design standards for OWTs, slamming from breaking waves is only included as an accidental load, much due to how the frequency and magnitude-dependent risk of large global slamming loads is considered low compared to that of other extreme wave loads. Investigating the significance of slamming from breaking waves, i.e. how the maximum loads compare with those from steep, non-breaking waves, will be an important part of the experimental post-processing.

The thesis includes four main segments: A review of design challenges related to the dimensional upscaling of bottom-fixed OWTs, a theoretical basis where models for kinematics and loads are presented, a part describing the execution and results of the experimental tests, and finally describing the development of the numerical model to be used in the validation of theoretical models.

As much of the literature study from the project thesis was deemed highly relevant for the master thesis, theoretical parts from sections 2, 3, 4 and 5.3 are reprinted directly from [Frimann-Dahl, 2014].

2 | Design Challenges for Large-Diameter Monopiles

Since the infancy of the commercial wind industry, the average wind turbine output ratings have grown. At the beginning of the 1980s the onshore turbines averaged at approximately 50 kW, and the output growth has been almost linear since then [Thresher et al., 2008]. The same trend has been observed for offshore turbines in the last years, resulting in large turbine dimensions. Vestas' V164-8.0 MW turbine, with a rotor diameter of 164 m, is currently the offshore wind turbine with the largest rated power output in the industry [Vestas, 2015]. A main driver in the growth of turbine dimensions can be understood by considering that the power output theoretically increases with the scaling factor squared (s^2) if geometrical similarity and linear scaling laws are assumed [Sieros et al., 2012]. Also, wind shear causes more energetic winds at larger altitudes, leading to an advantageous effect of placing the rotors higher. The cost (per MW installed) of maintenance and operation may also decrease by installing fewer but larger turbines for a given capacity wind park.

However, considering linear scaling, the mass of the turbine increases with the scaling factor cubed, s^3 . The difference in scale proportionality for power and mass is known as the square-cube law. According to [Twidell and Gaudiosi, 2009] engineering costs are roughly proportional to the mass, i.e. the material volume, so the costs of a growth in turbine dimensions will increase faster than the power output. Up to a certain point the design of wind turbines can overcome this by a continued optimization of material usage, securing a lower mass and thus reducing engineering costs. In addition, over-conservative industry standards have been altered to deal with this simplistic trend estimate [Thresher et al., 2008].

Challenges in creating large-scale offshore wind turbines thus lie in establishing standards that ensure sufficient safety in operation without becoming overly conservative. Also, a more complete understanding of the physics and the phenomena that may arise for larger dimensions are important when optimizing design of large turbines. Developing materials with extreme strength to mass ratios and more advanced control and measuring systems, ensuring reliability and safety, will be necessary for the feasibility of future large-turbine projects [Fichaux et al., 2011]. In this section, these challenges will be discussed in greater detail.

2.1. Upscaling offshore wind turbines

Many research projects have focused on aspects of upscaling wind turbine design, including DOWEC, UpWind, ICORASS and WindPact [Ashuri, 2012]. UpWind is especially interesting in this thesis as it deals with industry challenges at large, related to dimensional upscaling.

The UpWind consortium (2006-2011) was a European R&D collaboration consisting of 48 partners, counting wind energy specialists both from research institutions, academia and from the private sector. The project aimed at determining technological and economical obstacles to developing feasible large-scale offshore wind turbines. It focused on the physical phenomena and model behavior that are negligible for smaller turbines, but may be highly relevant when upscaling. Also, it examined scaling the standard NREL 5-MW reference turbine [Jonkman et al., 2009] to 20 MW, resulting in a rotor diameter of approximately 250 m [Fichaux et al., 2011]. The turbine was deemed clearly unfeasible, mostly because of a 880-tonne top tower mass and the fact that it was not possible to manufacture or install, in addition to being unprofitable. However, the project concludes that designing an operational 20-MW turbine is in fact feasible, given the development of some important innovations. The costs of some of these innovations are uncertain.

One example of such an innovation is the development of materials that can overcome the increased gravity load from the more massive rotor blades [Fichaux et al., 2011]. Instead of building heavier structures, UpWind investigated the idea of using smart control systems for individual blade pitching to reduce the aerodynamic loads. Also, they tested LIDAR assisted collective pitch control, where the upstream wind speed is measured in order to optimize pitch wrt. aerodynamic rotor loading. These are some of the innovations that can make future large-scale turbines feasible.

Two methods are often used in preliminary determination of turbine characteristics in upscaling; linear scaling and extrapolation of existing wind turbine data. Utilizing linear scaling laws, geometrical similarity is assumed, meaning that all geometrical parameters vary linearly except the gearbox, the generator and the power electronics. Furthermore, the tip speed is assumed constant [Ashuri, 2012].

In the extrapolation of existing data approach, trends in loading, component mass and costs are investigated with respect to the rotor diameter. Thus, estimations about larger turbines can be made. In some cases, such as in [Sieros et al., 2012], large scatter can occur because of differences in turbine design and wind

class. Intuitively, the uncertainties in upscaling increase with projected turbine size for any scaling method. Technical data from manufacturers for prospective large turbines are confidential, and thus the leap in turbine dimensions may be large in a trend analysis using extrapolated data.

Considering geometrical similarity and linear scaling laws, the increase in environmental turbine loads would be proportional to s^2 , the corresponding moments $\sim s^3$, whilst the bending stiffness $EI \sim s^4$. However, upscaling wind turbine loads is not a trivial task and in order to achieve realistic structural loads and responses, more sophisticated models must be employed than the two described above. Non-linear structural behavior and higher-order loads must be investigated in order to take higher-order effects into account. An example of such an effect is ringing, which will be covered in section 3.6. Many other phenomena that are not linearly scalable, are mentioned in [Sieros et al., 2012]. They include boundary layer effects, the probability of buckling or fracture, non-linearities related to large deflections, effects of inflow turbulence and variation in design choices. Thus, integrated analyses must be performed in order to capture the change in physical effects. In a coupled system with aerodynamic and hydrodynamic loads on a wind turbine, load contributions consisting of many different frequencies are present. Several unsteady aerodynamic phenomena resulting in oscillating aerodynamic forces, such as turbulent eddies, occur at the frequency of rotor rotation or multiples of this frequency. The rotational frequency is called 1P and the blade passing frequency 3P is three times 1P, relevant for a three-bladed turbine.

A problem that may occur in the upscaling of turbine loads is the interaction between the 6P frequency and the 2nd tower mode. This is due to the fact that the 2nd tower mode eigenfrequency decreases with a growth in turbine dimensions, in some cases closing in on the 6P frequency. Figure 2.1 illustrates this interaction, as the 2nd tower mode eigenfrequency and 6P frequency almost coincide. This is a driver in the design against fatigue. In order to optimize turbine design, the balance between ULS and FLS driven loads is vital, as dimensioning against one of these is often at the expense of the other. The balance is very dependent on the non-linearities in ULS loading [Suja-Thauvin et al., 2014].

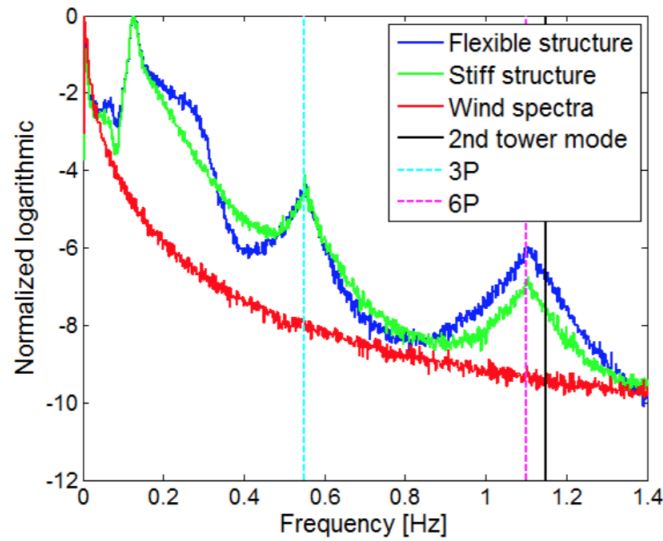


Figure 2.1.: Interaction between 6P and the 2nd tower mode [Suja-Thauvin et al., 2014].

In [Ashuri, 2012], an integrated aero-servo-elastic cost optimization procedure is employed to create an optimal 20-MW offshore wind turbine design. The drawback to such an approach is the huge design space of which the engineer needs to constrain. The conclusion of this study is, similarly to that of [Fichaux et al., 2011], that an upscaling to 20 MW is granted some key innovations. The main concern is the excessive growth in turbine mass. [Ashuri, 2012] points at five challenges in the upscaling:

- *Blade mass increase* (due to additional material in order to provide necessary blade stiffness). Solution: Utilizing materials with larger stiffness to mass ratios.
- *Tower mass and cost increase* (due to higher loads on the tower and an increase in tower top mass). Solution: Reductions in mass and loading (e.g. by developing more efficient control systems).
- *Blade root thickness* (in order to supply sufficient strength at the blade root). Solution: Designs are already feasible, but challenging for the engineer.
- *Blade and tower size* (due to the limited possibilities of component transportation on land). Solution: Upgrading infrastructure and transport vessels.

- *Nacelle installation* (due to the increase in tower height and nacelle weight).
Solution: Requires special installation vessels with improved carrying and lifting capabilities.

One of the primary challenges for the wind power industry will be to evaluate the necessary innovations from an economical and technical perspective.

2.2. Dynamic response of offshore wind turbines

Like most other offshore structures a wind turbine consists of several components, each with their own natural frequency. What differs an offshore wind turbine from other offshore structures, however, is the high degree of coupling between the structural components. This can be exemplified as large blade oscillations excite resonant motion in the tower, or vice versa, fast oscillations in the tower structure can dramatically change the incident wind load on a turbine blade [Hansen, 2008]. As mentioned, this means that the structural, aerodynamic and hydrodynamic models must be solved together, in fully aero-hydro-servo-elastic simulations.

The dynamic amplification factor DAF, is the ratio between the dynamic and static response:

$$DAF = \frac{u}{u_0} = \frac{u}{F_0/k} \quad (2.1)$$

where u_0 is the static response ($u_0 = \frac{F_0}{k}$, where $F = F_0 \cos(\omega t)$) and u is the dynamic response. The DAF is designed for harmonic excitation, as it is a function of F_0 .

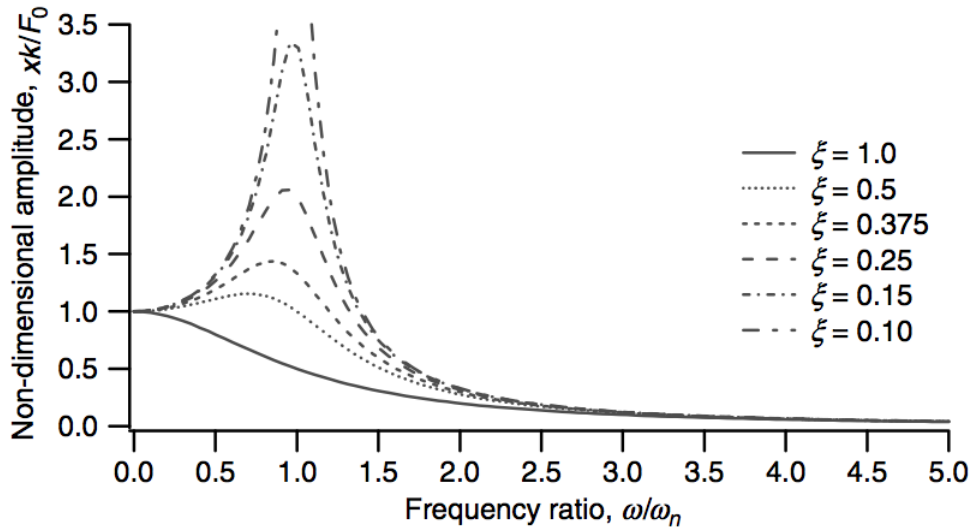


Figure 2.2.: A DAF for different damping levels [Manwell et al., 2009].

Figure 2.2 shows that the DAF depends on the damping level, and the response is intuitively reduced as the damping level is increased. For an undamped system the response will be infinite. The maximum response occurs at resonance i.e. $\beta = 1$.

2.3. Standard regulations in the design of offshore wind turbines

When designing offshore structures, handling uncertain environmental loads is inevitable. To consider design loads and in order to set up design criteria [Det Norske Veritas, 2014] describes four limit states relevant for offshore wind turbines:

- Ultimate limit states (ULS)
- Fatigue limit states (FLS)
- Accidental limit states (ALS)
- Serviceability limit states (SLS)

The limit states define the conditions by which a structure can operate according to the design requirements. The standards provide design criteria according to certain levels of load annual excess probabilities that the structures should be

dimensioned for. In [Det Norske Veritas, 2014] four main design approaches are used:

- Design by the partial safety factor method
- Design by direct simulation of combined load effect of simultaneous load processes
- Design assisted by testing
- Probability-based design

In the partial safety factor method the design criteria involve safety factors for each load contribution and structural component. These factors are determined such that an acceptable level of safety is satisfied, even for especially disadvantageous realizations of loads and structural resistance, or a combination of these. When the loads are considered, the following factors should be taken into account, regardless of design technique:

- Unfavorable load deviations off their characteristic values
- The possibility that different loads exceed their characteristic values simultaneously
- Uncertainties in the load effect modeling

In this thesis, the design assisted by testing method will be explored in part, by conducting experiments aiming to map the hydrodynamic loads on an idling turbine. Since only one environmental load is taken into account, no combined load effects are considered. Thus, if used in design, the hydrodynamic loads must be included in a procedure much like that of the partial safety factor method, where each environmental load is considered separately with a specified set of safety factors. The standard specifies that dimensioning assisted by performing model tests has to be supported by analytical design approaches.

2.3.1. Ultimate limit states (ULS)

The ultimate limit states define limits for a structure's maximum load-carrying capacity. Exceeding the ULS can lead to excessive yielding or buckling, brittle fracture, loss of static equilibrium (e.g. capsizing or overturning) or failure of critical components.

The characteristic value of the resulting combined load effect for design against ULS is defined by the 98 % quantile, i.e. an annual probability of exceedance \leq

0.02, meaning a 50-year return period. This is relevant in a more complete analysis than in this thesis, where no combined load effects will be considered.

Load factors γ_f are used both in operational and temporary conditions. For ULS, the load factors from permanent, variable functional and deformation loads are 1.0 in most cases. However, for environmental loading the load factors are 1.35 when the characteristic load is established as the 98 % quantile or 1.1 for abnormal wind load cases. In a situation where the permanent and the variable functional load factors are increased to 1.25, the environmental load factor can be reduced to 0.7, except when the environmental loads are to be combined with functional ship loads. These factors are summarized in [Det Norske Veritas, 2014].

2.3.2. Fatigue limit states (FLS)

The fatigue limit states are concerned with the possibilities of failure due to the cumulative damage effect of cyclic loading. Instead of looking at a certain quantile (as for ULS), the characteristic load effect history is determined by the expected load effect history, i.e. the load factors γ_f are 1.0 for all load categories. For FLS, cyclic loads may occur in the non-operational stages of structure life. These loads have to be included in the calculations of cumulative damage.

2.3.3. Accidental limit states (ALS)

The accidental limit states take into account loads caused by technical failure or generally abnormal operations, such as ship collisions, accidental crane drops, explosions, fire or slamming loads from rarely large breaking waves. ALS ensure structural integrity of locally damaged structures or flooding, as well as adequate structural resistance of the actual accidental load. In the design against ALS the annual probability of exceedance of the accidental load magnitude should not exceed 10^{-4} [NORSOK, 2007]. The partial safety factors are set to 1.0.

When an accident has occurred, minor local damage is tolerable. In such a damaged state, the structure should be able to survive environmental loads with an annual probability of exceedance of 10^{-2} . Thus, the ALS need to be checked on two levels [NORSOK, 2004].

[Haver, 2007] argues the importance of considering the 10^{-4} annual probability of exceedance ALS environmental loads. Four quantities are defined: The characteristic environmental load effect x_c is the load effect corresponding to a 10^{-2} annual probability of exceedance and the characteristic capacity y_c is taken as a

lower percentile of the distribution of elastic component capacity. γ_m and γ_f are material and load factors, respectively.

$$\gamma_f x_c \leq \frac{y_c}{\gamma_m} \quad (2.2)$$

Whilst the distribution function on the capacity side, y_c/γ_m , is usually well behaved, the nature of the load mechanism is not. This means that for very low annual-probability loads, the actual loads may be significantly greater than the estimated characteristic load. Thus, the design against ALS will only be sufficient if there is no significant shift in the shape of the tail of the load distribution in the 10^{-4} - 10^{-2} annual exceedance probability range.

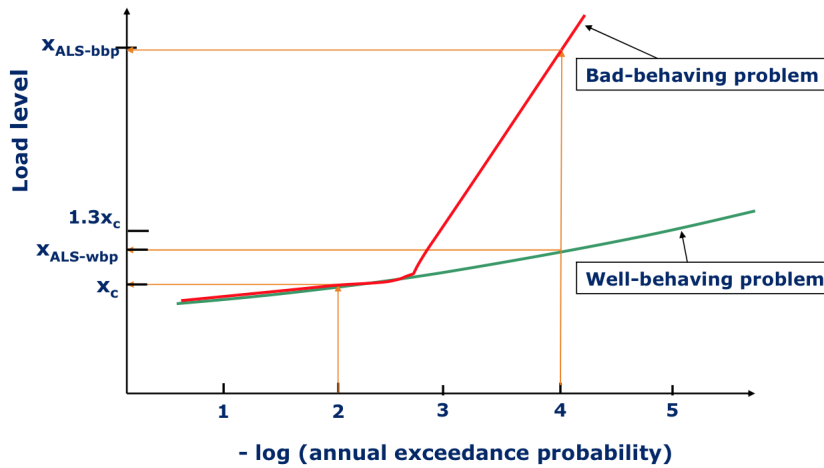


Figure 2.3.: Behavior of the distributions of environmental load mechanisms [Haver, 2007].

As figure 2.3 shows, for a ‘bad-behaving’ load mechanism, $\gamma_f x_c = 1.3 x_c \ll x_{ALS-bbp}$. Thus, the environmental load mechanism must be examined for annual exceedance probabilities much smaller than 10^{-2} . This is especially important for old structures, as the structural behavior alters over time. Similarly, as will be discussed in section 7.7, such ‘bad behavior’ in loading is relevant when considering non-linear phenomena, such as ringing.

2.3.4. Serviceability limit states (SLS)

The serviceability limit states define the tolerances for normal use of the structure. Examples of when SLS are used can be deflections or deformations of components,

which change the distribution of loads or the effect of the acting forces. Another example is vibrations in offshore structures causing discomfort.

For SLS the characteristic load effects depend on the specific operational requirements in each deviational case.

The load factors γ_f are 1.0 for all load categories, both for temporary and operational conditions.

2.3.5. Transient loads

Several operational states cause transient loads that should be considered for both ULS and FLS. These states are:

- Start up from stand-still or idling
- Normal shutdown
- Emergency shutdown
- Fault events
- Yawing

In [Det Norske Veritas, 2014] table 4-5, load cases containing different combinations of environmental loads are proposed in order to test the wind turbine in the operational states listed above. It provides 31 different load cases, each of which require approximately six 10-minute stochastic realizations, and in addition a range of wind speeds need to be considered. This amounts to around 2000 different load cases that have to be analyzed [Schlør, 2013].

The [IEC, 2006] standard contains similar operational states and 35 different load cases to analyze the structural integrity of the wind turbine during installation, operation and survival conditions.

In [NORSOK, 2007] it is stated that characteristic environmental loads should be elaborated analytically, if there are no significant uncertainties. If considerable uncertainties are present, however, the analytical results need to be verified against model tests.

3 | Wave Loads

3.1. Wave load components on an offshore structure

When calculating the wave loads on a structure, a wave theory able to represent the kinematics should be applied. The wave loads acting on a structure consist of both viscous and potential flow effects, and the kinematic wave models are derived assuming potential theory. This means that the fluid is assumed inviscid, i.e. viscous effects are not taken into account. The validity of wave theories will be discussed in section 3.5.3.

Force contributions from viscous effects:

- Viscous drag force
- Viscous pressure drag

The viscous drag force is due to frictional effects and thus depends on the Reynolds number Re and the relative roughness. The viscous pressure drag force is due to the pressure difference between the front and aft of the structure, i.e. separation effects. In other words, it depends on the width of the wake or position of the points of separation.

Force contributions from potential flow effects:

- Froude-Krylov force
- Diffraction force

The potential flow effects can be described by defining the diffraction and radiation problems, as done in [Greco, 2012]. In the diffraction problem, the body is assumed fixed and interacting with incoming waves with a wave potential Φ_0 . The resulting diffraction potential consists of two contributions, the incoming wave potential Φ_0 and the scattering potential Φ_S , giving

$$\Phi = \Phi_0 + \Phi_S \quad (3.1)$$

The impermeability condition specifying the impenetrability of a body, is introduced as

$$\frac{\partial \phi}{\partial n} = \frac{\partial(\phi_0 + \phi_S)}{\partial n} = 0 \quad (3.2)$$

using the spatial potentials.

The flow from ϕ_0 is assumed to penetrate the body as if it wasn't there, with the velocity $\frac{\partial \phi_0}{\partial n}$. This hydrodynamic pressure causes Froude-Krylov loads on the body.

In order for it to maintain its impermeability the diffraction/scattering potential is created such that equation (3.2) holds true. This means that

$$\frac{\partial \phi_S}{\partial n} = -\frac{\partial \phi_0}{\partial n} \quad (3.3)$$

The scattering potential causes hydrodynamic loads on the body called diffraction loads. Summing the contributions of the diffraction problem gives the excitation forces, i.e.

$$\begin{aligned} F_{exc,k}(t) &= F_{Froude-Krylov,k}(t) + F_{diffraction,k}(t) \\ &= -\int_{S_{0B}} \rho \frac{\partial \Phi_0}{\partial t} n_k dS - \int_{S_{0B}} \rho \frac{\partial \Phi_S}{\partial t} n_k dS \end{aligned} \quad (3.4)$$

where S_{0B} is the mean wetted surface of which the dynamic pressure contributions are integrated over.

In the radiation problem the structure is forced into oscillation in all six degrees of freedom with no incoming waves. This causes radiated waves with potential Φ_R . Similarly as for the diffraction problem, the potential can be integrated over the mean wetted surface. The resulting hydrodynamic terms are the added mass and damping forces, whereas the restoring force is connected with hydrostatics. The radiation problem is especially important for floating structures as they will have large displacements.

$$F_{exc,k}(t) = -\int_{S_{0B}} \rho \frac{\partial \Phi_R}{\partial t} n_k dS = \sum_{j=1}^6 [-A_{kj} \ddot{\eta}_j - B_{kj} \dot{\eta}_j], \quad k = 1, \dots, 6 \quad (3.5)$$

For a cylinder whose diameter is in the same order of magnitude as the wavelength, the inertia forces dominate, meaning that the drag forces are generally at least an order of magnitude smaller than the inertia forces. For a smaller structure ($\frac{D}{\lambda} \ll 1$) the drag force influence will be greater. Thus, using Froude scaling, the drag force coefficient on a model will be greater than in full scale.

In this thesis, the focus is on large-diameter monopiles. When dimensions increase the eigenfrequencies are decreasing, thus creating more inertia-dominated systems. This implies that the system inertia is too large for the displacement to mobilize stiffness forces, so dynamic equilibrium is acquired through inertia forces. In extreme cases the dominating load frequencies are considerably higher than the

first natural frequency. For harmonic loading, the dynamic equilibrium is given by

$$m\ddot{u} + c\dot{u} + ku = F_0 \sin\omega t \quad (3.6)$$

As seen in figure 3.1, the phase angle for a completely inertia-dominated system is π because of the large $\frac{\omega}{\omega_n}$ ratio. Thus, the harmonic load, displacement, velocity and acceleration will be as follows [Larsen, 2012]:

$$F(t) = F_0 \sin\omega t \quad (3.7)$$

$$u(t) = u_0 \sin(\omega t - \pi) \quad (3.8)$$

$$\dot{u}(t) = u_0 \omega \cos(\omega t - \pi) \quad (3.9)$$

$$\ddot{u}(t) = -u_0 \omega^2 \sin(\omega t - \pi) \quad (3.10)$$

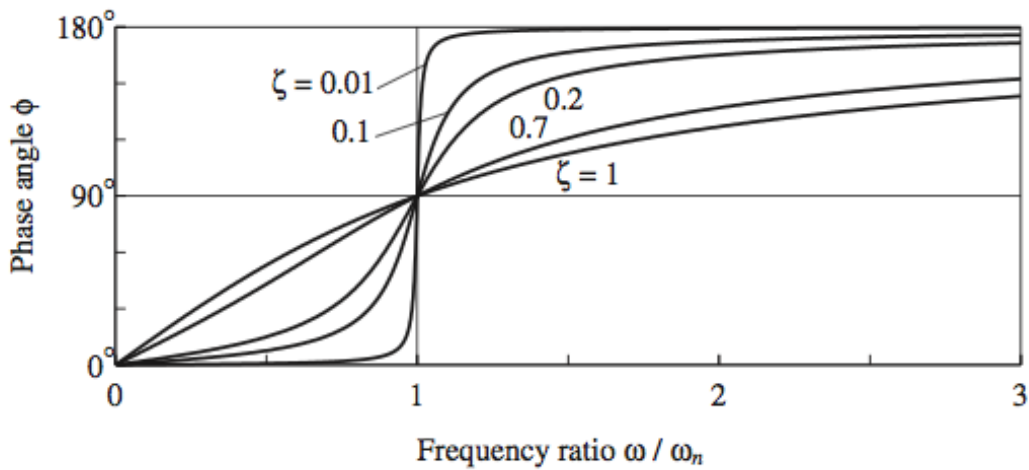


Figure 3.1.: The phase angle between a harmonic load and the response for different damping levels [Chopra, 2012].

The resulting dynamic response of a completely inertia-dominated structure is in counter phase ($\phi = \pi$) with the excitation, as shown in figure 3.2.

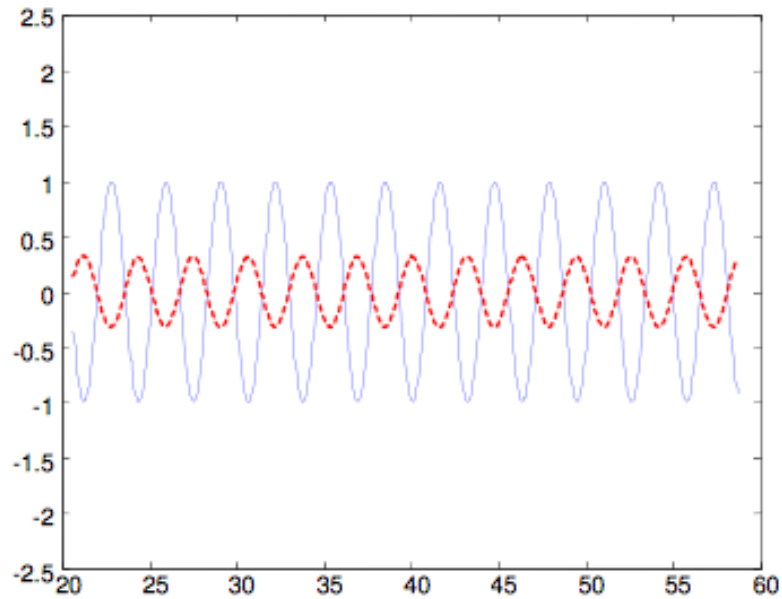


Figure 3.2.: The response of an inertia-dominated SDOF system in time. The solid line is the excitation $F(t)$ whilst the dashed red line is the resulting displacement $x(t)$. The figure is taken from [Tempel, 2006].

At the instance of maximum loading, $\omega t = \frac{\pi}{2}$, the dynamic equilibrium will be given by

$$\omega^2 u_0 m = F_0 + k u_0 \quad (3.11)$$

where the $\omega^2 u_0 m$ term is dominating because of the high load frequency ω . As can be seen in equation (3.11) the stiffness forces increase the response in this case. The external forces and stiffness forces are balanced by the inertia force.

The relative importance of inertia, drag and diffraction is illustrated in figure 3.3.

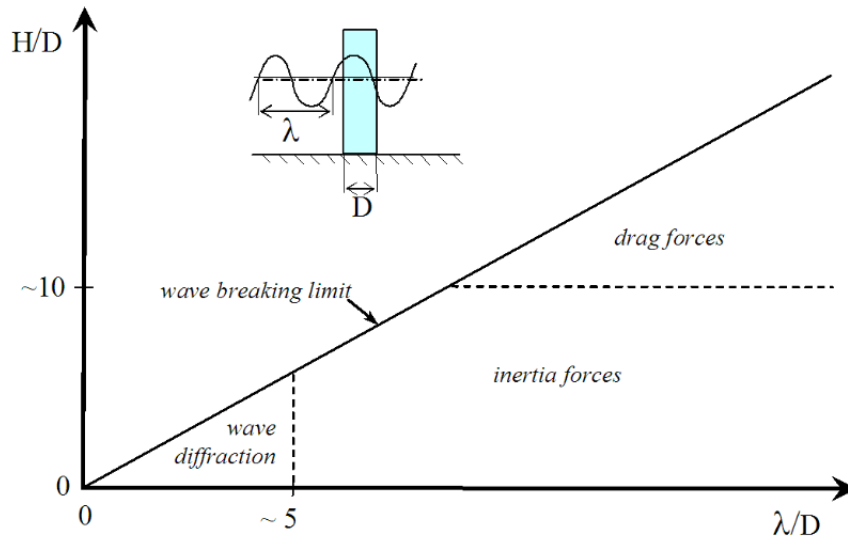


Figure 3.3.: Relative importance of inertia, drag and diffraction wave forces [Det Norske Veritas, 2014].

For slender structures figure 3.4 gives an overview of the magnitude ratio of drag and inertia forces.

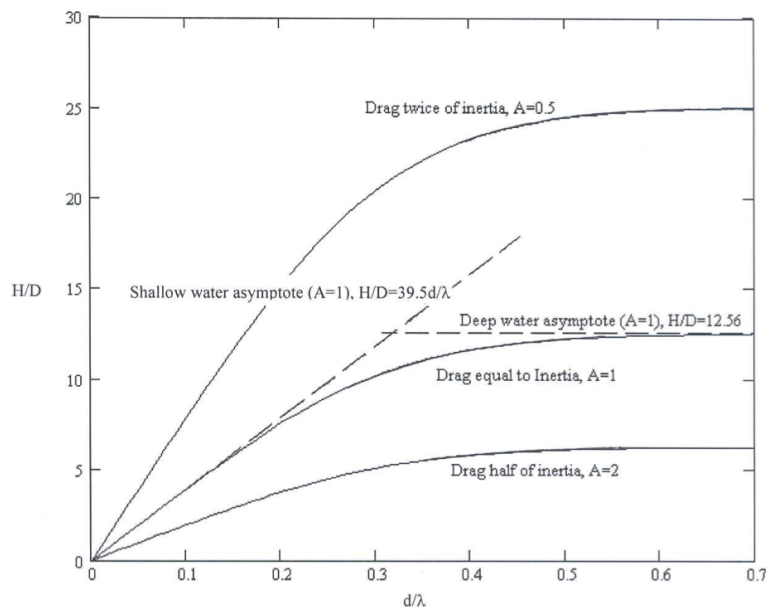


Figure 3.4.: Relative magnitude of drag and inertia forces for slender structures [Det Norske Veritas, 2014].

For small volume structures, $D < \frac{\lambda}{5}$, the Morison equation can be used, whereas for large volume structures, $D > \frac{\lambda}{5}$, diffraction has to be taken into account, so MacCamy & Fuchs theory should be applied.

3.2. Slender structures

As mentioned, the Morison equation can be used to estimate forces on slender structures, i.e. $D < 0.2\lambda$ in [Det Norske Veritas, 2014], assuming that the flow is undisturbed by the presence of the body. In equation (3.12) the horizontal force on a vertical cylindrical section of height dz is calculated.

$$dF = dF_M + dF_D = C_M \rho \pi \frac{D^2}{4} \ddot{x} dz + C_D \rho \frac{D}{2} |\dot{x}| \dot{x} dz \quad (3.12)$$

where C_D and C_M are the drag and inertia coefficients, respectively. The first term, the inertia force, consists of the Froude-Krylov and diffraction force. When $C_M = 2.0$ it is in agreement with potential theory. The second term, the drag force, represents the viscous effects. The drag coefficient must be found empirically, but [Det Norske Veritas, 2014] offers a method by which C_D can be estimated.

Integrating over the submerged cylinder length, the resulting horizontal force for non-breaking waves is given by

$$F = F_M + F_D = \int_{-d}^{\eta(t)} C_M \rho \pi \frac{D^2}{4} \ddot{x} dz + \int_{-d}^{\eta(t)} C_D \rho \frac{D}{2} |\dot{x}| \dot{x} dz \quad (3.13)$$

When integrating up to $z = 0$, neglecting the contribution from $z = 0$ to $z = \eta(t)$, a much smaller error will be introduced for an inertia-dominated system than a drag-dominated system since the maximum inertia force occurs when the wave elevation past the cylinder is at $z=0$ (maximum acceleration), whereas the the drag force has its maximum as the crest passes the cylinder (maximum velocity).

The phase difference between the two force contributions can be seen in figure 3.5.

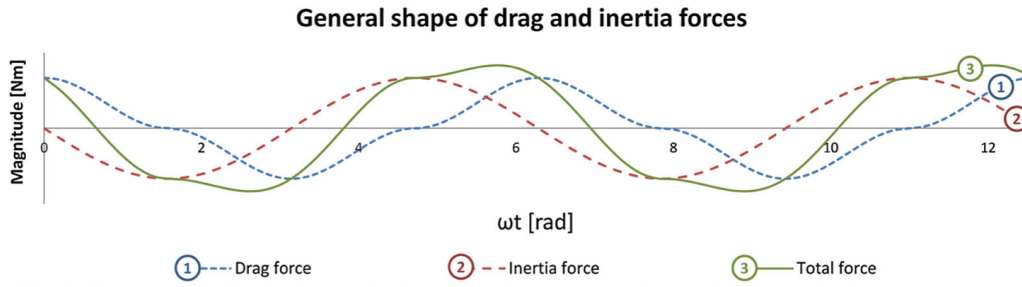


Figure 3.5.: The general shape of the Morison equation terms [Arany et al., 2014].

For an inertia-dominated structure the relative force contributions could be like in figure 3.6.

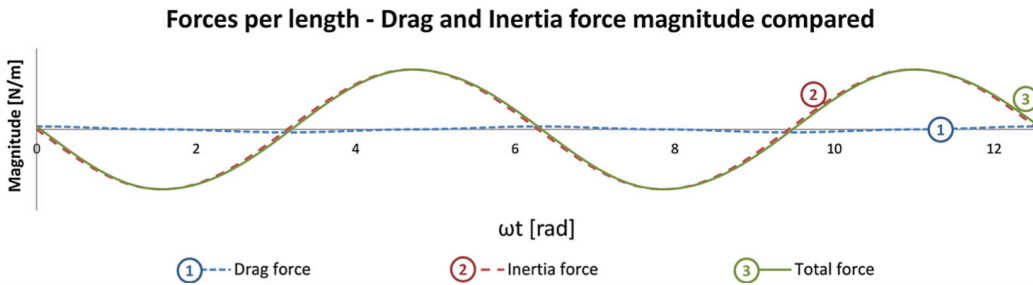


Figure 3.6.: Force contributions in an inertia-dominated system [Arany et al., 2014].

The Morison equation can also be expanded to include the relative motion of the wind turbine response and the fluid particles [Faltinsen, 1990]:

$$dF = \rho(1 + C_A) \frac{\pi D^2}{4} dz a_1 - \rho C_A \frac{\pi D^2}{4} dz \ddot{\eta}_1 + \frac{1}{2} \rho C_D D dz (u - \dot{\eta}_1) |u - \dot{\eta}_1| \quad (3.14)$$

where C_A is the added mass coefficient and $C_M = 1 + C_A$ is the inertia coefficient. $\ddot{\eta}_1$ and $\dot{\eta}_1$ are the horizontal turbine acceleration and velocity, respectively, and a_1 and u are the horizontal water acceleration and velocity.

3.3. Large-volume structures

For larger structures, specified as $D > 0.2\lambda$ in [Det Norske Veritas, 2014], the diffraction and reflection effects of the structures' presence can no longer be neglected. For these structures, the inertia force will be dominating and diffraction

theory must be used (see figure 3.3).

On a form equivalent to the Morison equation, considering linear wave theory, the large volume inertia coefficient can be given as a function of ka , where a is the cylinder radius [Chakrabarti, 1989]:

$$C_M = \frac{4}{\pi(ka)^2 \{ [J_1'(ka)]^2 + [Y_1'(ka)]^2 \}^{1/2}} \quad (3.15)$$

Here, J_1' and Y_1' are order one Bessel function derivatives of first and second kind, respectively. The phase between the maximum force on the pile and the incoming wave is

$$\tan \delta = \frac{J_1'(ka)}{Y_1'(ka)} \quad (3.16)$$

In [Det Norske Veritas, 2014] the horizontal large-volume maximum force is found through

$$F_{X,max} = \frac{4\rho g A \sinh[k(d + A \sin \alpha)]}{k^2 \cosh[kd]} \xi \quad (3.17)$$

and the moment arm about the seabed is

$$h_F = d \frac{kd \sinh[kd] - \cosh[kd] + 1}{kd \sinh[kd]} \quad (3.18)$$

where α and ξ are coefficients depending on kD , found in the standard. Equation (3.17) is valid for vertical cylinders with constant diameter. The diffraction solution is called the MacCamy & Fuchs solution, which is based on the assumption that the diffracted waves are sinusoidal.

3.4. Non-linear forces on a structure

Several effects create non-linear forcing on an offshore structure. The most important ones will be discussed briefly in this section.

In an irregular sea a structure will be impacted by varying second-order sum and difference frequency forces in addition to the loading from dominating wave frequencies [Haver, 2007]. The non-linear force terms are typically much smaller than the linear terms, but they are important to account for since their frequencies may coincide with the natural frequencies of the structure. In the development of non-linear waves, energy is distributed to higher and lower frequencies in the wave

spectrum, meaning that the probability of wave component frequencies coinciding with the structure's first eigenfrequency increases [Schl er, 2013].

There are different approaches to evaluating the magnitudes of the non-linear force terms, e.g. using a perturbation scheme (see the sections on Stokes waves (3.5.2.1) or the FNV model (3.6.1)) or considering the conservation of energy (as done in the derivation of the Rainey force model).

Non-linearities also occur as the motions of a body modifies the pressure and thus the force acting on it. In many cases, turbine responses are negligibly small at sea level, so they are not necessary to include in force calculations. In slamming loads from breaking waves, however, structural vibration can have a large effect on the global load.

Since the wave loads on a structure depend on the relative motion, irregular waves should be used in order to establish a realistic response pattern. However, non-linearity has often been neglected for irregular waves. A remedy has been to use linear irregular waves and e.g. fully non-linear stream function waves (valid for regular waves on a flat sea bed) in order to estimate extreme ULS wave loading. The idea behind this embedded stream theory method is to account for both the non-linear wave kinematics and the stochastic nature of the wave process. In short, the embedding theory includes both conservative and non-conservative aspects. It is conservative in the sense that the resulting accelerations and velocities are large, and non-conservative since higher-order harmonic resonance is not taken into account, as for the FNV model (which will be described in section 3.6.1). Even though the embedded stream function model is excessively used in the industry, the method is highly debated in academia. The major concern is that the inclusion of a non-real wave elevation in the largest maxima (the points of largest interest in a ULS analysis), means that there is no way to perform a quality check of the output force from a hydrodynamic point of view.

Integrating the Bernoulli pressure over the wetted surface to obtain the hydrodynamic force means integrating one linear term of the velocity potential and one squared velocity potential term. If the velocity potential is linear the squared term causes second-order effects. Higher-order velocity potentials cause non-linear effects of the same order, as well as the order squared. Since a monopile can be considered slender in most cases, the non-linear effects from the higher-order potentials are most important for the incident waves as the presence of the pile will not alter the incoming waves significantly [Rosenlund, 2013].

In addition, a variation in the wetted surface of which the pressure is integrated

over leads to a higher-order term, since both the pressure and upper integration limit depend on the incident surface elevation.

3.5. Wave kinematics

3.5.1. Linear wave theory

Linear waves are relevant when considering small-amplitude waves, i.e. waves with a small slope $\epsilon = \frac{2\pi\zeta_A}{\lambda} \ll 1$. Here, ζ_A is the wave amplitude and λ is the wavelength. For a sinusoidal wave, this wave steepness can easily be derived by finding the derivative of the wave profile, $\frac{d\zeta}{dx} = \frac{d}{dx}(\zeta_A \sin kx) = \zeta_A k \cos kx$. In addition to small-amplitude waves, the sea bottom is assumed horizontal and the free surface is horizontally infinite. Linear wave theory is often used as a first approximation in engineering practice and it is highly relevant for ocean engineering, where the water depth is large.

When the wave slope is small the distance between the unknown free surface and the horizontal mean free surface $z = 0$ is of the order $O(\epsilon)$. We can simplify the dimensionless wave potential $\Phi' = \frac{2\pi}{\zeta_A \omega \lambda} \Phi$ by Taylor expanding it and neglecting the non-linear terms, as in [Mei et al., 2005]. The methodology leads to the following approximate kinematic and dynamic boundary conditions on the free surface:

$$\frac{\partial \zeta'}{\partial t'} = \Phi'_{z'}, \quad z' = 0 \quad (3.19)$$

$$\frac{\partial \Phi'}{\partial t'} + \frac{2\pi g}{\omega^2 \lambda} \zeta' = -P'_a, \quad z' = 0 \quad (3.20)$$

where $\zeta' = \frac{\zeta}{\zeta_A}$, $z' = \frac{2\pi z}{\lambda}$ and $P'_a = -\frac{2\pi P_a}{\rho \zeta_A \omega^2 \lambda}$.

The only remaining terms are linear. If the boundary conditions are used for the known horizontal plane $z' = 0$ the following physical linear equations can be derived:

$$\nabla^2 \Phi = 0, \quad -h < z < 0 \quad (3.21)$$

$$\frac{\partial \Phi}{\partial n} = 0, \quad z = -h \quad (3.22)$$

$$\frac{\partial \zeta}{\partial t} = \frac{\partial \Phi}{\partial z}, \quad z = 0 \quad (3.23)$$

$$\frac{\partial \Phi}{\partial t} + g\zeta = -\frac{P_a}{\rho}, \quad z = 0 \quad (3.24)$$

which are the Laplace equation, the bottom kinematic, free-surface kinematic and the free-surface dynamic boundary conditions, respectively.

The free-surface dynamic and kinematic boundary conditions can be combined to

$$\frac{\partial^2 \Phi}{\partial t^2} + g \frac{\partial \Phi}{\partial z} = -\frac{1}{\rho} \frac{\partial P_a}{\partial t}, \quad z = 0 \quad (3.25)$$

The Bernoulli equation can also be linearized, expressing the total pressure inside a fluid:

$$\frac{P}{\rho} = -gz - \frac{\partial \Phi}{\partial t} \quad (3.26)$$

In the derivation of the velocity potential for a propagating linearized wave, a special form of the free surface is used:

$$\zeta(x, z, t) = \text{Re}\{Ae^{i(\mathbf{k} \cdot \mathbf{x} - \omega t)}\} = A \cos(\mathbf{k} \cdot \mathbf{x} - \omega t) \quad (3.27)$$

where the the real sign is often omitted for brevity, yielding:

$$\zeta(x, z, t) = Ae^{i(\mathbf{k} \cdot \mathbf{x} - \omega t)} \quad (3.28)$$

This surface elevation is seen to oscillate periodically with period $T = \frac{2\pi}{\omega}$ for a stationary observer. The wave oscillates around a mean free surface at $z=0$ with extremes at $z=-A$ and $z=A$. The wavelength is $\lambda = \frac{2\pi}{k}$.

A solution of the Laplace equation is seen to be

$$\Phi(x, z, t) = [A \sinh k(z+h) + B \cosh k(z+h)] e^{i(kx - \omega t)} \quad (3.29)$$

where A and B are constants.

Using the bottom boundary condition for a horizontal seabed ($\frac{\partial \Phi}{\partial z} = 0$, $z = -h$), the sinh term can be removed, giving:

$$\Phi(x, z, t) = B \cosh k(z+h) e^{i(kx - \omega t)} \quad (3.30)$$

In order to satisfy the free-surface boundary conditions, the constant B must be

$$B = -\frac{ig\zeta_A}{\omega} \frac{1}{\cosh kh} \quad (3.31)$$

giving

$$\Phi(x, z, t) = -\frac{ig\zeta_A}{\omega} \frac{\cosh k(z+h)}{\cosh kh} e^{i(kx - \omega t)} \quad (3.32)$$

In the derivation of B, $P_a = 0$ is assumed.

The dispersion relation on finite depth is found by using the combined free-surface boundary condition, resulting in

$$\omega^2 = gk \tanh kh \quad (3.33)$$

The speed of the wave form, which is called the ‘phase speed’, is given by

$$C = \frac{\omega}{k} = \sqrt{\frac{g}{k} \tanh kh} \quad (3.34)$$

For propagating linear waves, longer waves have higher phase speeds. This phenomenon is called ‘dispersion’.

As $\tanh kh \rightarrow 1$ when $kh \rightarrow \infty$, the phase speed for short waves/deep water can be written

$$C = \frac{g}{\omega} = \sqrt{\frac{g}{k}} \quad (3.35)$$

For $\tanh kh \rightarrow kh$ when $kh \rightarrow 0$, the phase speed of long waves/shallow water is

$$C = \sqrt{gh} \quad (3.36)$$

The features of propagating waves in deep and shallow water are summarized in [Mei et al., 2005]:

On deep water, $kh \gg 1$

$$(\phi, u, v, w, p) = \left(-\frac{ig}{\omega}, \frac{gk}{\omega}, 0, -\frac{igk}{\omega}, \rho g\right) \zeta_A e^{kz} e^{i(kx - \omega t)} \quad (3.37)$$

On shallow water, $kh \ll 1$

$$(\phi, u, v, w, p) = \left(-\frac{ig}{\omega}, \frac{gk}{\omega}, 0, 0, \rho g\right) \zeta_A e^{i(kx - \omega t)} \quad (3.38)$$

The shallow water results show that:

- the z-dependence disappears
- the vertical velocity is negligible
- the total pressure is $P = \rho g(\zeta - z)$, meaning a hydrostatic total pressure, since the dynamic pressure is $\rho g\eta$

The z-dependence for different depths is illustrated in figure 3.7. The water

depths at Dogger Bank are between 20 m - 45 m and thus characterized as intermediate in most cases.

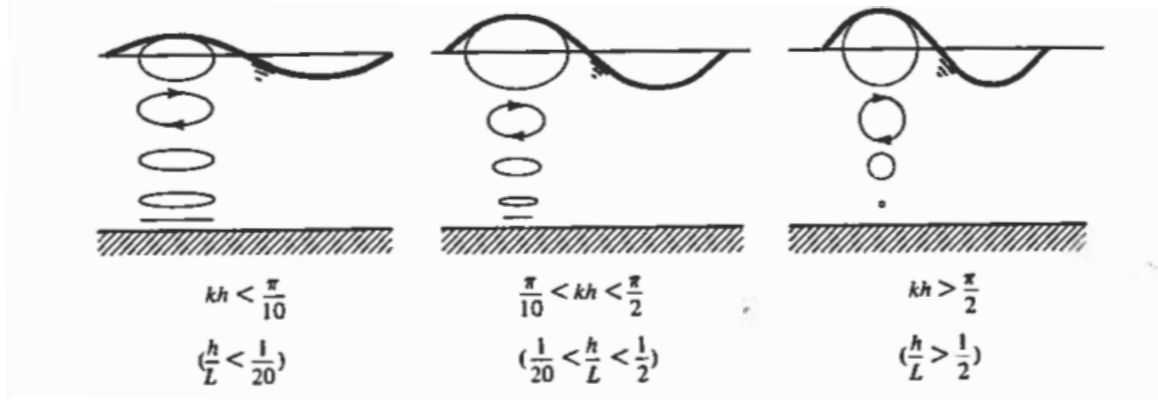


Figure 3.7.: z-dependence illustrated for linear waves in shallow, intermediate and deep water [Dean and Dalrymple, 1991].

Another velocity used to describe waves is the group velocity. This is the velocity of wave energy transport, or the velocity of the envelope amplitude around a locally sinusoidal wave train. At constant depth the group velocity is found by

$$C_g = \frac{d\omega}{dk} = \frac{C}{2} \left(1 + \frac{2kh}{\sinh 2kh} \right) \quad (3.39)$$

$\sinh kh \rightarrow 1$ for $kh \rightarrow \infty$ and $\sinh kh \rightarrow kh$ for $kh \rightarrow 0$, giving $C_g \simeq \frac{1}{2}C$ on deep water and $C_g \simeq C$ on shallow water. This means that on deep water, the individual waves will travel faster than the group envelope.

3.5.2. Non-linear wave theories

Non-linear wave kinematics can be employed directly in the Morison equation (3.13) by implementing the particle velocities and accelerations.

All the wave theories discussed in this section are symmetric about a vertical plane and thus they cannot be used in the modelling of asymmetric wave profiles.

The Laplace equation is linear since the velocity potentials are of first order. When the free surface boundary condition is applied at the still water level $z = 0$ there are no non-linear effects and the solution is thus linear. However, if the boundary condition is taken at the instantaneous free surface ($z = \zeta$) non-linear terms are introduced in the solution of the velocity potential. As the non-linear

velocity potential is valid up to the unknown surface elevation ζ , the problem at hand becomes complicated. A solution is a simplification using a combination of linear velocity potential contributions in a perturbation approach. This is known as Stokes wave theory.

3.5.2.1. Stokes wave theories

Stokes waves are periodic and found by a perturbation procedure of the flow variables such as the surface elevation or velocity potential, using the wave steepness $\epsilon = k\zeta_A$ as the expansion parameter. The wave steepness must be small ($\epsilon \ll 1$) as convergence is a measure of the validity of the Stokes waves, meaning that each term in the series must be smaller than the previous one. In fact, each of the velocity potential variables in equation (3.40) below is taken as having the same order of magnitude, so each term is smaller than the preceding one by a factor of $O(\epsilon)$. [Sarpkaya and Isaacson, 1981] gives the power series

$$\phi = \phi_1\epsilon + \phi_2\epsilon^2 + \phi_3\epsilon^3 + \dots O(\epsilon^n) \quad (3.40)$$

Substituting equation (3.40) into the the Laplace equation (3.41) and applying the seabed boundary condition, the velocity potentials can be found.

$$\frac{\partial^2 \phi_n}{\partial x^2} + \frac{\partial^2 \phi_n}{\partial z^2} = 0 \quad \text{for } n = 1, 2, \dots \quad (3.41)$$

$$\frac{\partial \phi_n}{\partial z} = 0 \quad \text{at } z = -d \quad \text{for } n = 1, 2, \dots \quad (3.42)$$

By collecting the terms proportional to each order of the wave steepness (as in equation (3.40)) the different wave potentials can be derived by letting each Laplace term be equal to zero, as shown equation (3.41).

1st-order Stokes theory is defined by the first term in the series, 2nd-order Stokes theory by the first two terms, and so on. Thus, 1st-order Stokes theory is in fact equal to linear wave theory. For each additional order of ζ_A^n a new harmonic will be introduced, so the nth-order solution will have a component oscillating with the nth harmonic of the wave circular frequency ω .

The solution has now been simplified, but the surface elevation ζ is still unknown. An approximate solution can be found by Taylor expanding the velocity potential

around $z = 0$, as done in [Sarpkaya and Isaacson, 1981]:

$$\phi(x, \zeta, t) = \phi(x, 0, t) + \zeta \frac{\partial \phi(x, 0, t)}{\partial z} + \frac{1}{2!} \zeta^2 \frac{\partial^2 \phi(x, 0, t)}{\partial z^2} + \dots \quad (3.43)$$

The free surface boundary condition is satisfied at a known surface $z = 0$ and thus a velocity potential solution can be found. By substituting the power series expression (3.40) into the resulting free surface boundary equations a successive approximation consisting of sets of linear equations can be found. The first order equation is homogeneous, whereas the second order equation is inhomogeneous and depends on the first-order potential. So it continues, each successive solution depending on the previous order potential. This results in a solvable system up to any velocity potential order. The algebra needed to obtain each solution becomes more extensive for every additional order, a tedious exercise if performed by hand. This was first done in [Skjelbreia and Hendrickson, 1962] up to fifth order.

In finite water depth, the following velocity potential and surface elevation are found for 2nd-order Stokes waves [Myrhaug, 2001]:

$$\phi = \phi_1 + \phi_2 = \frac{g\zeta_A}{\omega} \frac{\cosh k(z+h)}{\cosh kh} \sin(kx - \omega t) + \frac{3}{8} \zeta_A^2 \omega \frac{\cosh 2k(z+h)}{\sinh^4 kh} \sin 2(kx - \omega t) \quad (3.44)$$

$$\zeta = \zeta_A \cos(kx - \omega t) + \frac{1}{4} k \zeta_A^2 \frac{\cosh kh}{\sinh^3 kh} (2 + \cosh 2kh) \cos 2(kx - \omega t) \quad (3.45)$$

The second-order dispersion relation $\omega^2 = gk \tanh kh$ is the same as for linear theory. This is the result of calculations giving a nondimensional Φ_2 which is unbounded in time, meaning that it will increase to infinity. Therefore, $\omega_2 \equiv 0$ in equation (3.46).

$$\omega = \omega_1 + \epsilon \omega_2 + \epsilon^2 \omega_3 + \dots \quad (3.46)$$

From third order the dispersion relation correction in equation (3.46) applies.

An illustration of the resulting second-order Stokes surface profile composed by η_1 and $\epsilon \eta_2$ is given in figure 3.8.

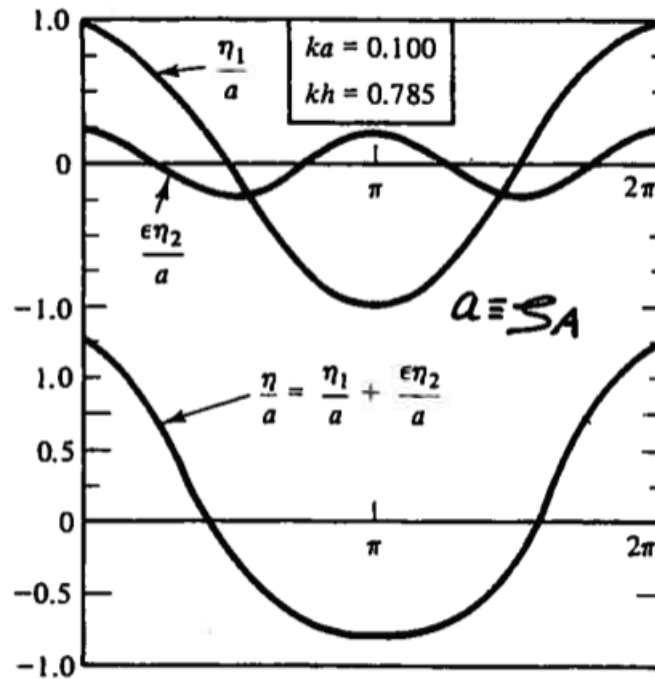


Figure 3.8.: A 2nd-order Stokes surface profile from [Dean and Dalrymple, 1991] reused in [Myrhaug, 2001].

As seen in the illustration, the resulting wave crests are steeper and the troughs are wider than for linear waves. The amplitude is higher and the trough is shallower by the same amount, so the wave height remains the same. Since the first and second-order dispersion relations are equal, the second-order wave cannot exist without the first-order component. They will propagate together as in figure 3.8.

To test convergence [Dean and Dalrymple, 1991] defines the parameter R as the ratio between an order n term and its preceding order term $n-1$, e.g. $R = \frac{\epsilon\Phi_2}{\Phi_1} = \frac{3}{8} \frac{k\zeta_A \cosh 2kh}{\cosh kh \sinh^3 kh}$, requiring $R \ll 1$. More on this in section 3.5.3.

Another requirement for the second-order Stokes wave is that there should be no anomalous bump, or local maxima, in the trough. This would occur if the second-order term becomes too large (see figure 3.8). By requiring that the second derivative in the trough ≤ 0 , a maximum wave steepness can be established:

$$k\zeta_A = \frac{\sinh^3 kh}{\cosh kh(2 + \cosh 2kh)} \quad (3.47)$$

As long as the water depth exceeds 15 % of the wavelength [Det Norske Veritas, 2014] recommends using 5th-order Stokes theory for regular waves. The velocity potential and surface elevation for 5th order Stokes waves are expressed in [Sarpkaya and Isaacson, 1981] on the form

$$\frac{k\phi}{c} = \sum_{n=1}^5 \phi'_n \cosh nks \sin n\theta \quad (3.48)$$

$$k\eta = \sum_{n=1}^5 \eta'_n \cos n\theta \quad (3.49)$$

where the calculations for ϕ'_n and η'_n , which are functions of k , d , H and T , were derived in [Skjelbreia and Hendrickson, 1962].

Since many of the higher order terms in Stokes wave theories blow out of proportions in shallow water, non-linear shallow water theories should be used instead. In the following, a few other non-linear wave theories, specifically those mentioned in [Det Norske Veritas, 2014], are briefly described.

3.5.2.2. Boussinesq wave theory

Boussinesq theory is relevant for weakly non-linear and moderately long waves in shallow water and are thus ideal in coastal work, but also often used in monopile wind turbine projects. In the derivation of the Boussinesq equations two expansion parameters are introduced:

$$\epsilon = \frac{A}{h} \ll 1 \quad (3.50)$$

$$\mu = kh \ll 1 \quad (3.51)$$

ϵ is a measure of the non-linearity of the wave and μ contains the dispersive properties.

For the full derivation of the Boussinesq equations interested readers should consult [Mei et al., 2005]. It involves a nondimensional perturbation analysis resulting in a depth-averaged horizontal velocity $\bar{\mathbf{u}}$ which is substituted into the equation of continuity and the momentum equation. Including the $O(\epsilon)$ and $O(\mu^2)$ terms, the Boussinesq equations are found as

$$\zeta_t + \nabla[(\epsilon\zeta + 1)\bar{\mathbf{u}}] = 0 \quad (3.52)$$

$$\bar{\mathbf{u}}_t + \epsilon \bar{\mathbf{u}} \cdot \nabla \bar{\mathbf{u}} + \nabla \zeta - \frac{\mu^2}{3} \nabla \nabla \cdot \bar{\mathbf{u}}_t = 0 \quad (3.53)$$

where equation (3.52) is the depth-averaged equation of continuity and (3.53) is the depth-averaged momentum equation.

It can be noted that in general, Boussinesq theory includes non-hydrostatic pressure and dispersion to the leading order μ^2 , unlike shallow water linear theory.

Some limiting cases of Boussinesq theory should be mentioned:

- Airy's theory for very long waves ($\epsilon \sim O(1) \gg \mu^2$)
Valid for arbitrary ϵ . Results in hydrostatic pressure and no dispersion.
- Linearized form ($\epsilon \ll \mu^2$)
Hydrostatic pressure and weak dispersion.
- Classical linearized waves, i.e. linear theory ($\epsilon, \mu^2 \rightarrow 0$)
Hydrostatic pressure and no dispersion.

3.5.2.3. Cnoidal wave theory

Cnoidal waves are a form of stationary non-linear waves meaning that it propagates at constant speed without changing shape. In order to establish such a permanent (i.e. stationary) wave for non-linear waves, the form of the linear wave solution, $e^{k(x-ct)}$, is sought. This means that a solution of

$$\phi = \phi(\xi) \quad (3.54)$$

is wanted, where

$$\xi = x - ct \quad (3.55)$$

A resulting equation describing the wave form is derived (in [Mei et al., 2005]) through a nondimensional perturbation approach of the Boussinesq equations (3.52) and (3.53):

$$-\frac{1}{2}\epsilon\zeta^3 + (c^2 - 1)\frac{\zeta^2}{2} + A_1 + A_2 = \frac{\mu^2}{6}\zeta'^2 \quad (3.56)$$

where A_1 and A_2 are integration constants.

For finite integration constants, the differential equation (3.56) can be solved in terms of cosine-elliptic (Cn) and sine-elliptic (Sn) functions (hence the name

‘cnoidal’), resulting in a wave with surface elevation

$$\zeta = \zeta_2 + (\zeta_3 - \zeta_2)Cn^2\left[\frac{3^{1/2}}{2}\frac{(\zeta_3 - \zeta_2)^{1/2}}{h^{3/2}}(x - ct - x_0)\right] \quad (3.57)$$

where the wave height $H = \zeta_3 - \zeta_2$.

As non-linearity will steepen the crests whilst dispersion will tend to counteract this effect by rather dispersing into waves of different lengths, these two traits must be in a dynamic equilibrium for a permanent wave to exist [Mei et al., 2005].

Cnoidal waves are periodic waves with wide troughs and high peaks with dispersion in shallow waters. The limiting cases of cnoidal waves are solitary waves for long waves and sinusoidal waves for small amplitude waves.

3.5.2.4. Solitary wave theory

Solitary waves is the long wavelength limiting case of cnoidal wave theory. It consists of a single peak with its entire surface elevation above the mean free surface $z=0$, and $|\zeta| \rightarrow 0$ as $|x| \rightarrow \pm\infty$. In this case the integration constants of equation (3.56) are zero and the equation reduces to

$$\zeta'^2 = 3\zeta^2\left(\frac{c^2 - 1}{\epsilon} - \zeta\right)\frac{\epsilon}{\mu^2} > 0 \quad (3.58)$$

We recognize the ϵ and μ parameters from Boussinesq theory. The solitary wave is supercritical, i.e. its phase velocity $c = \sqrt{g(h + A)}$ is larger than the shallow water linear wave (with phase velocity $c = \sqrt{gh}$), and c is seen to increase with the amplitude [Mei et al., 2005].

The wave is used for modeling long waves in particularly shallow water and is for example relevant for tsunamis.

3.5.3. The validity of wave theories

When choosing which wave theory to apply for a specific problem, [Det Norske Veritas, 2010] uses three parameters to determine the validity in each case:

- Wave steepness parameter $S = 2\pi\frac{H}{gT^2} = \frac{H}{\lambda_0}$
- Shallow water parameter $\mu = 2\pi\frac{d}{gT^2} = \frac{d}{\lambda_0}$
- Ursell parameter $U_r = \frac{H}{k_0^2 d^3} = \frac{1}{4\pi^2}\frac{S}{\mu^3}$

The Ursell number represents the degree of wave non-linearity versus the dispersive properties. The reader should bear in mind that for the Ursell limit of 26 in figure 3.9, U_r is defined differently than in equation (3.5.3). Since the phase velocity is independent of λ in shallow water but depends on λ in deep water, kd can be used as a measure of dispersion.

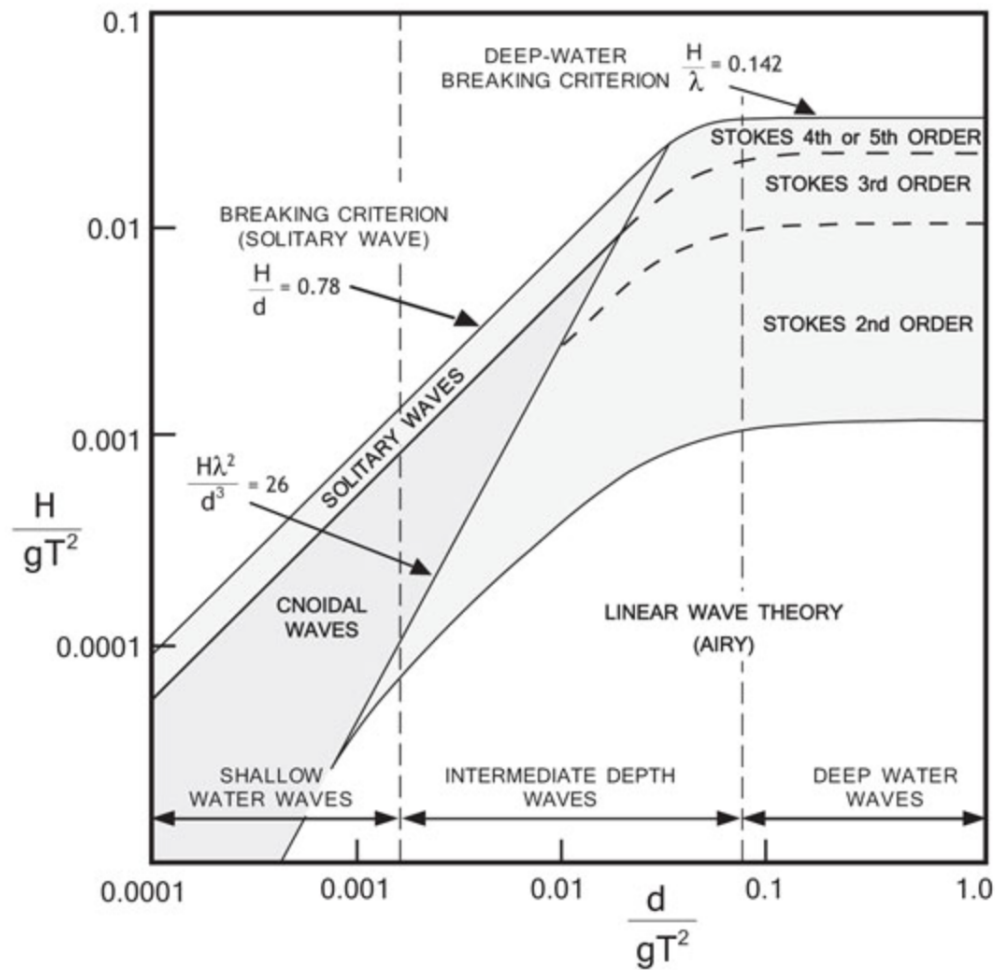


Figure 3.9.: Validity ranges for different wave theories, from [Flow Science, 2015] created using validity criteria in [Le Mehaute, 1976]. The same ranges are applied in [Det Norske Veritas, 2010].

The limit values for each parameter are summarized in [Det Norske Veritas, 2014]:

Theory	Applications	
	Depth	Approximate range
Linear (Airy wave)	Deep and shallow	$S < 0.006$; $S/\mu < 0.03$
2 nd order Stokes wave	Deep water	$U_r < 0.65$; $S < 0.04$
5 th order Stokes wave	Deep water	$U_r < 0.65$; $S < 0.14$
Cnoidal theory	Shallow water	$U_r > 0.65$; $\mu < 0.125$

Table 3.1.: Validity ranges of different wave theories, reproduced from [Det Norske Veritas, 2014]

The Stokes parameter R reduces to $R = 3e^{-2kh}k\zeta_A$ and $R = \frac{3}{8}\frac{k\zeta_A}{(kh)^3} = \frac{3}{8}U_r$ for deep and shallow water, respectively. For shallow water waves $kh \ll 1$, so there are obvious problems with convergence. 2nd-order Stokes theory will thus give unrealistic results on shallow water. Here, cnoidal waves are better suited.

By definition, the highest R value for deep water is found by letting $\frac{h}{\lambda} = \frac{1}{2}$ and $\frac{H}{\lambda} = \frac{1}{7}$ (to avoid wave breaking). Thus, the maximum R value in deep water is $R = \frac{3\pi}{7}e^{-2\pi} = 0.0025 \ll 1$, meaning $\epsilon\Phi_2 \ll \Phi_1$, so the convergence criteria is fulfilled.

In deep water the maximum steepness criterion (3.47) reduces to $k\zeta_A = 1/2$ (since $1/2$ is larger than the breaking steepness of $1/7$), so a anomalous bump will never occur. In shallow water, however, the requirement reduces to $U_r = \frac{k\zeta_A}{(kh)^3}$, which is stricter than the convergency requirement described above, so single-crestedness is the limiting wave steepness requirement for second-order Stokes waves.

In conclusion, and as illustrated in figure 3.9:

- Linear waves should be used for small wave steepness waves in finite or deep water depth.
- Stokes waves should be used for deep water and regular steep waves. 5th order Stokes waves are valid up to larger wave heights than 2nd order Stokes waves.
- Cnoidal waves are used for periodic waves in shallow water.
- Solitary waves are the long wave limit of cnoidal waves used for particularly large amplitudes in shallow water.

All the wave theories discussed in this section satisfy the seabed boundary condition exactly, but cnoidal theory does not fully satisfy the Laplace equation in the

fluid. All theories only approximately satisfy the dynamic free surface boundary condition.

3.5.4. Kinematics in irregular waves

As wave kinematics for both linear wave theory and Stokes wave theory are only given up to the still water level $z = 0$, an error will be introduced in the force integration if not corrected for. Stretching and extrapolation are widely used in the offshore industry because of the extensive use of linear deep water waves.

3.5.4.1. Grue's method

Grue's method is an approach for estimating the kinematics below the crests of irregular waves. For a crest height $z = \eta_m$ and a trough-to-trough period of T_{TT} giving $\omega = \frac{2\pi}{T_{TT}}$, the wave number k and local wave slope ϵ can be calculated by solving for a third-order Stokes wave, giving the non-linear dispersion relation and the non-dimensional surface elevation in equation (3.59).

$$\frac{\omega^2}{kg} = 1 + \epsilon^2, \quad k\eta_m = \epsilon + \frac{1}{2}\epsilon^2 + \frac{1}{3}\epsilon^3 \quad (3.59)$$

The horizontal velocity profile under the wave crest is given as

$$u(z) = \epsilon \sqrt{\frac{g}{k}} e^{kz} \quad (3.60)$$

Grue's method, however, is only valid for describing crest kinematics in deep water, so it should not be used in calculations for wind turbines at Dogger Bank.

3.5.4.2. Stretching

In the Wheeler stretching method wave kinematics from linear theory at the mean water level $z=0$ are shifted to the actual free surface $z = \eta$. It is thus a non-linear extension of linear theory, since the resulting horizontal force on the vertical pile will include a second-order wave amplitude term $\sim \zeta_A^2$. [Det Norske Veritas, 2010] gives the stretched vertical coordinates as

$$z = \frac{z_s - \eta}{1 + \eta/d}, \quad -d < z < 0, \quad -d < z_s < \eta \quad (3.61)$$

where η is the instantaneous free surface elevation and d is the water depth. In [Wheeler, 1970], where the method was presented, the author specifies that the incident waves no longer satisfy the Laplace equation after the z -coordinates are shifted.

The method is simply illustrated in figure 3.10.

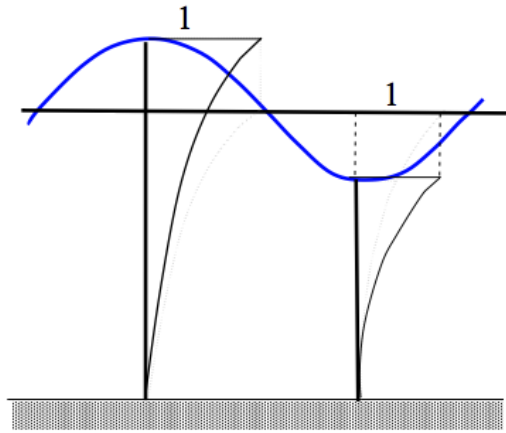


Figure 3.10.: Wheeler stretching [USFOS, 2010]

To show how Wheeler stretching creates a second-order force, the utilization of the stretching is exemplified for the inertia part of the Morison force and a linear surface elevation. The inertia force per unit length is given by (3.12):

$$dF_M = C_M \rho c \ddot{x} dz \quad (3.62)$$

where c is the cross-sectional area of the pile. Using linear wave theory the surface elevation is given by:

$$\zeta = \zeta_A \sin(\omega t - kx) \quad (3.63)$$

and the horizontal particle acceleration is:

$$a_x = \ddot{x} = \omega^2 \zeta_A \frac{\cosh k(z+h)}{\sinh kh} \cos(\omega t - kx) \quad (3.64)$$

Utilizing the Wheeler stretching approach, substituting (3.61) into (3.62) and in-

tegrating up to the linear surface:

$$\begin{aligned}
 F_M &= \int_{-h}^{\zeta} C_M \rho c \omega^2 \zeta_A \frac{\cosh k(\frac{z_s - \zeta}{1 + \zeta/h} + h)}{\sinh kh} \cos(\omega t) dz_s \\
 &= \int_{-h}^{\zeta} C_M \rho c \omega^2 \zeta_A \frac{\cosh k(\frac{z_s + h}{1 + \zeta/h})}{\sinh kh} \cos(\omega t) dz_s \\
 &= C_M \rho c \omega^2 \zeta_A \frac{\cos(\omega t)}{\sinh kh} \int_{-h}^{\zeta} \cosh k(\frac{z_s + h}{1 + \zeta/h}) dz_s \\
 &= C_M \rho c \omega^2 \zeta_A \frac{\cos(\omega t)}{\sinh kh} \frac{1 + \zeta/h}{k} [\sinh k(\frac{z_s + h}{1 + \zeta/h})]_{-h}^{\zeta} \\
 &= C_M \rho c \omega^2 \zeta_A \frac{\cos(\omega t)}{\sinh kh} \frac{1 + \zeta/h}{k} [\sinh kh - \sinh(0)] \\
 &= C_M \rho c \omega^2 \zeta_A \cos(\omega t) \frac{1}{k} (1 + \zeta/h) \\
 &= C_M \rho c \omega^2 \zeta_A \cos(\omega t) \frac{1}{k} (1 + \frac{\zeta_A}{h} \sin(\omega t)) \\
 &= C_M \rho c \omega^2 \frac{\zeta_A}{k} \cos(\omega t) + C_M \rho c \omega^2 \frac{\zeta_A^2}{2kh} \sin(2\omega t)
 \end{aligned} \tag{3.65}$$

The origin is placed in the center of the pile with the z -axis pointing upwards. The second term of (3.65) shows ζ_A^2 dependence, proving the non-linear effect of the Wheeler stretching implementation, introducing a sum-frequency force in finite water depth. Thus, the stretched Morison inertia force inhabits a second-harmonic contribution.

[Det Norske Veritas, 2010] suggests using a non-linear elevation record when stretching.

3.5.4.3. Extrapolation

By using a Taylor expansion or extrapolation of linear velocities and accelerations a model for the velocity and acceleration profiles up to the free surface can be established. In [Det Norske Veritas, 2010], this is done up to second order (including sum- and difference frequency effects), e.g. giving the following horizontal velocity profile:

$$u(z) = u^{(1)}(z) + u^{(2+)}(z) + u^{(2-)}(z), \quad z \leq 0 \tag{3.66}$$

$$u(z) = u^{(1)}(0) + \frac{\partial u^{(1)}}{\partial z} \Big|_{z=0} z + u^{(2+)}(0) + u^{(2-)}(0), \quad z > 0 \tag{3.67}$$

where $u^{(1)}(z)$, $u^{(2+)}(z)$ and $u^{(2-)}(z)$ the linear, sum- and difference-frequency velocity profiles, respectively.

As mentioned, Grue's method is only valid on deep water. [Stansberg, 2005] compares the three methods above, concluding that both Grue's method and the extrapolation method perform best in deep water. Grue's method overestimates the fluid velocities beneath $z=0$, whereas Wheeler stretching works well around the crest but underestimates around the still water level and underneath.

3.6. Ringing

One of the effects that may arise from non-linear wave loads on an offshore wind turbine is ringing. As the bottom-fixed turbines are placed in shallow or intermediate depths, one expects the degree of wave non-linearity to increase, and thus the forcing leading to ringing should become more frequent. This was verified in [Bredmose et al., 2012]. It may be especially important to assess ringing for wind turbines compared to other offshore structures, since the relatively larger top mass increases their sensitivity to dynamically amplified response.

The ringing phenomenon is a transient structural response characterized as a collection of resonant response cycles that quickly build up to a maximum before decaying at the eigenperiod with the structural damping [Haver, 2007]. It is connected with higher-order wave-body interaction effects, shown to occur when a structure is excited by high-frequency wave components close to the natural period in combination with a large quasi-static load from a high-amplitude wave. It can typically occur when a steep, non-linear wave impacts a pile. A few high-frequency oscillations, usually 3rd or 4th-order wave-frequency components, has been shown sufficient in exciting the first-mode [Chaplin et al., 1997]. The structural oscillation amplitudes are proportional to $\zeta_a^{excitation\ order}$, where ζ_a is the amplitude of the higher-order wave component and the excitation order is the wave component exciting the transient response. At excitation, the response shifts from peak period to eigenperiod dominated.

A typical ringing event from a steep non-linear wave is shown in figure 3.11.

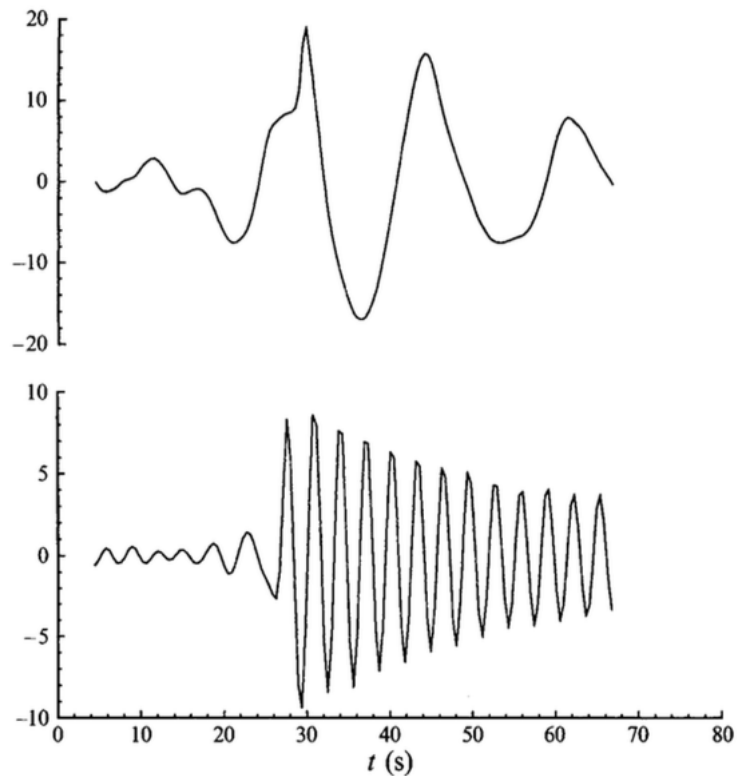


Figure 3.11.: The upper curve shows the incident wave history, whilst the lower curve depicts a typical ringing event shown by the measured tension oscillations at the structural eigenfrequency in the mooring wires of a TLP [Faltinsen et al., 1995].

It is often difficult to differ a ringing incident from other transient responses, such as the response induced by slamming, because they look alike. In fact, [Welch et al., 1999] characterizes response events from impact by breaking wave groups as ringing incidents. In the paper it is shown that ringing-like responses are excited by impact-like waves because they generate a continuous response spectrum, as opposed to the discontinuous separate spectrum peaks at multiples of the first mode, for Stokes waves.

Ringing events may be important in the design against ULS, as it is relevant in the estimation of the characteristic loads. [Det Norske Veritas, 2014] states that ringing is only of significance when combined with extreme first-order frequency effects, meaning that it is relevant for ULS only. For FLS, on the other hand, the phenomenon is usually not taken into consideration as it is so rare [Haver, 2007]. However, whether it is relevant for FLS is debated. This was discussed by

mathematician J. Grue of the University of Oslo in [Vogt, 2013] (pointed out by [Schl er, 2013]).

In [Grue and Huseby, 2002], ringing is achieved for moderately steep waves in an irregular sea, but for larger eigenfrequency to spectral peak frequency ratios than for the slender cylinders in [Malenica and Molin, 1994], as discussed in section 3.6.1. In addition, for both single waves and wave trains, [Grue and Huseby, 2002] investigated a secondary load cycle that appears approximately a quarter of a wave period after the main force peak. It creates a higher-harmonic wave force, typically corresponding to 10-15 % of the total peak-to-peak force in the same cycle. They found that the secondary cycles were shown to be less pronounced for single-wave events, and that there is a slight correlation between the occurrence of a secondary load cycle and ringing, due to the presence of a higher-harmonic load.

In [Chaplin et al., 1997], a high-speed camera was used in experiments with waves impacting a cylindrical pile. It is shown how the local breaking of water around the pile causes ventilation and then a collapse as the water from each side of the cylinder meet. This gives the secondary loading cycle shown in figure 3.12.

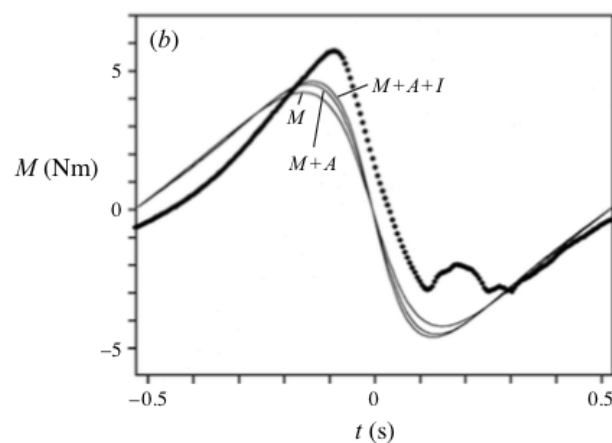


Figure 3.12.: Illustrating the secondary load cycle. The bold dotted curve represents moment records, whilst the other curves are moment estimations [Chaplin et al., 1997].

[Det Norske Veritas, 2014] only briefly mentions the ringing phenomenon, stating that ringing can occur if the typical wave frequency is not smaller than three or four times the lowest natural frequencies of the structure. If the natural frequency exceeds the spectral peak frequency f_p around five or six times then ringing will not occur.

The focus in the next section will be on a method which is able to capture ringing in numerical simulations. [Tromans et al., 2006] and [Haver, 2007], however, argue that there are no robust analytical methods to predict ringing. This will be discussed further in section 3.6.2.

3.6.1. The FNV model

The FNV model sets out to estimate the force from a deep-water, large-amplitude incident wave with a height similar to the cross-sectional dimensions of a cylindrical pile. Formally, the assumptions are $\epsilon = k\zeta_A \ll 1$, $\frac{R}{\zeta_A} \sim O(1)$ and $kR \ll 1$. The theory is derived through perturbation wrt. these wave-structure characteristics, assuming a vertical cylinder extending through the fluid surface with viscous effects neglected (meaning potential flow). This corresponds to the large incident wavelength assumption suitable for the inertia-dominated responses to be studied in this thesis. The model was developed in order to take the 3rd-order wave loads from large waves into account. In a similar study, [Malenica and Molin, 1994], the third harmonic of the force on a fixed circular cylinder was estimated, but the cylinder radius R was assumed much larger than the wave amplitude ζ_A , so $R/\zeta_A \sim O(1)$ is an essential characteristic of [Faltinsen et al., 1995]. In the paper they argue that the conventional perturbation analysis employed by [Malenica and Molin, 1994] and [Chau and Taylor, 1992] is not sufficient to evaluate ringing because of the small-amplitude assumption.

The derivation of the FNV theory sets out by defining the total diffraction potential ϕ_D , consisting of an incident and a scattering potential.

$$\phi_D = \phi_I + \phi_S \tag{3.68}$$

The loads are found using linear and non-linear velocity potentials. J.N. Newman later formulated the FNV theory for irregular sea in [Newman, 1996].

In long irregular waves, the most important high-frequency loads are due to the fluid-structure interaction, and not non-linearities in the incident waves. Thus the incoming waves are still described using the linear potential ϕ_I , non-linearities neglected [Newman, 1996]. The dispersion relation of ϕ_I is modified, however, so that it is accurate beyond linear theory. A higher-order scattering potential ψ is only relevant in the inner region, i.e. $r \sim O(a)$, where a is the cylinder radius.

The resulting potential is given by

$$\phi = \phi_I + \phi_S + \psi = \phi_D + \psi \quad (3.69)$$

where ϕ_I is the incident wave field, ϕ_S is the linear scatter and ψ is the higher-order scatter. A first-order, second-order and third-order force, F_1 , F_2 and $F_3^{(1)}$, respectively, are derived from the first-order potential ϕ_D , whilst a third-order force $F_3^{(2)}$ is found from ψ [Newman, 1996].

In [Krokstad et al., 1996] first-order complete diffraction simulations, second-order sum- and difference frequency simulations and third-order FNV terms are combined to a simplified load model valid for non-slender cylindrical structures. The model was partly developed in the Norwegian Joint Industry Project ‘Higher Order Wave Load Effects on Large Volume Structures’, and in the paper these results are validated against experiments for different diameter/peak wavelength ratios. Experiments for larger diameter structures than those valid in [Faltinsen et al., 1995] show that the FNV model significantly overestimates the second-order term, which means that it is affected by far field diffraction. The overestimation depends on the degree of non-linearity, i.e. the wave steepness. Thus, the 2nd-order force component is reduced in the [Krokstad et al., 1996] modified FNV model by introducing a so-called ‘fat body’ or MacCamy & Fuchs correction. Since the 3rd-order FNV component showed satisfactory agreement with experimental values, the unmodified term was used. Thus, the objective of [Krokstad et al., 1996] was to formulate a single model to simulate ringing response for a large range of natural frequencies using linear and quadratic transfer functions and the unmodified 3rd-order FNV contribution. The resulting force model is given in equation (3.70).

$$\begin{aligned} F_{FNV}(t) &= 2\pi\rho R^2 \int_{-h}^0 u_t(z) dz && O(\epsilon) \\ &+ 2\pi\rho R^2 u_t|_{z=0} \zeta^{(1)} + \pi\rho R^2 \int_{-h}^0 w u_z dz && O(\epsilon^2) \\ &+ \pi\rho R^2 \zeta^{(1)} (u_{tz} \zeta^{(1)} + w u_z - \frac{2}{g} u_t w_t)|_{z=0} + \pi\rho \frac{R^2}{g} u^2 u_t|_{z=0} \beta(h/R) && O(\epsilon^3) \end{aligned} \quad (3.70)$$

where $\beta(h/a) = \int_0^{h/a} [3\Psi_1(Z) + 4\Psi_2(Z)] dZ$. $\Psi_1(Z)$ and $\Psi_2(Z)$ can be found in [Newman, 1996].

As can be seen in equation (3.70), the 3rd-order wave force is not distributed, but acts as a point source close to the still water level. Even though the magnitude

of the 3rd-order force is much smaller than the magnitude of the 1st-order force, the 3rd-order moment contribution may be substantial due to the long moment arm.

The FNV bending moment up to fourth-order steepness $\epsilon = k\zeta_A$ is given in [Krokstad et al., 1996]:

$$\begin{aligned}
 M_{FNV}(t) &= 2\pi\rho R^2 \int_{-h}^0 z u_t(z) dz && O(\epsilon) \\
 &+ \pi\rho R^2 \int_{-h}^0 z w u_z dz && O(\epsilon^2) \\
 &+ \pi\rho R^2 u_t|_{z=0} \zeta^{(1)2} - \frac{\pi\rho}{g} R^3 u^2 u_t|_{z=0} \gamma(h/a) && O(\epsilon^3) \\
 &+ \frac{2}{3} \pi\rho R^2 u_{tz}|_{z=0} \zeta^{(1)3} + \frac{1}{2} \pi R^2 w u_z|_{z=0} \zeta^{(1)2} && O(\epsilon^4) \\
 &+ 2\pi R^2 u_t|_{z=0} \zeta^{(1)} \zeta_1^{(2)} + \pi\rho \frac{R^2}{g} u^2 u_t|_{z=0} \zeta^{(1)} \beta(h/a) && O(\epsilon^4)
 \end{aligned} \tag{3.71}$$

where $\gamma(h/a) = \int_0^{h/a} [3\Psi_1(Z) + 4\Psi_2(Z)] Z dZ$.

However, this bending moment may not give realistic results, since the 3rd-order force is taken as a point force instead of a distributed force. The effect will be more prominent in shallow water as the distribution will be close to the still water level $z = 0$. Equation (3.71) was never validated in the experiments.

3.6.2. Selecting force model

A key premise discussed in [Lighthill, 1979] is that the mechanisms generating viscous and inviscid force contributions are independent. Further the inadequacy of the Morison inertia term is argued, as it neglects the loads from non-linear potentials. With this backdrop, [Rainey, 1989] sets out to establish a non-linear equation for the potential-flow wave loading on a slender surface-piercing structure, aimed to replace the inertial term in the Morison equation (3.13).

The derivation of the Rainey model differs from the FNV method in the sense that it was not based on a perturbation approach, but rather derived with regard to the conservation of energy principle.

When choosing a force model to simulate realistic turbine behavior in ULS waves it is important to consider the theory's validity with respect to the relative structure-wave geometry, as well as depth conditions. The FNV model is based on the assumptions of deep water, a pile radius similar to the wave height and a large

incident wavelength relative to the cross-sectional dimensions. With the [Newman, 1996] extension it is also applicable in irregular waves. [Malenica and Molin, 1994] perturbation theory assesses the third harmonic of the fixed-cylinder force with the pile radius much larger than the wave amplitude ($R \gg \zeta_A$). Rainey theory deals with potential flow forces on a small-radius pile.

In figure 3.13 the response bending moment from different order FNV loads are simulated. The results show that the 3rd-order force creates a large dynamic amplification since the frequency of the 3rd harmonic part of the force (the wave frequency tripled) is close to the first natural frequency of the structure. The ringing phenomenon is illustrated in the large transient response.

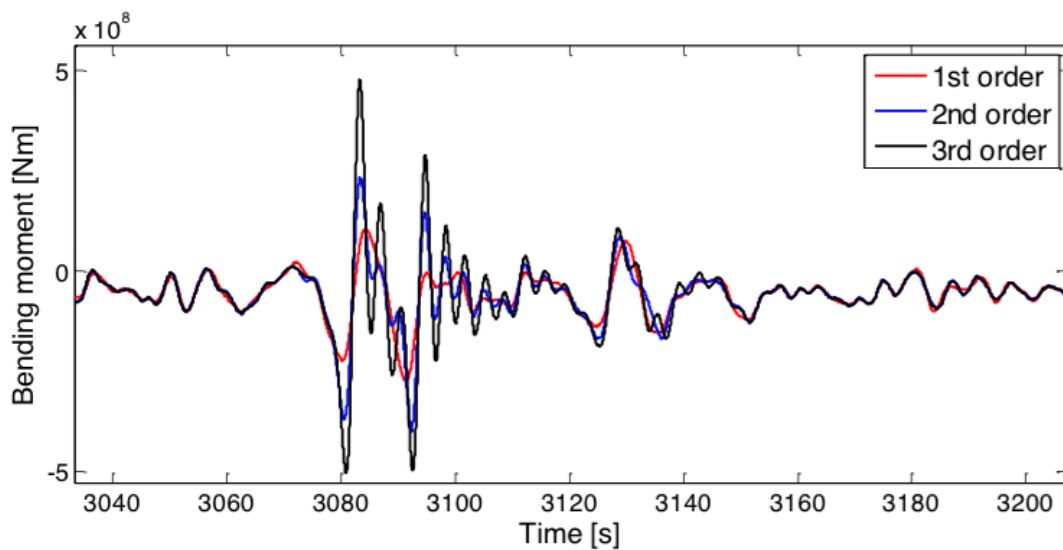


Figure 3.13.: Simulation of the FNV bending moment at the point of maximum utilization [Suja-Thauvin et al., 2014].

It is important to differentiate between orders and harmonics, harmonics being multiples of the circular wave frequency ω , that is 2ω , 3ω , etc. Because of coupling effects there are 1st and 3rd harmonics in the 3rd-order term and 2nd and 4th harmonics in the 4th-order term of the FNV. So, in general, truncation at the 3rd-order load may be too conservative since 2nd-order diffraction will not be included.

This causes problems with the perturbation convergence, as higher-order terms include lower-order harmonics, implying that adding higher orders may cause a less accurate result. By considering the FNV force terms it is understood that before adding an additional order the amplitude will be conservative (overestimated),

whereas the period may be underestimated if not enough non-linear terms are present for high-frequency loads. The problem with perturbation schemes is that it is not possible to determine whether the solution has converged, as one cannot check the result with an error estimate.

The Rainey model mixes kinematic harmonics. Assuming linear kinematics it constitutes a 3rd-order strip force. Assuming arbitrary input kinematics, however, the global force is integrated up to the non-linear surface elevation, increasing the order accordingly. Even higher order contributions are included in the moment as the moment arm varies with the order of the wave steepness. As opposed to the FNV model, where the maximum order force is of 3rd order and the maximum order moment is of 4th order, control of the steepness order is lost when using the Rainey procedure. According to [Tromans et al., 2006], there is agreement between [Lighthill, 1979], Rainey theory and FNV theory up to the second-order, second-harmonic terms when regular waves in infinite water depth are utilized. Generally the third-harmonic, third-order Rainey and FNV forces do not correspond, but agreement can be achieved through the surface disturbance addition F_{SD} to the Rainey force [Rainey, 1995]. This considers the rate of change of energy related to the surface disturbance of a non-slender body.

The third-harmonic Rainey contribution was found to be around half of the third-harmonic FNV term when the ψ term is included [Faltinsen et al., 1995]. This implies that the third-order Rainey is unconservative on deep water.

The idea that ringing is caused by the 3rd harmonic in the 3rd-order wave load is debated. In [Rainey, 2007], it is argued that ringing is a fully non-linear phenomenon, not a weakly non-linear one, so the 3rd harmonic excitation argument is too simple. The argued strong non-linearity is due to the fact that the ringing vibration envelope follows the shape of the secondary loading cycle. As described in section 3.6, the secondary loading cycle is related to the local breaking flow of a wave around the pile circumference (see also [Rainey, 2007]), i.e. a strongly non-linear phenomenon. It is further argued that the natural period of the pile can be set at much higher multiples of the wave frequency than the third harmonic and ringing would still take place.

The intrinsic assumption of utilizing the wave kinematics at the cylinder centerline, instead of at the cylinder wall, as done in both the FNV and Rainey models, may lead to an error in the integrated forces. This error depends on the wave characteristics and cylinder radius (as the force magnitude is related to the instantaneous wave condition at the cylinder wall).

[Tromans et al., 2006] concludes that neither the FNV or Rainey force models are sufficient in modeling the non-linearities that take form in the steep incoming wave problem, especially emphasizing how they fall short in not accounting for the secondary loading cycle. No force model that includes hydrodynamic interaction is operated with kinematics higher than second-order, except [Malenica and Molin, 1994], but that is for regular waves only. On the basis of the importance of incoming wave non-linearity and the neglect of the secondary load cycle effects, [Tromans et al., 2006] concludes that between the Rainey and FNV models, the Rainey model seems to be the best tool of the two in order to predict ringing. This is due to the possibility to implement a fully non-linear kinematic model in the Rainey equations, which is not possible in FNV theory as it is based on a perturbation approach.

In order to take the fluid interaction with the structure into account and resolving the secondary load cycle flow around the cylinder, a CFD model can be used. However, such a model is too CPU extensive to be applicable as a primary tool in design, but is commonly used to benchmark other hydrodynamic force models [Schlører, 2013].

[Det Norske Veritas, 2010] specifies how numerical structural models may be insufficient, implying that ringing in many cases should be validated against model tests, referring to NORSOK N-001 and N-003. In both [NORSOK, 2004] and [NORSOK, 2007], ringing is described and model testing is suggested in order to verify that no important feature has been overlooked.

The reason why the FNV theory is widely used, even though it is not universally accepted, is that it agrees well with experiments, in addition to being conservative (truncated at the 3rd order) when its assumptions are satisfied.

It should be noted that the assumption of deep water will not be valid for large waves at Dogger Bank. However, since the diffraction disturbance only reaches a vertical distance in the order of magnitude $\sim O(D)$ beneath the surface, creating a finite-water FNV model should be physically feasible. A simplification of such a model will in fact be included in the numerical program in this thesis work. Whether this will give a conservative or non-conservative result is not known [Suja-Thauvin et al., 2014], but the outcome of the coded numerical model is discussed in section 7.

In this thesis work, two FNV models will be employed, both a conventional deep-water version and a variant where the finite-water form of the vertical decay of kinematics and dispersion relation, are included (see section 6.2). To illustrate the

non-linear effects captured by FNV, a Morison model with Wheeler stretching is also included. The procedure to include a slamming model in Morison is discussed in section 4.2.

4 | Slamming

4.1. Fundamentals of slamming

Slamming is an impulse loading from water on a body resulting in high pressure peaks. This can occur for instance when a ship bottom out of the water hits the surface at high velocity or when a breaking wave impacts a wind turbine tower. Slamming loads are characterized by having short durations and being localized in space.

To describe the physics of slamming, [Faltinsen, 1990] simplifies the problem to a horizontal cylinder that is forced through an initially calm water surface at constant speed V . The assumptions of a small submergence, a blunt body form and a two-dimensional flow are made. The submergence of the body is defined by the lowest point being a distance Vt relative to the initial flat surface. In addition, other assumptions are made in order to derive the slamming force magnitude:

- Irrotational flow in an incompressible fluid is assumed in order to use potential theory
- The fluid accelerations are much larger than the gravitational acceleration, $a \gg g$
- The normal vector $n_1 \ll n_3$, meaning that the boundary condition can be approximated $\frac{\partial \Phi}{\partial z} = -V$ on $z = 0$ as the body enters the water

A problem arises when using the assumption of an incompressible fluid, as a compressible air pocket will form when a flat body enters the water. The problem can be solved by using the second and third assumptions listed above. The derivation of the resulting vertical force on the body is given in [Faltinsen, 1990], where the Bernoulli equation and the velocity potential on the body, taken from [Newman, 1977], are utilized.

$$F_3 = V \frac{d}{dt} \left(\rho \frac{\pi}{2} c^2 \right) = V \frac{d}{dt} A_{33flatplate} \quad (4.1)$$

where $c = c(t)$ is the wetted length, V is the constant cylinder velocity and $A_{33flatplate}$ is the heave added mass of a flat plate when $\omega \rightarrow \infty$.

The corresponding slamming coefficient is defined as

$$C_s \equiv \frac{F_3}{\frac{1}{2}\rho V^2 2R} \quad (4.2)$$

When approximating the wetted two-dimensional surface length, two models are commonly used, the von Karman solution and Wagner's approach. Since we are interested in the hydrodynamic pressure, the wetted area due to spray can be excluded in both approximations, as the pressure in this region will be very close to the atmospheric pressure. The difference in the approximations arise from where the wetted lengths are measured. In the case of von Karman, the wetted length is measured from the initial calm water level, and is found directly from geometry:

$$c^2(t) = 2VtR - V^2t^2 \quad (4.3)$$

This results in a slamming coefficient of $C_s = \pi$. The value has proven too small, e.g. by experiments in [Campbell and Weynberg, 1980], where the slamming coefficient was found to be $C_s = 5.15$ [Faltinsen, 1990].

Wagner's solution gives the wetted length by approximating a free-surface elevation due to the body entrance (see figure 4.1). The result of this is a wetted length of

$$c(t) = \sqrt{VtR} \quad (4.4)$$

which is $\sqrt{2}$ times larger than the von Karman wetted length at the undisturbed free surface.

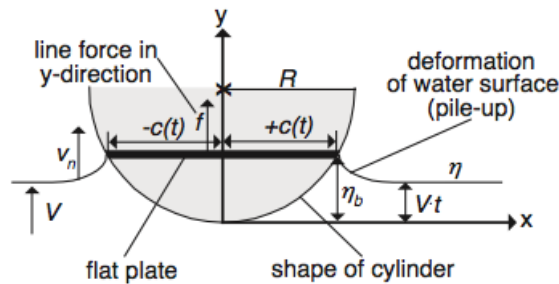


Figure 4.1.: The Wagner wetted length [Wienke and Oumeraci, 2005]

The Wagner slamming coefficient is 2π , which is higher than the [Campbell and Weynberg, 1980] value.

The pressure coefficient is found from

$$C_p = \frac{p}{\frac{1}{2}\rho V^2} = \frac{4}{\sqrt{4\left(\frac{Vt}{R}\right) - \left(\frac{x}{R}\right)^2}} \quad (4.5)$$

giving

$$C_{pmax} = \frac{\left(\frac{dc}{dt}\right)^2}{V^2} \quad (4.6)$$

which is

$$C_{pmax, von Karman} = \frac{0.5R}{Vt} \quad \text{at } |x| = 2\sqrt{VtR} \quad (4.7)$$

for the von Karman solution and

$$C_{pmax, Wagner} = \frac{R}{Vt} \quad \text{at } |x| = \sqrt{2VtR} \quad (4.8)$$

for the Wagner approach.

According to the [Campbell and Weynberg, 1980] experiments, the von Karman pressure is of satisfactory magnitude, but the position of the pressure peak is inaccurate. Looking at the Wagner pressure peak it is approximately twice the experimental size in magnitude, but occurs at the correct location. However, experimental errors cannot be ruled out.

When plotting the maximum pressure in time, $C_p \rightarrow \infty$ as $t \rightarrow 0$. This is unphysical and due to the incompressible fluid assumption. A correction has to be implemented, as the maximum pressure, called the acoustic pressure, is

$$p_{ac} = \rho c_e V \quad (4.9)$$

where c_e is the velocity of sound in water. The value of this parameter varies dramatically depending on the amount of air in the water. In breaking waves the amount of air is high.

For an offshore wind turbine, analyses of the global slamming loads is an important part of the design verification. [Faltinsen, 1990] describes the derivation of the force on a rigid cylinder entering the water at a constant velocity V . By starting out with a momentum consideration with no incident wave effects and infinite water depth, the following formula for the force is found

$$F_3 = \frac{d}{dt}(A_{33}V) + \rho g \Omega \quad (4.10)$$

where Ω is the submerged volume and A_{33} is the high-frequency added mass in heave.

Equation (4.10) can be modified to include incident wave effects, assuming linear deep-water incident waves of

$$\phi_0 = \frac{g\zeta_A}{\omega} e^{kz} \cos(\omega t - kx) \quad (4.11)$$

and a large wavelength relative to the diameter of the cylinder, meaning that the diffraction caused by the body can be neglected.

The modification of equation (4.10) gives

$$F_3 = \rho\Omega(t)\frac{dw}{dt} + \rho g\Omega(t) - \frac{d}{dt}(A_{33}(\frac{d\eta_3}{dt} - w)) \quad (4.12)$$

where w is the vertical fluid velocity in the incident waves, $\Omega(t)$ is the instantaneous submerged body volume and η_3 is the vertical motion of the body.

For a breaking wave impact, the linear wave correction will not be sufficient.

4.2. Slamming loads from waves

Global loads from wave slamming on a monopile structure are characterized by a short impact duration, after which the structure will oscillate transiently at its first eigenfrequency, decaying with the structural damping. Such a load can be caused by either a non-breaking wave of large steepness or a breaking wave. A plunging breaker develops when a wave's steepness becomes so large that it unstabilizes. At this point, particle velocities in the crest exceed that of the wave celerity, implying a transition from potential to kinetic energy. Due to their short duration, wave forces from breakers on a structure cannot be analyzed using conventional non-breaking wave force formulae, such as the conventional Morison equation. As shall be described in this section, an approach has been to add an impact force term F_I to the Morison equation in order to account for the global slamming force.

In regions where bottom-fixed wind turbines are commonly placed, such as sand banks or other shallow areas, breaking waves often arise and propagate in the proximity of the turbine towers. However, extreme stresses from wave loads are most often due to large, very non-linear, but non-breaking waves [Okan et al., 2002]. Nonetheless, with increased shallow water activity within the offshore wind

power industry, much research has been done on deterministic global slamming loads from breaking waves, some of which will be presented in this section.

According to [Marino et al., 2013], the slamming loads from steep and breaking waves may also induce wind turbine ringing. The ringing occurrence discussed in the paper is found to be a result of either hydroelastic interaction stemming from high-frequency, non-linear wave components, or from ringing vibrations at the eigenfrequency from the impact of breaking waves. Breaking waves have been shown to induce two high-frequency responses, one very-high-frequency vibration for the second tower fore-aft eigenfrequency and one at the natural frequency of the structure, resulting in a large amplification of the pile top displacement.

In figure 4.2 from [Marino et al., 2013], linear and non-linear wave elevation models (top) and their resulting base shear forces (second), base overturning moment (third) and top displacements (bottom) are shown to illustrate the inadequacy of linear models in steep irregular sea states.

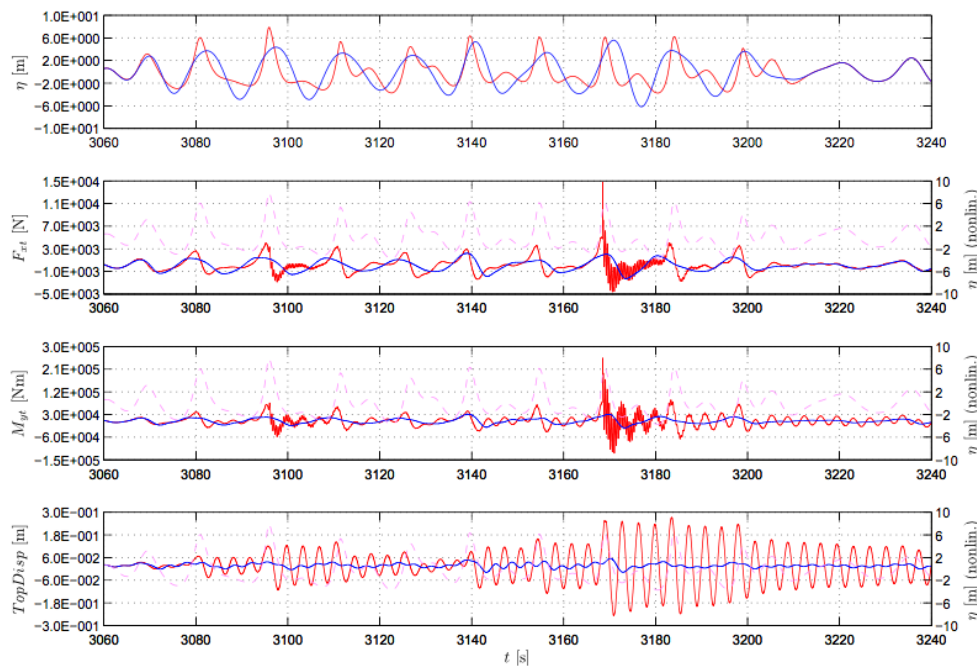


Figure 4.2.: Ringing from breaking and non-breaking waves for linear (blue) and non-linear (red) wave elevation models [Marino et al., 2013].

Impact from a steep non-breaking wave occurs at approximately $t=3095$ s, amplifying the oscillation frequencies for around one $T_p=15$ s period, followed by smaller ringing events, whose oscillation amplitudes depend on the local wave

steepness. The breaking wave impact, seen to give much larger forces and responses than for the non-breakers, is found at 3168.5 s.

[Marino et al., 2011] suggests that there is currently no systematic and accurate method to simulate these loads on wind turbines since the commonly used wave theories cannot model highly non-linear effects, but only irregular linear waves or weakly non-linear regular waves. This concern was also discussed in section 3.4.

The hydrodynamic model used in [Marino et al., 2013] and figure 4.2 is based on fully non-linear potential flow, utilizing an additional term for the impulse load in the Morison equation, as established in [Wienke and Oumeraci, 2005]:

$$f(t) = f_D(t) + f_M(t) + f_I(t) \quad (4.13)$$

[Wienke and Oumeraci, 2005] assessed the impulsive term by conducting large-scale experiments using plunging breakers to measure the impact on vertical and inclined slender cylinders.

$$f_I(t) = \begin{cases} \rho R v_1^2 [2\pi - 2\sqrt{\frac{v_1}{R}t} \tanh^{-1} \sqrt{1 - \frac{1}{4} \frac{v_1}{R}t}], & \text{for } 0 \leq t \leq \frac{1}{8} \frac{R}{v_1} \\ \rho R v_1^2 [\pi \sqrt{\frac{1}{6} \frac{1}{\frac{v_1}{R}t'}} - \sqrt[4]{\frac{8}{3} \frac{v_1}{R}t'} \tanh^{-1} \sqrt{1 - \frac{v}{R}t'} \sqrt{6 \frac{v_1}{R}t'}], & \text{for } \frac{3}{32} \frac{R}{v_1} \leq t' \leq \frac{12}{32} \frac{R}{v_1} \end{cases} \quad (4.14)$$

Here, $t' = t - \frac{R}{32v_1}$ and v_1 is the impact velocity. v_1 is difficult to determine, but common approximations are to use Grue's method or stream function theory. In [Wienke and Oumeraci, 2005] the impulse duration for a vertical cylinder is found from

$$t_d = \frac{13 R}{32 V} \quad (4.15)$$

assuming that the area of impact is struck by the vertical face of a plunging breaker, as illustrated in figure 4.3.

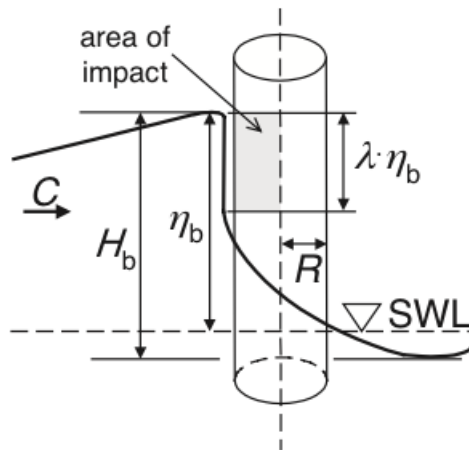


Figure 4.3.: The impact area for a plunging breaker [Wienke and Oumeraci, 2005].

The load from a breaking wave in the proximity of the wind turbine tower depends on the wave breaking type, since the wave kinematics are different for each case.

- *Spilling breakers*: Occur in deep and shallow water
- *Plunging breakers*: Occur primarily in shallow waters, but also frequent in deep water
- *Surging breakers*: Occur in shallow water only

These are categorized cases of breaking waves, but there also exist intermediate variants which are more difficult to classify [Myrhaug, 2001].

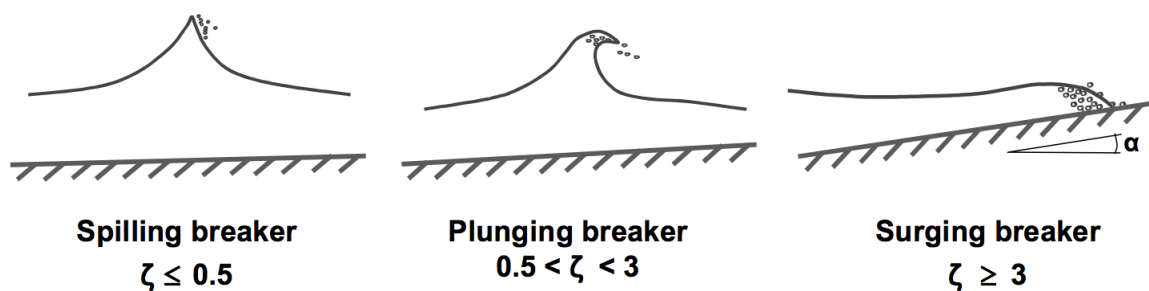


Figure 4.4.: Different types of breaking waves [Kühn, 2001].

The surf similarity parameter ζ , which depends on the seabed slope α , determines the type of breaking wave

$$\zeta = \tan \alpha \sqrt{\frac{gT^2}{2\pi H}} \quad (4.16)$$

For a plunging breaker, the impact force in [Det Norske Veritas, 2014] is found by

$$F = \frac{1}{2}\rho C_s A u^2 \quad (4.17)$$

where A is the exposed area of the cylinder. This area depends on where the wave breaks relative to the structure. The slamming coefficient for a smooth cylinder is limited by $3.0 \leq C_s \leq 2\pi$. [Det Norske Veritas, 2014] uses the assumed impact duration (4.15) for a plunging wave that breaks immediately in front of a vertical cylinder.

As seen in equation (4.17) the impact force is proportional to the normal component of the breaker velocity squared, similar to the drag term in the Morison equation. The difference between these two cases, however is the nature of the impact, as the drag loading is steady state, whilst the slamming impact force is of short duration resulting in a transient response pattern [Haver, 2007].

For spilling and surging breakers the force on a pile is calculated in a strip-wise manner, where the instantaneous force per length is given by

$$f = \frac{1}{2}\rho C_s D u^2 \quad (4.18)$$

The slamming coefficient has been estimated empirically and is given in [Nestegård et al., 2004]:

$$C_s(s) = 5.15 \left[\frac{D}{D + 19s} + \frac{0.107s}{D} \right] \quad (4.19)$$

Here, $0 < s < D$ describes the penetration of the wave surface, i.e. the horizontal distance from the impact point on the cylinder to the sloping water surface corresponding to $s = Ct$, giving $C_s(D) = 0.8$ and $C_s(0) = 5.15$ as in [Campbell and Weynberg, 1980].

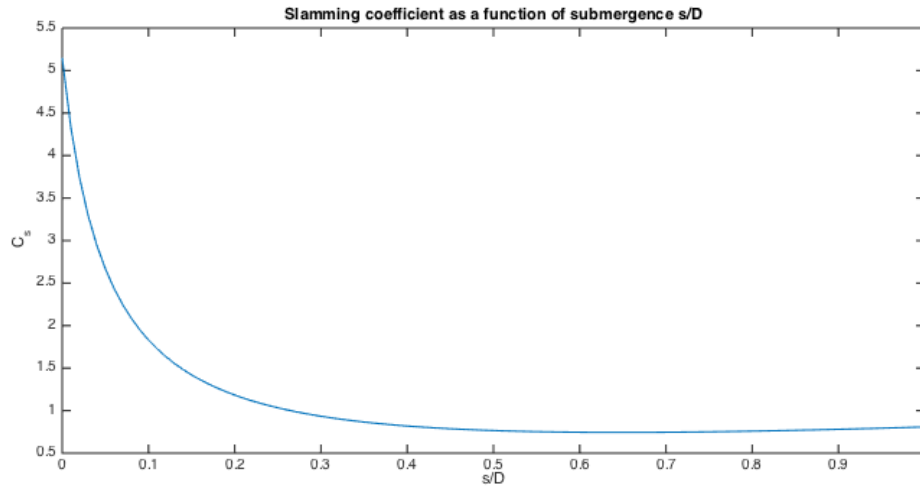


Figure 4.5.: The [Nestegård et al., 2004] slamming coefficient as a function of submergence.

In [Nestegård et al., 2004], the viscous drag term and the slamming force term are merged into one celerity squared-dependent term, as in equation (4.18). Below the wave trough and when the cylinder is fully submerged beneath a wave crest, the force model corresponds to the conventional Morison equation with $C_s(D) = C_D = 0.809$ according to the limit value $s=D$ of equation (4.19). However, it is important to note that in general, the slamming force and the drag term of Morison are not in phase in the [Nestegård et al., 2004] model, as the slamming force only acts as an addition to the drag force. Thus, the slamming coefficient has to be a function of time, $C_s = C \cdot s(t)$. This is found to be true as $s = s(z, t)$. A rendition of the resulting load, with and without the slamming term methodology, is found in figure 4.6.

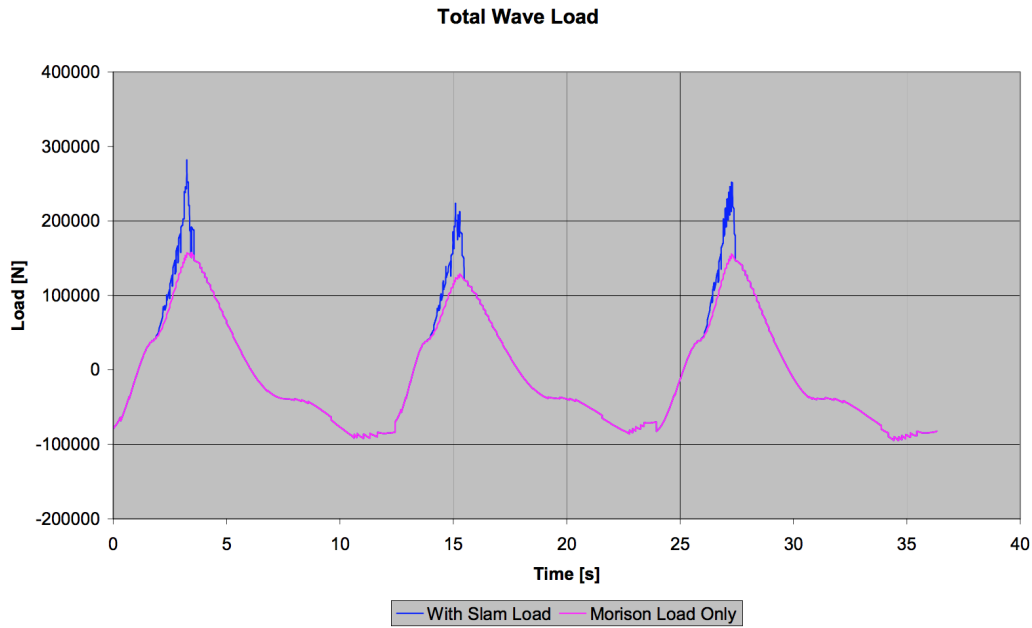


Figure 4.6.: The resulting load, with and without the slamming load component [Nestegård et al., 2004].

The slamming model for a spilling or surging breaker from [Nestegård et al., 2004] and [Det Norske Veritas, 2014] will be implemented in the numerical program of this thesis.

The time-dependent slamming coefficient is defined in equation (4.20), and is in fact the basis of equation (4.19), assuming a constant phase velocity $C = u$ during the impact duration.

$$C_s = \frac{2}{\rho D} \frac{dA^{2D}}{ds} \quad (4.20)$$

$A^{2D}(s)$ is the two-dimensional high-frequency added mass limit, which depends on s . Equation (4.20) shows that C_s is a function of the rate of change of added mass with submergence. This is the dominant part of the loading during the impact of a steep wave on a vertical cylinder and imperative for modelling the resulting high-frequency response, which is not obtainable from the conventional Morison load. This is an essential point, as it is the main objective of introducing the slamming coefficient.

The Campbell and Weynberg experiments were performed utilizing a horizontal cylinder penetrating a flat water surface, giving a uniform velocity distribution,

except at the ends. This is in line with the assumption of a vertical breaking wave front, disregarding the end effects. The slamming load assumptions can be fulfilled to a large extent if looking at specific deterministic wave breaker impact incidents. However, if the force model of [Nestegård et al., 2004] is to be used for entire wave elevation time series, where the majority of the waves are non-breaking, the assumption of a uniform wave celerity is faulty as the particle velocity varies with z .

The horizontal water particle velocity of equation (4.18) is assumed equal to the phase velocity, i.e. the wave celerity of the incoming wave. In [Nestegård et al., 2004] it is estimated using linear theory. It varies sinusoidally, from $u = \alpha c$ at the crest and trough to $u = 0$ at the MWL, where the steepness parameter α ($\alpha \leq 1$ and $\alpha = 1$ for a breaking wave) is assumed equal to 0.3 for all cases. Wheeler stretching is utilized in the wave elevation.

[Det Norske Veritas, 2014] characterizes ship collision as a primary concern in ALS. In the offshore wind industry, large global slamming loads are treated as ALS loads with a certain predicted frequency and magnitude. However, since ship impact is considered more crucial in the risk assessment, global slamming loads are not dimensioning.

A problem with many of the established slamming methods is that they offer no stochastic view of the breaking wave impacts, so they are difficult to implement in dimensioning.

In [Choi, 2014], a comparison of existing conventional methods using wave and structural analysis models to calculate breaking wave slamming, is given. As in [Marino et al., 2013], the structural analysis models that were considered use an impulsive slamming force F_I to estimate the breaking wave impact:

$$F_T = F_M + F_D + F_I \quad (4.21)$$

The impulsive slamming force is found through

$$F_I = \rho R C_b^2 C_s \lambda_c \eta_b \quad (4.22)$$

where R is the pile radius, C_b is the wave celerity at breaking, C_s is the slamming coefficient, λ_c is the curling factor and η_b is the maximum surface elevation at breaking. The difference between (4.17) and (4.22) mainly lies in how the impact area is estimated.

The impact force in equation (4.22) can be split into the two-dimensional line force (4.23) multiplied by the factor $\lambda_c \eta_b$.

$$f_L = C_s \rho R C_b^2 \quad (4.23)$$

The impact of a breaking wave spreads out from a single point in the radial and tangential direction, as in figure 4.7. This means that the impact can be assumed to occur simultaneously along the entire impacted area. Thus, the three-dimensional impact force F_I corresponds to the line force f_L multiplied by $\lambda_c \eta_b$, which is the impact area height (see figure 4.3) [Wienke and Oumeraci, 2005]:

$$F_I = \int f_L dz = f_L \cdot \lambda_c \cdot \eta_b \quad (4.24)$$

Intuitively, this area height factor has a great effect on the magnitude of the impact force. A low wave with a large curl will generate a small F_I .

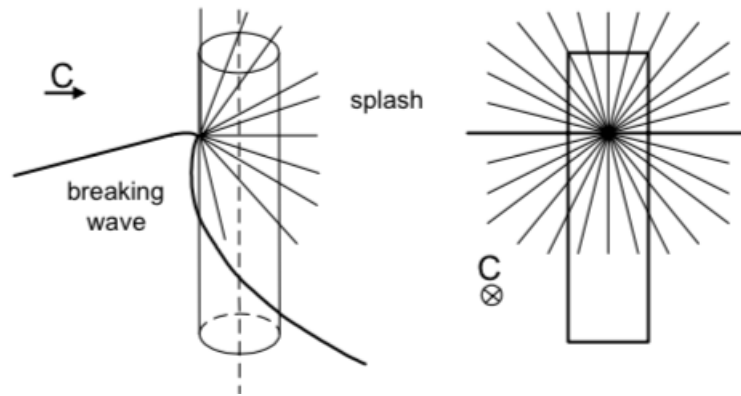


Figure 4.7.: The impact of a breaking wave [Wienke et al., 2005].

A problem with these methods is that the slamming coefficient C_s and curling factor λ_c need to be determined empirically. So far, experiments to establish these parameters have shown considerable scatter, even with nominally identical waves. In table 4.1 from [Choi, 2014], values from several experimental studies are compared:

	Slamming coefficient	Curling factor	Impact distribution
[Goda et al., 1966]	π	0.4-0.5	Uniform
[Sawaragi and Nochino, 1984]	π	0.90	Triangular
[Tanimoto et al., 1986]	π	0.5-0.66	Triangular
[Wienke and Oumeraci, 2005]	2π	0.2-0.6	Uniform
[Arntsen et al., 2011]	4.3	0.67	Triangular

Table 4.1.: A comparison of slamming coefficients and curling factors, from [Choi, 2014].

The source concludes that estimating the magnitude of a breaking wave impact from empirical coefficients is inaccurate. A reason is that the impacts greatly depend on the effect of air entrapment in pockets and the entrainment of air bubbles. Breaking patterns and the asymmetry of the waves cause the air entrapment to differ slightly for each experiment test. Also, only minor changes in bathymetry have been shown to have a large effect on the impact force. Finally, the structural response can cause dynamic amplification due to hydroelastic effects. The structural response will be large if the breaking wave impact force frequency is close to the structure's natural frequency.

[Wienke et al., 2005] compared the time history of the impact force F_I in [Goda et al., 1966] with the one elaborated in [Wienke and Oumeraci, 2005] (equation (4.14)), as shown in figure 4.8. This is just one example of the discrepancies in slamming models. The force decrease is slower and the initial slamming coefficient value is lower in the [Goda et al., 1966] model.

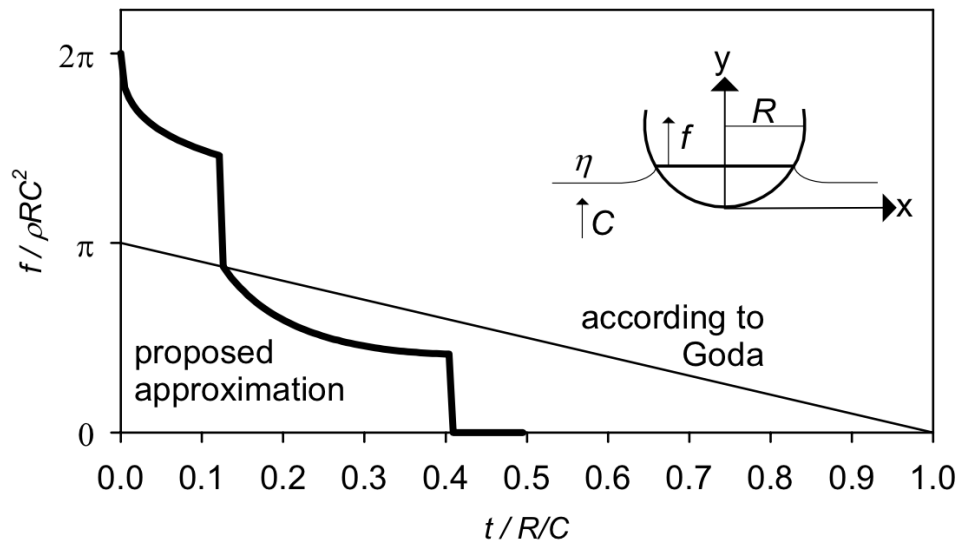


Figure 4.8.: Comparison of the slamming coefficient (C_s) time histories for two impact force models [Wienke et al., 2005].

The most important differences between the two models lie in two assumptions [Wienke et al., 2005]:

- Pile-up effect
- Radial spreading

The radial spreading has already been discussed, implying that the impact can be assumed simultaneous along the cylinder height. This assumption is most accurate for a vertical plunging breaker wall, as in figure 4.3. When there is a non-negligible angle between the breaker front and the pile, the model inaccuracy must be considered. The pile-up effect is the increased wetted surface taken into account by Wagner in figure 4.1, which means that the maximum force increases and the impact duration is reduced. [Goda et al., 1966] rather used von Karman theory, where the wetted surface is calculated by considering an undisturbed flat water surface. The novelty of the [Goda et al., 1966] paper, as opposed to the original [von Kármán, 1929], was the inclusion of the impact area height $\lambda_c \eta_b$.

With a known structural response function, it is possible to predict the evolution of the force of a slamming incident. The increased impact duration of [Goda et al., 1966] introduces a lag in the structural response and thus the force history. This is illustrated in figure 4.9.

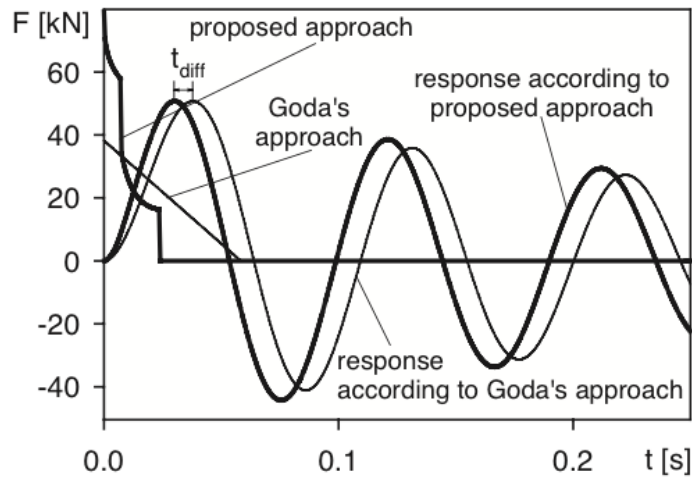


Figure 4.9.: Force development for a breaking wave. A comparison of the Wienke and Goda force models [Wienke and Oumeraci, 2005].

At global impact, the structure will start to oscillate, generating a dynamic force contribution in addition to the quasi-static one. The resulting dynamic part of the force is found by subtracting the quasi-static part from the total force, as illustrated in figure 4.10A-B.

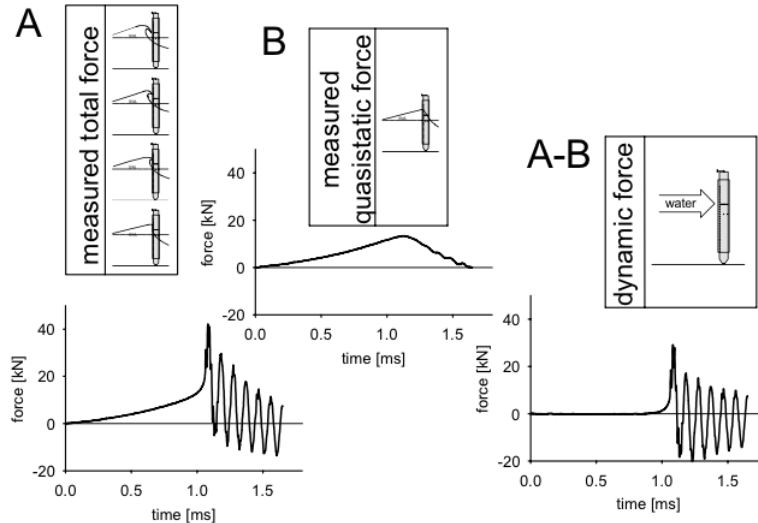


Figure 4.10.: Slamming load composition [Wienke et al., 2005]. Figure A shows the total slamming load history of a breaking wave. Figure B shows the quasistatic load history, whilst figure A-B shows the resulting dynamic part of the force.

The frequency of the dynamic force (A-B) oscillations is the eigenfrequency of the pile, and the force amplitude depends on the amplitude of the impacting wave [Wienke and Oumeraci, 2005].

[Hallowell et al., 2015] points out that the [Wienke and Oumeraci, 2005] experiments are performed under idealized conditions in a wave flume, whilst the conditions for ocean-installed offshore wind turbines are more complex. The model does not consider non-linear irregular waves, free surface particle velocities or the spatial variation of the slam. The varying real-life breaking wave characteristics is a limitation of the [Wienke and Oumeraci, 2005] model.

5 | Model Testing of a Pile with a Flexible Rotational Spring

The objective of the model testing was to provide data for stochastic analyses and the deterministic validation of load models in the numerical response program. ULS sea states were run in the experiments.

The structure represents an idling turbine, as no aerodynamic damping was taken into account. Waves were the only environmental load included. Wave elevations, pile-top accelerations, shear forces and response moments were measured for post-processing.

5.1. Principles of model testing

Performing model tests can be a valuable demonstration of the performance of a structural design. The accuracy of the test data increases with model size, but so does the trial cost.

In order to achieve similar behavior in model and full scale it is necessary to utilize scaling laws when constructing the model. For similarity in forces the following conditions apply in testing [Steen, 2014]:

- *Geometrical similarity*: Same shape for model and full scale, i.e. a constant length relation $\lambda = L_F/L_M$ exists for all structural dimensions and environmental length scales.
- *Kinematic similarity*: Velocity and acceleration ratios have to be equal in model and full scale, implying that an incoming flow will encounter the same relative geometrical paths in both scales.
- *Dynamic similarity*: The different force components make out the same proportions of the total force in model and full scale.

Satisfying different scaling laws simultaneously is usually not achievable in a model test. Common practice is to utilize Froude scaling, where similarity in the Froude number F_N is given as [Chakrabarti, 1994]:

$$F_N = \frac{v_M^2}{gD_M} = \frac{v_F^2}{gD_F} \quad (5.1)$$

which is established by demanding similarity in the ratio between inertia and gravitational forces:

$$\frac{F_i}{F_g} \propto \frac{\rho u^2 D^2}{\rho g D^3} = \frac{u^2}{gD} \quad (5.2)$$

Similarity in this force ratio is achieved through equality in Froude number as well as geometrical and kinematic similarity.

Froude number similarity is generally obtainable in a flow with a free surface as the gravitational effects dominate, whilst other influences like viscosity, surface tension and roughness are often negligibly small [Chakrabarti, 1994]. In Froude scaling, the model and full scale accelerations are equal [Chakrabarti, 1994].

$$\dot{u}_M = \dot{u}_F \quad (5.3)$$

This is called Froude's law.

Relevant sizes are scaled according to the geometric similarity, i.e. $L_M = \lambda L_F$. It gives $u_M = \sqrt{\lambda} L_F$ and $F_M = \lambda^3 F_F$, since $F = mg$, where the mass $m = \rho L^3$ and the acceleration is equal. The moment is found by $M_M = \lambda^4 M_F$. Some of the scaled sizes are illustrated in figure 5.1.

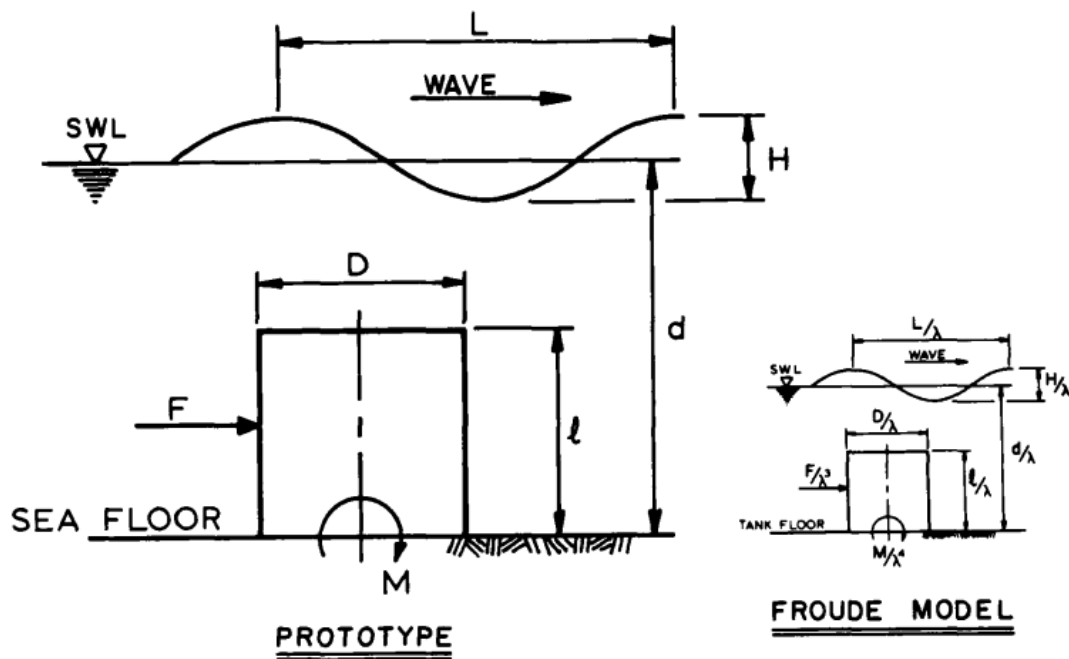


Figure 5.1.: Froude scaling of dimensional parameters [Chakrabarti, 1989].

5.2. A discussion on the model roughness

The Reynolds number Re is defined as the ratio between inertia forces and viscous forces [Chakrabarti, 1994]:

$$\frac{F_i}{F_v} \propto \frac{\rho v^2 D^2}{\mu v D} = \frac{\rho v D}{\mu} = \frac{v D}{\nu} = Re \quad (5.4)$$

Obtaining similarity in Reynolds number is usually not possible in model testing due to a much lower flow velocity in the model tank. Thus, in order to accomplish geometrical similarity and to realistically model viscous effects for large Reynolds numbers, an additional surface roughness is introduced to compensate for the differences in scale.

For structures whose dimensions are of one order of magnitude smaller than the wavelengths, the wave forces are said to depend on the Reynolds number [Chakrabarti, 1994], i.e. the forces generally no longer scale with λ^3 . When $O(D) \sim O(\lambda)$ the viscous drag forces will be negligibly small compared with the inertia forces and Re becomes insignificant.

The Keulegan-Carpenter number KC is a commonly used parameter to determine the relative importance of drag and inertia.

$$KC = \frac{u_{max} T}{D} \quad (5.5)$$

where u_{max} is the maximum horizontal water particle velocity, T is the wave period and D is the pile diameter. Similarity in KC is obtained if the wave height/cylinder diameter-ratios are equal in model and full scale. KC follows Froude's law, but the inertia and drag coefficients C_M and C_D , however, do not, as they depend on Re .

The drag force coefficient dependency on Re is large in the sense that it varies with the state of the flow regime, which is roughly characterized as either laminar, transitional or turbulent. In the turbulent flow regime C_D is almost constant with Re . Empiric testing shows that for $Re < 10^5$ the boundary layer flow will most likely be laminar, whilst turbulence occurs for $Re > 10^6$. In model testing, the low flow velocity and small model dimensions most often lead to a Re in the laminar range, whilst it is turbulent in full scale. This may have a large impact on the drag force, as a laminar flow causes a considerably higher C_D (see figure 5.2). When using Froude scaling, corrections for the Re can be employed. Also, flow tripping

is often applied, inserting a roughness farthest upstream on the model in order to trip a laminar flow to become turbulent.

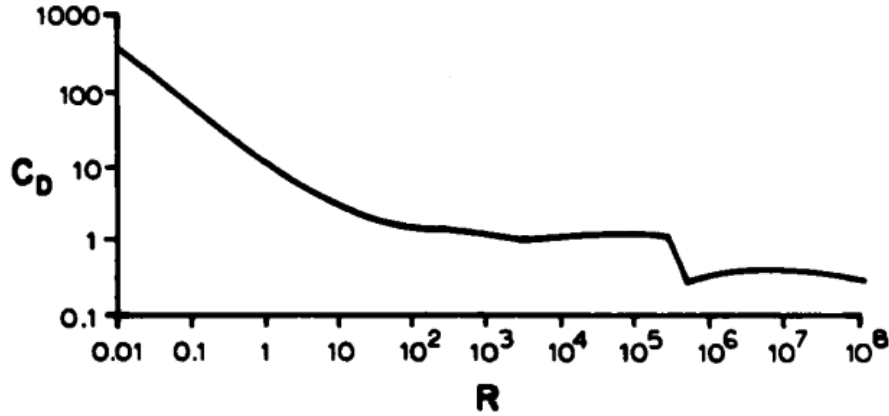


Figure 5.2.: C_D variation with Re [Chakrabarti, 1989].

By assuming linear wave theory the particle velocity can be written

$$u = u_0 \cos \omega t \quad (5.6)$$

giving a particle acceleration of

$$\dot{u} = -\omega u_0 \sin \omega t \quad (5.7)$$

which substituted into the nondimensional force from the Morison equation (3.13) gives [Chakrabarti, 1989]:

$$\frac{f}{\frac{1}{2}\rho D u_0^2} = -\frac{\pi^2 C_M}{KC} \sin \omega t + C_D |\cos \omega t| \cos \omega t \quad (5.8)$$

from which the ratio between the nondimensional drag and inertia force can be established:

$$\frac{f_D}{f_I} = \frac{C_D KC}{\pi^2 C_M} \quad (5.9)$$

[Chakrabarti, 1989] compares the intermediate and deep water ratio of the maximum total drag and inertia forces on a cylinder extending from the sea bed to the

mean water level:

$$\begin{aligned} \frac{F_D}{F_I} &= \frac{C_D KC}{2\pi^2 C_M} \frac{2kd + \sinh 2kd}{2\sinh^2 2kd} && \text{intermediate depth} \\ \frac{F_D}{F_I} &= \frac{C_D KC}{2\pi^2 C_M} && \text{deep water} \end{aligned} \quad (5.10)$$

Disregarding C_D and C_M , which are almost constant in a turbulent regime, the deep-water relation is seen to only be a function of KC , whilst the intermediate depth ratio also depends on the depth parameter kd . At low KC numbers the total force is clearly inertia dominated. At $KC = 4$, $\frac{F_D}{F_I} = 10\%$, increasing the maximum total force by less than 0.5% (due to the relative phase) [Chakrabarti, 1989].

In the model testing performed in this thesis work a 144 mm-diameter cylinder is to be tested. With a 1:48 scale the corresponding full-scale diameter is 6.9 m.

As a preliminary illustration of how the roughness should be considered in the ULS model testing, figure 5.3 is utilized. [Mathiesen et al., 2014] gives the 50-year return period maximum significant wave height for Creyke Beck B location 2, as $H_{s,max} = 10.2 \text{ m}$, with a corresponding peak period $T_p = 15.2 \text{ s}$. As an estimate, linear wave theory is employed with the given H_s , T_p values and the 20.9 m depth. The maximum particle velocity at the MWL is found to be $u_{max} = 3.7 \text{ m/s}$.

$$KC = \frac{u_{max} T}{D} = \frac{3.7 \cdot 15.2}{6.9} = 8.2 \quad (5.11)$$

Even if the specified KC number in figure 5.3 is higher ($KC = 20$), the curves are used as an illustrative exercise, giving an indication to how the roughness should be taken into account. The full scale Reynolds number will be

$$Re_{FS} = \frac{u_{max} D}{\nu} = \frac{3.7 \cdot 6.9}{10^{-6}} = 2.6 \cdot 10^7 \quad (5.12)$$

whilst the model scale Reynolds number is approximately

$$Re_{MS} = Re_{FS} / \lambda^{1.5} = 3.5 \cdot 10^5 \quad (5.13)$$

Looking at figures 5.3 it is understood that the C_D and C_M are in a Re-sensitive region for a Reynold number of $O(10^5)$. By introducing an increased roughness, e.g. by fastening sand paper to the cylinder surface, a leftward shift of the curves would imply more stable C_D and C_M parameters for the Re range of the model

scale testing. However, considering the model-scale Re in equation (5.13), one could argue that for the largest wave incidents, the Reynolds number is sufficiently high to have entered stable C_D , C_M regions.

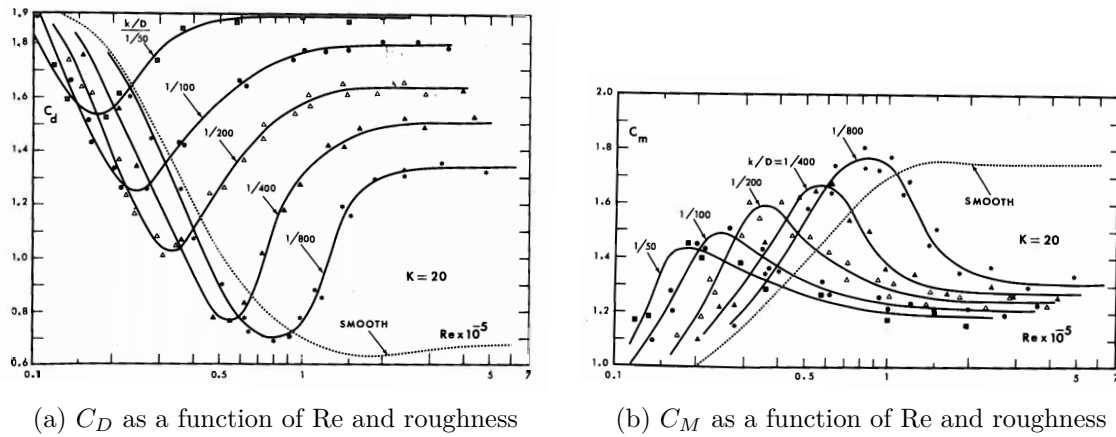


Figure 5.3.: C_D and C_M variation with Re and roughness ($KC = 20$). From [Sarpkaya, 1976], reprinted in [Sarpkaya and Isaacson, 1981].

With 10 cm marine growth the full-scale roughness is $k/D=1/69$. Reading off figure 5.3 with the calculated parameters, the following C_D and D_M values are found.

	Model scale (smooth)	Full scale ($k/D=1/69$)
C_D	0.65	1.85
C_M	1.8	1.2

Table 5.1.: Approximate C_D and C_M values in model and full scale.

Despite the reduction of model scale effects with roughness, it was decided against testing with a rough model. By introducing a new parameter of which the effects were uncertain, both a smooth and rough model should have been tested to understand the viscous effects. However, due to time limitations in the testing facility, only a smooth model was used, as testing with a rough model may in fact have introduced more questions than answers. Even though the quality of non-ringing loads may be less robust, many studies on ringing have been performed using smooth models, as it has been shown that ringing is independent of the surface roughness [Krokstad, 2015]. Thus, a smooth model was chosen as not

to risk underestimating the frequency and effect of ringing, since the maximum loads are the primary concern in this thesis.

5.3. Irregular sea

When looking at the sea surface its irregular nature is evident and thus it has to be described by a combination of regular waves of different wave frequencies. A first approximation to this is long-crested waves, in which all waves propagate in the same direction. [Myrhaug, 2007] gives the surface elevation of long-crested waves as

$$\zeta(x, t) = \sum_{n=1}^N \zeta_{An} \cos(\omega_n t - k_n x + \epsilon_n) \quad (5.14)$$

where ζ_{An} and ϵ_n are the wave amplitude and relative phase of wave n , respectively. The phase angles are assumed stochastically independent with an identical, rectangular distribution.

For short-crested waves a propagation direction θ is introduced for each of the different sinusoidal wave components. Similarly as for long-crested waves, the wave components are summed to give the surface elevation. For short-crested waves, however, a double sum is used to account for the propagation directions.

$$\zeta(x, y, t) = \sum_{i=1}^I \sum_{j=1}^J \zeta_{Aij} \cos(\omega_i t - k_i x \cos \theta_j - k_i y \sin \theta_j + \epsilon_{ij}) \quad (5.15)$$

Using a directional wave spectrum $S(\omega, \theta)$ for ζ as a measure of the wave energy density, the volume within $S(\omega_i, \theta_j) \Delta\omega \Delta\theta$ is the total wave energy per unit area for the wave components within the small intervals $\Delta\omega$ and $\Delta\theta$. Here, ω_i and θ_j are the middle values of the respective intervals. By letting $\Delta\omega, \Delta\theta \rightarrow 0$, the total wave energy per unit area can be written

$$\frac{E}{\rho g} = \int_0^{2\pi} \int_{-\infty}^{\infty} S(\omega, \theta) d\omega d\theta \quad (5.16)$$

As $\frac{1}{2} \zeta_{Aij}^2$ is also a measure of the wave energy per unit area for $\Delta\omega \Delta\theta$, the wave amplitudes at a certain frequency and direction can be found by [Myrhaug, 2007]

$$\zeta_{Aij} = \sqrt{2S(\omega_i, \theta_j) \Delta\omega \Delta\theta} \quad (5.17)$$

The standardized wave spectra assume a stationary and ergodic wave process and the surface elevation has a Gaussian distribution with zero mean. The stationarity implies that within a short time interval the mean and variance will be constant, whilst ergodicity implies that a single realization can be assumed representative for the wave process.

Wave statistics can be derived from the wave spectrum, many of which are defined through spectral moments, given by:

$$m_n^\omega = \int_0^\infty \omega^n S(\omega) d\omega \quad (5.18)$$

The significant wave height, i.e. the mean of the highest third of the waves in a sea state, is estimated by

$$H_{m0} = 4\sqrt{m_0} \quad (5.19)$$

where m_0 is the zero moment, corresponding to the variance, i.e. the area under the spectrum. H_{m0} is the estimate of H_s when it is calculated from the spectrum.

A 20-min to 3-hour sea state duration is usually assumed [Myrhaug, 2007]. In this thesis, 3-h stationarity is utilized, giving a constant peak period and significant wave height within this time interval.

The JONSWAP ('Joint North Sea Wave Project') spectrum is commonly used to describe pure-wind sea states in the North Sea. It is a three-parameter spectrum defined by the peak period T_p , the significant wave height H_s and the peak enhancement factor γ . The empirical γ factor applied on the Pierson-Moskowitz spectrum to achieve JONSWAP, is based on hindcast data from North Sea measurements.

$$S(f) = \frac{5}{16} H_s^2 T_p \left(\frac{f}{f_p}\right)^{-5} \exp\left[-\frac{5}{4} \left(\frac{f}{f_p}\right)^{-4}\right] (1 - 0.287 \ln \gamma) \gamma^{\exp[-0.5(\frac{f-f_p}{f_p \sigma})^2]} \quad (5.20)$$

is found in [Mathiesen et al., 2014] with

$$\sigma = \begin{cases} 0.07, & \text{for } f \leq f_p \\ 0.09, & \text{for } f > f_p \end{cases} \quad (5.21)$$

and

$$\gamma = 42.2 \left(\frac{2\pi H_s}{g T_p^2}\right)^{\frac{6}{7}} \quad (5.22)$$

[Mathiesen et al., 2014] suggests that the TMA spectrum may be proposed for the Dogger Bank area in a later version of the metocean report. The TMA spectrum is a finite-depth modified variant of the JONSWAP spectrum, based on measurements from Bockstigen in the Baltic Sea [Bergdahl, 2009]. In [Det Norske Veritas, 2010], $S_{TMA}(\omega, d)$ is given by

$$S_{TMA}(\omega, d) = S_{JONSWAP}(\omega) \phi(\omega, d) \quad (5.23)$$

where $\phi(\omega, d)$ is a dimensionless, frequency-dependent depth function that redistributes the spectral values with ω :

$$\phi(\omega, d) = \frac{\omega^5 \frac{\partial k}{\partial \omega}}{2g^2 k^3} = \frac{\cosh^2 kd}{\sinh^2 kd + \frac{\omega^2 d}{g}} \quad (5.24)$$

Use of the spectrum is valid where refraction and diffraction are negligible, meaning that the bathymetry slope is small ($\leq 1 : 100$) and sea bed characteristics are smoothly varying [Bishop and Donelan, 1989]. Also, the wind sea is assumed to be in a steady state condition, implying that the use of the TMA spectrum in a fetch or duration limited region would be conservative.

An important aspect when considering the TMA-spectrum is that it considers the dissipation of energy due to shallow water effects, meaning that compared to the JONSWAP spectrum, energy is lost. This is illustrated by the ϕ factor in figure 5.4.

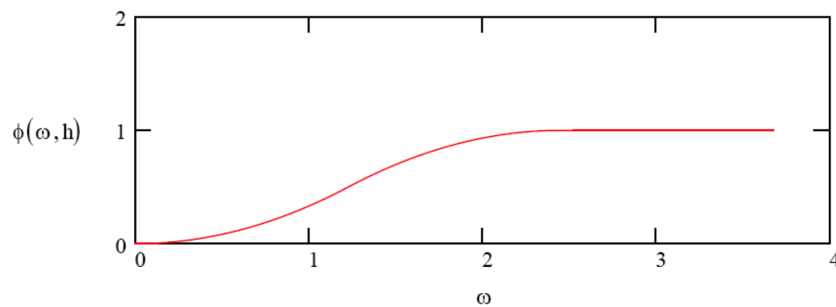


Figure 5.4.: The frequency and depth-dependent ϕ parameter of the TMA spectrum, given as a function of ω [Bergdahl, 2009].

For the experiments in the tank, the irregular time series were generated using

IrregWaveSeries.m for k waves up to the Nyquist frequency. The wave elevation in the time domain is found through the real part of the inverse discrete Fourier transform applied on the complex wave components in the frequency domain (X_k), shown in equation (5.30). X_k corresponds to the amplitude of the waves of each frequency component and includes the relative component phases, as indicated in equation (5.25). The procedure to find the wave elevation, which is applied in Realize.m (see appendix D), for $k=N/2$ waves is given by [Newland, 1993]:

$$X_k = a_k - ib_k = \zeta_{An} e^{-i\epsilon_n} \quad (5.25)$$

For a continuous function, a_k and b_k are given by

$$a_k = \frac{1}{T} \int_0^T \zeta(t) \cos(\omega_{N/2} t) dt \quad (5.26)$$

$$b_k = \frac{1}{T} \int_0^T \zeta(t) \sin(\omega_{N/2} t) dt \quad (5.27)$$

whilst for a discrete series, equation (5.25) can be rewritten as

$$\begin{aligned} X_k &= \frac{1}{T} \sum_{n=1}^N \zeta_{An} e^{-i\omega_{N/2} n\Delta t} \Delta \\ &= \frac{2}{N} \sum_{n=1}^N \zeta_{An} e^{-i\omega_{N/2} n\Delta t}, \quad k \in [1, N/2 - 1] \end{aligned} \quad (5.28)$$

where $\Delta = \frac{T}{N/2}$, X_k are the complex wave components, N is the number of sampling points, T is the time duration, Δt is the time spacing between each sampling point and $\omega_{N/2}$ is the Nyquist frequency, which is the largest frequency included in the time series. It is found by

$$\omega_{N/2} = \frac{2\pi k}{T} = \frac{2\pi N/2}{T} = \frac{\pi N}{T} = \frac{\pi T/\Delta t}{T} = \frac{\pi}{\Delta t} \quad (5.29)$$

The wave amplitudes for each frequency component in the spectrum are found using the long-crested wave reciprocal of equation (5.17), i.e. $\zeta_{An} = \sqrt{2S(\omega_n)\Delta\omega}$ up to $N/2-1$ [Myrhaug, 2007].

The time-domain wave elevation can now be found from the real part of the

inverse discrete Fourier transform of X_k :

$$\zeta_n = a_0 + \sum_{n=1}^{N/2} (a_k \cos(\omega_{N/2} n \Delta t) + b_k \sin(\omega_{N/2} n \Delta t)) \quad (5.30)$$

where

$$a_0 = \frac{1}{N} \sum_{n=1}^N \zeta_{An} \quad (5.31)$$

and

$$a_{N/2} = \frac{1}{N} \sum_{n=1}^N \zeta_{An} \cos(\omega_{N/2} n \Delta t) \quad (5.32)$$

In the MATLAB implementation the user specifies a wanted time step (the sampling frequency of the wavemaker is 50 Hz), the ramp duration at the beginning and end of the time series (applied to avoid abrupt wavemaker motion) and the total duration of the time series (3-h sea states were used in this thesis).

Each seed has a random, uniformly distributed phase between 0 and 2π , so the irregular waves can be generated using the linear wave process equation (5.14). In order to be able to reproduce the time series the rng function was used in MATLAB. For a specific seed number, rng(seed) generates the same random number to be used in the specification of the phase. In this thesis, the seed number was chosen as a function of the run number (1-20, as there are 20 seeds) and H_s , implying that for the same significant wave height on different water depths, the same phases are selected. This enabled an explicit analysis of the effects of changing the water depth, as two specific different-depth seeds could be compared directly.

5.4. Wavemaker theory

A wavemaker theory that has proven to provide satisfactory regular and irregular wave series in the small wave flume at MARINTEK is the Biésel transfer function for a piston wavemaker, equation (5.33).

$$\frac{H}{S} = 2 \frac{\cosh(2kh) - 1}{\sinh(2kh) + 2kh} \quad (5.33)$$

It is based on linear potential flow theory, meaning that the wave number k can

be found from the linear dispersion relation $\omega^2 = kg \tanh kh$. H/S is the wave height-to-stroke ratio, where H is the linear wave height. The Taylor-linearized Biésel equation is derived assuming small stroke displacements and velocities. A complete derivation is not going to be provided here, but interested readers can consult [Dean and Dalrymple, 1991].

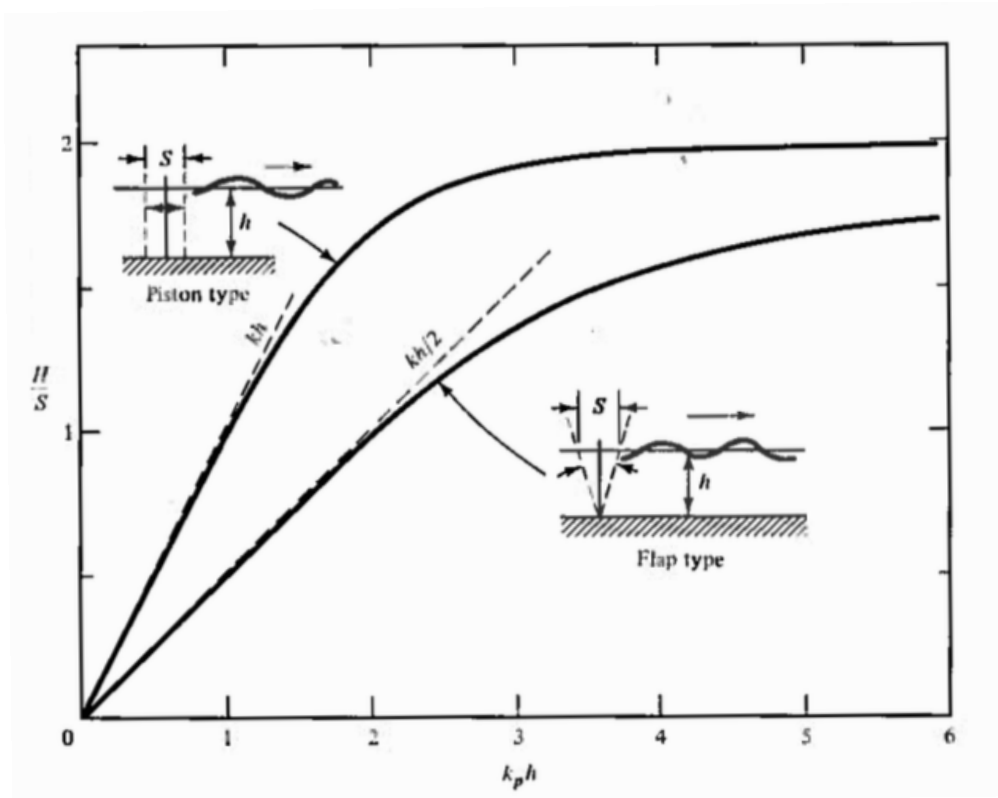


Figure 5.5.: The Biésel transfer function [Dean and Dalrymple, 1991].

The MATLAB-generated time series that were run in the wave tank corresponded to the ideal time series appearing at the wavemaker. As the wave speed depends on the wave period, the time series were not the same when they arrived at the structure. In a stochastic analysis this does not matter as the energy of the sea state is the same with or without an x -translation of the time series, i.e. H_s and T_p remain the same.

5.5. MATLAB implementation

The MATLAB routines utilized in the generation and post-processing of regular and irregular waves are shown in figures 5.6 and 5.7, respectively. The yellow entries are main programs, the mint-colored entries are subroutines and the light gray are data files. The green arrows indicate input, whilst the red are output.

In the generation of regular waves, `findk.m` is used to determine the wave number in order to find the wave height for the given steepnesses. `MechTF.m` and `biesel.m` are the mechanical and wave height-to-stroke transfer functions, respectively, whilst `write2mcl.m` writes the wavemaker input file, containing the stroke and the trigger signal for saving measured data. `CheckRegular.m` is the regular post-processing routine handling test output, as found in section 7.2.

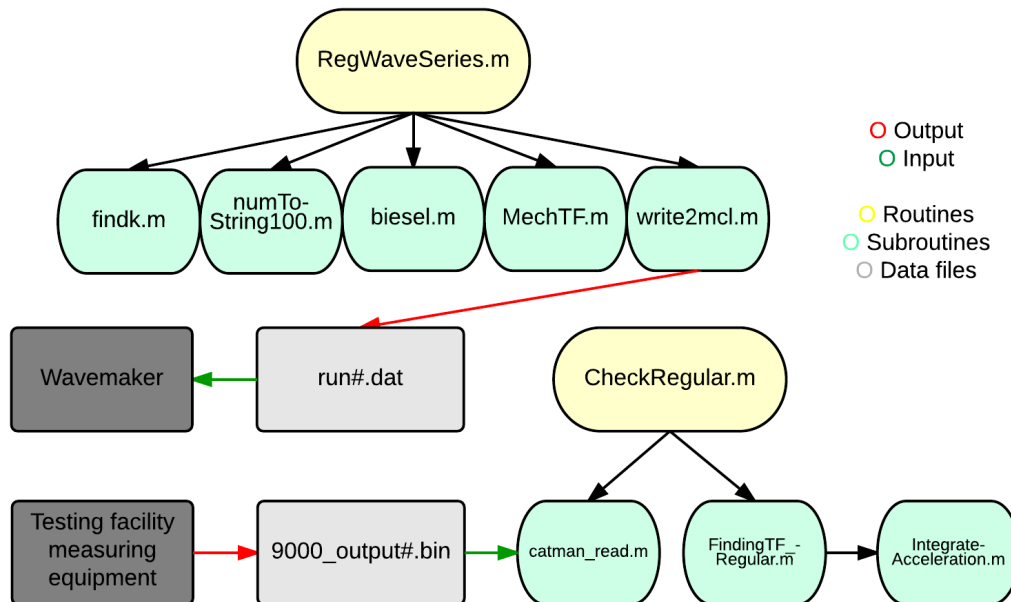


Figure 5.6.: Flow chart for generating and post-processing the regular waves.

The irregular waves are generated using the `Realize.m` routine, following the procedure presented in section 5.3. The JONSWAP spectrum is utilized, specified by the Pierson Moskowitz spectrum multiplied by a peak enhancement factor γ . `CreateBatch.m` generates the `.dat` wavemaker input file using the transfer functions and `write2mcl.m`, just as for the regular waves.

The binary files containing the measured test data are read using the `catman_read.m` routine in the irregular post-processing program `CompareFiles.m`. Through Fourier analyses, the subroutine `Compare.m` finds the sea state values, H_s and T_p , for the wavemaker input and output specified 'run#.dat' and '9000_output#.dat', respectively.

`Gumbel.m` finds the 0.05 and 0.95 confidence intervals for the Gumbel distributions and `GumbelPlot.m` plots the Gumbel regression line for the measured shear forces and moments. A Butterworth filter routine is included to separate the peak frequency-dominated responses and the eigenfrequency-dominated responses, as in figure 7.31. `CompareSpectra.m` and `CompareFMSpectra.m` set up the resulting wave spectrum and force and moment spectra. `CompareHsTpPlot.m` visualizes the measured H_s , T_p values for each seed.

The post-processing is covered in section 7.

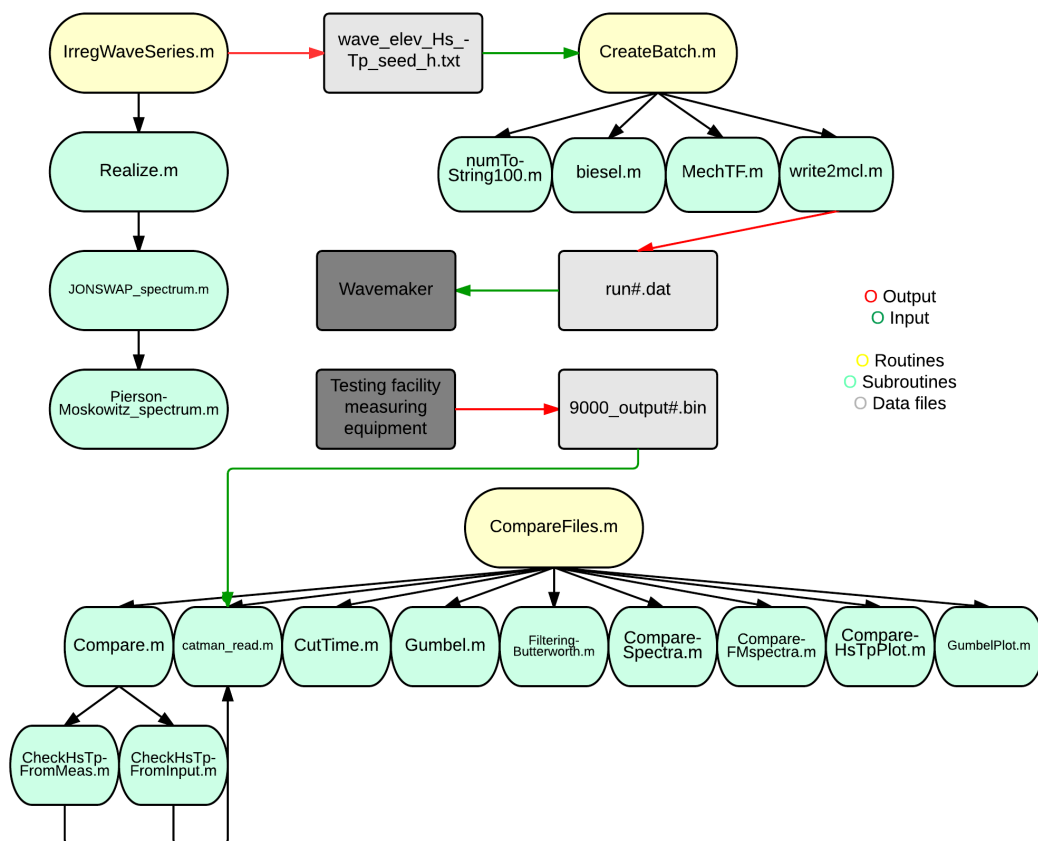


Figure 5.7.: Flow chart for generating and post-processing the irregular waves.

MATLAB version R2014b has been utilized in the thesis work. The delivered routines are listed in appendix D and attached as a compressed file in the electronic submission. All the routines included in delivery are developed in collaboration with Loup Suja-Thauvin, except where otherwise specified, that being the Biésel transfer function, `biesel.m` (by Trygve Kristiansen of MARINTEK) and a routine to find the wave number, `findk2.m` (by prof. II Jørgen Krokstad).

5.6. Dogger Bank site characteristics

Statkraft has part ownership and is responsible for the development and operation of the wind turbine park at Creyke Beck B (see figure 5.8), enclosing locations 1, 2 and 3 in figure 5.9. Thus, these are of primary concern when selecting sea states for model testing. Since met mast measurements are available for location 2, only this position will be considered. Wind loads are not a concern in this thesis, but the possibility to employ met mast measurements and wave load tests for the same location can be valuable in other work springing out from the testing. Metocean data from [Mathiesen et al., 2014] will be utilized in the test specifications.

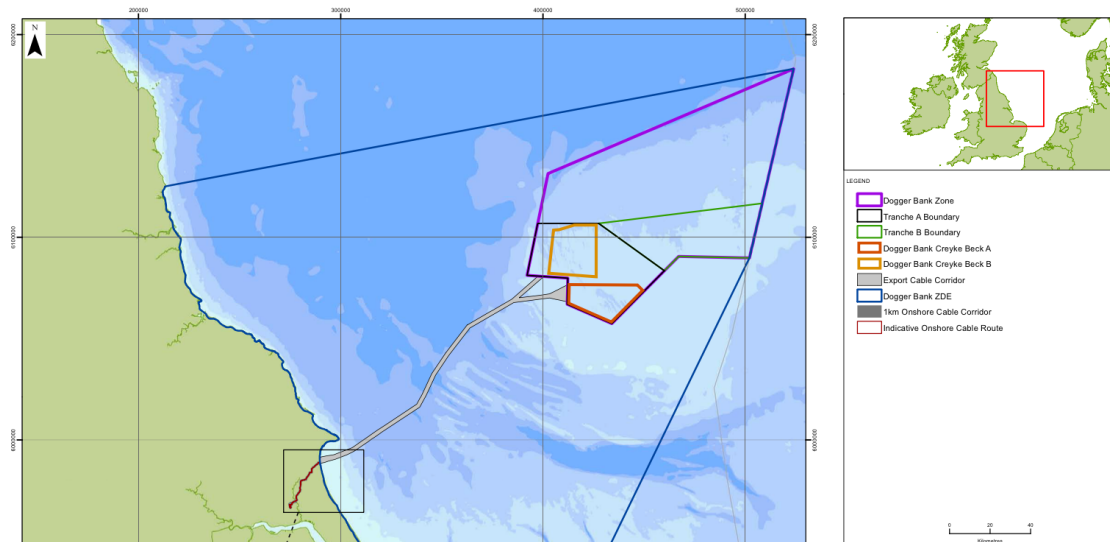


Figure 5.8.: The Dogger Bank Creyke Beck locations [Royal HaskoningDHV, 2013]. The area marked yellow is Creyke Beck B.

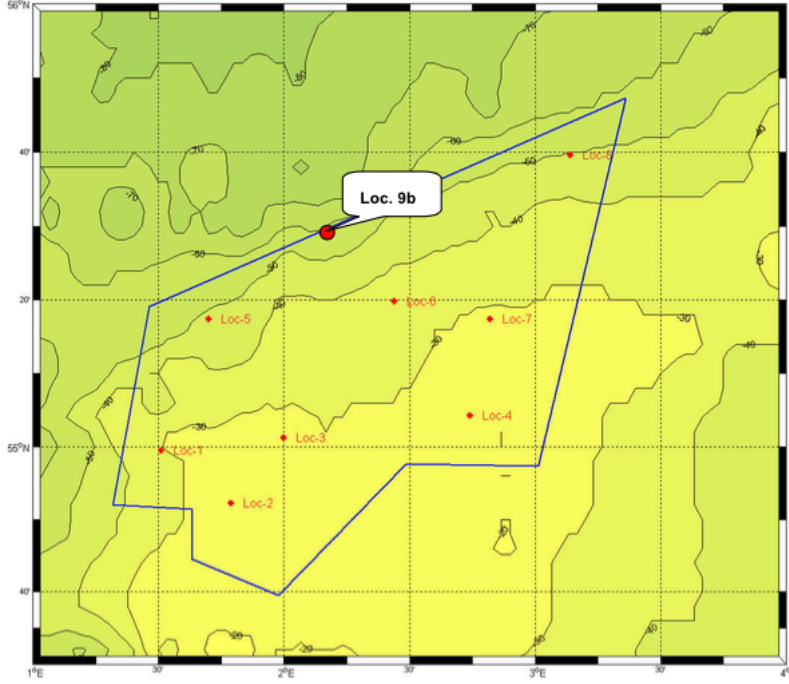


Figure 5.9.: Metocean data locations at Dogger Bank [Mathiesen et al., 2014].

5.6.1. Contour plot for location 2 of Creyke Beck B

The contour plot to be used in testing is calculated using the [Mathiesen et al., 2014]-recommended LoNoWe (Lognormal-Weibull) significant wave height distribution f_{H_s} , equation (5.35). The contours are visualized using PlotHsTpGraph.m (see appendix D). The long-term variation of sea states is given by the joint PDF for H_s and T_p :

$$f_{H_s T_p}(h_s, t_p) = f_{H_s}(h_s) \cdot f_{T_p|H_s}(t_p|h_s) \quad (5.34)$$

Here, the LoNoWe distribution of H_s is

$$f_{H_s}(h_s) = \begin{cases} \frac{1}{\sqrt{2\pi} \alpha h_s} \exp\left(-\frac{(\ln(h_s) - \theta)^2}{2\alpha^2}\right), & \text{for } h_s \leq \eta \\ \frac{\beta}{\rho} \left(\frac{h_s}{\rho}\right)^{\beta-1} \exp\left[-\left(\frac{h_s}{\rho}\right)^\beta\right], & \text{for } h_s > \eta \end{cases} \quad (5.35)$$

and the conditional lognormal distribution of T_p is

$$f_{T_p|H_s}(t_p|h_s) = \frac{1}{\sqrt{2\pi} \sigma t_p} \exp\left(-\frac{(\ln(t_p) - \mu)^2}{2\sigma^2}\right) \quad (5.36)$$

where

$$\begin{aligned}\mu &= a_1 + a_2 h_s^{a_3} \\ \sigma^2 &= b_1 + b_2 \exp(-b_3 h_s)\end{aligned}\tag{5.37}$$

All the coefficients used in equations (5.35)-(5.37) are given for location 2 in [Mathiesen et al., 2014] and rendered in table 5.2.

β	1.315
ρ	1.546
η	2.802
α	0.591
θ	0.313
a_1	0.889
a_2	0.913
a_3	0.300
b_1	0.005
b_2	0.123
b_3	0.486

Table 5.2.: Parameters used in the calculations of the LoNoWe H_s distribution and the conditional lognormal T_p distribution [Mathiesen et al., 2014].

The resulting contour plots are found in section 5.8.2, when discussing the irregular sea states to be tested.

5.6.1.1. A discussion on the validity of the sea states

According to [Det Norske Veritas, 2014], load case 6.1 for combined ULS loads on a parked turbine, the 50-year water level should be used in testing. Two water levels are included, a high and a low, and whichever gives the most unfavorable load conditions should be applied in design. The high water level corresponds to the 98 % quantile in the distribution of the annual maximum water level, and the low water level is the 2 % quantile in the distribution of the annual minimum water level. In the case of the high water level, the longer moment arm could generate the most unfavorable load. However, the increased wave non-linearity of a lower water level creates a larger average maximum load as well, so choosing between the two is not trivial and must be tested for.

There are no distributions of annual maximum or minimum water levels in the metocean report, [Mathiesen et al., 2014]. However, the mean water level, HAT, LAT and the 50-year storm surge are given. HAT and LAT are the highest and

lowest astronomical tides, respectively. They are the maximum and minimum levels that can be predicted under average meteorological effects and will not occur every year [The United Kingdom Hydrographic Office, 2015]. These values can be further amplified by weather effects such as a storm surge. As the 50-year storm surge could be combined with the HAT for the high water level, this level is probably on the conservative side, whilst the low water is probably non-conservative as it only considers the LAT.

The original intention was to use the following values for the high and low values in the experiments:

$$\begin{aligned} h_{high} &= MWL + HAT + 50 - year\ storm\ surge \\ &= 20.9\ m + 1.45\ m + 1.5\ m \approx 23.9\ m \end{aligned} \tag{5.38}$$

$$\begin{aligned} h_{low} &= MWL + LAT \\ &= 20.9\ m + (-1.55\ m) \approx 19.4\ m \end{aligned} \tag{5.39}$$

In model scale the values correspond to $h_{high} = 0.50\ m$ and $h_{low} = 0.40\ m$, as $\lambda = 48$. However, due to the large amount of breaking waves for initial lab testing, using specified 50-year return period sea states, larger water level values have been chosen. In order to test the effects of the longer moment arm versus increased non-linearity, comparable sea states with high $H_{s, effective}/H_{s, nominal}$ ratios were needed. Thus, it was decided to use full-scale water levels $h = 20.9\ m$ and $h = 30\ m$, corresponding to $h = 0.435\ m$ and $h = 0.625\ m$ in model scale, respectively.

[Mathiesen et al., 2014] states that the shallow water values of H_s larger than 8 m are probably too high in the metocean report. It further approximates the highest extremes to be 10 % too high, but recommends the use of the given values in design unless other proof of conservatism is found.

In [Engebretsen, 2012], the author argues that the grid resolution of the NORA10 hindcast model employed in the metocean report [Mathiesen et al., 2014] is too coarse to properly take shallow water effects on Creyke Beck B into account. If so, the significant wave height and peak period data provided in the metocean report are not reliable, and thus they do not serve well as the basis for a realistic analysis of the conditions at location 2.

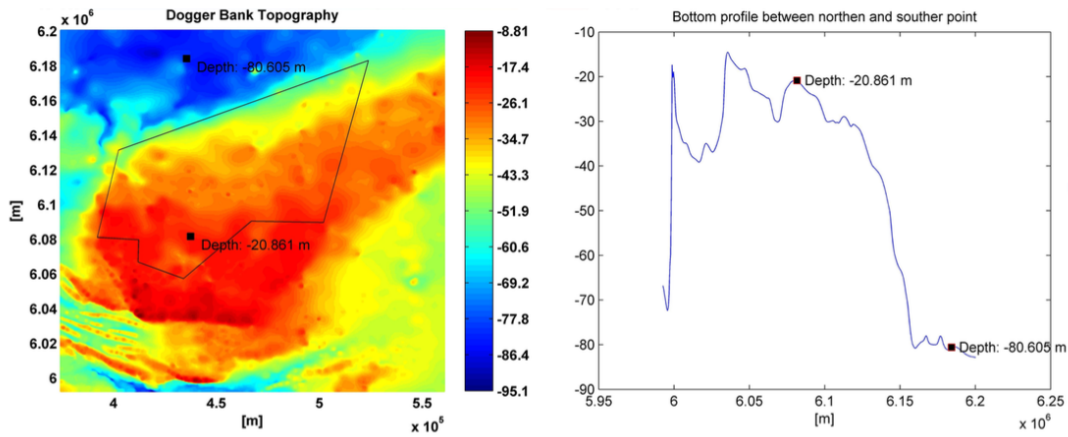


Figure 5.10.: Dogger Bank topography, taken from [Engebretsen, 2012].

As a reference point, [Engebretsen, 2012] employs NORA10 hindcast data for a location north of the Creyke Beck region, illustrated in figure 5.10. In this point the water depth is large enough to neglect shallow water effects, so the sea state parameters are assumed to be predicted well by NORA10 data. Applying a numerical model to account for shallow water effects, such as shoaling, refraction, diffraction and wave breaking, the H_s and T_p are estimated in a southern point on Creyke Beck B (also provided in figure 5.10), which is close to location 2 and with approximately the same water depth. An overview of a southern point comparison between the results of a numerical simulation and the NORA10 hindcast data is provided in table 5.3. Sea state values in the southern point for the three largest 50-year return-period storms originating in the northern point are shown. The results show that the significant wave height may be greatly overestimated in the metocean report, even by more than the suggested 10 % prediction. However, the results are not verified, and they are only given for 50-year return-period storms, so they could not be used directly in the experiments.

Sea states	Numerical model		NORA10 hindcast model		H_s	T_p
	H_s [m]	T_p [s]	H_s [m]	T_p [s]	discrepancy [%]	discrepancy [%]
1	7.42	16.89	10.20	15.98	-27.25	5.69
2	7.31	15.38	8.60	15.03	-15.00	2.33
3	7.08	14.64	8.30	14.45	-14.70	1.31

Table 5.3.: H_s , T_p values in the southern point for the three largest 50-year storms originating in the northern point. Results from [Engebretsen, 2012].

5.7. Experimental setup

The objective was to determine the forces and moments from wave loads, including slamming loads, on a pile structure in irregular sea states representing the site conditions at a Dogger Bank location. The test results were utilized in a validation of the selected theoretical load models discussed in section 3.6.2.

5.7.1. Testing facility and model setup

The model testing took place in the small wave flume at MARINTEK, Trondheim. The flume setup is illustrated in figures 5.11 and 5.12.

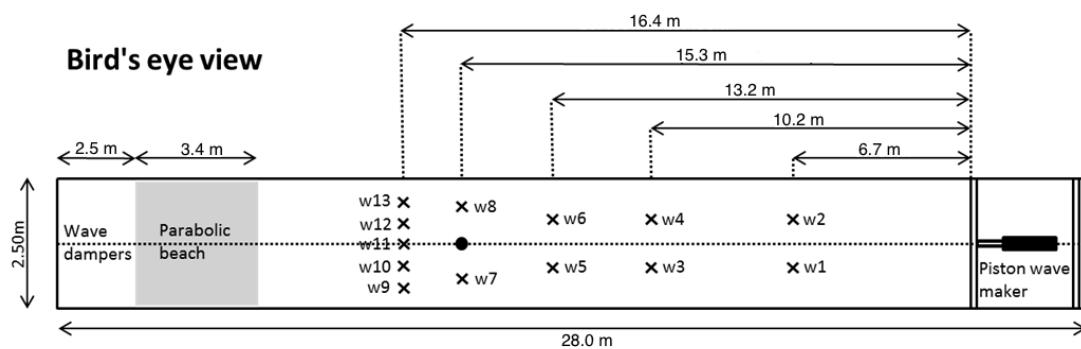


Figure 5.11.: A bird's eye view of the model tank setup, courtesy of T. Kristiansen (MARINTEK), but with slight modifications from the original.

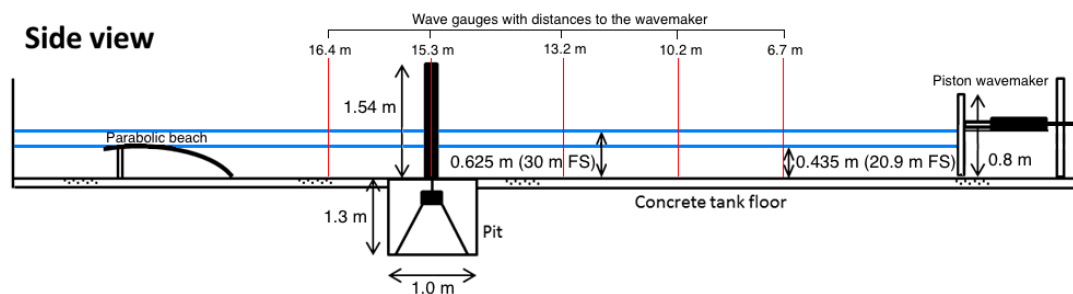
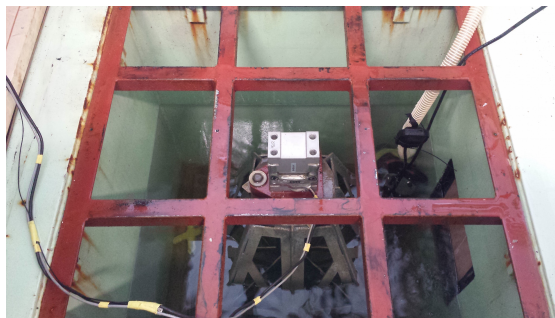


Figure 5.12.: A side view of the model tank setup, courtesy of T. Kristiansen (MARINTEK), but with modifications from the original.

The tank is 28 m long and 2.5 m wide with a bottom-fixed, perforated, parabolic, wave-absorbing beach at the end. The piston wavemaker was installed in November through December 2014, in order to improve shallow-water wave generation.

Compared with the previous wavemaker it is also supposed to reduce parasitic harmonics for regular waves [Kristiansen and Bachynski, 2015]. There is a less than 1 cm variation in bottom topography, meaning that the water depth varies around 2 % of the water depths.

The monopile model was attached to an intermediate piece acting as the spring giving the mudline stiffness. The spring was fastened to the force/moment transducer, which, through another intermediate piece, was mounted on the tower that was placed on the bottom of the pit, as illustrated in figures 5.12 and 5.13a. The plexiglass plate surrounding the lowest part of the pile was designed to have a minimal opening to the pit, as to avoid additional bias error loads on the model beneath the mudline. The tower was designed to be rigid, and previous tests showed that compared to the base spring (with a specified stiffness of 3000 Nm/rad) it is stiff enough for an inverted pendulum-like first mode, to be discussed in section 7.3.



(a) Tower, intermediate piece and force/moment transducer



(b) Submerged tower

Figure 5.13.: Contents of the tank pit.

The full-scale diameter is 6.7 m, but including a modelled 10 cm marine growth around the cylinder circumference, the total diameter is 6.912 m, giving 144 mm in model scale. A top mass of 5.04 kg, consisting of clamps and a metallic piece, was placed as in figure 5.14 at a height of approximately 1.54 m above the tank floor.

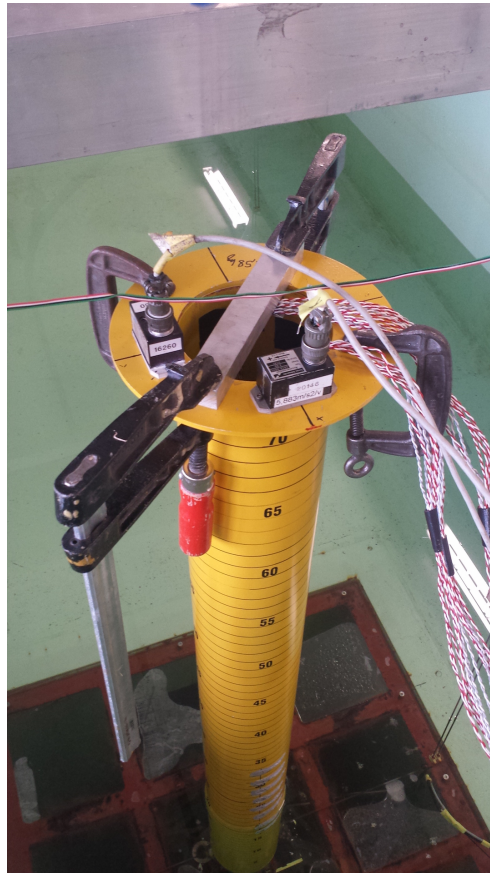


Figure 5.14.: The top mass and the accelerometers.

Scaling factor $\lambda = 48$	Model scale	Full scale
Diameter	0.144 m	6.912 m
Top mass	5.04 kg	556.83 tonnes
Pile density	2700 kg/m ³	2700 kg/m ³
Pile height	1.54 m	73.9 m

Table 5.4.: Model test parameters

5.7.1.1. Parabolic beach

The perforated parabolic beach plates have a 8 % porosity and its height should, from in-house experience, be adjusted so that the highest point is approximately 1.5 cm above the still water for each water depth. This was done to achieve maximum wave absorption.

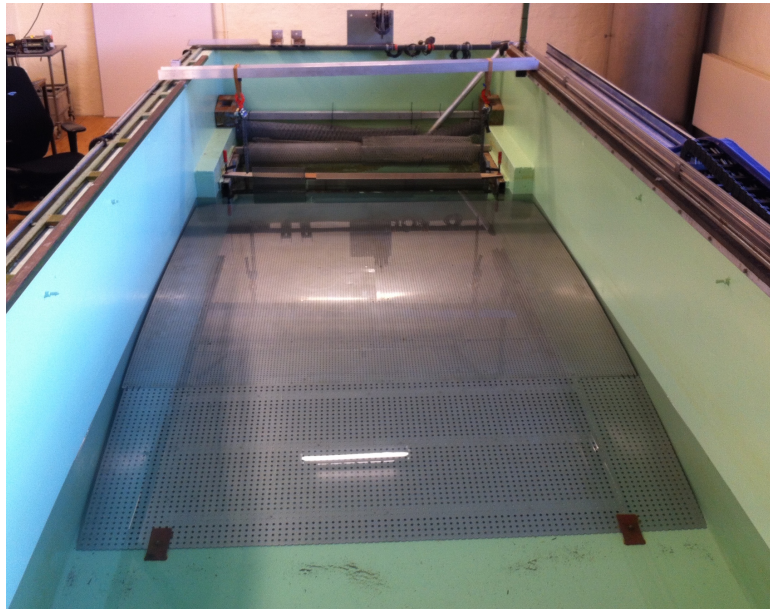


Figure 5.15.: The parabolic beach

5.7.1.2. Wavemaker

The piston wavemaker generates waves through translational piston board motion. It is driven by an electric actuator located approximately 60 cm above the tank floor.

The wavemaker transfer function consists of a mechanical transfer function and a hydrodynamic wave-to-motion transfer function. The latter transforms the desired surface elevation time series to wavemaker motion, called stroke, whilst the former converts prescribed stroke to actual wavemaker motion.

The wave-to-motion transfer function used is the Biésel function presented in section 5.4, as this has proven to give satisfactory wavemaker accuracy in previous lab tests in the small wave flume. This is an indication that neither the tank basin or the wavemaker inhabit any grave irregular behaviors.

In general, the mechanical transfer function is frequency and amplitude dependent, but in this case the amplitude dependency was found to be negligible. The mechanical transfer function had previously been established by running tests with 31 periods, every half a second from 3 s to 18 s in full scale. The result is a frequency dependent factor to be multiplied with the stroke. This is especially important for high frequencies, where the factor is large. Linear extrapolation between the period points was applied in order to determine the value in each case.

For periods smaller than 3 s and larger than 18 s, the 3-s and 18-s values were used, respectively. It had been tested for different water depths, but showed little dependency of h . Thus, the transfer function established for a water depth of 0,56 m was used in the experiments.

In order to test whether it was possible to create a better match between the wanted and obtained wavemaker stroke, a new mechanical transfer function was found using the same procedure as described above. The result is shown in figure 5.16. When using the new mechanical transfer function, however, the wanted stroke output did not improve. There was especially a problem for the high frequencies, where the wavemaker had trouble keeping up, meaning that its inertial capacity limit was exceeded. This is exemplified for regular waves in section 7.2.

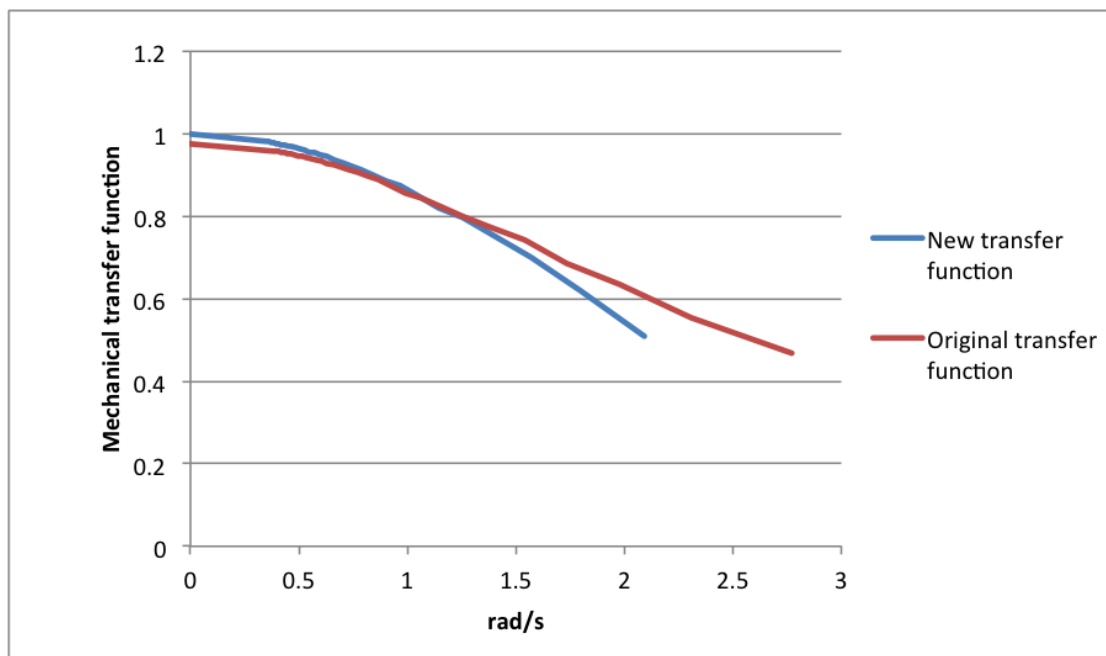


Figure 5.16.: Comparing mechanical transfer functions.

An additional factor 1.03 was multiplied with the stroke, since the cross sectional tank area is approximately 3 % larger than the piston board.

The wavemaker motion was measured and saved in order to check repeatability and to verify the correspondence of the wave calibration and model tests.

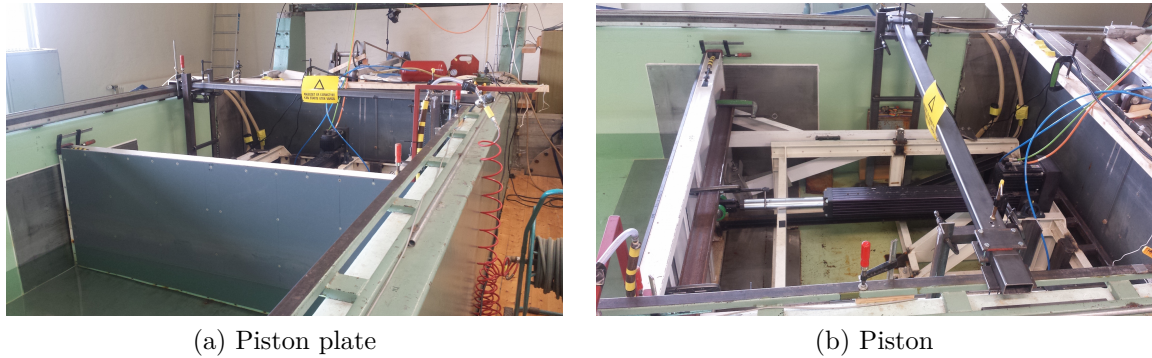


Figure 5.17.: The wavemaker

5.7.2. Instrumentation

The instrumentation included a force/moment transducer, 23 force gauges, two accelerometers, two video cameras and 13 wave gauges. The measurement sampling frequency was 200 Hz.

5.7.2.1. Force and moment transducers

The force and moment transducers, shown in figure 5.13a, had been modified by MARINTEK technicians to function in the testing facility. It measures shear forces up to approximately 7500 N in the longitudinal tank direction, which greatly exceeds the expected maximum forces in the experiments. Watertight strain gauges are glued to the force transducer to measure the moment.

The equipment had been pre-calibrated for similar tests in the tank [Kristiansen and Bachynski, 2015], and this calibration was utilized as the transducer had previously shown little drift in calibration with time. However, to check their accuracy, the transducers were tested during the experiments, applying weights and a pulley with a string attached to the top of the pile, as shown in figure 5.18. The tests included three masses and the results were as follows:

Mass	Moment arm	Applied force	Measured force	$\frac{F_{meas}}{F_{applied}}$	Applied moment	Measured moment	$\frac{M_{meas}}{M_{applied}}$
1.02 kg	1.52 m	10.01 N	10.4 N	1.04	15.21 Nm	16.5 Nm	1.08
2.59 kg	1.52 m	25.41 N	25.6 N	1.01	38.62 Nm	41.0 Nm	1.06
3.59 kg	1.52 m	35.22 N	35.0 N	0.99	53.53 Nm	58.0 Nm	1.08

Table 5.5.: Testing the force and moment transducer.

Even though the $M_{\text{measured}}/M_{\text{applied}}$ varied between 1.06 and 1.08, the testing procedure was inaccurate and limited in terms of using only three testing points. The tests were meant to check whether the measured moments were within the correct order of magnitude. Thus, the calibration was kept as was and no correction was applied in post-processing.

In addition to checking transducer calibration, the pulley system was utilized to test the specified foundation stiffness value of 3000 Nm/rad. By considering the displacement of the pile top, the stiffness could be estimated as in table 5.6.

Mass	Pile top displacement from initial position	θ	Applied moment	Estimated stiffness
1.02 kg	0.7 cm	0.0046 rad	15.21 Nm	3307 Nm/rad
2.59 kg	1.8 cm	0.0118 rad	38.62 Nm	3273 Nm/rad
3.59 kg	2.9 cm	0.0191 rad	53.53 Nm	2806 Nm/rad

Table 5.6.: Testing the force and moment transducer.

The accuracy of the test depended on approximate eyesight folding rule measurements and was based on the assumption that the pile itself is completely rigid, in order to find the deflection angle θ . Thus, the objective of the test was to verify a ballpark figure for the stiffness. Results from table 5.6 show that the specified 3000-Nm/rad stiffness is reasonable.

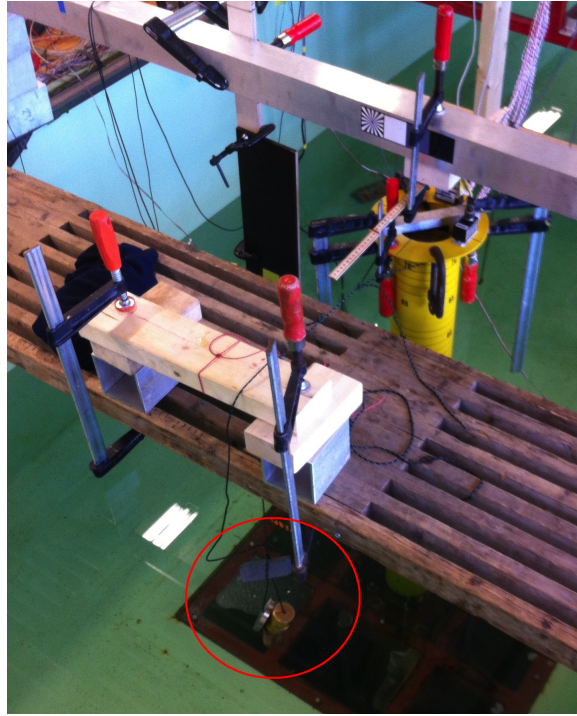


Figure 5.18.: Checking the force/moment transducer calibration and the base stiffness, using a pulley system. The weights are circled.

5.7.2.2. Force gauges

There were 23 force gauges installed on the model, 8 in front and on the back, and 7 on side. Their full-scale vertical positions above the sea floor are found in table 5.7. The calibration was performed linearly, using two calibration points, 0 and 0.2 kg.

Front (0°)			Back (180°)			Side (90°)		
Gauge #	Vertical pos. [m]	Sensor range [N]	Gauge #	Vertical pos. [m]	Sensor range [N]	Gauge #	Vertical pos. [m]	Sensor range [N]
1	33	110	9	33	110	17	33	110
2	31	5	10	31	5	18	31	5
3	29	5	11	29	5	19	29	5
4	27	5	12	27	5	20	27	5
5	25	5	13	25	5	21	25	5
6	23	5	14	23	5	22	23	5
7	20	110	15	20	110	23	20	110
8	18	110	16	18	110			

Table 5.7.: Vertical full scale pressure gauge positions.

The sensors placed at 18 m, 20 m and 33 m are less sensitive and have larger ranges than the others.

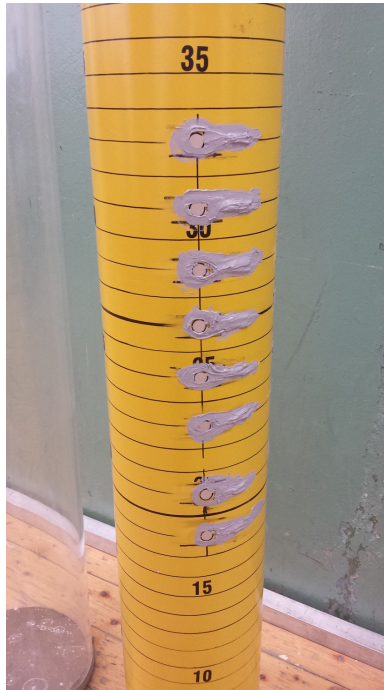


Figure 5.19.: Force gauges in the front of the pile (upstream).

5.7.2.3. Accelerometers

Two accelerometers were operated in the experiments, one for the wave propagation direction (x-direction) and the other for the transverse horizontal direction (y-direction). The accelerometers had also been pre-calibrated, and this calibration was used in the experiments. Their purpose was to validate the force/moment transducer results, logging the model top motions. The transverse accelerometer was employed to expose undesirable transverse wave loads. The accelerometer placements are shown in figure 5.14.

5.7.2.4. Video cameras

A video camera was placed upstream of the monopile model, whilst another had rear view. If an interesting incident was found in the measurements then video could be used to shed light on the cause. They recorded continuously during the days of model testing. A MATLAB routine, FindHourInCamera.m, was established for the purpose of finding specific events. Usually, high-speed cameras can

be used in order to determine wave celerity upon structural impact, which is essential when numerically estimating a slamming load. However, as shall be discussed, wave gauge data is primarily used for this purpose in the thesis.

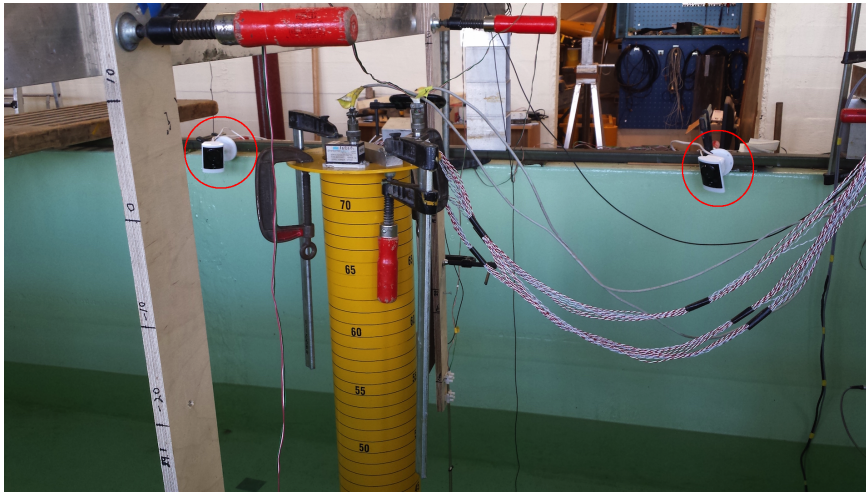


Figure 5.20.: The camera placements

5.7.2.5. Wave gauges

Thirteen capacitance type wave gauges were utilized, denoted w1-w13 in figure 5.11. Their positions were equal in the wave calibration and the model runs, except that wave gauge w8 was moved to the model position during wave calibration. Their vertical positions varied with water depth.

The wave gauges were linearly calibrated for each water depth. For $h=43.5$ cm four calibration points were utilized, whilst five calibration points were used for $h=62.5$ cm. In the experiments the lower point of the wave gauges were placed 15 cm and 30 cm above the tank floor, respectively.

5.8. Selecting waves for testing

Regular tests were included in the test matrix mainly as a means of testing the performance of the tank facility and the numerical program. The deterministic and stochastic analyses were performed using data from the irregular wave runs.

During the experiments, the need to run special, bi-chromatic waves became evident, as shall be discussed in section 7.4. The special waves are therefore included in this section.

5.8.1. Regular time series

The regular wave runs were performed at both depths, h_{high} and h_{low} , for different steepness and period waves. The selected steepnesses were 1/30, 7/180, 2/45, 1/20 and 1/18, which constituted five points with constant spacing between the maximum 1/18 and minimum 1/30. Five periods, 15 s, 12 s, 10 s, 7.5 s and T_1 were chosen in order to test a wide range, giving 25 tested regular waves in total. The first structural eigenperiod T_1 varies with the water depth and thus a decay test had to be run in order to complete the regular and bi-chromatic test matrices.

The generated regular waves are given in figure 5.21. The plotted values are the input values, so the stroke is the specified input to the wavemaker in [mm]. The trigger signal is used as the saving switch, logging the measured data when changing from 1 to 0.

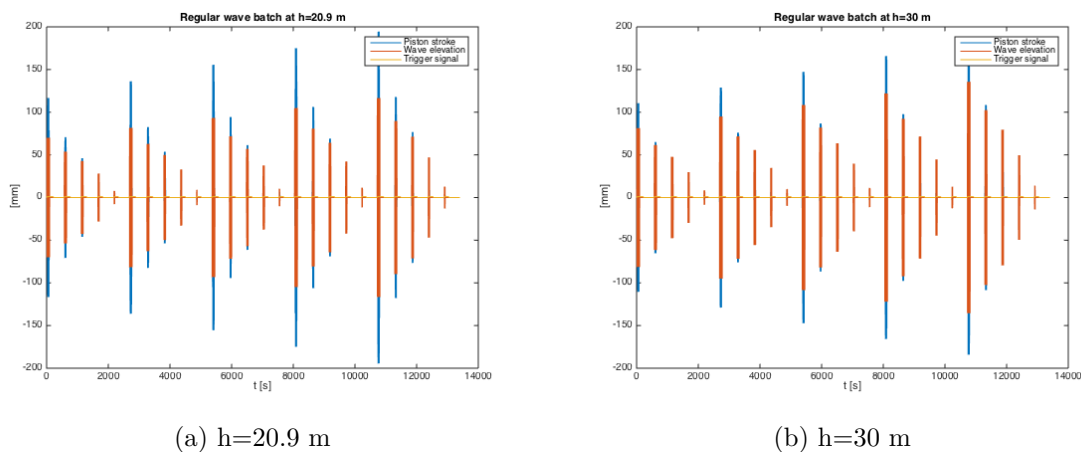


Figure 5.21.: The regular wave batches given in [mm]. Legend: Piston stroke (blue), wave elevation (red), trigger signal (yellow).

The complete regular test setup is found in section 5.8.3.

5.8.2. Irregular time series

The irregular wave runs served two purposes, as they provided the basis for both the stochastic and deterministic analyses. The greatest loads for each sea state were found, and the largest maxima were selected and utilized in the comparative study of numerical load models.

The idling turbine assumption is stressed, as the aerodynamic damping of an operative turbine would cause a large reduction in turbine response. Thus, the loads would be greatly overestimated as the effect of dynamic amplification on loading is significant.

As the TMA spectrum, presented in section 5.3, includes the dissipation of energy in shallow water (illustrated by the ϕ factor in figure 5.4), it was decided against using it in the experiments, as it would have complicated the comparison of specified H_s and achieved H_s . For increased control and insight in the mechanisms reducing the significant wave height, such as wave breaking, the JONSWAP spectrum was employed.

The first approach to selecting sea states for the irregular waves was twofold. First, to select H_s , T_p combinations given by the maximum H_s value for each return period (10, 50, 100, 1 000 and 10 000 years) and its corresponding T_p . Second, selecting H_s , T_p combinations for the maximum wave steepness along the upper limit of the contour line.

However, model trials showed a large amount of wave breaking right after the wavemaker for the large H_s , T_p values. This caused a dramatic loss of wave energy, and the effective output wave spectrum would be drastically altered compared to the nominal input spectrum. This could mean that the sea states defined by each sea state given in [Mathiesen et al., 2014] are too rough. This supports the conclusion of [Engebretsen, 2012], discussed previously.

Contour plots are based on a statistical viewpoint and chosen points must be evaluated considering whether the sea state is physically realistic. Criteria for the maximum wave height before breaking are included in figure 5.22. The breaking criterion in [Det Norske Veritas, 2010] is given by

$$\frac{H_b}{\lambda} = 0.142 \tanh\left(\frac{2\pi h}{\lambda}\right) \quad (5.40)$$

where H_b is the maximum wave height before breaking, λ is the wavelength and h is the water depth. The breaker curves are calculated using linear wave theory on finite water depth, meaning that an iterative procedure was used to find kh . As seen in figure 5.22, some of the H_s , T_p combinations are deemed unphysical due to wave breaking.

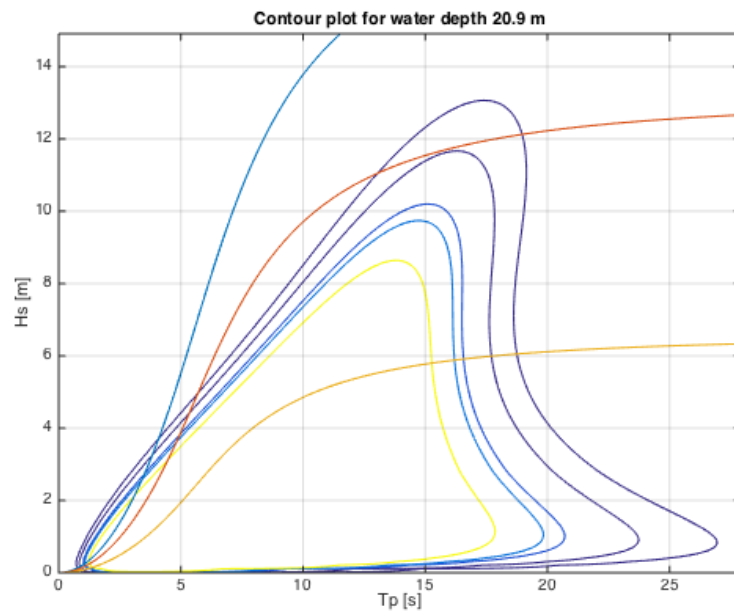


Figure 5.22.: Contour plot for extreme waves with return periods 10, 50, 100, 1000 and 10000 years for location 2, Creyke Beck B. Three curves show the wave breaking criteria for wave steepnesses $1/20$, $1/10$ and $1/7$, based on linear wave theory on finite water depth (see equation (5.40) for steepness $1/7$).

Since the first approach for selecting sea states was unsuccessful, another method had to be pursued. The full-scale T_p values 11.25 s and 15 s were chosen as they are approximately the third and fourth multiples of the first structural eigenperiods. The full-scale H_s values were chosen for return periods 10, 50 and 1000 years at $T_p = 11.25$ s, as well as one lower H_s value, $H_s = 6.71$ m, to ensure a sea state with a low amount of breaking. The H_s , T_p points are shown in figure 5.23. The same H_s values were used for $T_p = 15$ s.

The contour plot is only valid at the lower water depth since it is based on location 2 where $h=20.9$ m.

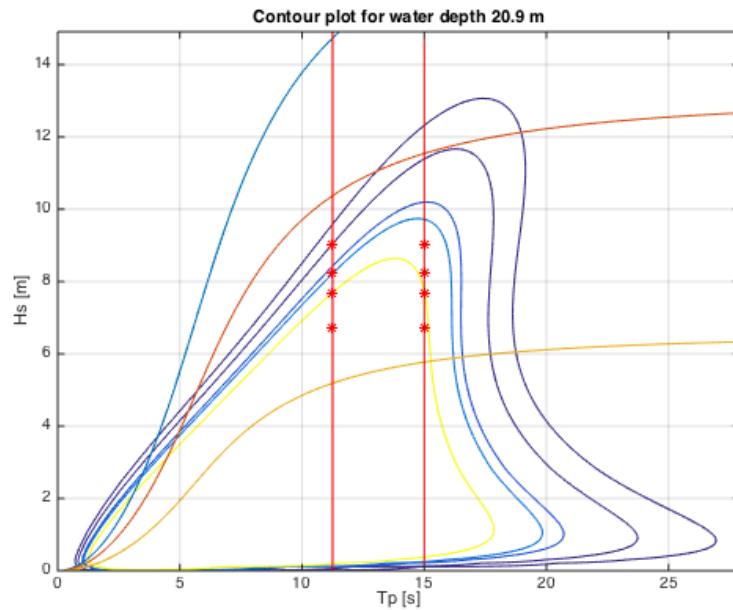


Figure 5.23.: Irregular H_s , T_p points shown in the contour plot for Creyke Beck B, location 2.

The problem with this approach is that the selection of sea states gives a return period for the load, not the response of the structure. A comprehensive testing scheme would thus cover a wide range of load regimes, but not necessarily an equally broad set of responses. This means that the problem is approached the wrong way. In order to base the experiments on a response return period, however, extensive testing must be performed beforehand, either in the wave flume or numerically, as done in [Gaidai and Krokstad, 2014]. This was not done in this thesis, as the time in the towing tank was limited.

Twenty seeds were tested for each sea state with 3-hour full scale durations. The final irregular test matrix is found in section 5.8.3.

5.8.3. Test matrix

The resulting test matrix includes 50 regular and 320 irregular runs. As discussed in section 7, the need to create special, bi-chromatic tests meant that more wave runs were included in the matrix. The tests were run in batches, typically lasting several hours, meaning that they could be run overnight. The model tests and wave calibrations were run almost continuously during two weeks.

The regular tests performed were as follows:

$h \cdot \lambda$ [m]	$T \cdot \sqrt{\lambda}$ [s]	S	Seeds	Type	Duration
20.9	3.77	1/30	1	Regular	$40 \cdot T + 8$ min
"	7.5	"	"	"	"
"	10	"	"	"	"
"	12	"	"	"	"
"	15	"	"	"	"
"	3.77	7/180	"	"	"
"	7.5	"	"	"	"
"	10	"	"	"	"
"	12	"	"	"	"
"	15	"	"	"	"
"	3.77	2/45	"	"	"
"	7.5	"	"	"	"
"	10	"	"	"	"
"	12	"	"	"	"
"	15	"	"	"	"
"	3.77	1/20	"	"	"
"	7.5	"	"	"	"
"	10	"	"	"	"
"	12	"	"	"	"
"	15	"	"	"	"
"	3.77	1/18	"	"	"
"	7.5	"	"	"	"
"	10	"	"	"	"
"	12	"	"	"	"
"	15	"	"	"	"
30	3.94	1/30	"	"	"
"	7.5	"	"	"	"
"	10	"	"	"	"
"	12	"	"	"	"
"	15	"	"	"	"
"	3.94	7/180	"	"	"
"	7.5	"	"	"	"
"	10	"	"	"	"
"	12	"	"	"	"
"	15	"	"	"	"
"	3.94	2/45	"	"	"
"	7.5	"	"	"	"
"	10	"	"	"	"
"	12	"	"	"	"
"	15	"	"	"	"
"	3.94	1/20	"	"	"
"	7.5	"	"	"	"
"	10	"	"	"	"
"	12	"	"	"	"
"	15	"	"	"	"
"	3.94	1/18	"	"	"
"	7.5	"	"	"	"
"	10	"	"	"	"
"	12	"	"	"	"
"	15	"	"	"	"

Table 5.8.: The test matrix for regular waves.

Two water depths, five steepnesses and five period variations were run in the regular setup, giving a total duration of 7.45 h. This includes the 40 periods and 8-minute resting time between each run.

The irregular tests are summarized in table 5.9.

$h \cdot \lambda$ [m]	$T_p \cdot \sqrt{\lambda}$ [s]	$H_s \cdot \lambda$ [m]	γ	Seeds	Type	Duration
20.9	11.25	6.71	2.32	20	Irregular	$20 \cdot 34 \text{ min}$
"	"	7.69	2.61	"	"	"
"	"	8.22	2.76	"	"	"
"	"	9.04	3.00	"	"	"
"	15	6.71	1.42	"	"	"
"	"	7.69	1.59	"	"	"
"	"	8.22	1.69	"	"	"
"	"	9.04	1.83	"	"	"
30	11.25	6.71	2.32	"	"	"
"	"	7.69	2.61	"	"	"
"	"	8.22	2.76	"	"	"
"	"	9.04	3.00	"	"	"
"	15	6.71	1.42	"	"	"
"	"	7.69	1.59	"	"	"
"	"	8.22	1.69	"	"	"
"	"	9.04	1.83	"	"	"

Table 5.9.: The test matrix for irregular waves.

The irregular wave test setup consisted of two water depths and eight sea state variations with twenty seeds, giving a duration of $2 \cdot 8 \cdot 20 \cdot 34 \text{ min} = 10\,880 \text{ min} = 7.6 \text{ days}$. Excluding the special wave tests, the entire test program lasted 447 min (regular tests) + 10 880 min (irregular tests) = 11 327 min = 189 h, or approximately 7.9 days. It was run both with the model installed and for the wave calibration tests.

5.8.4. Regular wave regimes

Based on a linear wave iteration procedure to find the wave number on finite water depth, theoretical regular wave characteristics can be found. These characteristics are summarized in the tables below.

Regular wave heights h = 20.9 m	T=3.77 s	T=7.5 s	T=10 s	T=12 s	T=15 s
S=1/30	0.7397	2.7058	4.1026	5.1676	6.7115
S=7/180	0.8630	3.1568	4.7864	6.0288	7.8301
S=2/45	0.9862	3.6078	5.4702	6.8901	8.9487
S=1/20	1.1095	4.0587	6.1540	7.7514	10.0673
S=1/18	1.2328	4.5097	6.8377	8.6126	11.1859

Table 5.10.: Full-scale theoretical regular wave heights at h = 20.9 m.

Regular wave heights h = 30 m	T=3.94 s	T=7.5 s	T=10 s	T=12 s	T=15 s
S=1/30	0.8079	2.8564	4.5765	5.9014	7.8071
S=7/180	0.9426	3.3325	5.3392	6.8850	9.1083
S=2/45	1.0772	3.8085	6.1020	7.8685	10.4095
S=1/20	1.2119	4.2846	6.8647	8.8521	11.7106
S=1/18	1.3465	4.7607	7.6275	9.8357	13.0118

Table 5.11.: Full-scale theoretical regular wave heights at h = 30 m.

The following Ursell numbers are found using the equation on page 31, $U_r = \frac{H}{k_0^2 d^3} = \frac{1}{4\pi^2} \frac{S}{\mu^3}$.

Ursell numbers h = 20.9 m	T=3.77 s	T=7.5 s	T=10 s	T=12 s	T=15 s
S=1/30	0.0010	0.0626	0.3520	1.0511	4.0095
S=7/180	0.0012	0.0731	0.4107	1.2263	4.6778
S=2/45	0.0013	0.0835	0.4693	1.4014	5.3461
S=1/20	0.0015	0.0940	0.5280	1.5766	6.0143
S=1/18	0.0017	0.1044	0.5867	1.7518	6.6826

Table 5.12.: Theoretical regular wave Ursell numbers at h = 20.9 m.

Ursell numbers h = 30 m	T=3.94 s	T=7.5 s	T=10 s	T=12 s	T=15 s
S=1/30	0.0004	0.0212	0.1190	0.3554	1.3557
S=7/180	0.0005	0.0247	0.1389	0.4146	1.5817
S=2/45	0.0006	0.0282	0.1587	0.4739	1.8076
S=1/20	0.0007	0.0318	0.1785	0.5331	2.0336
S=1/18	0.0007	0.0353	0.1984	0.5923	2.2595

Table 5.13.: Theoretical regular wave Ursell numbers at h = 30 m.

Regular wave regimes h = 20.9 m	T=3.77 s	T=7.5 s	T=10 s	T=12 s	T=15 s
S=1/30	2nd-order Stokes	2nd-order Stokes	2nd-order Stokes	Cnoidal	Cnoidal
S=7/180	2nd-order Stokes	2nd-order Stokes	2nd-order Stokes	Cnoidal	Cnoidal
S=2/45	5th-order Stokes	5th-order Stokes	5th-order Stokes	Cnoidal	Cnoidal
S=1/20	5th-order Stokes	5th-order Stokes	5th-order Stokes	Cnoidal	Cnoidal
S=1/18	5th-order Stokes	5th-order Stokes	5th-order Stokes	Cnoidal	Cnoidal

Table 5.14.: Theoretical regular wave regimes for h = 20.9 m.

Regular wave regimes h = 30 m	T=3.94 s	T=7.5 s	T=10 s	T=12 s	T=15 s
S=1/30	2nd-order Stokes	2nd-order Stokes	2nd-order Stokes	2nd-order Stokes	Cnoidal
S=7/180	2nd-order Stokes	2nd-order Stokes	2nd-order Stokes	2nd-order Stokes	Cnoidal
S=2/45	5th-order Stokes	5th-order Stokes	5th-order Stokes	5th-order Stokes	Cnoidal
S=1/20	5th-order Stokes	5th-order Stokes	5th-order Stokes	5th-order Stokes	Cnoidal
S=1/18	5th-order Stokes	5th-order Stokes	5th-order Stokes	5th-order Stokes	Cnoidal

Table 5.15.: Theoretical regular wave regimes for h = 30 m.

As shown in tables 5.14 and 5.15, waves within both the 2_{nd}-order Stokes, the 5_{th}-order Stokes and the cnoidal wave regimes were run, as defined in [Det Norske Veritas, 2010] (see table 3.1). Not surprisingly, the long and steep waves on shallow water gave the highest non-linearity, as illustrated by the Ursell parameter in tables 5.12 and 5.13.

5.9. System testing

5.9.1. Model wave radiation and tank reflections

During the decay test in x-direction the model was observed to start oscillating a while after the decay motions had died away. This is shown in figure 5.24, occurring at around $t=80$ s. The phenomenon is found to be caused by wavemaker reflections of the waves radiated by the model during the decay test.

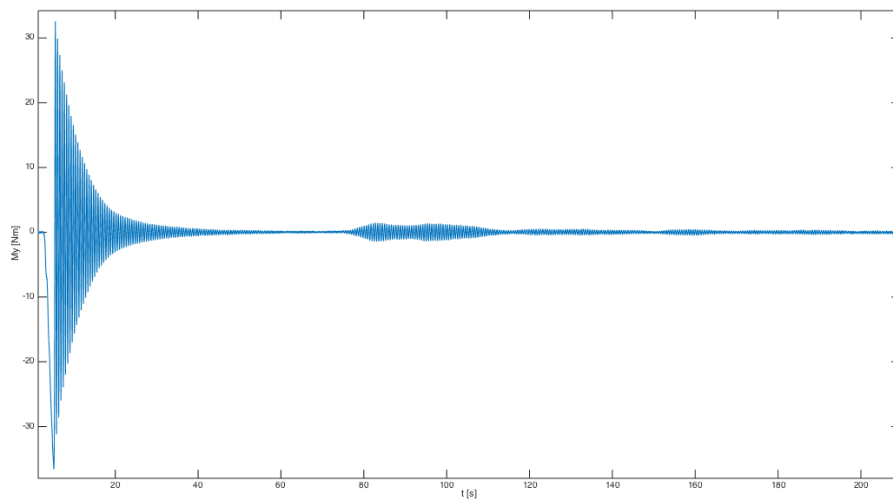


Figure 5.24.: An illustration of the wavemaker reflection of the radiated waves from the flexible model during a decay test.

Figure 5.25 shows the wave elevation at wave gauge 8 (next to the pile) during the decay test. In figure 5.25b it is seen that the wave period of the radiated waves matches the first eigenperiod $T=0.54$ s at $h=20.9$ m.

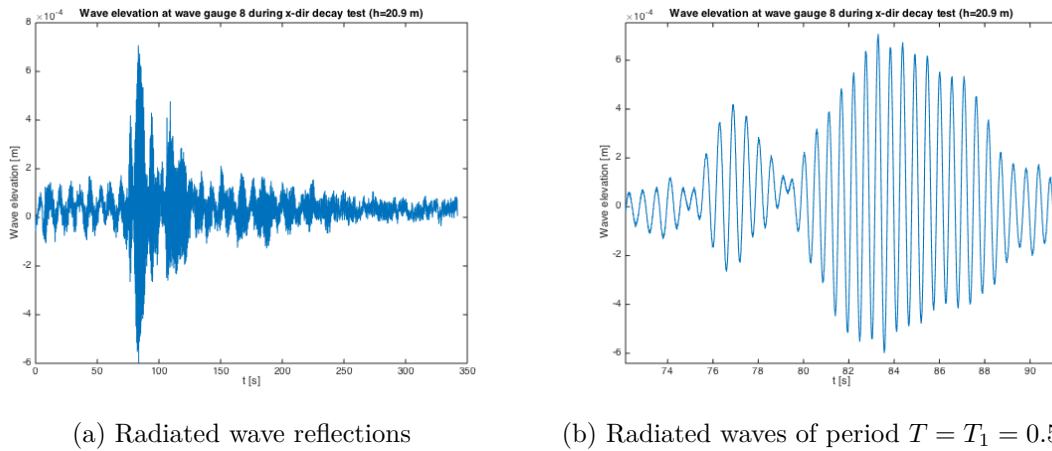


Figure 5.25.: The wave elevation at wave gauge 8 during a decay test in water depth $h=20.9$ m.

The linear wavelength of a 0.54 s wave at $h=0.435$ m is 0.46 m, or approximately three times larger than the model diameter. Figure 3.4 shows that diffraction is non-negligible for $\lambda/D \lesssim 5$, which is in line with what is discussed here. Using equation (3.39) gives the group velocity assuming linear theory, $C_g = 0.42$ m/s. This means that the radiated wave should use approximately 73 s travelling the 50.5-m distance to the wavemaker and back, which coincides with the measurements in figures 5.24 and 5.25.

Observations made while running the tests revealed that the model seemed to be frequently excited at the first mode and it was almost never at rest during the runs. This occurred even when it should not have been excited, in periods of small wave amplitudes and for a variety of wave frequencies. An idling turbine is lightly damped, which was also the case for the tested pile, meaning that once the model was excited it took a long time for its motions to die out. However, the self-excitation due to the wave radiation probably also had a large impact on the frequent first-mode motion.

5.9.2. Testing the force gauges

Force gauges 7, 11, 13, 15, 18, 22 and 23 (see table 5.7) were never operational and are therefore not included in this section. Measurements from the gauges, exemplified for a sea state at $h = 30$ m in figure 5.26, show that the largest peaks generally have no corresponding large peaks at neighboring gauges in the same time

instance. A closer look at the force and wave elevation realizations for the same sea state (figure 5.27), shows how the largest peaks occur as a local phenomenon, and typically not for the largest or steepest waves. This explains why the neighboring gauges do not display the same large force.

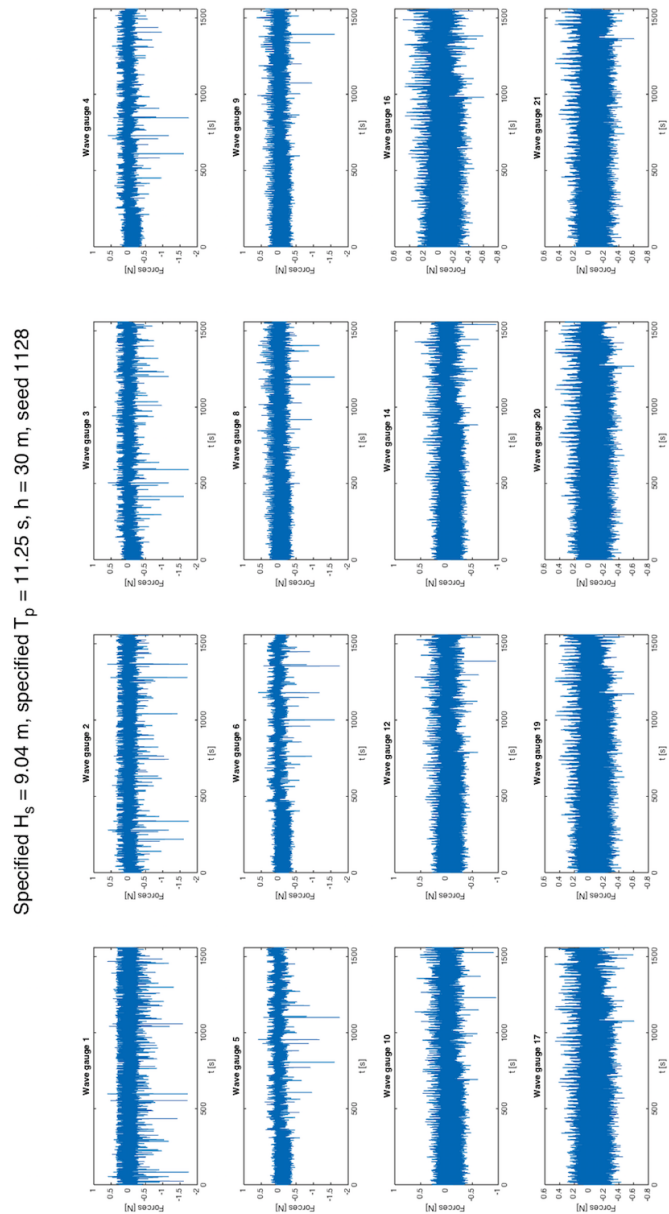


Figure 5.26.: Measurements for each of the operative force gauges, exemplified for a specific seed at $h = 30$ m.

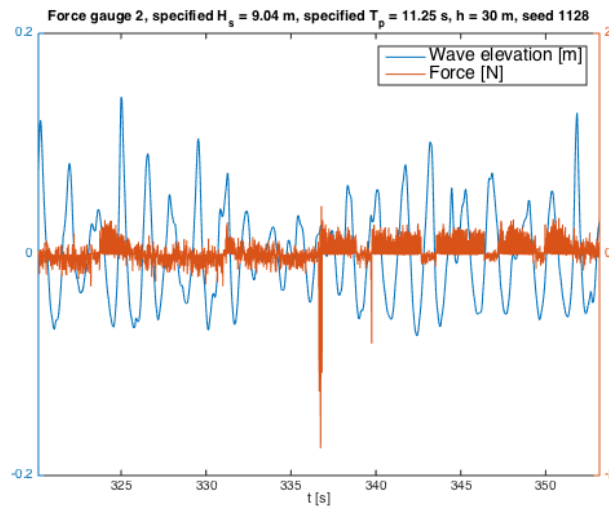


Figure 5.27.: Model scale force gauge measurements plotted with the wave elevation at wave gauge 7.

At $h=20.9$ m, most of the gauges are above the still water level. The resulting forces, exemplified for gauge 2 in figure 5.28, for the same sea state as in figure 5.27, show that the highest peaks are very large compared to the values at $h = 30$ m. In addition, all the maxima are equal, with a value of 1500 N.

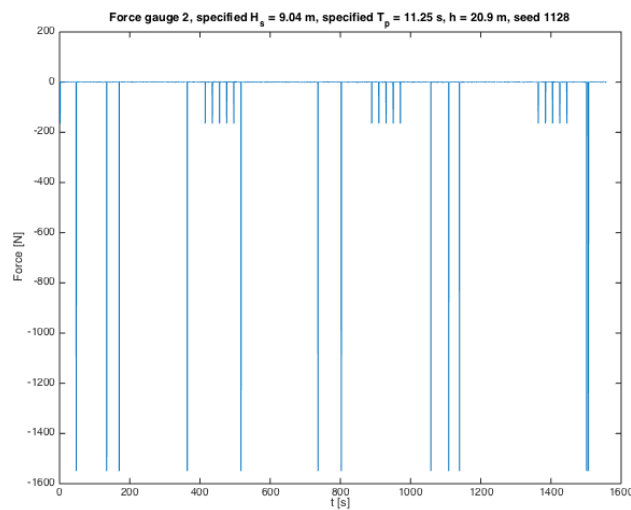


Figure 5.28.: The realization for force gauge 2 at $h=20.9$ m.

The intention of installing force gauges was to detect slamming events and to

determine the slamming pressure distributions in the deterministic analyses. Testing the gauges, however, revealed that they could be used for neither. Since the largest peaks were local pressure maxima, the pressure distributions could not be determined since the neighboring gauges did not detect the same events. In addition, the large peaks for the lower water depth put the validity of the magnitude of the measured forces into question.

5.9.3. Testing the accelerometers

If the pile was held still at an angle, a constant, non-zero acceleration was measured. This constant value corresponded well (within the error of the angle measurement) with the decomposed gravitational acceleration component.

An iterative MATLAB routine was developed to correct for the effect. The program first calculated the position of the pile top ($pos1$) based on the acceleration measurements ($acc1$). Based on $pos1$ the theoretical gravitational acceleration component ($g1$) at the accelerometer position was derived. By subtracting $g1$ from the measured acceleration, a second acceleration ($acc2$) was found. The procedure was repeated iteratively, starting with the calculated accelerations, but the solution never converged. Thus, a small error was expected in the measured accelerations as a function of the pile deflection angle.

6 | Numerical Model

6.1. Objective and assumptions

The numerical model was developed in MATLAB, serving as a simple single degree-of-freedom (SDOF) system to test responses with load models and verify them against the experimental tests results. In that way, the damping level could be adjusted and the responses found experimentally could be adapted to the new ξ . `PileResponse.m` solves the differential equation of motion (6.1) by specifying known model parameters, found in table 6.1.

As specified in [NORSOK, 2007], both experimental tests and numerical evaluations exhibit clear limitations. However, through apt utilization, each tool can be used to partially circumvent the constraints of the other.

The model consists of a totally rigid, hollow cylinder filled with (still) water up to the water depth h . The pile rotates about its base in the two-dimensional plane of the incoming wave, with a linear stiffness and damping (found in the decay tests, see section 7.1).

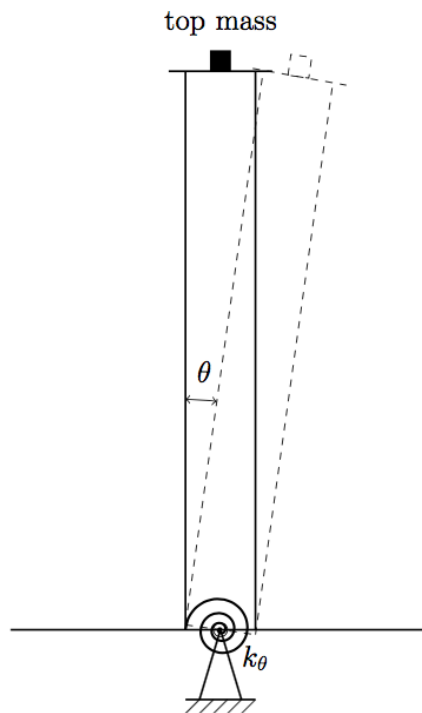


Figure 6.1.: The SDOF model

	Numerical model parameters
Diameter	0.144 m
Top mass	5.60 kg
Height	1.54 m
Wall thickness	6 mm
Density	2700 kg/m ³
Rotational stiffness k_θ	3400 Nm/rad
Added mass coefficient C_A	1.0

Table 6.1.: Model test parameters

The pile top mass consists of the mass of the flange in addition to weights applied to achieve a realistic first eigenperiod. The weights have a collective mass of 5.04 kg, whilst the flange disc amounts to 0.56 kg. The flange is a circular holed-out disc with thickness 5 mm, outer diameter 24.5 cm and inner diameter 13.5 cm.

The one degree-of-freedom equation of motion is

$$I\ddot{\theta} + c_\theta\dot{\theta} + k_\theta\theta = M(t) \quad (6.1)$$

The moment of inertia parameters are found assuming a point top mass and that the water inside the pile comprises a non-moving column, i.e. no sloshing motion.

$$\begin{aligned} I_{water-filled\ cylinder} &= \frac{1}{3}[m_{pile} L_{pile}^2 + m_{added\ mass} h^2 + m_{water\ inside\ pile} h^2] \\ &= \frac{1}{3}[\rho_{pile}\pi(R_{outer}^2 - R_{inner}^2) L_{pile}^3 \\ &\quad + \rho\pi C_A R_{outer}^2 h^3] \\ &\quad + \rho\pi R_{inner}^2 h^3 \end{aligned} \quad (6.2)$$

$$I_{top\ mass} = (m_{flange} + m_{weights}) L_{pile}^2$$

$$I = I_{water-filled\ cylinder} + I_{top\ mass}$$

The rotational stiffness k_θ was found from a trial-and-error best fit of the eigenperiod using the decay test (CompareDecay.m). The resulting measured and numerical decay comparisons are shown in figure 6.2.

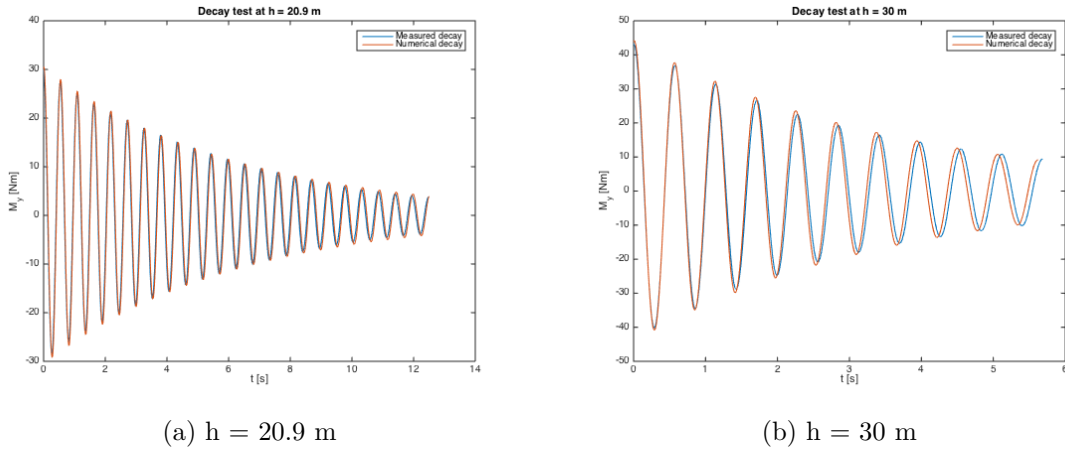


Figure 6.2.: Comparing the measured decays with the numerical calculations.

The measured and numerical decays agree well in terms of the damping level at both water depths. The damping ratios from measured decay tests are established in section 7.1. The numerical eigenperiod is a fraction too high at $h=20.9$ m, whilst the opposite is the case at $h = 30$ m. In order to use the same stiffness value for both water depths, this was the best result when varying the rotational stiffness to fit the experimental decay test.

6.2. Implementation of the load models

The load models used in this thesis are Morison with Wheeler stretching and FNV. Variants for both deep and intermediate water depths are included, differentiated in two places:

- The vertical distribution of the kinematic properties (deep: $\phi \propto e^{kz}$, shallow: $\phi \propto \frac{\cosh k(z+h)}{\cosh kh}$)
- The dispersion relation (deep: $\omega^2 = kg$, shallow: $\omega^2 = kg \tanh kh$)

A validation of the deep-water FNV implementation, applying the [Newman, 1996] extensions for an irregular sea, is given in appendix D. The following intermediate-depth equations are used:

$$\phi = \frac{igA}{\omega} \frac{\cosh k(z+h)}{\cosh kh} e^{i(\omega t - kx)} \quad (6.3)$$

giving the following wave elevation, defined by the linear Bernoulli equation on the free surface:

$$\eta = -\frac{1}{g} \frac{\partial \phi}{\partial x} \Big|_{z=0} = Ae^{i(\omega t - kx)} \quad (6.4)$$

The horizontal velocity:

$$u = \frac{\partial \phi}{\partial x} = \frac{kg \cosh k(z+h)}{\omega \cosh kh} Ae^{i(\omega t - kx)} \Rightarrow u|_{z=0} = \frac{kg}{\omega} Ae^{i(\omega t - kx)} \quad (6.5)$$

The vertical velocity:

$$w = \frac{\partial \phi}{\partial z} = \frac{ikg \sinh k(z+h)}{\omega \cosh kh} Ae^{i(\omega t - kx)} \Rightarrow w|_{z=0} = i\omega Ae^{i(\omega t - kx)} \quad (6.6)$$

The horizontal acceleration:

$$\dot{u} = \frac{\partial u}{\partial t} = ikg \frac{\cosh k(z+h)}{\cosh kh} Ae^{i(\omega t - kx)} \Rightarrow \dot{u}|_{z=0} = ikg Ae^{i(\omega t - kx)} \quad (6.7)$$

The vertical acceleration:

$$\dot{w} = \frac{\partial w}{\partial t} = -kg \frac{\sinh k(z+h)}{\cosh kh} Ae^{i(\omega t - kx)} \Rightarrow \dot{w}|_{z=0} = -\omega^2 Ae^{i(\omega t - kx)} \quad (6.8)$$

As the FNV load formulae were derived assuming deep water [Faltinsen et al., 1995], it is inconsistent to estimate the kinematics using an intermediate depth potential. Thus, without modifying the FNV load formulae, using finite depth wave properties is based on a faulty assumption. The objective here is to determine how the inclusion of finite depth characteristics influences the numerical congruence with the experimental results.

The FNV model requires linear wave input. As the measured waves are real and non-linear, a linearization is performed by cutting high and low wave frequencies (as done in FreqDomain.m, see figure 6.3). This is a common approach industrially. The cut-off frequencies are set to half of the spectral peak frequency (low) and (high), if below the Nyquist frequency:

$$\omega_{max} = \sqrt{\frac{2g}{H_s}} \quad (6.9)$$

The high frequency cut-off is given in [Det Norske Veritas, 2010], shown to fit experimental data well for a second-order model. The lower cut-off frequency was

selected as the resulting filtered measured spectra compared well with the linear input spectra.

In `ForcesMorison.m` and `ForcesFNV.m`, 50 vertical pile elements are used in the integration of the Morison force and the 2nd-order potential of FNV.

The moment arm is set equal to the water depth for the Morison load and the first and second-order FNV forces. This is a conservative assumption, obviously, as the forces are vertically distributed. Using the water depth as the moment arm is a standard assumption for the 2nd-order FNV force. The logic behind the assumption is the rapid decay of the 2nd-order kinematics, which is less accurate at shallow water. The relative decay/water depth implies a more conservative moment arm assumption at 20.9-m depth than at 30 m. The 3rd-order FNV force is said to act locally at the free surface [Faltinsen et al., 1995], since it quickly attenuates with z , negligible below a depth comparable to the cylinder diameter. This was discussed in section 3.6.1.

The inertia coefficient C_M is set to 2.0, as in accordance with the first-order FNV component. The drag coefficient $C_D = 0.809$, as in [Nestegård et al., 2004].

As mentioned on page 57, the slamming model used in the numerical analysis is the inclusion of the slamming coefficient in the conventional Morison equation with Wheeler stretching, as described in [Nestegård et al., 2004] and in section 4.2. The slamming coefficient is found in the subroutine `slamcoeff.m`, and included in `ForcesMorison.m`.

The model is specified for the use on an individual chosen wave, as the user specifies the occurrence of its peaks in time at wave gauge 5 and 7, upon which the routine calculates the phase velocity. The upcrossing determines the starting point of cylinder submergence (s), which increases with the constant phase velocity within an upcrossing. The slamming coefficient of equation (4.5), is only given for η values above the MWL, as specified in [Nestegård et al., 2004], and is otherwise set to $C_s = C_D = 0.809$. The α factor is set to 1 in this thesis, since the focus is on slamming from breaking waves, but the value can be altered in `PileResponse.m`.

A spilling breaker is assumed, as specified for equations (4.18) and (4.19). Thus, the slamming model should not be used as a substitute for the conventional Morison model for an entire wave elevation time series, but rather in the deterministic analysis of a single spilling breaker wave event.

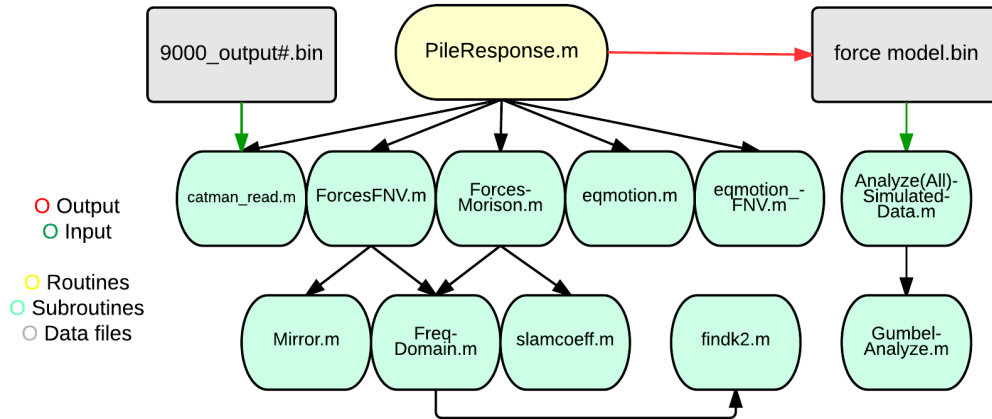


Figure 6.3.: Flow chart for the numerical model.

6.3. Program testing

Using the sinusoidal normalized moment $M = e^{i\omega t}$, the transfer function for the SDOF rotational system is found as

$$H(\omega) = \frac{1}{-I\omega + c_{\theta}i\omega + k_{\theta}} \quad (6.10)$$

Three transfer functions are plotted in figure 6.4. They are the transfer functions of the numerical model (6.10), the corresponding theoretical values (6.10) and measurement data points (6.11). The measured value transfer function is given by

$$TF = \frac{\theta \text{ [rad]}}{M \text{ [Nm]}} \quad (6.11)$$

To capture the excitation loads, the lowest steepness ($S = 1/30$) regular waves are chosen and the frequencies above $1.5 \cdot f^{(1)}$ ($f^{(1)}$ is the measured reciprocal of the regular input wave frequency) are filtered out, as to remove the dynamic amplification (see figure 6.6). This is done for both the response moment and the acceleration at the top of the pile. In order to find θ , the acceleration is integrated twice and transformed to a rotational value rather than a translational one, as done in IntegrateAcceleration.m and FindingTF_Regular.m. Mean values for the regular waves corresponding to full scale periods 15 s, 12 s, 10 s and 7.5 s are

plotted in figures 6.4 and 6.5.

With the amplitude equal to 1 Nm the normalized moment gives the transfer function for the numerical model in figure 6.4. The figure shows that the absolute value of the theoretical transfer function fits well with that of the numerical routine.

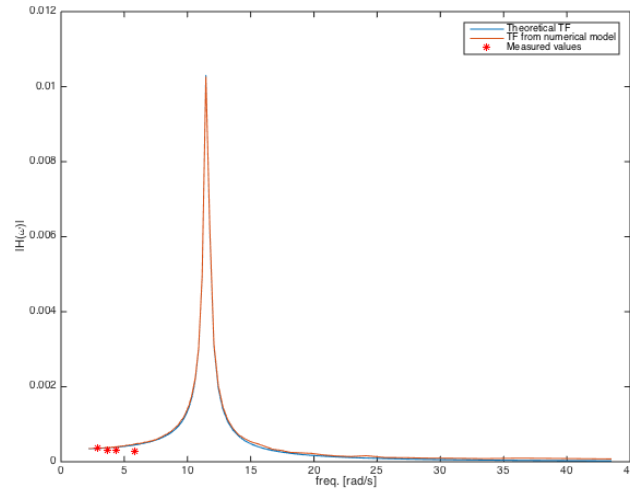


Figure 6.4.: Comparing the absolute value of the transfer function $|H(\omega)|$ with the numerical model output.

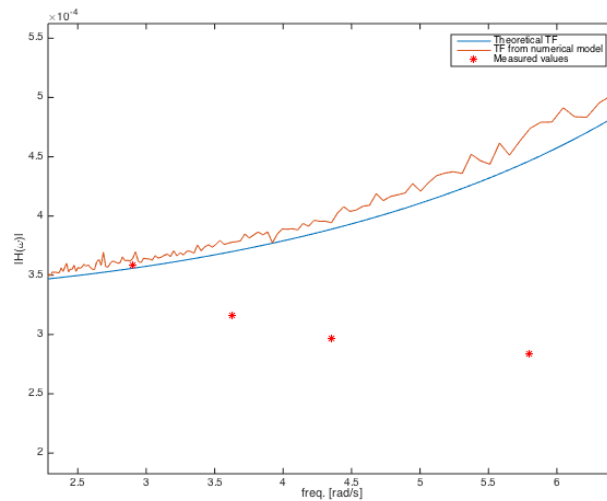


Figure 6.5.: Zooming in on the measured transfer function values.

As the dynamic amplification is filtered out the measured value transfer function should give a constant value for different frequencies. Figure 6.5, however, shows that it is decreasing with f . A reason for this might be that the accelerometer measurements are affected by the gravitational acceleration as the accelerometer is tilted (see section 5.9.3).

Since the measured transfer function values agree quite well with those for the theoretical and numerical models, they contribute to validating the numerical model response, although only for linear response without dynamic amplification. Hydrodynamic loads on a flexible structure are affected by the elastic structural response, whilst for a more rigid structure the hydrodynamic excitation load can be found directly from measurements. Thus, a stiffer model could have been used in order to find the excitation loads at higher frequencies.

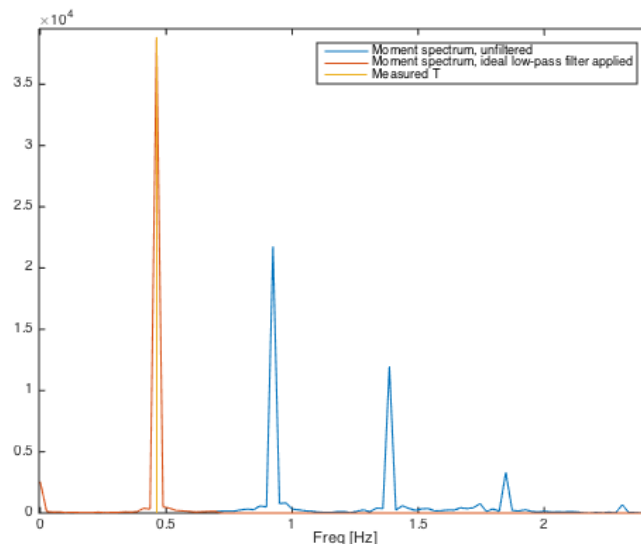


Figure 6.6.: Moment spectrum with a low-pass ideal filter with a cut-off frequency at $1.5 \cdot f^{(1)}$.

A large FNV force event is shown in figure 6.7 for the deep-water version of the FNV model. The second and third order are in the same order of magnitude. In a conventional perturbation approach, as presented in the Stokes waves section 3.5.2.1, each succeeding order is reduced by an order of magnitude ϵ . In the FNV approach, on the other hand, the orders of magnitude of the second- and third-order contributions are comparable for practical-steepness waves, de-

spite including different harmonics and powers of the amplitude. Because of the vertical integration, however, the second-order contribution can become more significant, resulting in a $O(\epsilon^4)$ contribution, whereas the third-order force is of $O(\epsilon^5)$ [Faltinsen et al., 1995].

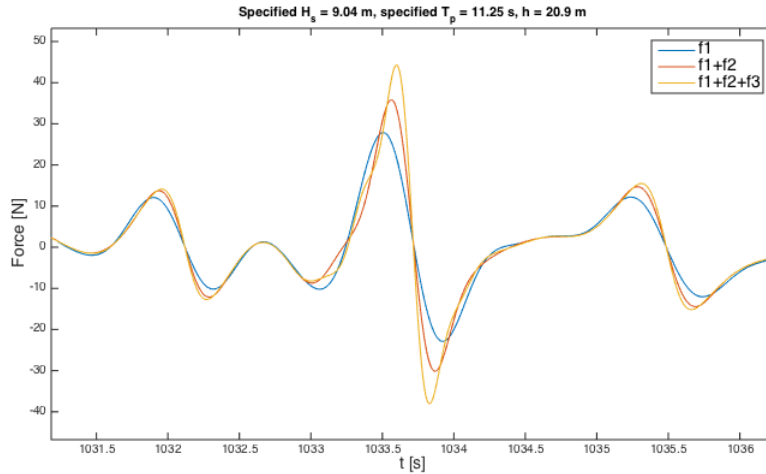


Figure 6.7.: Illustrating the relative FNV contributions order of magnitude for a large force event at $h=20.9$ m.

Top-of-pile acceleration spectra for the least and most steep sea states are provided in figures 6.8.a and 6.8.b. They clearly show the large relative response of the deep-water FNV model compared to Morison and the measured data.

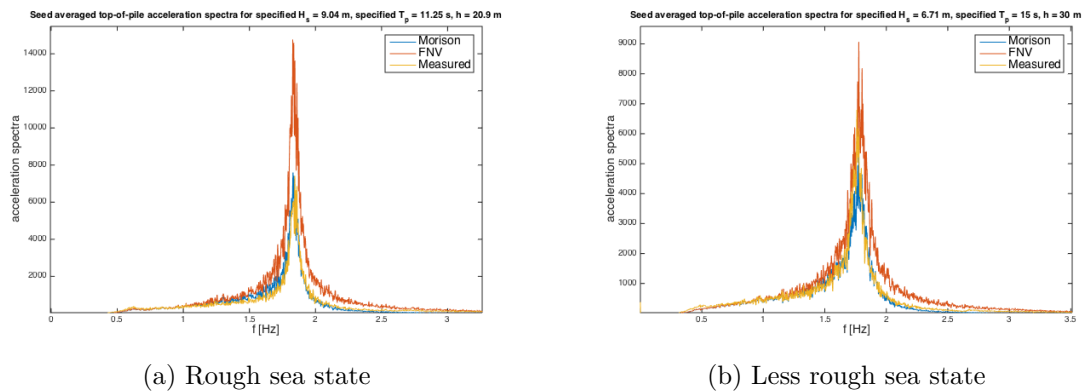


Figure 6.8.: Seed-averaged top-of-pile acceleration spectra compared.

7 | Results and Discussions

7.1. Decay test

In the decay test, the structure was displaced and released, allowing a free decay of the structure. This was done in both the x and y-directions for both water depths. The decay of the moment about the y axis in water depth $h=20.9$ m is shown in figure 7.1.

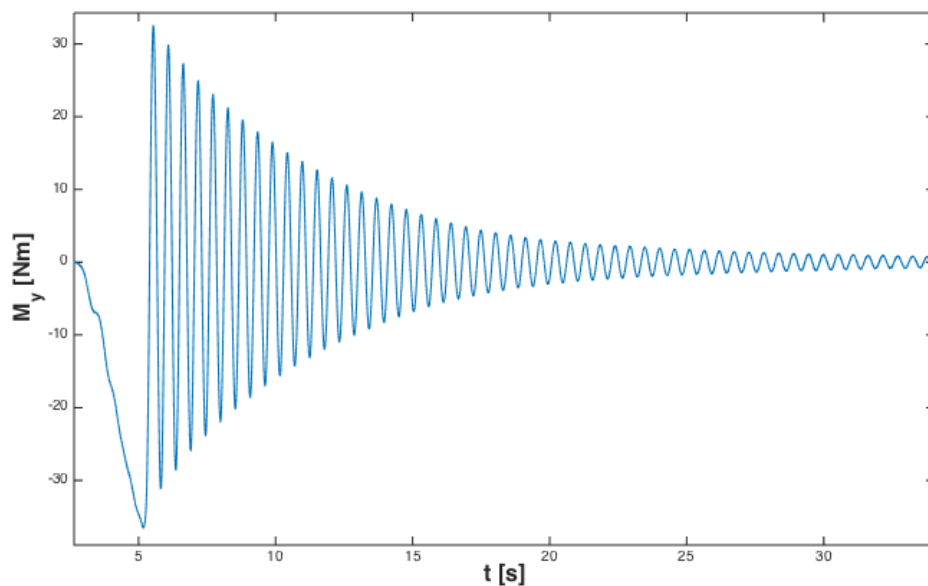
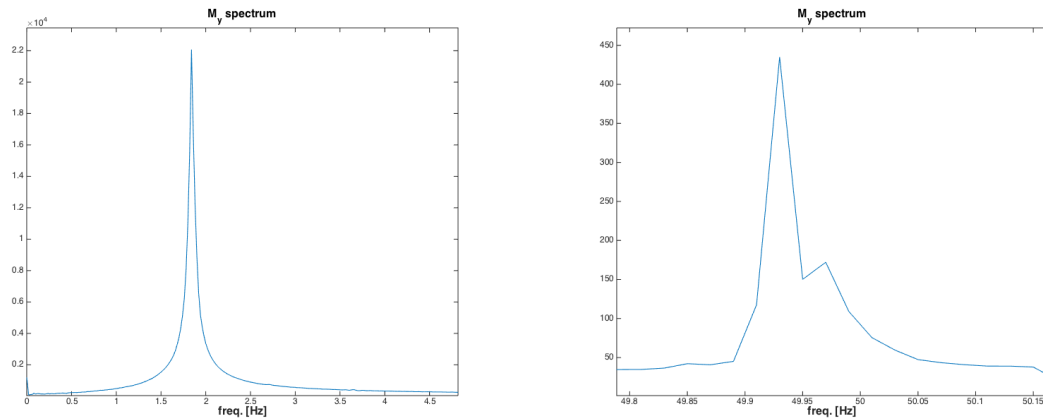


Figure 7.1.: The decay test in x-direction in the form of a M_y time series.

The first and second mode eigenperiods were found through a spectral analysis using a discrete Fourier transform of the resulting moment time series. The spectrum of M_y at $h=20.9$ m is shown in figure 7.2a. A small spectral peak occurred at 49.9 Hz, i.e. the second mode eigenfrequency, as given in figure 7.2b. The resulting eigenperiods are given in table 7.1.



(a) M_y spectrum cut-out showing the first mode eigenfrequency at $h=20.9$ m. (b) M_y spectrum cut-out showing the first mode eigenfrequency at $h=20.9$ m.

Figure 7.2.: Moment spectrum cut-outs from the decay test giving the first and second mode eigenfrequencies, respectively.

The moment transducer used in the experiments only measured M_y , so for the decay test in the y -direction, a_y of the y -direction accelerometer was employed. The results are plotted in figure 7.4. The first eigenfrequency, found using the same spectral analysis as in the x -direction, was found at 7.36 Hz, corresponding to a 0.14-s eigenperiod, 0.94 s in full scale. This means that the stiffness in y -direction is much larger than in x -direction, which is desired to avoid excessive parasitic transverse motion. The experiment was meant to be two-dimensional. The eigenfrequency in y -direction should be noted, as motions at that specific frequency may be found in the measurement post-processing. At $h=20.9$ m, in the y -direction, a small peak was found at the same second eigenperiod as in the x -direction. This could be the x -direction second mode, but it is expected that the second modes are similar in both directions, since they depend on the stiffness of the pile itself, which should be equal in all directions.

The four decay tests are found in figures 7.3 and 7.4 with respective eigenperiods in table 7.1.

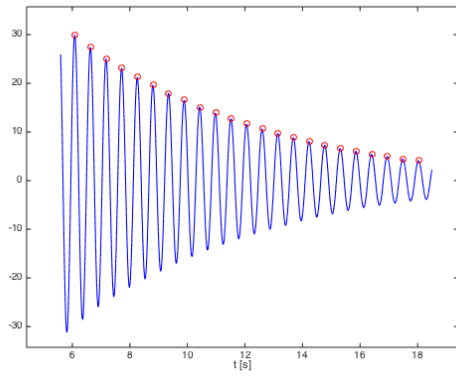
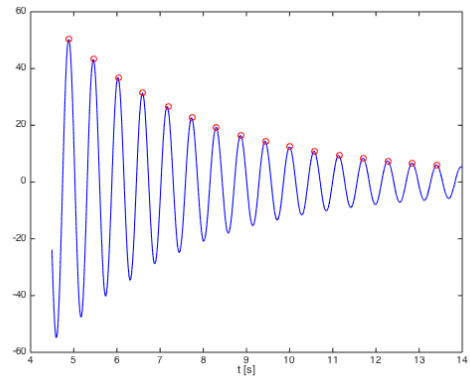
(a) $h=20.9$ m(b) $h=30$ m

Figure 7.3.: Decay test in the x-direction (tank longitudinal), showing time series of M_y [Nm]. The oscillation maxima are marked.

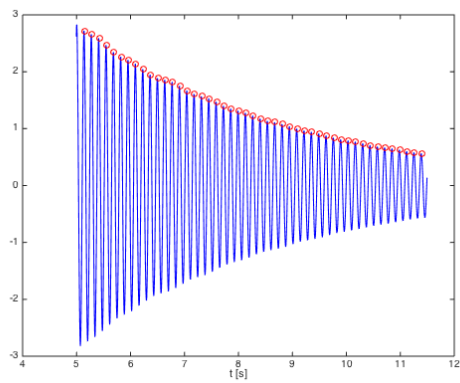
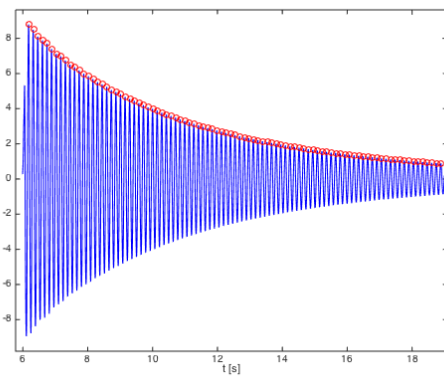
(a) $h=20.9$ m(b) $h=30$ m

Figure 7.4.: Decay test in the y-direction (tank transverse), showing time series of a_y [m/s^2]. The oscillation maxima are marked.

Eigenperiods	x-direction		y-direction	
	Model scale	Full scale	Model scale	Full scale
First mode eigenperiod h=20.9 m	0.54 s	3.77 s	0.14 s	0.94 s
Second mode eigenperiod h=20.9 m	0.02 s	0.14 s	0.02 s	0.14 s
First mode eigenperiod h=30 m	0.57 s	3.94 s	0.14 s	0.98 s
Second mode eigenperiod h=30 m	0.02 s	0.14 s	0.02 s	0.14 s

Table 7.1.: Eigenperiods at the two water depths.

The decay tests were also used to determine the damping of the system. Theory from [Steen, 2014] was used in the evaluation, resulting in the MATLAB routine `damping.m` (see appendix D). Considering two successive oscillation amplitudes of a decay test, x_i and x_{i+1} , the logarithmic decrement becomes

$$\Lambda = \ln\left(\frac{x_i}{x_{i+1}}\right) \quad (7.1)$$

For a single degree-of-freedom system exhibiting non-linear damping, the equation of motion in a free decay can be written

$$M\ddot{x} + B_1\dot{x} + B_2\dot{x}|\dot{x}| + Cx = 0 \quad (7.2)$$

and the standardized form, dividing by M , yields

$$\ddot{x} + p_1\dot{x} + p_2\dot{x}|\dot{x}| + p_3x = 0 \quad (7.3)$$

The damping ratio ξ is defined as

$$\xi = \frac{p}{p_{cr}} = \frac{p}{2M\omega_0} \quad (7.4)$$

where p is the actual damping and p_{cr} is the critical damping. Further, the logarithmic decrement as a function of the damping ratio, is

$$\Lambda = \xi\omega_0 T_d = 2\pi \frac{\xi}{\sqrt{1-\xi^2}} \quad (7.5)$$

where ω_0 and T_d are the undamped eigenfrequency and the damped eigenperiod, respectively. For a lightly damped system, roughly $\xi < 0.2$, the logarithmic decrement can be approximated as

$$\Lambda = 2\pi\xi \quad (7.6)$$

In order to obtain the linear and non-linear damping coefficients the logarithmic decrement can be plotted against the mean amplitude for each decay test oscillation. The linear damping coefficient p_1 is approximated by the linear regression line intersection with the Λ -axis, whilst the non-linear coefficient p_2 is the regression line slope. In such an approach, the first oscillations should be discarded because of transient effects and the smallest oscillations omitted because of inaccuracies. Figures 7.5 and 7.6 show the approach used for the decay tests at $h=20.9$ m and $h=30$ m in both x and y-directions.

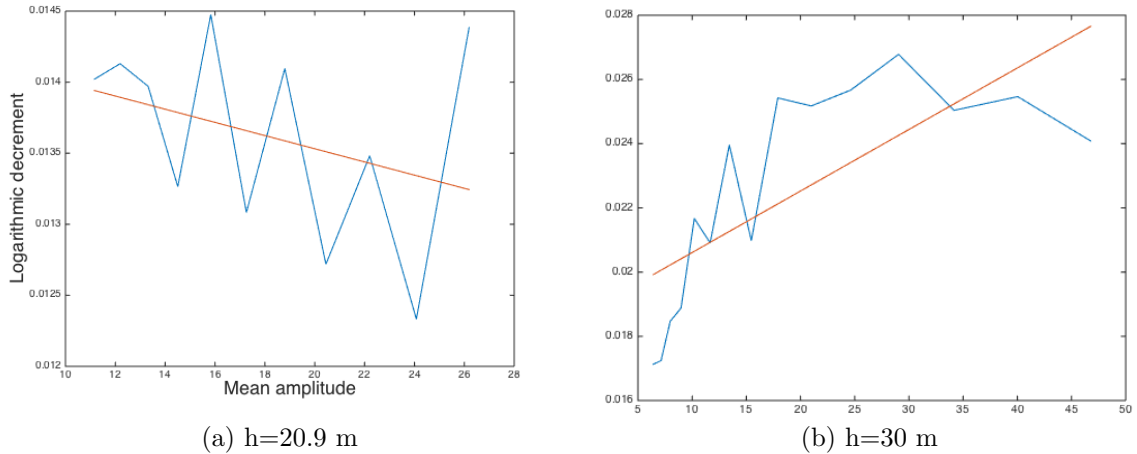


Figure 7.5.: Logarithmic decay plotted against mean amplitudes for decay tests in x-direction.

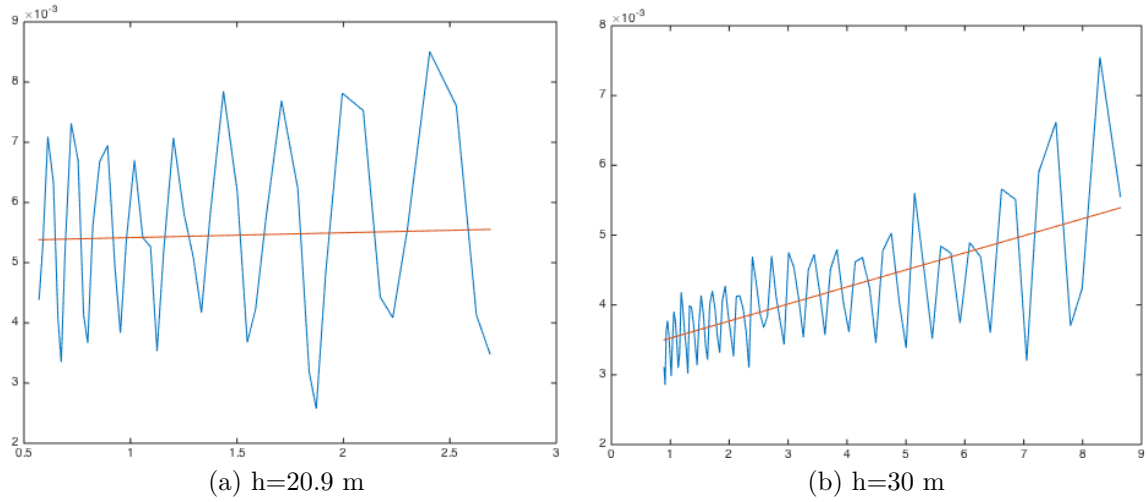


Figure 7.6.: Logarithmic decay plotted against mean amplitudes for decay tests in y-direction.

The results show that in the decay test in x-direction at $h=20.9$ m, figure 7.5a, the non-linear damping coefficient is negative. However, in all the cases the non-linear damping is negligibly small, as shown in table 7.2, meaning that slight inaccuracies or irregularities in testing may be the cause of the negative coefficient value. In further numerical analyses the damping is assumed linear.

Since the non-linear damping is negligible the damping ratio can be found directly using the mean value for the experimental logarithmic decrement.

$$\xi = \frac{1}{\sqrt{1 + \left(\frac{2\pi}{\ln(\text{mean}(\frac{x_i}{x_{i+1}}))}\right)^2}} \quad (7.7)$$

Damping coefficients	x-direction				y-direction		
	p_1	p_2	p_1/p_2	ξ	p_1	p_2	p_1/p_2
$h = 20.9$ m	0.015449	-0.000085	-181.545049	0.0140	0.005335	0.000081	66.064696
$h = 30$ m	0.018693	0.000192	97.560534	0.0249	0.003281	0.000244	13.428167

Table 7.2.: Linear and non-linear damping coefficients for each decay test.

A dry decay test, to determine how much of the damping is due to wave generation, was never performed. However, in [Kristiansen and Bachynski, 2015] the same model had previously been tested without water, although with a slightly smaller additional top mass of 4.08 kg (flange disc not included). In those tests,

which should be comparable, the dry decay damping ratio was 0.5 %. Thus, from table 7.2 it can be found that damping from wave generation corresponds to approximately 64 % at $h=20.9$ m and 80 % at $h=30$ m.

Just as for real, full scale offshore wind turbines the bottom part of the pile is filled with water. This causes sloshing, which commonly increases the damping of the structure, if constructed correctly. For a badly-tuned pile, however, the sloshing can excite the structure and thus decrease the damping.

Due to low levels of damping, [Damgaard et al., 2013] could approximate a measured system damping ξ_1 for the first eigenmode of an OWT as a linear combination of the following damping contributions:

$$\xi_1 = \xi_{steel} + \xi_{aero} + \xi_{water} + \xi_{tower} + \xi_{soil} \quad (7.8)$$

corresponding to the steel hysteretic, aerodynamic, wave making and viscous hydrodynamic, tower oscillation and soil damping ratios, respectively. The offshore wind turbine in question, placed at a 20-m water depth, had a tower height of 53.0 m and a monopile diameter of 5.0 m, i.e. a little smaller dimensions than the pile tested in this thesis. In the article, ξ_{steel} was estimated to 0.19 %, ξ_{tower} was deemed negligible and ξ_{soil} was determined to approximately 1.00 %. A theoretical estimation of ξ_{water} was taken from [Leblanc and Tarp-Johansen, 2010], giving $\xi_{water} \approx 0.12$ % for a 4.7-m diameter turbine at 20-m depth. It was found that due to the small relative velocities for the turbine structure, the viscous hydrodynamic damping was small compared to the wave-radiation damping. For an idling turbine, the relevant damping ratios from [Damgaard et al., 2013] add up to a level of 1.31 % at $h = 20$ m. Comparing with the damping ratio of $\xi = 1.40$ % at $h = 20.9$ m in table 7.2, implies that the structure tested in this thesis work is realistically damped. However, if the dry decay test mentioned above is within the correct order of magnitude, then the hydrodynamic damping is considerably more important in the model tests than in [Damgaard et al., 2013] (where the hydrodynamic damping amounted to 9 % at $h=20$ m). This could mean that the resulting ξ at $h=30$ m is too large compared the trend in [Damgaard et al., 2013], but still within a reasonable level of damping.

7.2. Regular wave post-processing

The resulting wave elevation characteristics in the regular wave runs are summarized in tables 7.3 and 7.4. The wavemaker in general had trouble generating the shortest waves corresponding to $T = T_1$ (see figure 7.7), as the inertial limit of the wavemaker was exceeded. All the regular wave realizations are shown in appendix A.

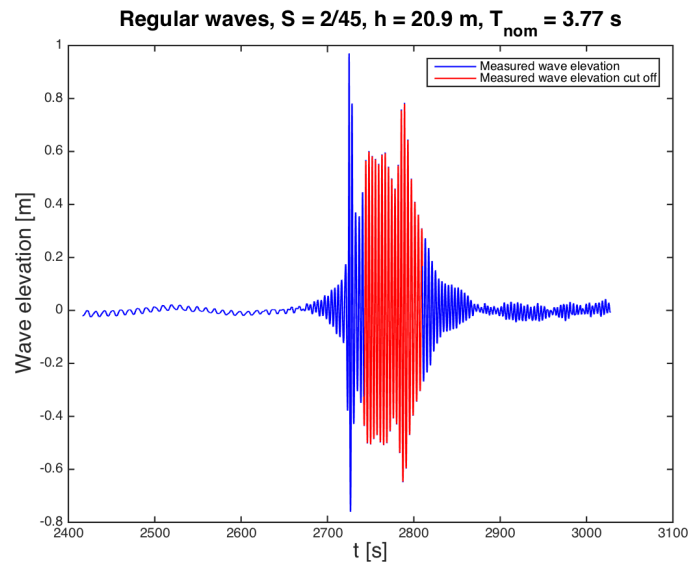


Figure 7.7.: An eigenperiod regular wave realization at $h = 20.9$ m.

Figure 7.8 shows how the response moment builds up for the eigenfrequency waves, due to dynamic amplification. For the longer waves, the structure is never excited at the first mode (as seen in the moment spectrum of figure 7.9b), so no such build up is observed as there is negligible dynamic amplification. In this thesis, the regular waves are mainly used as a linear validation of the numerical model (see section 6.3) and to test tank performance.

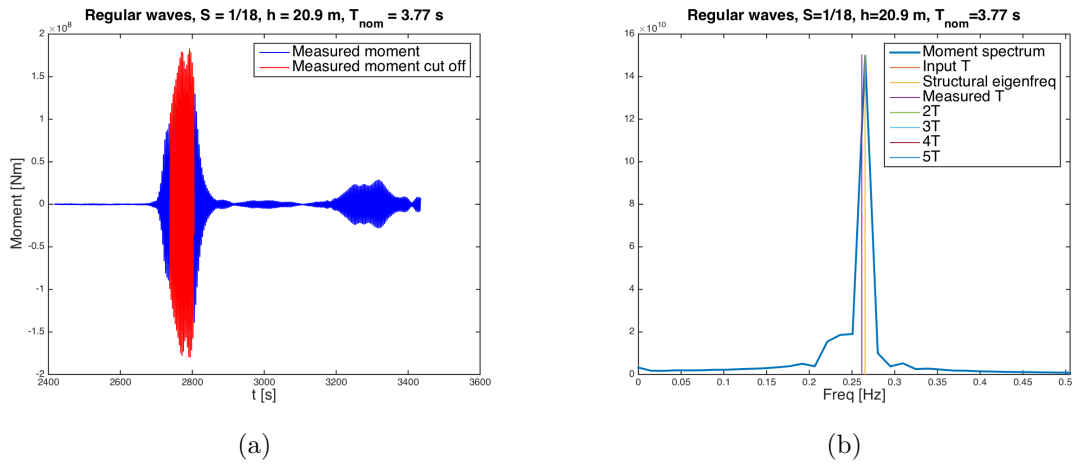


Figure 7.8.: Showing the moment build-up for the eigenfrequency waves.

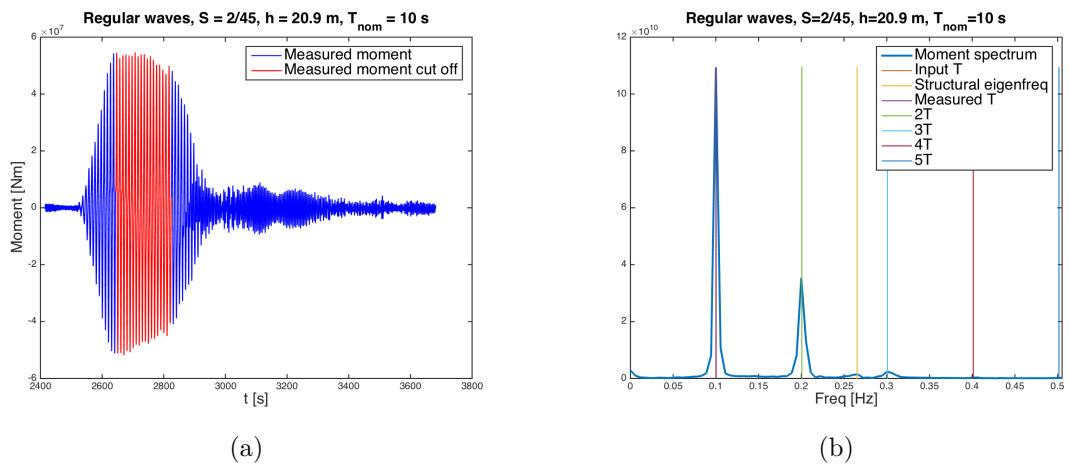


Figure 7.9.: No moment build-up to the long 10-s regular waves.

The following data related to the resulting wave characteristics of the regular waves are taken from the wave calibration runs, in order to omit diffraction and reflection effects from the presence of the model. The wave elevation time series are measured at wave gauge 7.

S_{nom}	T_{eff} [s]	T_{nom} [s]	$T_{\text{eff}}/T_{\text{nom}}$	H_{eff} [m]	H_{nom} [m]	$H_{\text{eff}}/H_{\text{nom}}$
1/30	14.99	15.00	1.00	7.24	6.71	1.08
1/30	12.00	12.00	1.00	5.55	5.17	1.07
1/30	10.00	10.00	1.00	4.39	4.10	1.07
1/30	7.49	7.50	1.00	2.73	2.71	1.01
1/30	3.78	3.77	1.00	0.82	0.74	1.11
7/180	14.98	15.00	1.00	8.59	7.83	1.10
7/180	11.99	12.00	1.00	6.45	6.03	1.07
7/180	9.99	10.00	1.00	5.15	4.79	1.08
7/180	7.50	7.50	1.00	3.20	3.16	1.01
7/180	3.79	3.77	1.01	0.94	0.86	1.09
2/45	15.00	15.00	1.00	8.93	8.95	1.00
2/45	11.99	12.00	1.00	7.55	6.89	1.10
2/45	10.00	10.00	1.00	5.80	5.47	1.06
2/45	7.49	7.50	1.00	3.70	3.61	1.02
2/45	3.80	3.77	1.01	1.06	0.99	1.07
1/20	14.96	15.00	1.00	7.75	10.07	0.77
1/20	11.98	12.00	1.00	8.56	7.75	1.10
1/20	10.03	10.00	1.00	6.51	6.15	1.06
1/20	7.49	7.50	1.00	4.13	4.06	1.02
1/20	3.84	3.77	1.02	1.10	1.11	0.99
1/18	15.10	15.00	1.01	7.46	11.19	0.67
1/18	11.99	12.00	1.00	9.03	8.61	1.05
1/18	10.01	10.00	1.00	7.45	6.84	1.09
1/18	7.50	7.50	1.00	4.62	4.51	1.02
1/18	3.86	3.77	1.02	1.21	1.23	0.99

Table 7.3.: Resulting effective wave periods and wave heights for each nominal steepness at $h=20.9$ m.

Wave non-linearity increases with steepness and period, as shown in table 5.14 on page 99. The largest-steepness wave with a nominal period of 15 s is seen to give an effective wave height of only 67 % of the nominal value. This is due to a large amount of breaking, which demonstrates the non-feasibility of such a large wave at the specific water depth.

The non-breaking waves are generally too large. A reason for this might be an overcompensating mechanical transfer function.

The effective wave periods are seen to match the nominal values well for all cases at $h = 20.9$ m. The largest $T_{\text{eff}}/T_{\text{nom}}$ are found for the short eigenperiod waves, where a regular shape was never achieved, since the inertial limit of the wavemaker

was exceeded for the required quick oscillatory stroke motion, as illustrated in figure 7.7.

The results of table 7.3 are plotted in figures 7.10 and 7.11.

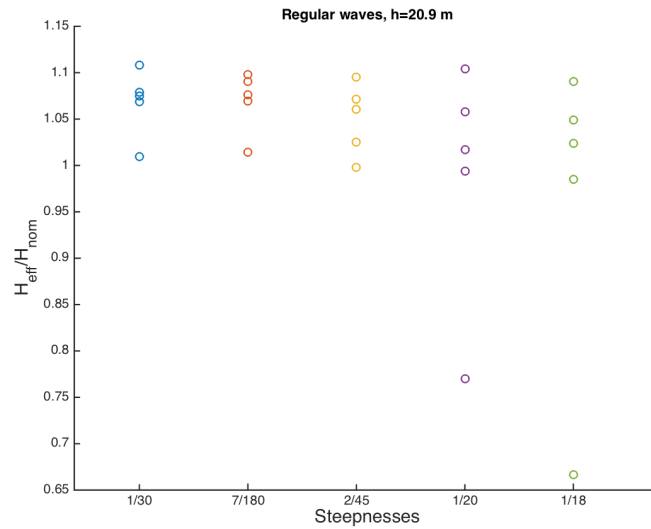


Figure 7.10.: The nominal and effective wave heights of the regular tests at $h = 20.9$ m.

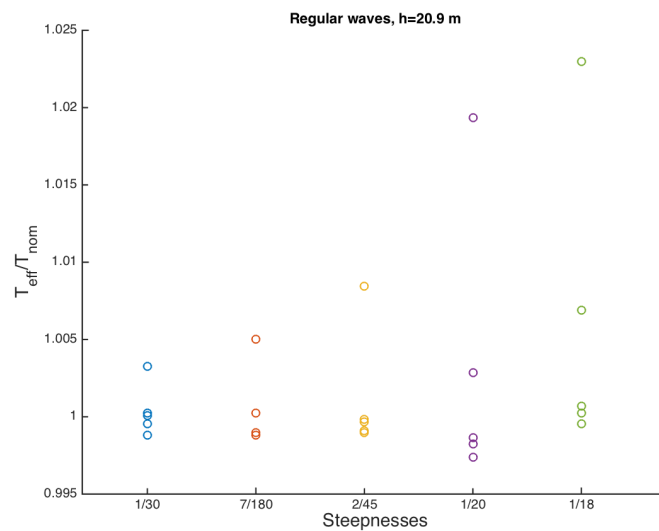


Figure 7.11.: The nominal and effective wave periods of the regular tests at $h = 20.9$ m.

S_{nom}	T_{eff} [s]	T_{nom} [s]	$T_{\text{eff}}/T_{\text{nom}}$	H_{eff} [m]	H_{nom} [m]	$H_{\text{eff}}/H_{\text{nom}}$
1/30	15.00	15.00	1.00	8.06	7.81	1.03
1/30	12.00	12.00	1.00	6.49	5.90	1.10
1/30	10.01	10.00	1.00	5.07	4.58	1.11
1/30	7.51	7.50	1.00	3.03	2.86	1.06
1/30	3.95	3.94	1.00	0.85	0.81	1.06
7/180	15.00	15.00	1.00	9.57	9.11	1.05
7/180	12.00	12.00	1.00	7.62	6.88	1.11
7/180	9.99	10.00	1.00	5.89	5.34	1.10
7/180	7.51	7.50	1.00	3.55	3.33	1.07
7/180	3.94	3.94	1.00	1.01	0.94	1.07
2/45	15.01	15.00	1.00	11.01	10.41	1.06
2/45	11.99	12.00	1.00	8.72	7.87	1.11
2/45	9.99	10.00	1.00	6.72	6.10	1.10
2/45	7.50	7.50	1.00	4.09	3.81	1.07
2/45	3.96	3.94	1.00	1.22	1.08	1.14
1/20	14.98	15.00	1.00	11.92	11.71	1.02
1/20	11.99	12.00	1.00	9.66	8.85	1.09
1/20	10.01	10.00	1.00	7.45	6.86	1.08
1/20	7.51	7.50	1.00	4.55	4.28	1.06
1/20	4.00	3.94	1.02	1.36	1.21	1.12
1/18	15.01	15.00	1.00	14.31	13.01	1.10
1/18	12.00	12.00	1.00	10.60	9.84	1.08
1/18	10.01	10.00	1.00	8.31	7.63	1.09
1/18	7.50	7.50	1.00	5.17	4.76	1.09
1/18	4.03	3.94	1.02	1.55	1.35	1.15

Table 7.4.: Resulting effective wave periods and wave heights for each nominal steepness at $h=30$ m.

At the larger water depth, the $H_{\text{eff}}/H_{\text{nom}}$ ratios are seen to be high for all steepnesses and periods, suggesting limited wave breaking. The measured wave periods match the nominal values well, and as for $h = 20.9$ m, the largest $T_{\text{eff}}/T_{\text{nom}}$ values are found for the eigenperiod waves, but the largest value of 1.02 indicates a satisfactory wave period agreement.

Due to the difference in the amounts of breaking, stochastic comparisons of loading for the two water depths could only have been done for the lower wave heights. However, the regular wave runs will not be analyzed stochastically.

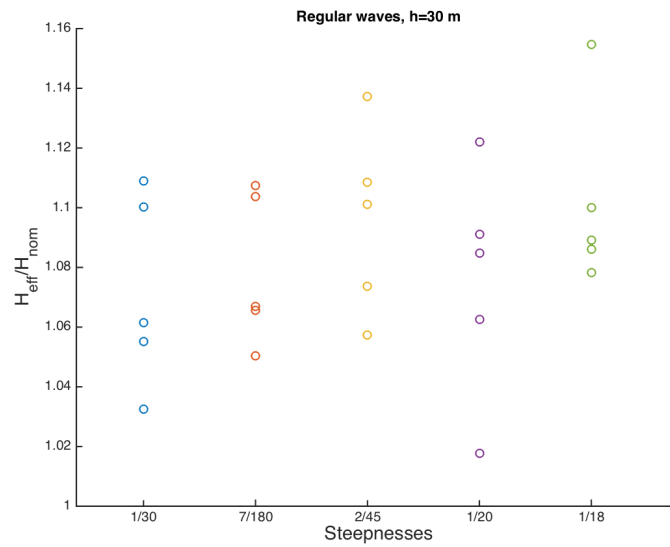


Figure 7.12.: The nominal and effective wave heights of the regular tests at $h = 30$ m.

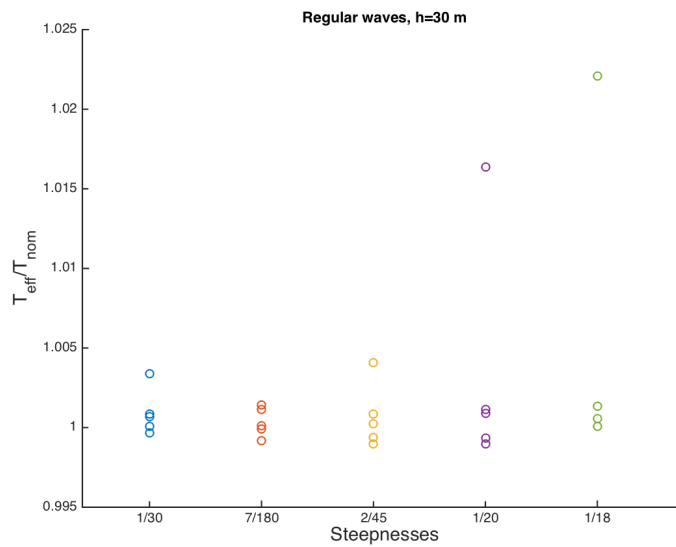


Figure 7.13.: The nominal and effective wave periods of the regular tests at $h = 30$ m.

The resulting wave regimes of the measured waves can be compared with those in section 5.8.4. Except for a few regular wave runs, tables 7.5 and 7.6 correspond

well with the theoretical regular waves in tables 5.14 and 5.15. It is seen that all the regular waves are categorized by a non-linear wave theory.

Regular wave regimes h = 20.9 m	T=3.77 s	T=7.5 s	T=10 s	T=12 s	T=15 s
S=1/30	2nd-order Stokes	2nd-order Stokes	2nd-order Stokes	Cnoidal	Cnoidal
S=7/180	5th-order Stokes	5th-order Stokes	5th-order Stokes	Cnoidal	Cnoidal
S=2/45	5th-order Stokes	5th-order Stokes	5th-order Stokes	Cnoidal	Cnoidal
S=1/20	5th-order Stokes	5th-order Stokes	5th-order Stokes	Cnoidal	Cnoidal
S=1/18	5th-order Stokes	5th-order Stokes	Breaking	Cnoidal	Cnoidal

Table 7.5.: Measured regular wave regimes for h = 20.9 m.

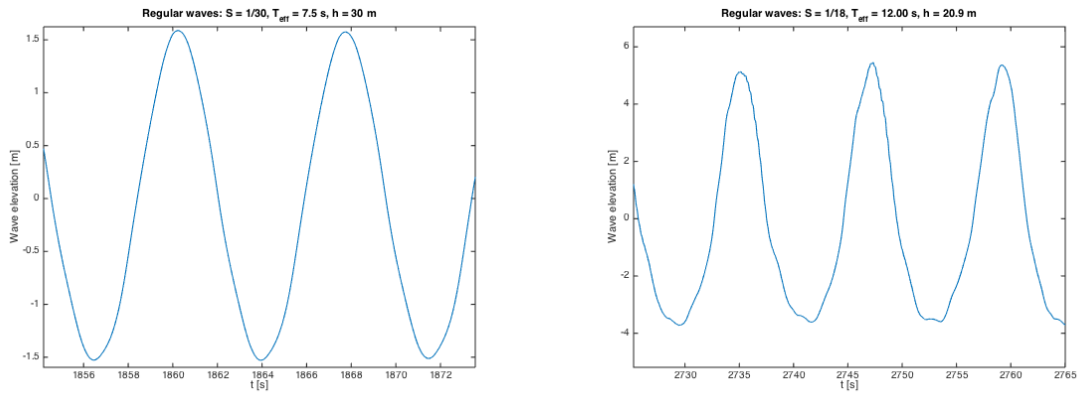
Regular wave regimes h = 30 m	T=3.94 s	T=7.5 s	T=10 s	T=12 s	T=15 s
S=1/30	2nd-order Stokes	2nd-order Stokes	2nd-order Stokes	2nd-order Stokes	Cnoidal
S=7/180	5th-order Stokes	5th-order Stokes	2nd-order Stokes	5th-order Stokes	Cnoidal
S=2/45	5th-order Stokes	5th-order Stokes	5th-order Stokes	5th-order Stokes	Cnoidal
S=1/20	5th-order Stokes	5th-order Stokes	5th-order Stokes	5th-order Stokes	5th-order Stokes
S=1/18	5th-order Stokes	5th-order Stokes	5th-order Stokes	5th-order Stokes	5th-order Stokes

Table 7.6.: Measured regular wave regimes for h = 30 m.

At 20.9-m water depth the steepest 10-s wave is categorized as a breaking wave, due to the large $H_{\text{eff}}/H_{\text{nom}}$ ratio.

Figure 7.14 shows regular wave realizations with periods 7.5 s and 12 s, steepnesses 1/30 and 1/18 and depths 30 and 20.9 m, respectively. The higher waves at shallower water in figure 7.14b, are more peaked with relatively shallower, wider troughs than the less non-linear waves in figure 7.14a.

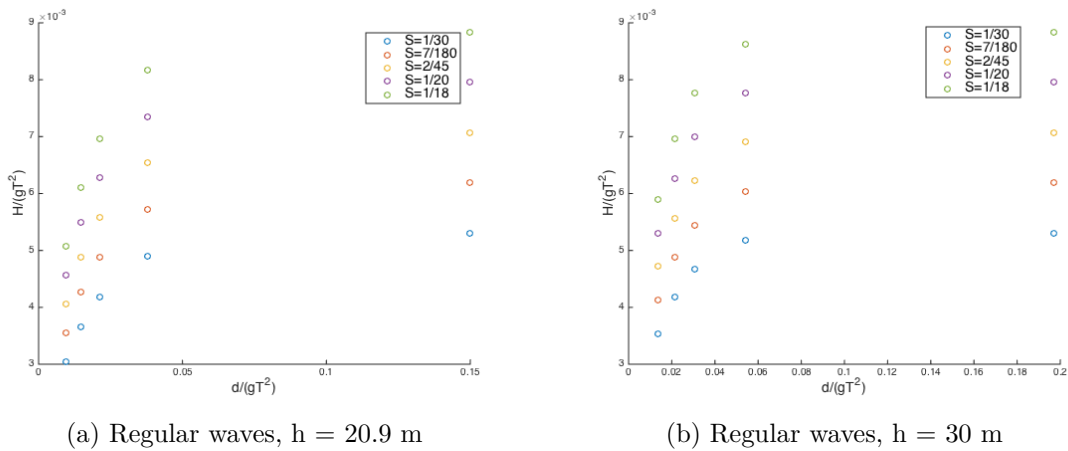
7.2. Regular wave post-processing



(a) Regular waves, $T_{\text{eff}} = 7.5$ s, $S = 1/30$, $h = 30$ m (b) Regular waves, $T_{\text{eff}} = 12.00$ s, $S = 1/18$, $h = 20.9$ m

Figure 7.14.: Showing non-linear features of steep waves at shallower water (b), compared with less steep regular waves (a).

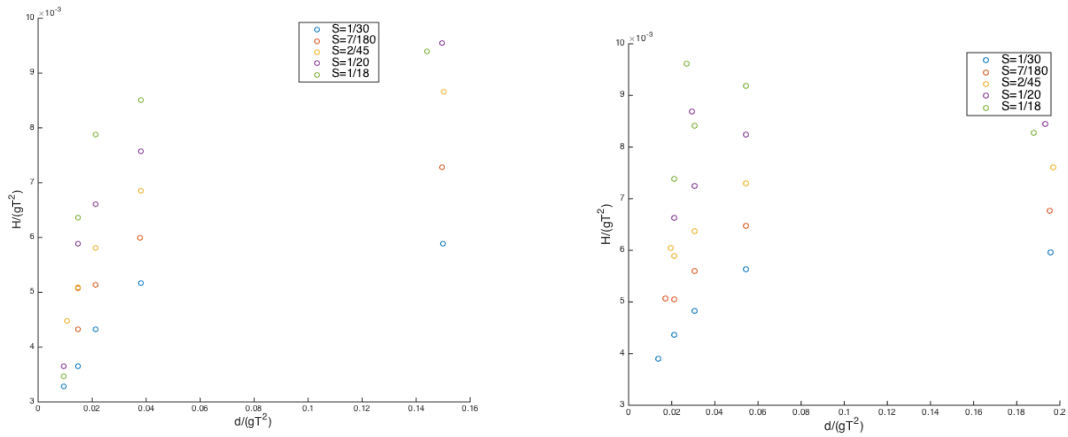
In the categorization of the regular waves, the data points of figures 7.15 and 7.16 are evaluated according to the criteria in figure 3.9.



(a) Regular waves, $h = 20.9$ m

(b) Regular waves, $h = 30$ m

Figure 7.15.: Plots to determine the theoretical regular wave regimes, as from tables 5.14 and 5.15.

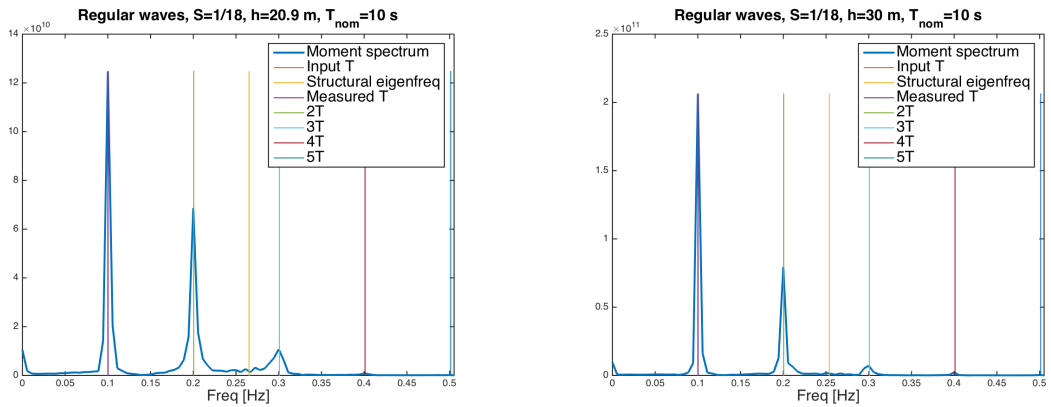


(a) Regular waves, $h = 20.9$ m

(b) Regular waves, $h = 30$ m

Figure 7.16.: Data for categorizing the measured regular wave series.

The non-linearity of waves can be illustrated by the response moment spectra. In figure 7.17, regular waves of the same stepness and period are compared for the two water depths. In both cases, $H_{\text{eff}}/H_{\text{nom}} = 1.09$ and $T_{\text{eff}}/T_{\text{nom}} = 1.00$. The relative importance of the second and third multiple of the wave period is larger at the lower water depths. This means that the second and third-order effects are larger for the shallow water wave, which, not surprisingly, implies a larger degree of non-linearity.



(a) $h = 20.9$ m

(b) $h = 30$ m

Figure 7.17.: Effect of water depth on higher-harmonic response moment contributions.

For an increasing steepness and wave period the same tendency is observed. The higher-harmonic moment responses are relatively larger in both cases, as seen in figures 7.18 and 7.19, respectively. The trend is less prominent for the steepness than the period, but it is observable in figure 7.18.

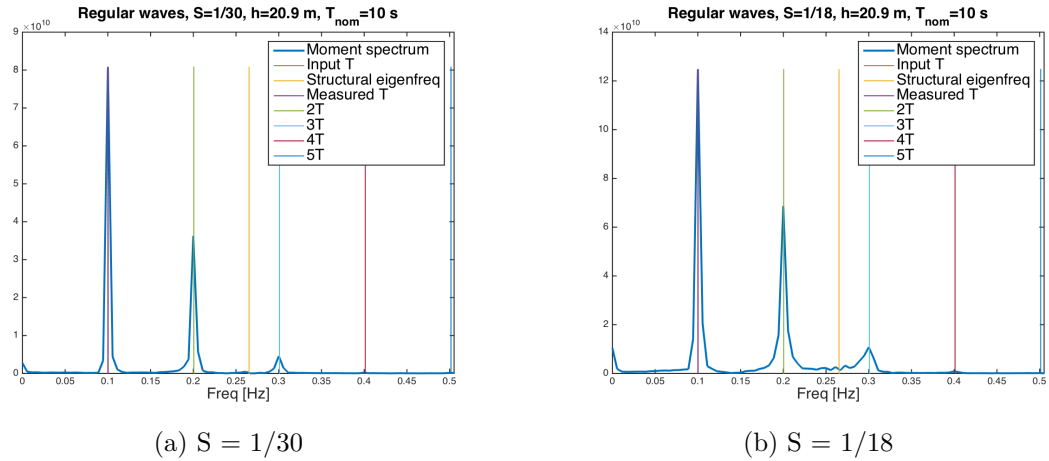


Figure 7.18.: Effect of steepness on higher-harmonic response moment contributions.

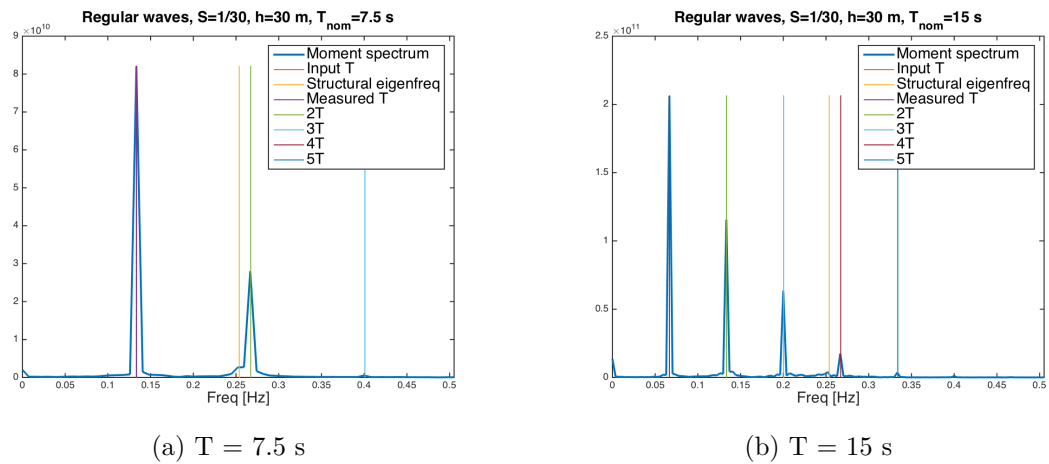
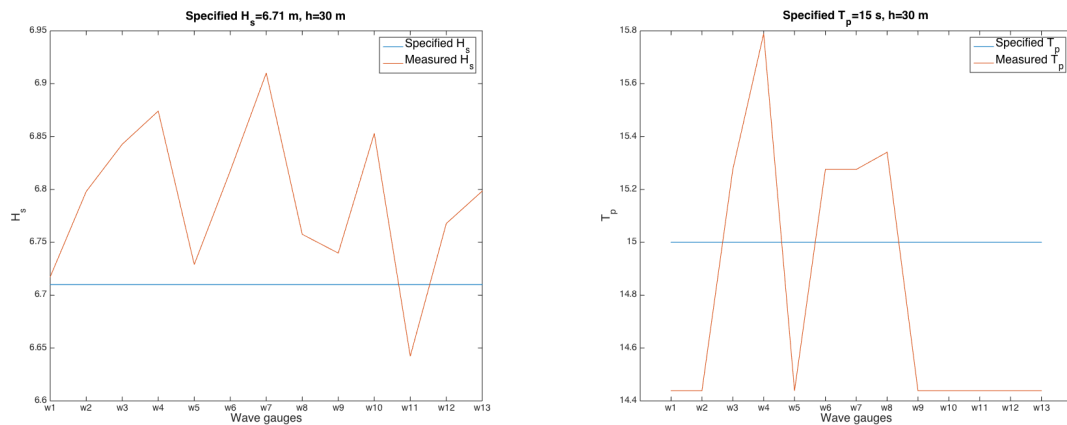


Figure 7.19.: Effect of the wave period on higher-harmonic response moment contributions.

7.3. Irregular wave post-processing

The measurements for each wave gauge correspond quite well in terms of resulting H_s and T_p values, exemplified for an irregular run of $H_s=6.71$ m and $T_p=15$ s, shown in figure 7.20. The back row of wave gauges, w9-w13 in figure 5.11, were found to give peculiar results in some cases, not corresponding to the other wave gauges. Gauge 5 was unstable, as illustrated in figures 7.20b and 7.21a, and thus omitted in post-processing.

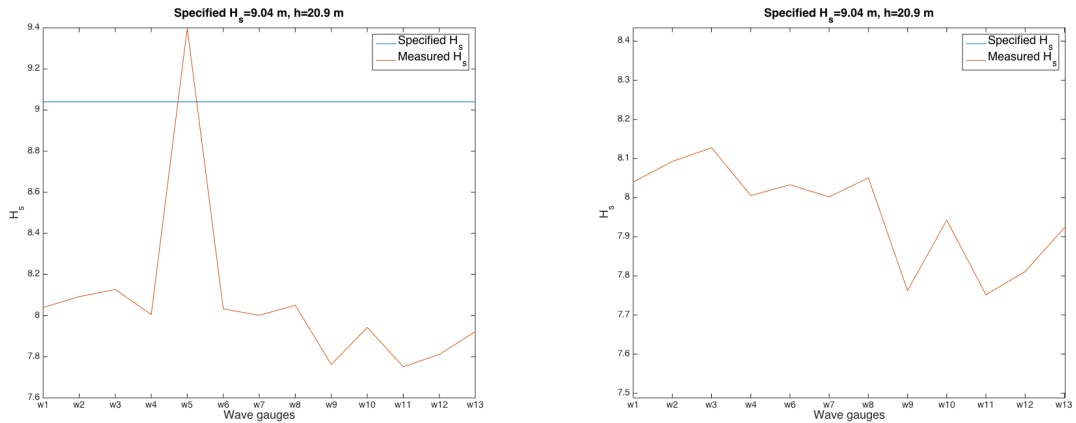


(a) Comparing significant wave height measurements.

(b) Comparing peak period measurements.

Figure 7.20.: Wave gauge measurement comparisons.

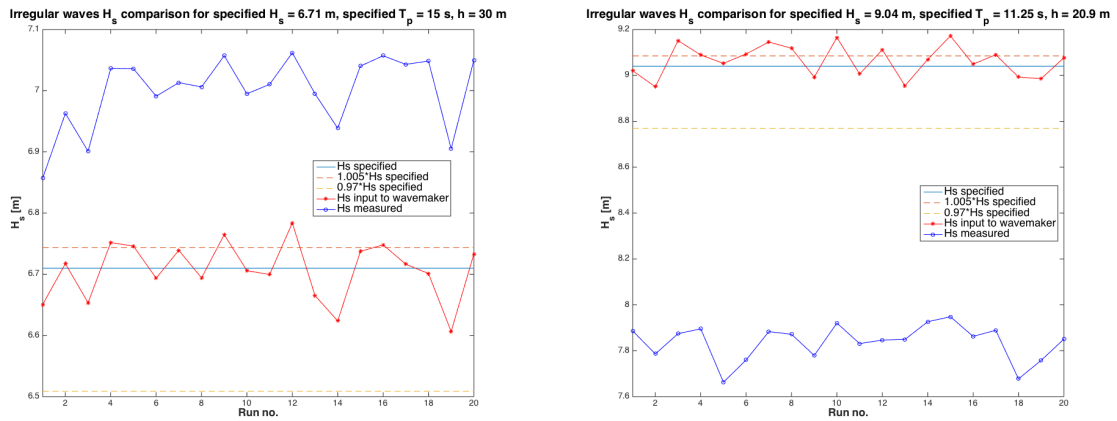
Figure 7.21b ($H_s=9.04$ m, $h=20.9$ m) shows how the significant wave height is reduced with distance from the wavemaker. The same tendency is not found in figure 7.20a, which is for a lower H_s and a larger water depth. This is in line with observations, as the high- H_s sea states were seen to exhibit much breaking.



(a) Evolution of the significant wave height along the tank length. (b) Omitting the unstable wave gauge 5.

Figure 7.21.: Measured H_s for the different wave gauges shows wave breaking along the tank.

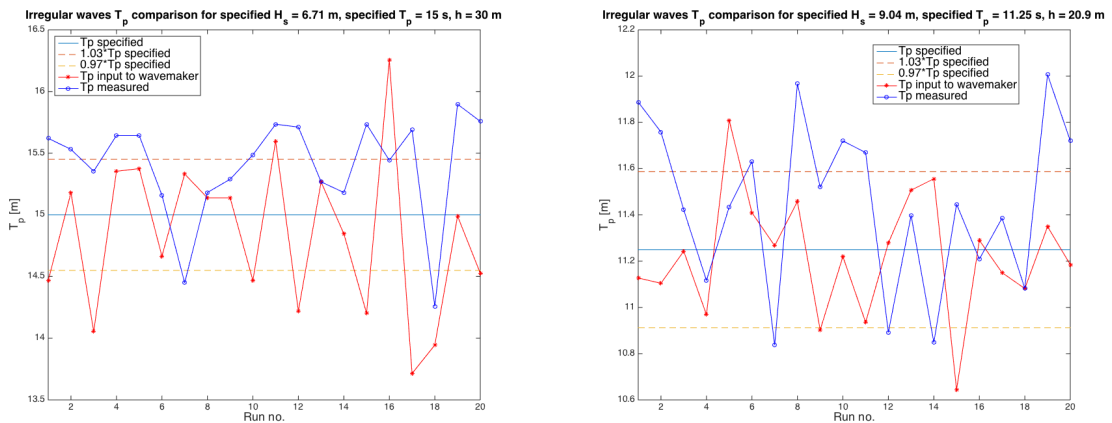
In figures 7.22 and 7.23 the resulting H_s , T_p values for the steepest and least steep sea states are compared. The results are based on calibrated wave runs measured at wave gauge 7. Similar to the results of the regular waves, the measured wave heights (blue) for the steepest waves are seen to be considerably lower than the nominal input values (red). This is not surprising as breaking is expected for the larger sea states in accordance with figure 5.23, where linear theory breaking criteria are given for different steepnesses. Breaking was seen to occur for many of the largest waves and is considered to be the reason for the H_s discrepancy. For the nominal $H_s=6.71$ m sea state, the effective H_s exceeds the nominal values, which was also typically the case for the non-breaking regular waves.



(a) Effective H_s for each seed in the least step (b) Effective H_s for each seed in the steepest irregular time series

Figure 7.22.: Comparing effective H_s values for different steepness irregular sea states.

A larger correspondence is seen for the T_p values than for H_s , for both steepnesses. The same trend was seen for the wave heights and periods of the regular waves.



(a) Effective T_p for each seed in the least step (b) Effective T_p for each seed in the steepest irregular time series

Figure 7.23.: Comparing effective T_p values for different steepness irregular sea states.

An example 20-seed-averaged wave spectrum is given in figure 7.24.

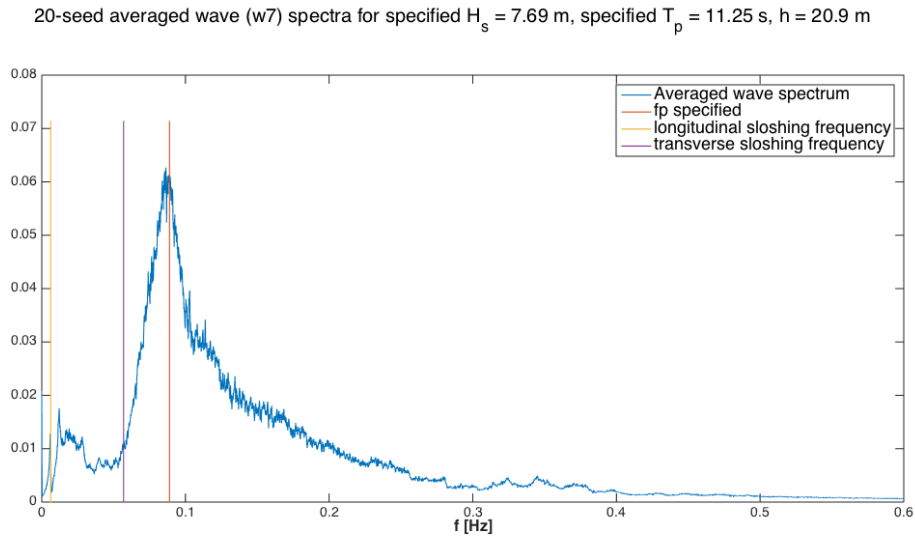


Figure 7.24.: Averaged wave spectrum

The sloshing frequencies are found using equation (7.9) from [Faltinsen and Timokha, 2009].

$$T_{sloshing} = \frac{2\pi}{\sqrt{\frac{g\pi \tanh(\pi h/l)}{l}}} \quad (7.9)$$

where l is the length or width of the tank, for the longitudinal and transverse sloshing periods, respectively. A distinct peak is found at the longitudinal sloshing frequency, as in figure 7.25, but no similar peak is found for transverse sloshing. The peaked area in the frequency range above the longitudinal sloshing frequency is low-frequency noise in the tank, perhaps residue from previous wave runs.

20-seed averaged wave (w7) spectra for specified $H_s = 7.69$ m, specified $T_p = 11.25$ s, $h = 20.9$ m

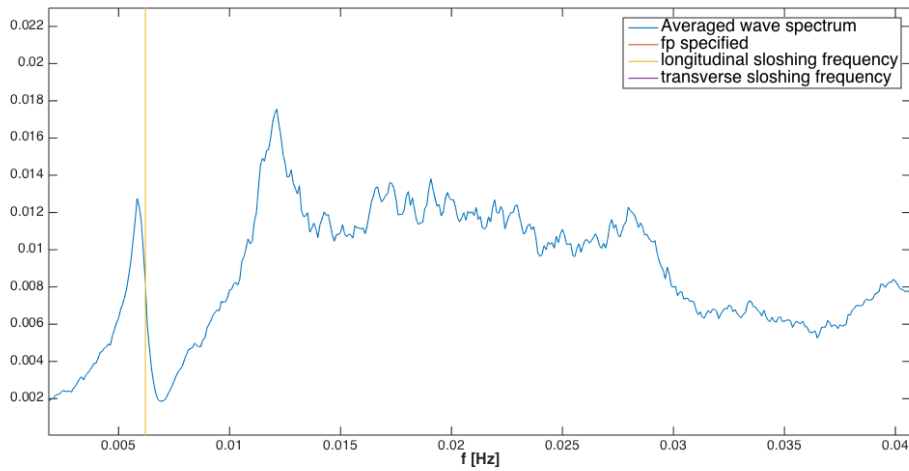
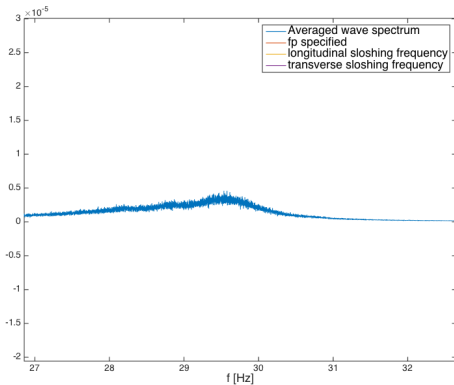


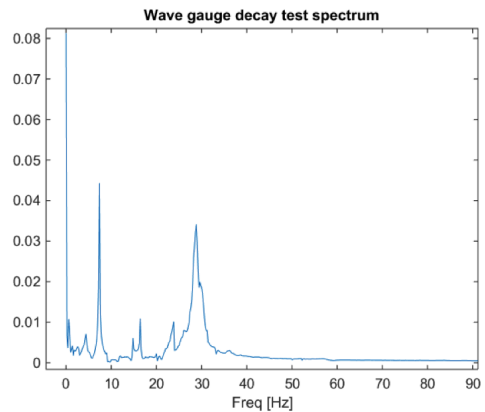
Figure 7.25.: Longitudinal sloshing

A small peak was discovered around 29.5 Hz (see figure 7.26a), found to be a wave gauge eigenfrequency, as shown in the spectrum of a wave gauge decay test of gauge 7 (w7), in figure 7.26b.

20-seed averaged wave (w7) spectra for specified $H_s = 6.71$ m, specified $T_p = 11.25$ s, $h = 20.9$ m



(a) A small wave spectrum peak showing one of the wave gauge eigenfrequencies.



(b) The wave gauge decay test spectrum.

Figure 7.26.: Illustrations of the wave gauge eigenfrequencies.

In figure 7.27 a force and moment spectrum comparison is exemplified for the 20-seed-averaged spectra for a certain sea state. It is observed that the highest peaks

are opposite for the force and moment. An explanation is found by considering the particle velocity profiles for the different frequencies. The low-frequency, long waves imply more shallow-water wave characteristics. On deep water, the particle velocity decreases with e^{kz} in linear theory. This gives a larger moment arm than on shallow water, where the vertical particle velocity distribution is more uniform. Thus, the relative force/moment significance ratio decreases for higher frequencies.

20-seed averaged moment and force spectra for specified $H_s = 7.69$ m, specified $T_p = 11.25$ s, $h = 20.9$ m

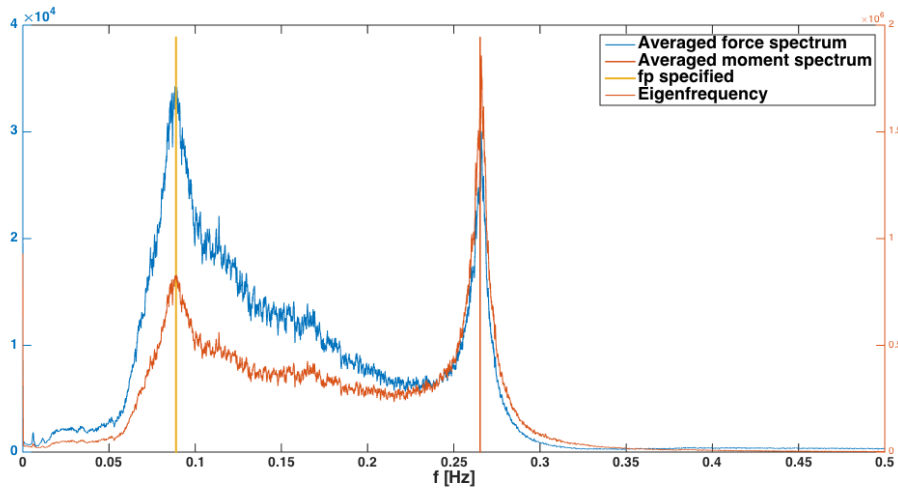


Figure 7.27.: Comparing force and moment spectra

Figure 7.27 also shows another phenomenon characterizing the experiments, which is illustrated by an unrealistically large eigenfrequency peak. As a comparison, a more realistic soil bending moment spectrum is supplied in figure 7.28, which is taken from a FEDEM analysis of a large-diameter bottom-fixed WT. It shows how wave excitation causes a much larger spectrum peak than the eigenfrequency, which is usually the case. The relatively low foundation stiffness compared with the high stiffness of the pile in the experiments creates an artificially conservative inverted pendulum-like mode shape, instead of a more realistic cantilever-like first mode. By ‘conservative’ it is implied that for the same point load, the rigid pile would achieve a larger top displacement compared to a realistic, curved mode shape. In combination with the self-excitation mechanism described in section 5.9.1 and the low (but realistic) damping level, the conservative mode shape creates a situation of considerable first-mode motion occurring almost continuously during the wave runs. This gives a larger relative dynamic compared to quasi-

static effect than for full scale monopiles. The result is the high eigenfrequency peak in figure 7.27.

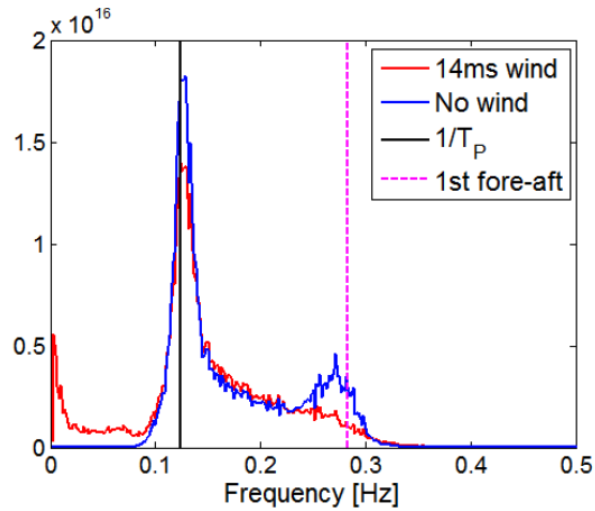


Figure 7.28.: Realistic bending moment spectrum from [Suja-Thauvin et al., 2014].

Since the frequent first-mode excitation is probably caused by a combination of real physics and experimental limitations it is difficult to separate the relative importance of the different effects.

Mean H_s , T_p values, as well as mean and maximum force and moment measurements of all the 20 seeds in each sea state, are presented in tables 7.7 to 7.10.

7.3. Irregular wave post-processing

H _s specified [m]	T _p specified [s]	h=20.9 m					
		Mean H _s	Mean H _s	Mean red. %	Mean T _p	Mean T _p	Mean red. %
		wm input [m]	measured [m]	H _s achieved	wm input [s]	measured [s]	T _p achieved
9.04	15.00	9.04	7.95	12.04	14.87	15.06	-1.44
8.22	15.00	8.21	7.52	8.41	15.02	14.93	0.46
7.69	15.00	7.66	7.15	6.66	14.86	15.25	-2.63
6.71	15.00	6.71	6.44	3.96	14.84	15.18	-2.47
9.04	11.25	9.06	7.95	12.30	11.22	11.38	-1.41
8.22	11.25	8.24	7.57	8.13	11.24	11.62	-3.43
7.69	11.25	7.68	7.24	5.85	11.12	11.51	-3.53
6.71	11.25	6.71	6.61	1.43	11.15	11.56	-3.77

Table 7.7.: Effective H_s, T_p values at h=20.9 m, considering all 20 seeds of each sea state.

H _s specified [m]	T _p specified [s]	h=30 m					
		Mean H _s	Mean H _s	Mean red. %	Mean T _p	Mean T _p	Mean red. %
		wm input [m]	measured [m]	H _s achieved	wm input [s]	measured [s]	T _p achieved
9.04	15.00	9.04	9.16	-1.39	14.87	15.37	-3.50
8.22	15.00	8.21	8.44	-2.79	15.02	15.49	-3.29
7.69	15.00	7.66	7.91	-3.24	14.86	15.33	-3.23
6.71	15.00	6.71	6.93	-3.38	14.84	15.27	-3.12
9.04	11.25	9.06	8.86	2.30	11.22	11.19	0.22
8.22	11.25	8.24	8.29	-0.64	11.24	11.32	-0.72
7.69	11.25	7.69	7.76	-0.92	11.29	11.36	-0.66
6.71	11.25	6.73	6.91	-2.80	11.22	11.18	0.26

Table 7.8.: Effective H_s, T_p values at h=30 m, considering all 20 seeds of each sea state.

H _s specified [m]	T _p specified [s]	h=20.9 m					
		Mean max.	Mean max.	Maximum max.	Maximum max.	Quantile	Quantile
		force [MN]	moment [MNm]	force [MN]	moment [MNm]	force [MN]	moment [MNm]
9.04	15.00	5.36	222.27	7.11	279.98	6.83	295.01
8.22	15.00	4.96	199.87	6.62	246.27	6.28	254.43
7.69	15.00	4.80	192.65	5.73	219.53	5.63	241.14
6.71	15.00	4.32	169.47	5.08	209.44	5.21	219.13
9.04	11.25	5.11	209.35	5.70	249.06	5.99	259.92
8.22	11.25	5.03	202.73	5.71	234.14	5.75	234.05
7.69	11.25	4.82	195.30	5.96	231.39	5.66	238.70
6.71	11.25	4.64	180.68	6.24	213.72	5.84	222.02

Table 7.9.: Maximum loads for each sea state at h=20.9 m.

H _s specified [m]	T _p specified [s]	h=30 m					
		Mean max.	Mean max.	Maximum max.	Maximum max.	Quantile	Quantile
		force [MN]	moment [MNm]	force [MN]	moment [MNm]	force [MN]	moment [MNm]
9.04	15.00	7.16	325.87	9.14	433.38	9.02	422.37
8.22	15.00	6.62	292.93	7.92	379.12	8.13	386.97
7.69	15.00	6.34	280.06	7.41	334.29	7.79	352.17
6.71	15.00	5.18	213.93	5.77	248.83	5.96	257.10
9.04	11.25	7.86	362.13	9.40	440.15	9.46	451.15
8.22	11.25	7.29	329.10	8.61	405.32	8.82	415.46
7.69	11.25	6.93	312.35	7.93	360.71	7.79	356.31
6.71	11.25	6.05	262.84	6.99	306.24	7.01	314.90

Table 7.10.: Maximum loads for each sea state at h=30 m.

The mean and max. maximum moments of tables 7.9 and 7.10 are plotted in figures 7.29 and 7.30.

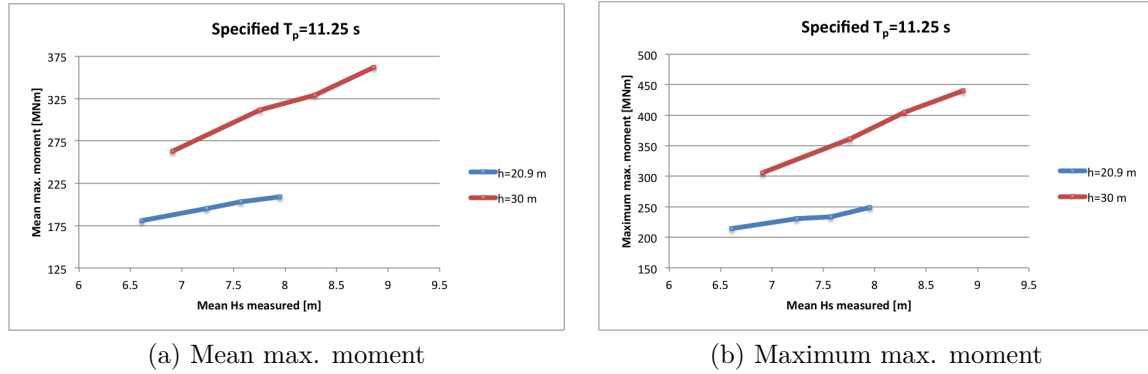


Figure 7.29.: Comparing averaged max. moments as a function of measured H_s for $T_p=11.25$ s.

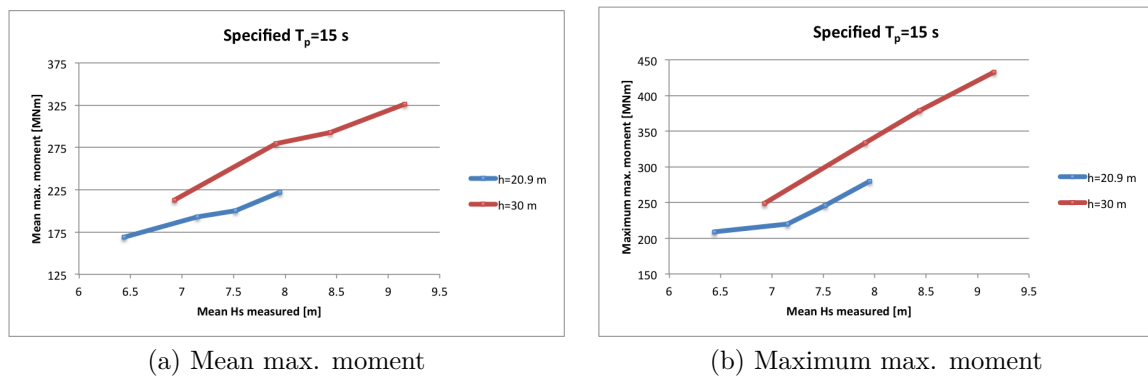


Figure 7.30.: Comparing averaged max. moments as a function of measured H_s for $T_p=15$ s.

A concern when considering the experimental results is whether the maximum moments occur at an artificially large eigenfrequency peak, as discussed on page 137. The vital question in the analyses of the experimental results is whether the first-mode motion alters the extreme wave loads.

Ringing is a response-dominated phenomenon, seen to arise when the first mode is triggered by high-frequency wave components occurring at the same time as a quasi-static extreme wave. Usually, the addition to the resulting total response moment from the first-mode response is around 30-50 % ([Suja-Thauvin et al.,

2014], [Krokstad, 2015]). Even though the claim is debated, the occurrence of ringing is said to be damping independent, i.e. the extreme response is memoryless. Evidence showing the contrary is undocumented, but in experiments examining the transition between springing (where the first mode is excited) and ringing shows that the damping level is significant for the outcome. This clearly relates to the present low-damping study. However, the mentioned study was never published [Krokstad, 2015], and thus it cannot be rendered in this thesis. The question remains whether the stated damping independence requires a certain damping level lower limit.

In figure 7.31, fifth-order high-pass and low-pass Butterworth filters were applied on a moment time series, giving the high and low frequency parts of the moment (see figure 7.33). The cut-off frequency was set to the mean of the spectrum peak frequency and the first mode eigenfrequency. The result is an eigenfrequency-dominated high-frequency part and a peak frequency-dominated low-frequency part (figure 7.33).

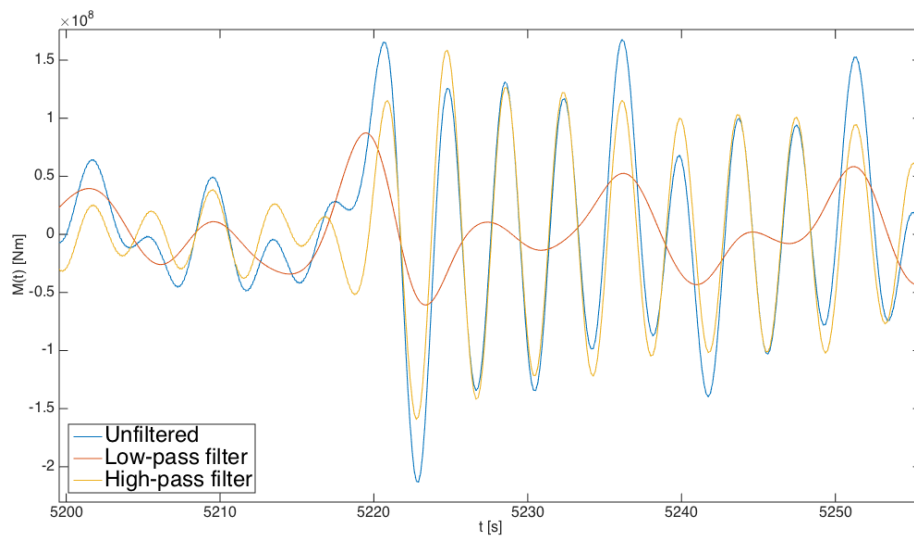


Figure 7.31.: A low-pass (red) and high-pass (yellow) filter applied on a moment time series (blue), for the largest moment of the sea state $H_s=7.69$ m, $T_p=15$ s, $h=20.9$ m, seed 1600.

With the low damping in the experiments we might not be able to adjust the damping level using numerical tools. A weakness of the experiments is that only one damping level was used. More damping levels would give a more robust

validation using the numerical program, as well as an increased understanding of the effect of damping on the occurrence of ringing in a lightly damped system.

From figure 7.31 it is seen that the continuously triggered first-mode, i.e. the high-frequency part, dominates the resulting response moment. Thus, in extreme loading for a lowly-damped system, the quasi-static load seems insignificant compared to the first-mode response. This means that the system may be insensitive to non-linear 3rd and 4th-order components of an extreme wave. For a system without self-excitation and a higher damping level, this is not the case. As will be discussed in section 7.4.1, ringing might not be a problem if the high-frequency components of an extreme wave become unimportant.

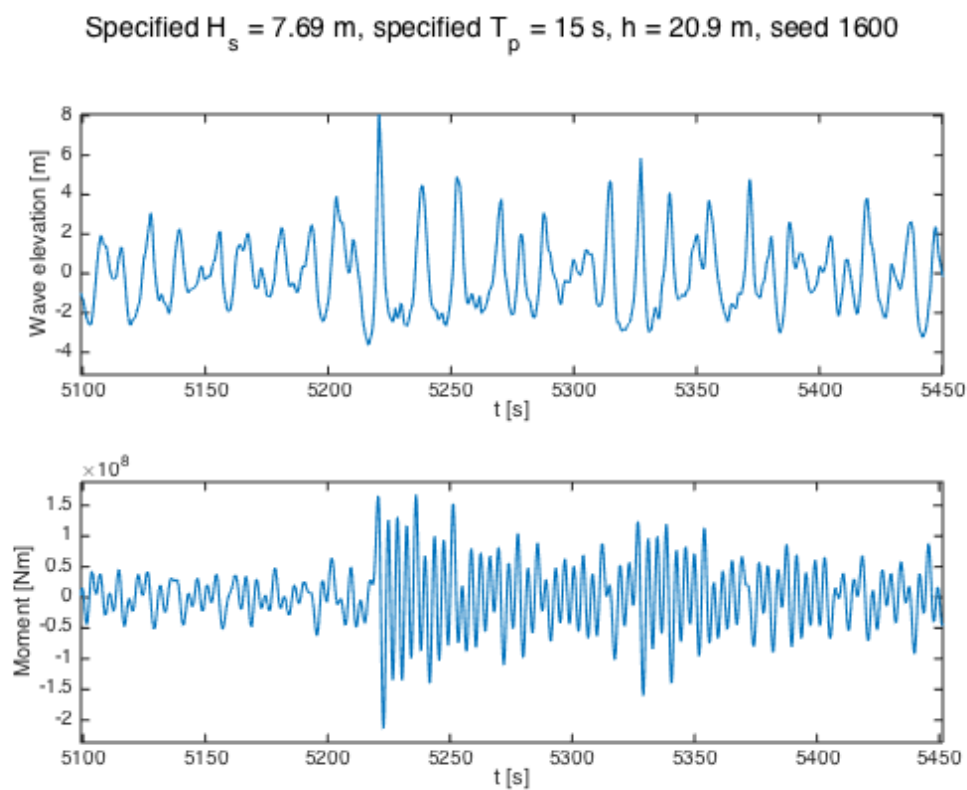


Figure 7.32.: The wave elevation and moment time series corresponding to the event in figure 7.31.

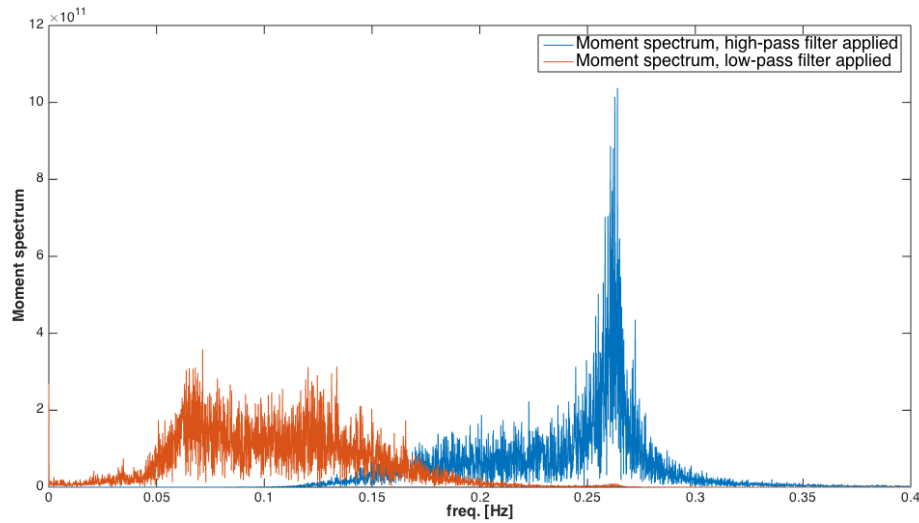


Figure 7.33.: The resulting low-pass and high-pass contributions of the moment spectrum after applying the ideal fifth-order Butterworth filter.

7.3.1. Comments on the execution of the irregular test program

A few problems occurred while running the irregular waves. For all seeds of $T_p=11.25$ s at $h=20.9$ m and the two smallest sea states of the same peak period at $h=30$ m, the input stroke to the wavemaker was generated without any high-frequency cut-off. The same approach had been used for similar experiments in the wave flume without problems. However, during the irregular 11.25-s T_p runs at $h=30$ m, the wavemaker began making loud, mechanical noises and was vibrating at a high-frequency. Small, transverse waves occurring by the wavemaker was also observed. In figure 7.34, the $H_s=6.71$ m, $T_p=11.25$ s sea state stroke spectra at both $h=20.9$ m ('piston out old') and $h=30$ m ('piston out new'), are compared. The high-frequency vibrations around 8-9 Hz are visible.

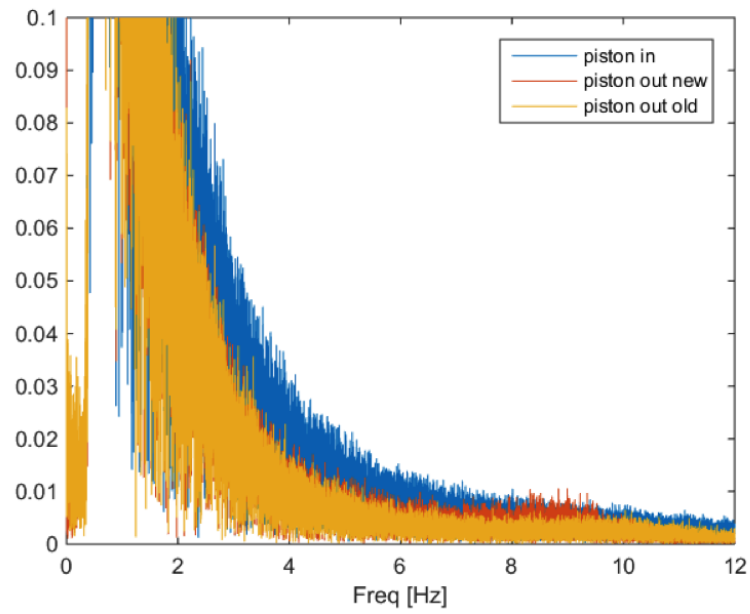


Figure 7.34.: Comparing piston stroke spectra

A 3-Hz frequency cut-off was applied to the remaining irregular sea states, as exemplified in figure 7.35.

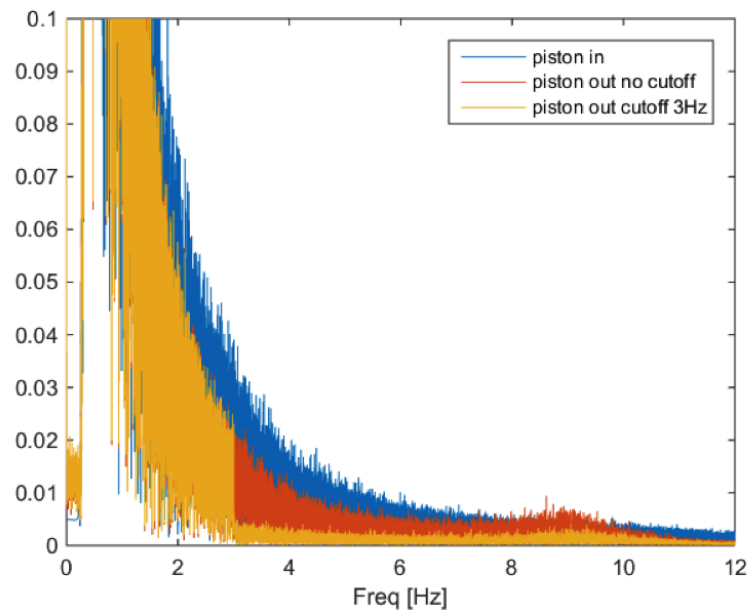


Figure 7.35.: Application of the 3-Hz filter

The cut-off was tested by running an irregular sea state of $H_s=6.71$ m, $T_p=15$ s at $h=30$ m. The difference in stroke is found in figure 7.36, whilst the wave elevations are found in 7.37a. As seen in figure 7.37b the filter had little effect on the wave elevation time series. A comparison of H_s showed that it increased from 6.63 m to 6.66 m, corresponding to a 0.45 % increase, after the filter was applied. A probable reason for the negligible difference is that the inertial limit of the wavemaker is already exceeded at 3 Hz.

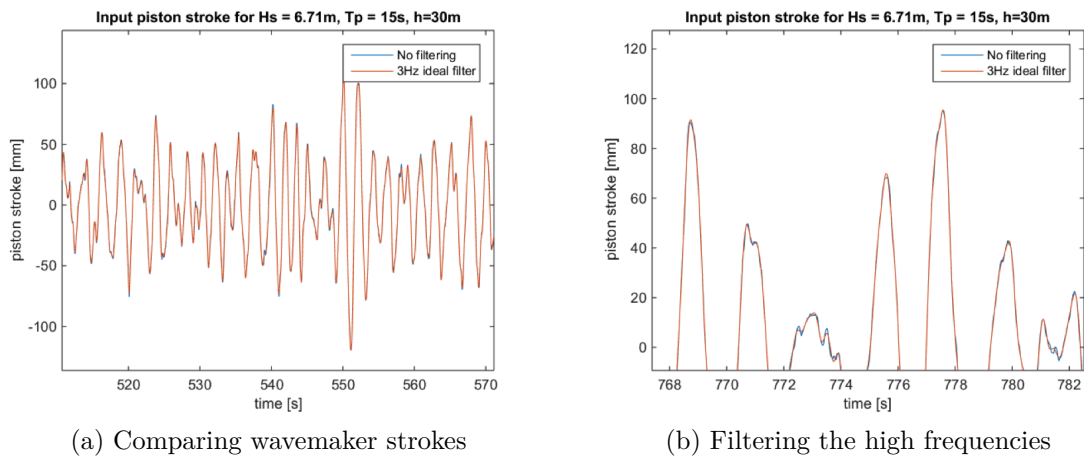


Figure 7.36.: Effects of the high-frequency filter on the wavemaker stroke.

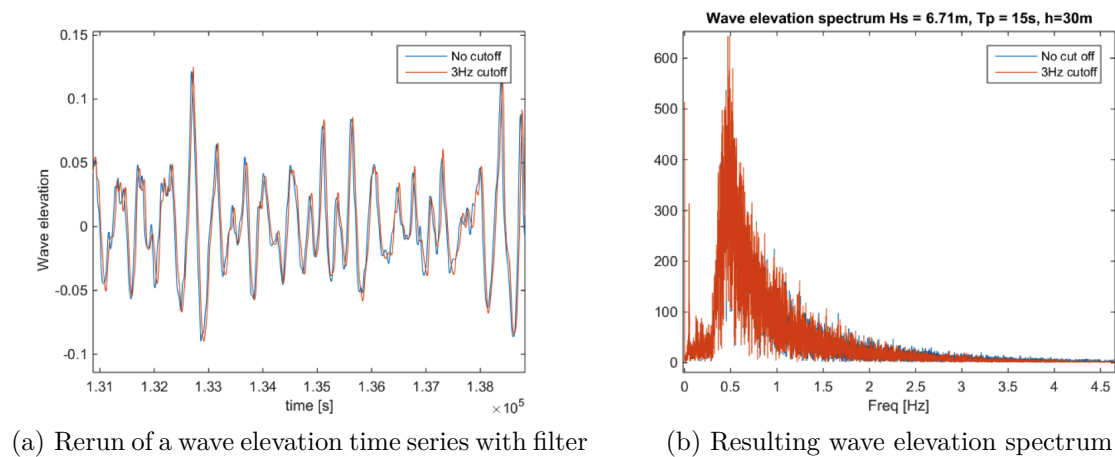


Figure 7.37.: Applying a high-frequency filter had little effect on the resulting wave elevations.

7.4. Special, bi-chromatic wave tests

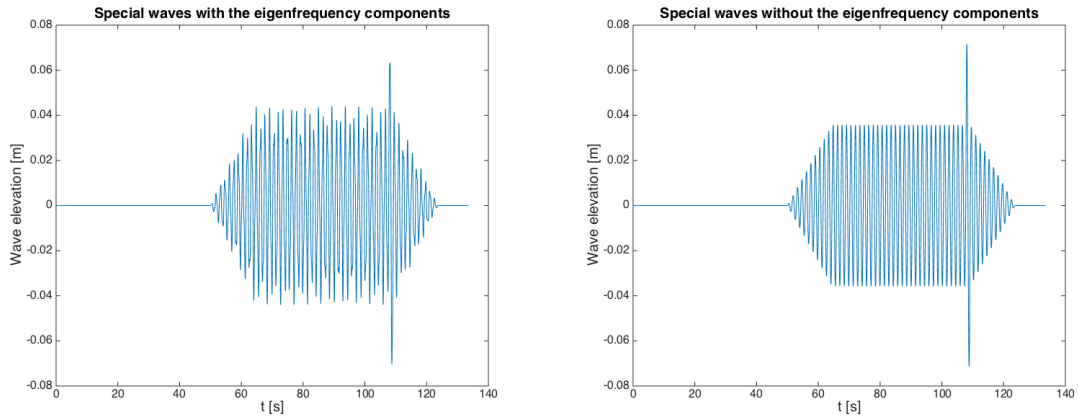
The crucial problem that occurs for the lightly-damped system is whether the response loads can be scaled with the damping level in the numerical program. If so, the occurrence of non-linear phenomena generating large response maxima, such as ringing, must remain unchanged when the excessive first-mode motion is introduced.

In order to understand this essential aspect, additional bi-chromatic, special wave tests were designed and run. The basic assumption of our lowly damped system is that the load is independent of the response in a linear system. Ringing is a response-dominated phenomenon, shown to occur on the impact of a large-amplitude wave with high-frequency components close to the eigenfrequency. A quasi-static part results from the large wave and the 3rd or 4th-order frequency component excites the first-mode. Only a few succeeding high-frequency cycles have proven sufficient for ringing to occur [Chaplin et al., 1997], causing a shift from peak frequency-driven to eigenfrequency-driven response, as discussed in section 3.6.

The purpose of the special wave tests was to see whether the occurrence of ringing is different for the two cases, with and without the eigenfrequency component. If so, it would strongly imply that the maximum moments in the irregular runs would be faulty compared with the real-life structure, on a stochastic level.

The designed special waves were non-steep, low-frequency regular waves with a single large embedded extreme wave, combined with eigenfrequency waves of different steepnesses. To test the effect of first-mode motion on the maximum loads, the same waves were tested without the eigenfrequency component. The response loads were to be compared. The two wave combinations are illustrated in figure 7.38.

If the high-frequency parts of the extreme, non-linear wave proved unimportant, i.e. if ringing is induced for the mono-chromatic waves only, it might imply that ringing will not be a problem for the self-excited, lightly damped, conservative mode shape system. It would also provide an indication to whether and how much the measured maximum loads were underestimated or overestimated.



(a) The eigenfrequency component is present

(b) No eigenfrequency component

Figure 7.38.: A special wave run with and without the eigenfrequency component. The wave periods are $T=3.94$ s and $T=10$ s, at $h=30$ m. The steepness of the 10-s extreme wave is twice the steepness of the other 10-s waves.

$h \cdot \lambda$ [m]	Eigenfreq. wave		Low-steepness, long wave		Extreme wave		Phase [rad]
	S	T [s]	S	T [s]	S	T [s]	
30	0.0165	3.94	1/40	10	1/20	10	0
30	0.0165	3.94	1/40	10	1/20	10	$\pi/2$
30	0.0165	3.94	1/40	10	1/20	10	π
30	0.0165	3.94	1/40	10	1/20	10	$3\pi/2$
30	0.0330	3.94	1/40	10	1/20	10	0
30	0.0330	3.94	1/40	10	1/20	10	$\pi/2$
30	0.0330	3.94	1/40	10	1/20	10	π
30	0.0330	3.94	1/40	10	1/20	10	$3\pi/2$
30	0.0495	3.94	1/40	10	1/20	10	0
30	0.0495	3.94	1/40	10	1/20	10	$\pi/2$
30	0.0495	3.94	1/40	10	1/20	10	π
30	0.0495	3.94	1/40	10	1/20	10	$3\pi/2$
30	0.0660	3.94	1/40	10	1/20	10	0
30	0.0660	3.94	1/40	10	1/20	10	$\pi/2$
30	0.0660	3.94	1/40	10	1/20	10	π
30	0.0660	3.94	1/40	10	1/20	10	$3\pi/2$
30	0.0825	3.94	1/40	10	1/20	10	0
30	0.0825	3.94	1/40	10	1/20	10	$\pi/2$
30	0.0825	3.94	1/40	10	1/20	10	π
30	0.0825	3.94	1/40	10	1/20	10	$3\pi/2$

Table 7.11.: The test matrix for special waves.

In order for the eigenfrequency waves and the 10-s waves to reach the structure simultaneously, the slower eigenfrequency waves were shifted, as in figure 7.39. The time translation was calculated using the group velocity for linear waves on finite water depth, as given in equation (3.39).

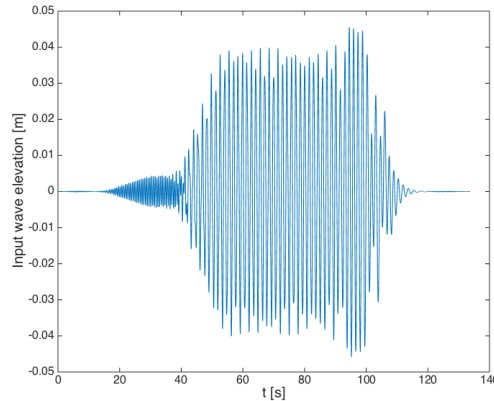


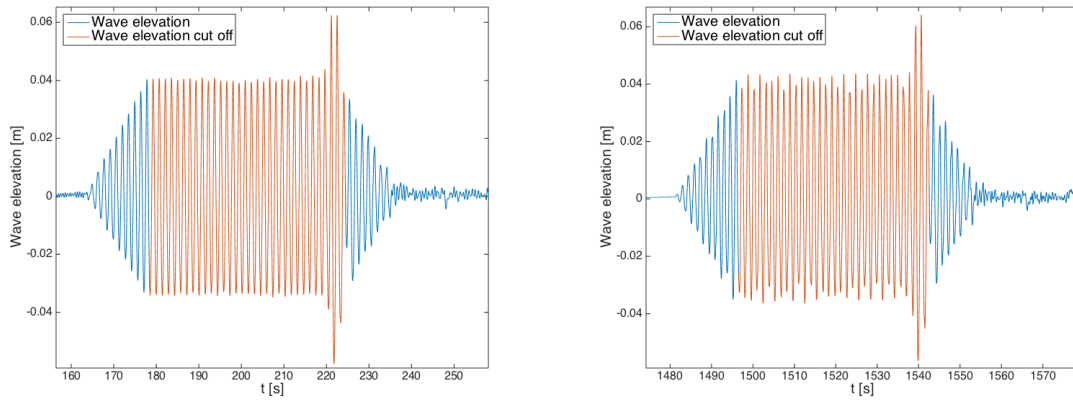
Figure 7.39.: The eigenfrequency waves are generated before the 10-s waves.

Since ringing is a response-dominated phenomenon, the phase difference between the waves should have an effect, so phases were introduced in testing as seen in table 7.11.

7.4.1. Special wave post-processing

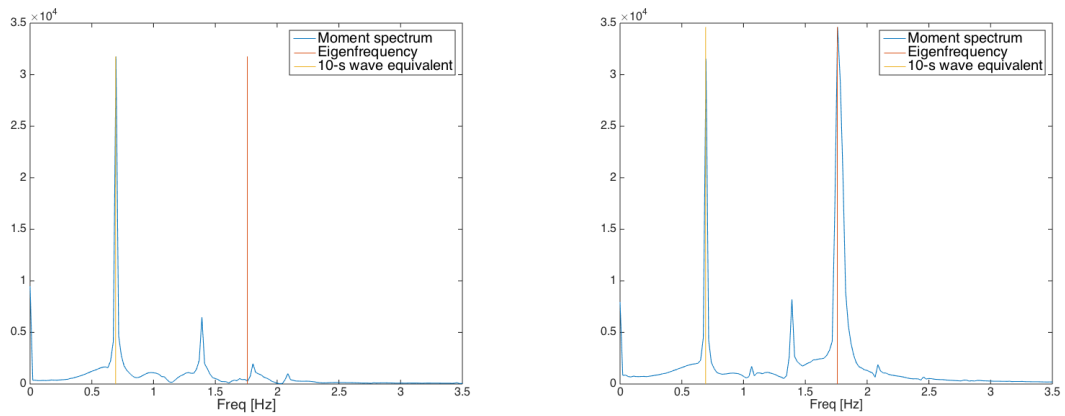
A resulting special wave realization measured at wave gauge 7 is found in figure 7.40b. It shows that two extreme peaks were present at the end of the time series, instead of the several peaks that were present for the wavemaker input (figure 7.39), as some of the extreme waves merged during propagation. Several configurations were tested and this proved to be the closest resemblance of the desired time series of figure 7.38a.

The results showed that we were unable to trigger ringing artificially for either wave combination. It was also shown that variation in the phase between the different wave components had little effect.



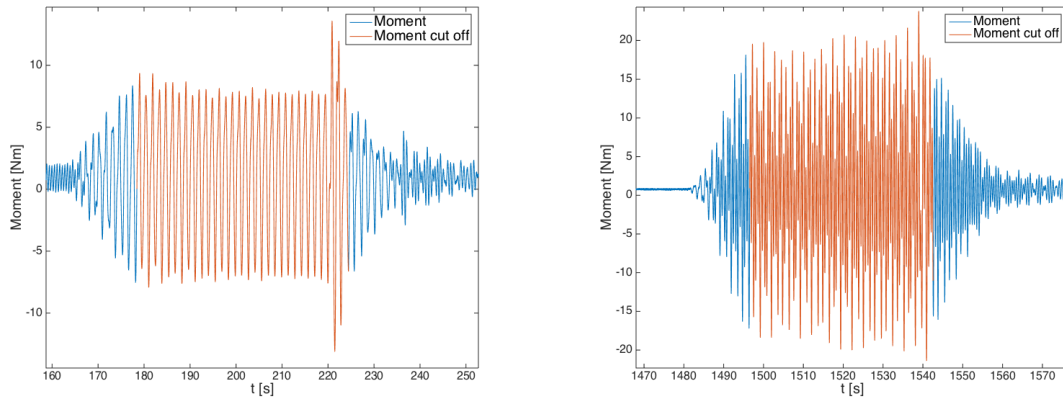
(a) Wave elevation, no eigenfrequency component (b) Wave elevation with the eigenfrequency component

Figure 7.40.: Comparing wave elevations with and without the eigenfrequency component.



(a) Moment spectrum, no eigenfrequency component (b) Moment spectrum with the eigenfrequency component

Figure 7.41.: Comparing moment spectra with and without the eigenfrequency component.



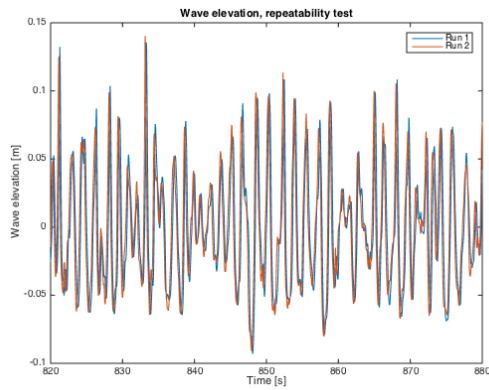
(a) Moment time series, no eigenfrequency component (b) Moment time series with the eigenfrequency component

Figure 7.42.: Comparing moment time series with and without the eigenfrequency component.

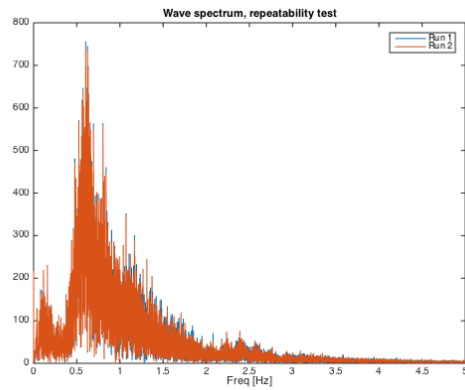
Figure 7.42 shows the effect of dynamic amplification, quantified to approximately a factor of 2.5, in this case (see moment axis values). The effect of dynamic amplification is well documented, and also shown previously in this thesis, in figure 7.31. The results of the special tests gave little certain knowledge, as we were unable to trigger ringing. Thus, based on these tests, on a stochastic level we are not able to draw any firm conclusions to whether the maximum loads are underestimated or overestimated for an adjustable damping level.

7.5. Repeatability

In order to check the repeatability of the measurements, a few irregular sea states were repeated. They were all for $T_p=11.25$ s, with H_s 7.69 m, 8.22 m and 9.04 m. Comparing the repeated runs in general showed little variation in measured H_s , with less than a 1 % discrepancy in all cases. The maximum moment, however, displayed a larger inconsistency, ranging from approximately a 2 % to a 13 % deviation. Since the largest discrepancy occurred in highly non-linear conditions, small differences in wave elevation might cause a wave to break where it didn't in the first realization. This could be a reason for the variation in maximum moments. However, in a stochastic analysis this will probably not have a large effect on the results on average. Examples of repeated test results follow:

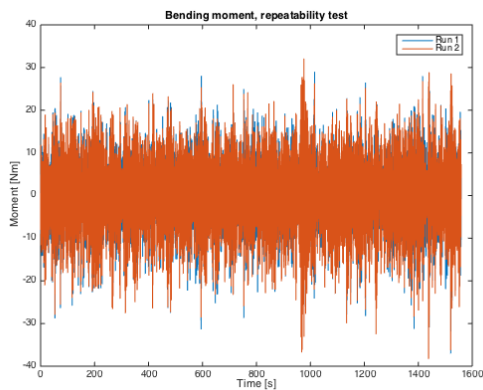


(a) Wave elevation time series cut-out

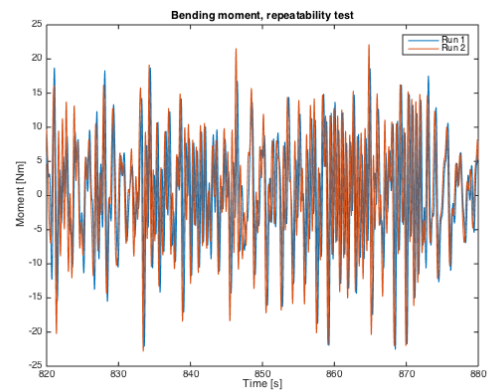


(b) Comparing wave spectra

Figure 7.43.: Comparing wave elevations in a repeated test of $H_s=7.69$ m, $T_p=11.25$ s. The measured H_s were 7.23 m and 7.28 m, corresponding to a difference of 0.7 %.



(a) Bending moment time series



(b) Bending moment time series cut-out

Figure 7.44.: Comparing bending moments in a repeated test of $H_s=7.69$ m, $T_p=11.25$ s. The measured maximum moments were 32.1 Nm and 29.0 Nm, corresponding to a difference of 10.0 %.

7.6. Checking the results of the wave calibration

Utilizing measured wave elevation realizations at wave gauge 7, the resulting significant wave heights and peak periods were compared, giving the seed-averaged values in tables 7.12 and 7.13. The mean percentage values are calculated from

$$H_{s,\%} = \frac{H_{s, \text{wave calibration}} - H_{s, \text{with model}}}{(H_{s, \text{wave calibration}} + H_{s, \text{with model}})/2} \cdot 100 \quad (7.10)$$

$$T_{p,\%} = \frac{T_{p, \text{wave calibration}} - T_{p, \text{with model}}}{(T_{p, \text{wave calibration}} + T_{p, \text{with model}})/2} \cdot 100 \quad (7.11)$$

h=20.9 m	$H_{s,\%}$ [%]				$T_{p,\%}$ [%]			
	6.71 m	7.69 m	8.22 m	9.04 m	6.71 m	7.69 m	8.22 m	9.04 m
11.25 s	-2.65	-2.08	-1.95	-1.41	-0.85	-0.85	-1.56	0.63
15 s	-0.07	-0.04	-0.23	-0.17	0.71	-0.26	0.83	0.79

Table 7.12.: Seed-averaged percentage values for the significant wave height and peak period for all sea states at $h = 20.9$ m.

h=30 m	$H_{s,\%}$ [%]				$T_{p,\%}$ [%]			
	6.71 m	7.69 m	8.22 m	9.04 m	6.71 m	7.69 m	8.22 m	9.04 m
11.25 s	1.37	2.66	2.02	2.35	0.96	0.22	0.51	0.45
15 s	0.97	1.65	1.51	1.68	0.84	-1.75	-0.62	0.04

Table 7.13.: Seed-averaged percentage values for the significant wave height and peak period for all sea states at $h = 30$ m.

Comparing with the repeatability checks (section 7.5), where the variation in H_s for the tested sea states was less than 1 %, the results of tables 7.12 and 7.13 show that the reflection and diffraction effects of the model presence do not introduce significant deviations in the measured wave elevations. All H_s variations were within an interval of a 3 % reduction to a 3 % increase, while the T_p stayed within a 2 % reduction to a 1 % increase interval.

In figure 7.45 a comparison of wave calibration and model testing wave elevations are exemplified for $H_s = 7.69$ m, $T_p = 15$ s at $h = 30$ m.

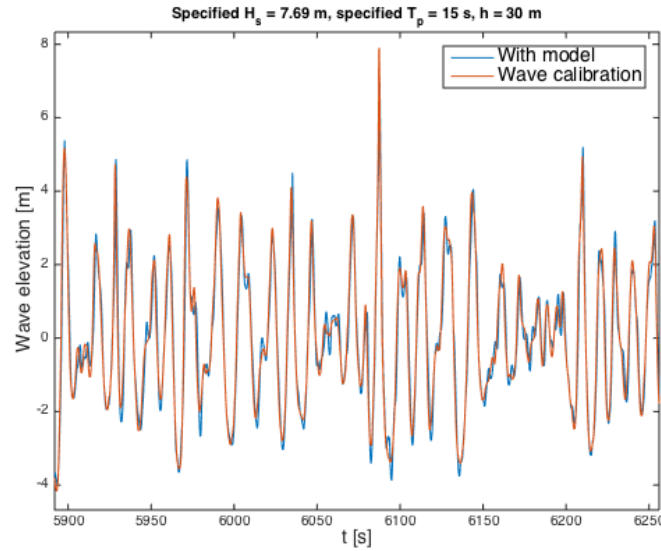


Figure 7.45.: Comparing the measured wave elevations from the model tests and wave calibration runs for a given sea state seed.

7.7. Stochastic analysis

The quantile forces and moments found in tables 7.9 and 7.10 are the 95 % Gumbel quantiles, as [NORSOK, 2007] states that for clearly non-linear response problems, either 90 % or 95 % should be applied, referring to [Kleiven and Haver, 2003].

[Næss and Moan, 2012] describes a procedure of classical extreme value theory, which can be utilized to estimate the experimental extreme wave loads. We assume a set of statistically independent random variables (e.g. wave heights in a sea state) X_1, X_2, \dots, X_n , which are identically distributed with a distribution function F_X . The maximum values, corresponding to the largest waves in a set of sea states, is given by $M_n = \max\{X_1, X_2, \dots, X_n\}$. The distribution of maxima is found to be

$$F_{M_n} = [F_X(x)]^n \quad (7.12)$$

For the derivation of the distribution of maxima, interested readers are referred to [Myrhaug, 2007].

The first assumption of independent random variables is questionable when considering response loads, especially for lightly damped systems where the largest responses tend to be clumped. Large response peaks occur subsequently when

the response is not damped out. However, the assumption is conservative as the estimated extreme values will be larger than the real ones.

The extreme value distribution is studied as the number of samples approaches infinity, $[F_X(x)]^n$ for $n \rightarrow \infty$. As $F_X(x) < 1$, $[F_X(x)]^n \rightarrow 0$ as $n \rightarrow \infty$, so in order for the distribution of maxima to stabilize at some value other than 0, a rescaling is introduced:

$$M_n^* = \frac{M_n - b_n}{a_n} \quad (7.13)$$

where the constants $a_n > 0$ and b_n determine where M_n^* stabilizes for a sufficiently large n .

A generalized extreme value distribution can be established for the maxima:

$$G(x) = \exp\left\{-\left[1 + \gamma\left(\frac{x - \mu}{\sigma}\right)_+^{-1/\gamma}\right]\right\} \quad \text{for } -\infty < \mu < \infty, \sigma > 0, -\infty < \gamma < \infty \quad (7.14)$$

where $[z]_+ = \max(z, 0)$, μ is a location parameter, σ is a scale parameter and γ is a shape parameter. The limiting case as $\gamma \rightarrow 0$ is the Gumbel distribution, given in equation (7.15), which is used in [Det Norske Veritas, 2010] and which will also be applied in this thesis.

$$G(x) = \exp\left\{-\exp\left[-\frac{x - \mu}{\sigma}\right]\right\} \quad \text{for } -\infty < x < \infty \quad (7.15)$$

In MATLAB, the μ and σ values are found from a least-square error linear regression in the Gumbel coordinate system, giving

$$\sigma = \frac{1}{P_1} \quad (7.16)$$

$$\mu = -P_2 \sigma \quad (7.17)$$

where the linear Gumbel fit is expressed by

$$y_{\text{linear Gumbel fit}}(x) = P_1 x + P_2 \quad (7.18)$$

The Gumbel fits in figures B.1 and B.2 (in appendix B) show that the maximum moments follow the linear Gumbel regression for each seed in all the sea states. This might illustrate an important consequence of the frequent first-mode excitation in the experiments: that it linearizes the response. When the structure is constantly excited at the first mode, the relative effect of the 3rd and 4th-order load

contributions might diminish. The largest response moments were expected to be the result of non-linear phenomena such as ringing, causing rightward deviations off the regression lines. This would imply larger moments than those achieved from linear response. Such a bend-off trend is illustrated in [Suja-Thauvin et al., 2014]. The tendency cannot be found in any of the Gumbel fits, neither for the force nor moment data. This means that either ringing occurrences are rare or that the first-mode motion creates such large loads that ringing becomes insignificant.

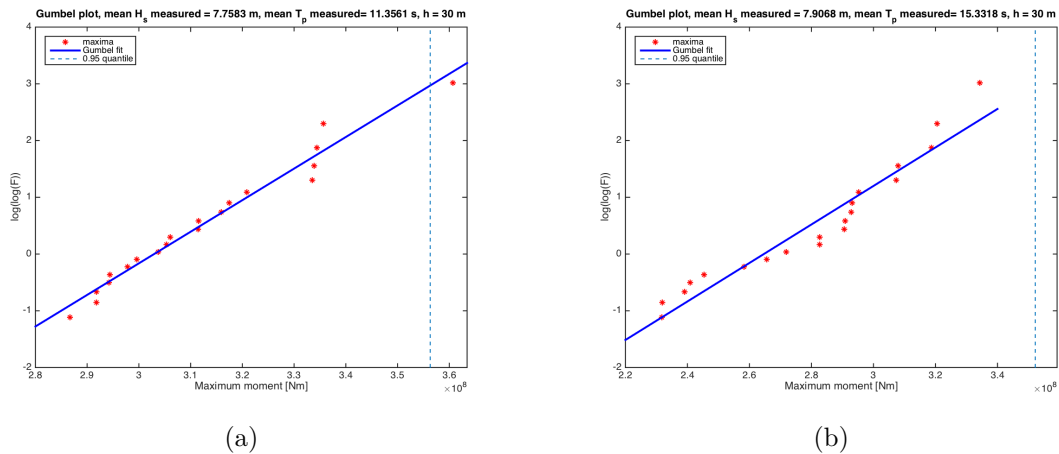


Figure 7.46.: Linear Gumbel fits of the maximum moments for each seed, exemplified for two different sea states at $h = 30$ m.

The Gumbel regression plots give a relation between maximum measured moments and their respective probabilities of occurrence. Whether a measured moment point is above or below the linear curve should be random without non-linearities present. Non-linear effects creating larger moment loads would create a rightward bending trend because the larger loads develop for the same probability of occurrence.

The cumulative distribution for the measured moments (of which the Gumbel plots are based) of the sea state of figure 7.46b is found in figure 7.47.

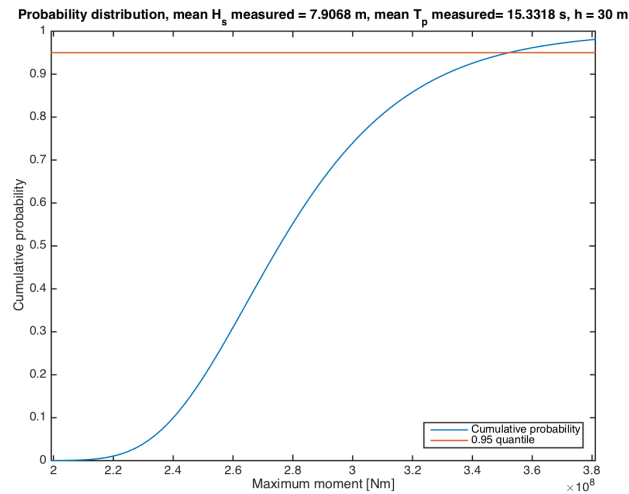


Figure 7.47.: The cumulative distribution for the measured moments.

The largest measured response moments for each seed of the roughest and least rough sea states were examined. It turned out that in all cases first-mode oscillations were always present after the largest moment incident. For the roughest sea state, the burst-like transient ringing pattern was evident in most events. This could explain why no non-linear bend-off trend is observed in the Gumbel fits, as all the largest responses may involve non-linear phenomena. However, this is questionable, as the excessive first-mode motion made it difficult to separate linear response from non-linear ringing phenomena. Usually, only the large waves excite dynamic amplifications in a system, and otherwise the responses are quasi-static. In these experiments, however, the system can almost never be considered quasi-static.

In most cases, the $n=20$ seeds run in the experiments seem to be sufficient for a stabilization in accordance with the renormalized distribution of maxima (equation (7.13)). However, in one case, shown in figure 7.48b the 5 % and 95 % maxima quantiles seem not to have stabilized. This means that running 20 seeds might not be enough to be certain of the moment maxima order of magnitude. In figure 7.48b, the two last runs are the ones that cause the discrepancy, so they might as well have arisen from faulty measurements and be deemed non-representative, as they are well outside the scatter range of the first 18 measurements.

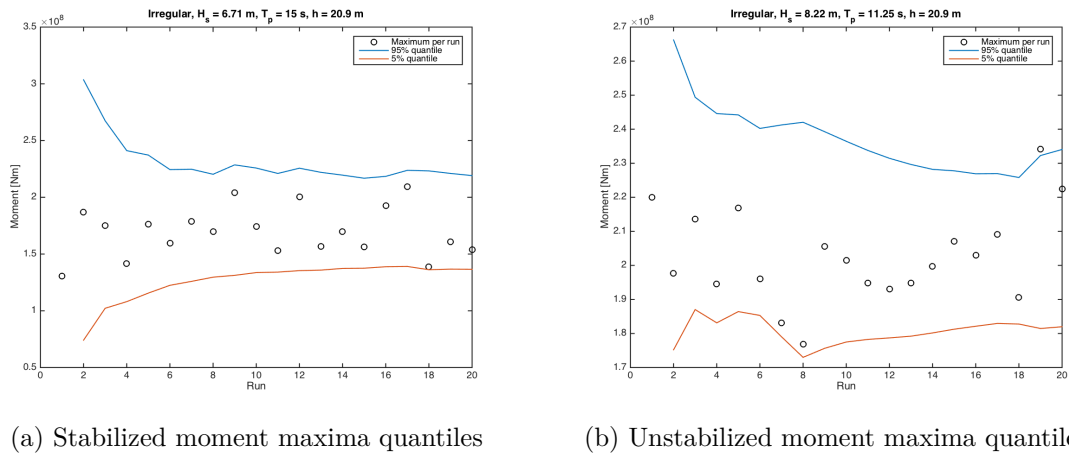
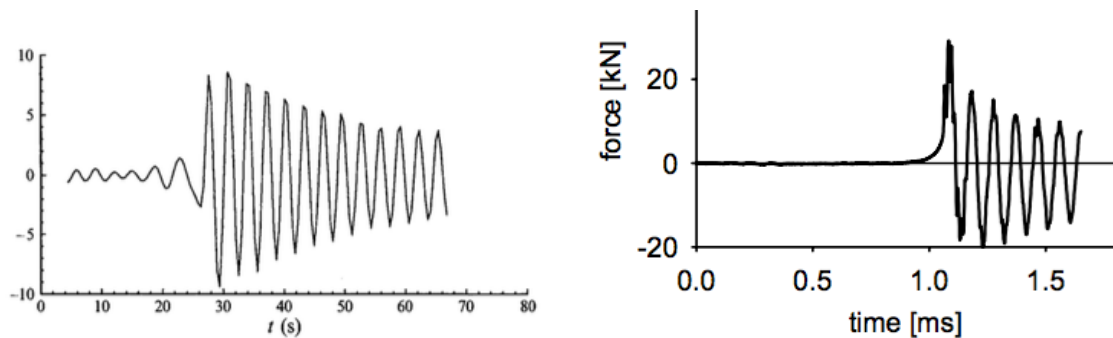


Figure 7.48.: Comparing the stabilization of moment maxima quantiles.

7.8. Response from breaking wave events

In figure 7.49, an idealized ringing event induced by higher-order wave components and a slamming event, are shown. The quasi-static part of the slamming force has been filtered out, so only the high-frequency response load remains. The development of the slamming load is characterized by an abrupt increase in force, and the magnitude of the excitation impulse force is often significantly larger than the maximum of the second force cycle. The evolution of the ringing event is smoother than slamming, the first response cycle maximum not as abrupt and not as large relative to the other cycle maxima. Otherwise, the progression of the responses are fairly similar, decaying with the eigenfrequency at a certain damping level.



(a) Idealized ringing event, illustrated by a time series of the tension in TLP wires. (b) Idealized slamming event where the quasi-static load contribution has been filtered out.

Figure 7.49.: Idealized ringing [Faltinsen et al., 1995] and slamming [Wienke et al., 2005] events. See also figures 4.10 and 3.11.

Since ringing is triggered by first-mode excitation combined with an extreme wave, the frequent first-mode motion in the experiments creates a difficulty in distinguishing between the two phenomena, as the first mode is also triggered when a global slamming load occurs. This means that both response patterns appear similar in the measured response moment time series. Thus, separating the two is an ad hoc exercise that could be performed by setting up automatized criteria with respect to load duration and maxima magnitude ratios. However, this would be an inaccurate exercise involving a lot of uncertainty as to whether the specific events are placed in the correct category.

The characterization problem could have been evaded with functioning force gauges, but as discussed in section 5.9.2, the gauge output was unstable and unreliable.

Even though the responses are similar the loading mechanisms of a breaking wave slamming event and a non-linear wave ringing excitation event involve a lot of differences. In the former case, a large degree of separation with run-up and spray occurs at impact and the flow does not smoothly adjoin at the back of the pile. The latter event is characterized by smoother fluid motion and stream coalescence behind the cylinder. Usually, due to the short-duration load, a slam generates a smaller response than an excited structure at ringing. In such an event, the slamming impulse is more of a local phenomenon, creating large local pressures in the impacted area. The importance of the impact duration will be discussed in more detail later in this section.

As discussed in section 4.2, the global slamming loads on an OWT are charac-

terized as ALS events, less important because the impact from ships are deemed a graver concern [Det Norske Veritas, 2014]. The result of not automatically being able to distinguish between slamming and ringing from the experimental data obtained, is that a stochastic analysis of slamming cannot be performed, so the categorization in the DNV standard can only be discussed from a deterministic point of view.

The largest maximum moments of all the different sea state seeds at both water depths (see the Gumbel fits in appendix B) were examined in order to study what phenomena gave the largest response loads. Of the 16 total number of sea states, 14 video-taped events were investigated (for $T_p = 11.25$ s and $h = 20.9$ m, significant wave heights 6.71 m and 7.69 m were run before the camera was installed). The videos showed that all the largest moments, except one, arose from events where a breaking wave impacted the structure. The non-breaking wave occurred for one of the least rough sea states, $H_s = 6.71$ m, $T_p = 15$ s, $h = 30$ m. Even though the wave was not breaking, the impact showed clear resemblance of an impulse load, giving a large run-up with spray and an uneven flow resulting on the pile backside.

As all the breaking wave events generating the largest responses showed the same general characteristics in impact and response, only one of the events is shown in this section. The selected event corresponds to the largest measured moment ($M_y = 4.4 \cdot 10^8$ Nm, full scale) for the sea state specified by $H_s = 9.04$ m, $T_p = 11.25$ s, $h = 30$ m. The pictures in figures 7.50 to 7.55 show the impact of the breaker, creating a large run-up with spraying water. The breaker wall separates on impact and does not immediately adjoin behind the cylinder. Figure 7.56 shows the measured wave elevation, shear force and the response moment time histories, illustrating the structure's decay oscillations with the eigenperiod. A considerable dynamic excitation is observed, both in the video and in figure 7.56.

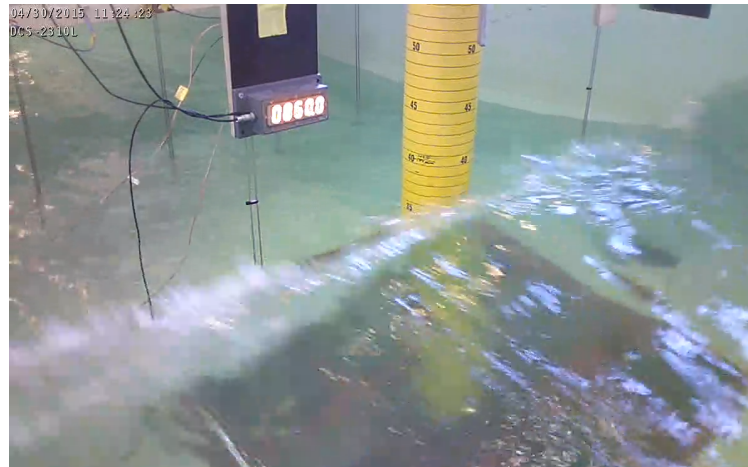


Figure 7.50.: Incoming breaking wave wall

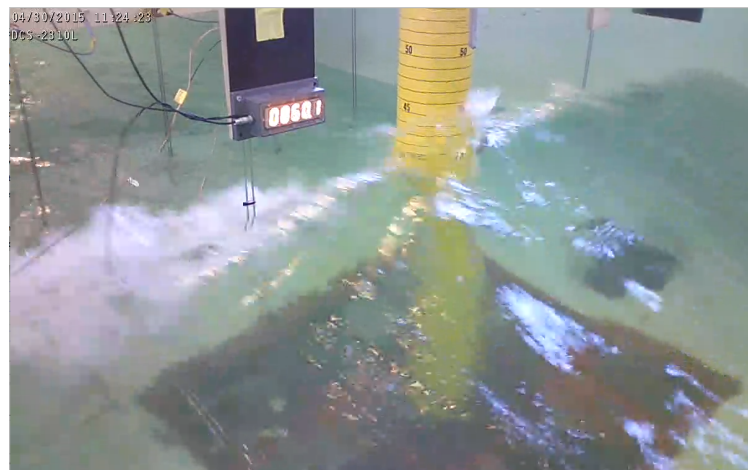


Figure 7.51.: Wave breaker impact

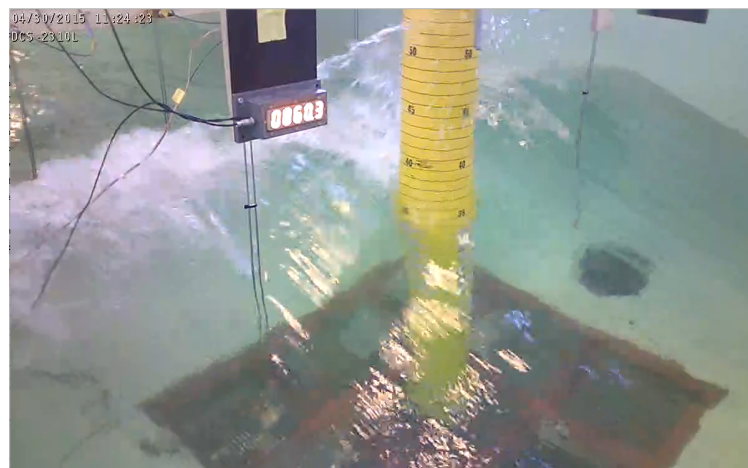


Figure 7.52.: Water run-up and spray is observed

The same event can be viewed from behind the structure:

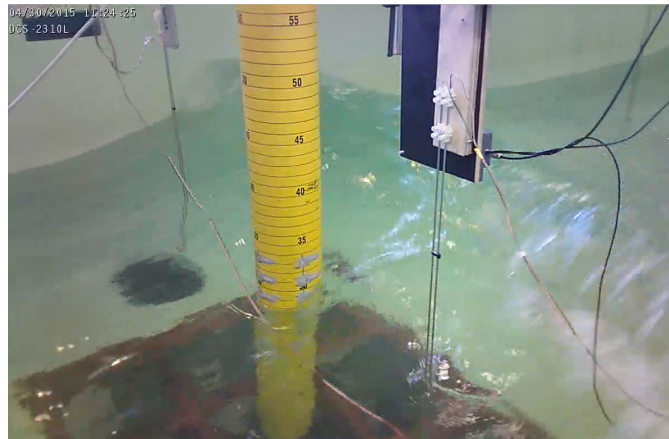


Figure 7.53.: Incoming breaking wave wall, viewed from behind the structure

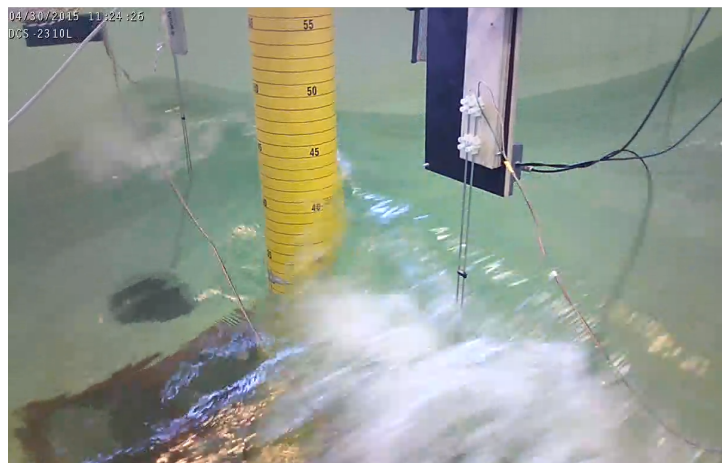


Figure 7.54.: Wave breaker impact, viewed from behind the structure

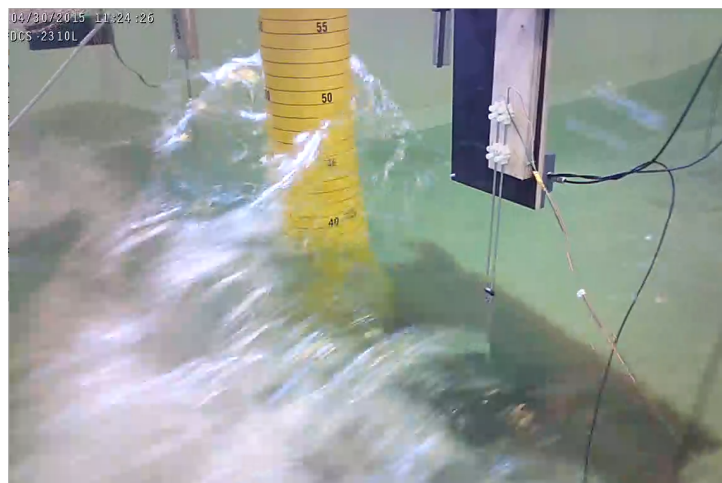


Figure 7.55.: Water run-up and spray is observed from behind the structure

During the impact from a breaking wave, wave-structure interaction is relevant in two time scales. One time scale is related to the period of the incident wave and its non-linear components. The other is related to the duration of the impulse. When the duration is comparable to the eigenperiod the hydrodynamic and structural problems are coupled, i.e. hydroelastic effects can result from structural vibrations. When $t_d \ll T_n$, the magnitude of the impulse is important as the dynamic amplification is negligible.

The measurements of the breaking wave event are converted to full scale values in figure 7.56. The figure shows an event of which the excitation mechanism is difficult to characterize as neither a large excitation force or evidence of a secondary load cycle are observed.

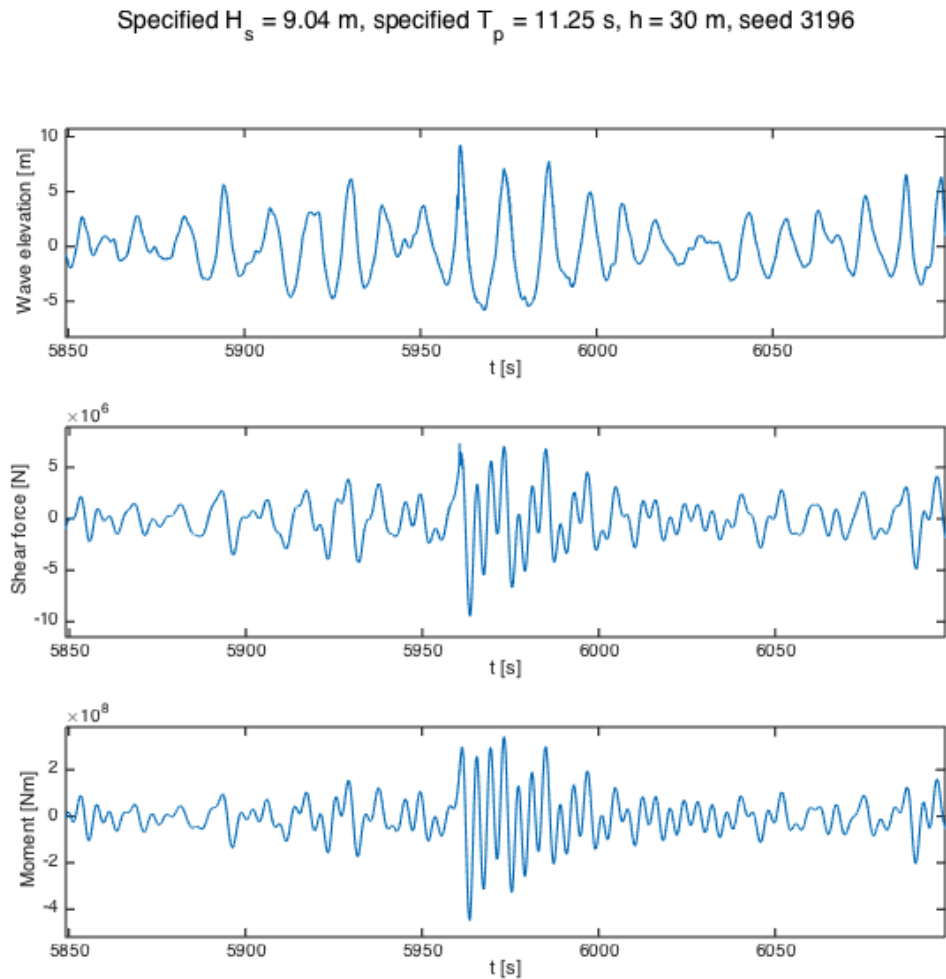


Figure 7.56.: Full scale wave elevation and response moment of the slamming event.

In figure 7.57, a zoom-in on the event is supplied. The shear force measurements show a small peak around $t=5960.5$ s, which is in slight anticipation of the wave peak, since the wave gauge is placed along the pile centerline. The small shear force peak is induced by the slamming impulse, but due to the 200-Hz sampling frequency it was not properly captured. For an impact duration in the order of only several milliseconds, an f_s of a few kHz is required to acquire a sufficient sampling. Following the miniature peak are high-frequency oscillations lasting about 1.5 s. It is difficult to determine their origin, as it is evident from the coarse resulting curve of zooming in further, that the sampling frequency is too low to capture the effect. They are probably due to impulse excitation of higher modes, which dampen rapidly.

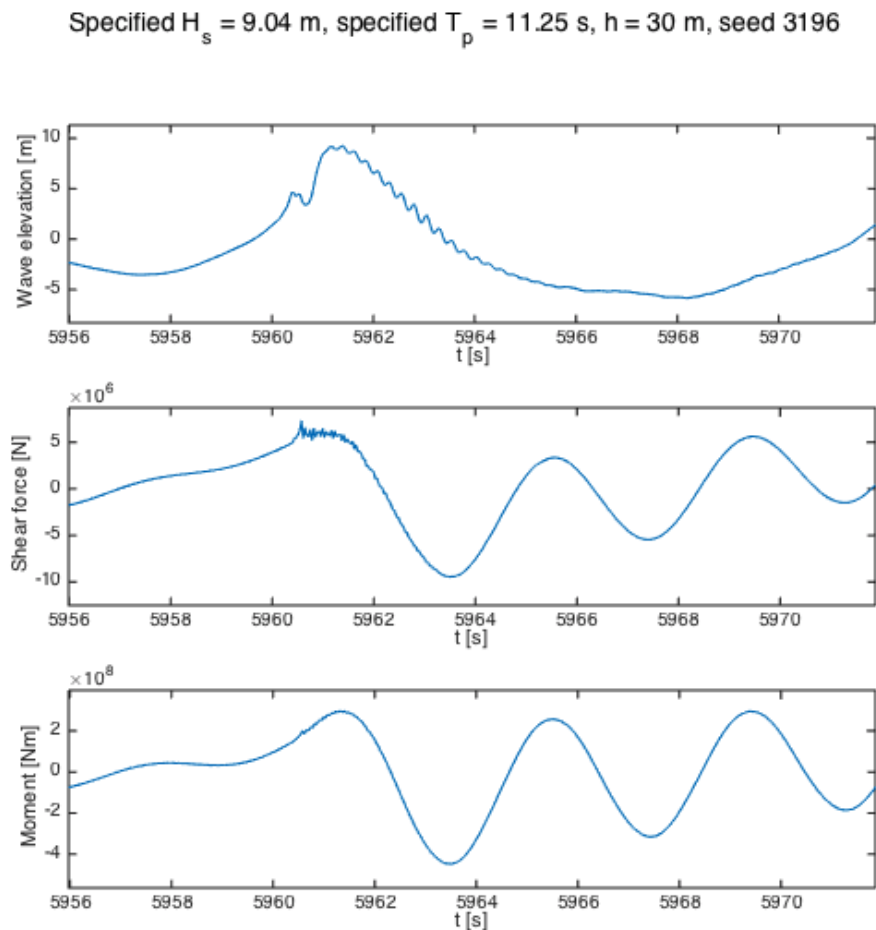


Figure 7.57.: Full scale wave elevation and response moment of the slamming event.

The high-frequency components of the wave elevation after impact have periods of approximately 0.25 s in full scale, corresponding to approximately 28 Hz in model scale. This is the eigenfrequency of the wave gauge, found to be approximately 29.5 Hz for $h=20.9$ m in figure 7.26a.

With the tools and measurements available, that being an insufficient sampling frequency and a flexible pile, the load shape and duration of the slam cannot be determined accurately. Thus, equation (4.15) will be used to find the impact duration. It is based on the assumption of a plunging breaker with a vertical wave front, breaking just before pile impact. In order to find the duration, the wave celerity is needed. The large breaking wave is stable enough to be recognized for the measured time series at both wave gauges 5 and 7, as seen in figure 7.58. The wave peak passes gauge 5 at 5955.0 s and gauge 7 at 5961.4 s (full scale), giving a model-scale difference of 0.92 s. The distance between the two gauges is approximately 2.05 m, so assuming a constant wave celerity gives $C = 2.2$ m/s and a rise-time $t_d = 0.013$ s. With the eigenperiod of 0.57 s, the t_d/T_1 ratio is found to be 0.023. The validity of the vertical wave front assumption is debatable. Nonetheless, the 2.3 % t_d/T_n ratio is an indication of the short duration, and even if the ratio is inaccurate by a factor of 4 or 5, the duration would still be characterized as very short, well outside the duration ranges giving significant dynamic amplification.

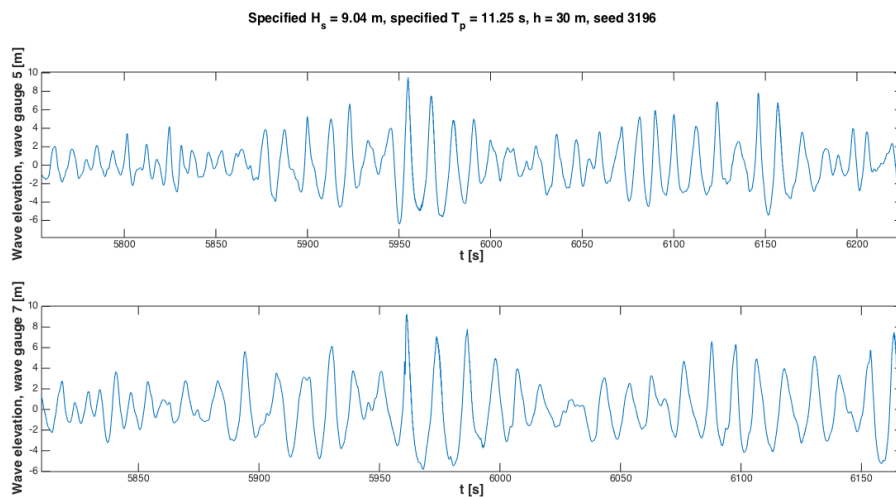


Figure 7.58.: Full scale slamming event wave elevations at wave gauges 5 and 7.

In the analysis of the effect of an impulse load on a structure, [Larsen, 2012] names two phases: Phase 1 lasts the duration of the impact force, whilst in phase

2 the structure is vibrating freely. A distinction is often made related to whether the maximum response occurs within the duration of impact (phase 1) or in the free vibration phase (phase 2). A rough characterization is made, approximately specifying a long impulse as $t_d/T_n > 0.5$ and a short impulse as $t_d/T_n < 0.2$. The breaking wave impact of figure 7.56 is well within the short impulse category, implying that the maximum response will occur in phase 2.

In figure 7.59, [Chopra, 2012] illustrates when the first (and largest) response peak occurs for a rectangular impulse shape as a function of t_d/T_n .

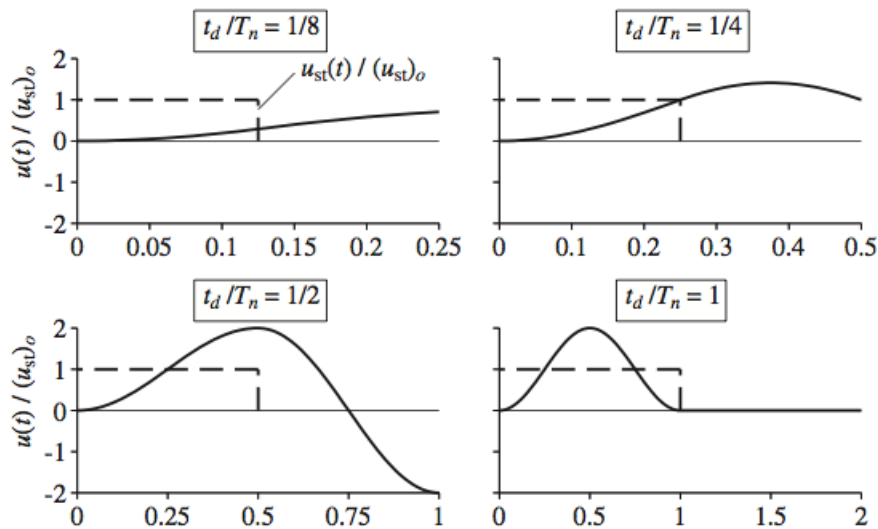


Figure 7.59.: Dynamic response of an undamped single-degree-of-freedom system from a rectangular impulse [Chopra, 2012]. The dashed lines correspond to the static solution $u_{st}(t)$.

For a short impulse duration the shape of the loading is seen to be irrelevant in figure 7.60, as the dynamic response is equal for both the rectangular, half-sine cycle and triangular impulse shapes. In addition, the DAF is negligible within the short time span. No local peak will occur in the forced vibration phase and the response can be assumed to build up from zero at the beginning of phase 2 (as the contribution in phase 1 is so small) to a response peak in the free vibration phase. The DAF will be proportional to the area under the impulse curve.

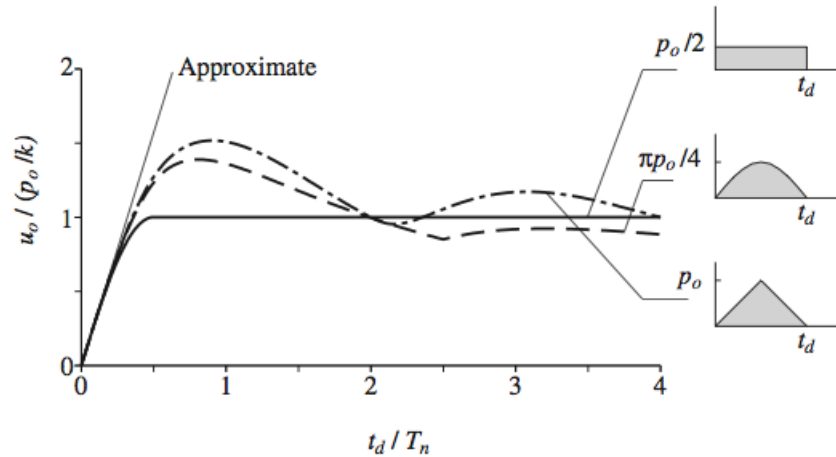


Figure 7.60.: Shock spectra from [Chopra, 2012] for three different impulse shapes of equal area as a function of the ratio between the impulse duration and the first natural period of the system.

[Larsen, 2012] describes a simplified procedure for the calculation of the response from a short impulse load. A single degree-of-freedom system initially at rest is impacted by a force $P(t)$. Resisting forces from damping and stiffness will gradually increase from zero, but in the beginning the motion is only resisted by inertial effects, thus giving the acceleration

$$\ddot{u}(t) = \frac{P(t)}{m} = \frac{I}{m} \quad (7.19)$$

where m is the mass of the system. This implies that the damping is negligible when determining the maximum response of a slamming event. For a lightly damped system (as in the experiments) the damping is only relevant after several response periods [Larsen, 2012].

The velocity of the structure at the end of the impulse duration can be found by integration:

$$\dot{u}(t_d) = \int_0^{t_d} \frac{P(t)}{m} dt \quad (7.20)$$

The system displacement at $t = t_d$ is, as mentioned, approximately equal to zero and proportional to $\dot{u}_d t_d$. A new time variable is introduced, starting at the end of the impulse, $\bar{t} = t - t_d$. When the structure is no longer affected by the load it

will oscillate freely, resulting in a structural displacement of:

$$u(\bar{t}) = \frac{\dot{u}_d}{\omega_n} \sin \omega_n \bar{t} = \frac{I}{m\omega_n} \sin \omega_n \bar{t} \quad (7.21)$$

where

$$I = \int_0^{t_d} P(t) dt \quad (7.22)$$

$P(t)$ is the impulse function, corresponding to a specific shape in figure 7.60.

The maximum response is found by assuming free oscillations, giving

$$u_{max} = \frac{I}{m\omega_n} = \frac{I}{\sqrt{km}} \quad (7.23)$$

The example is derived for a translational system, but the same logic applies for a rotational one. For $\frac{t_d}{T_n} < \frac{1}{4}$ the described method supplies almost exact solutions. The results will be inexact for $\frac{1}{4} < \frac{t_d}{T_n} < \frac{1}{2}$ and meaningless for $\frac{t_d}{T_n} > \frac{1}{2}$ since the maximum response will manifest in phase 1 [Chopra, 2012].

For a short-duration impulse the magnitude of the impulse is decisive as implied by equation (7.23). As discussed, the duration of the load of the analyzed breaking wave event can be established to some degree of accuracy. However, without the means to determine the magnitude and shape of the impulse load, i.e. without a sufficiently high sampling frequency and a more rigid pile foundation, the maximum response cannot be determined. Thus, the excitation mechanism cannot at present be established based on this procedure.

In order to determine important wave frequencies in the wave elevation around the breaking wave event, a fast Fourier transform wavelet analysis was performed. A sliding time window was used, covering one peak period in each frame step. However, no significant third or fourth-order wave elevation contributions were observed. Nonetheless, non-linear wave-structure interaction could still be the reason for a steep wave-induced ringing excitation, so the approach does not disprove anything. If such components had been found, it could substantiate a hypothesis of a non-linear component-induced ringing. However, firm conclusions could not have been drawn. In figure 7.61 the wavelet analysis is exemplified for one of the frames.

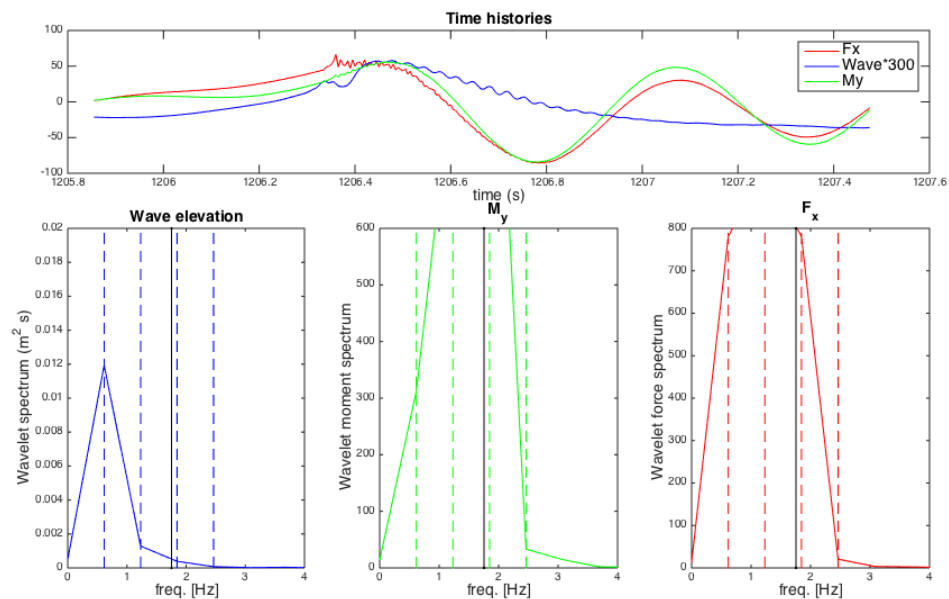


Figure 7.61.: Wavelet analysis [Lugni, 2015] around the breaker event of figure 7.56.

Even if the excitation mechanisms are not unequivocally determined, it is surprising that the largest measured moment response loads for all sea states arise from the impact of breaking waves. Two options must be considered; either the large breaking waves are commonplace in a shallow-water region such as Dogger Bank, or the breaking waves occurring in the experiments are unrealistically large or frequent.

In the wave tank, the large waves of the rough 9.04-m H_s sea states break excessively, reducing the effective significant wave heights, as rendered in tables 7.7 and 7.8. Many of these waves were observed to propagate almost the entire length of the tank before breaking at impact with the structure. As specified in [Engebretsen, 2012], shoaling and refraction effects from a rapid decrease in water depth, ultimately causing some of the deep water waves to break, often develop several tens of kilometers away from the wind park regions of Dogger Bank. There are large differences in the relative distances comparing the tank and Dogger Bank. Thus, it seems plausible that the frequency and amplitudes of the largest breaking waves generated in the tank are exaggerated compared with realistic occurrences, as considerable dissipation of energy takes place when a wave breaks.

However, if the maximum response loads are in fact driven by non-linear wave

component-induced ringing, then a certain lower limit damping level for idling turbines could be set to reduce the maximum responses. This would also reduce the frequent first-mode motion observed in the experiments, even though this phenomenon is not a result of realistic excitation in full scale. As mentioned, for impulse load-induced responses the largest maxima are independent of the level of damping.

7.9. Results from the numerical program

Numerical response moments for two force models are exemplified in figure 7.62. The illustration shows the same breaking-wave event as in figure 7.56, but with model-scale values. The numerical response moments are established through

$$M_{response} = \theta \cdot k_{\theta} \quad (7.24)$$

as given in [Langen and Sigbjörnsson, 1979]. The angular response θ is calculated in PileResponse.m, solving the equation of motion (6.1).

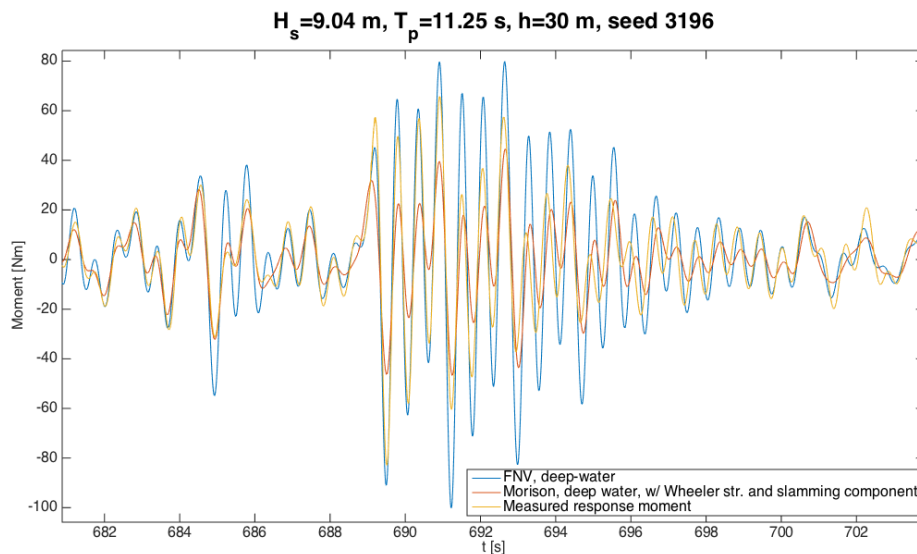


Figure 7.62.: Realizations of response moments are exemplified, comparing the measured moment with the deep-water FNV and the deep-water Morison with Wheeler stretching and slamming ($H_s=9.04$ m, $T_p=11.25$ s, $h=30$ m).

The FNV model gives a conservative result whilst the Morison model underestimates the response in this example. The inertia dominance for the sea state and at the event are illustrated in figures 7.63 and 7.64, respectively.

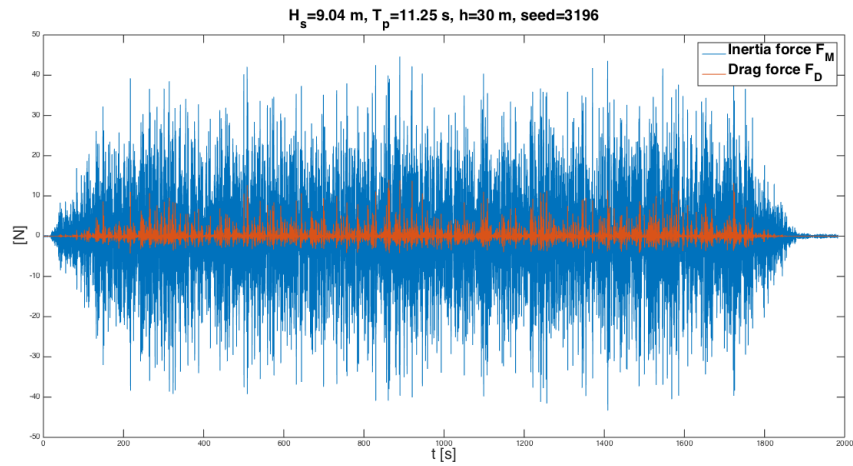


Figure 7.63.: Inertia dominance for the entire sea state seed

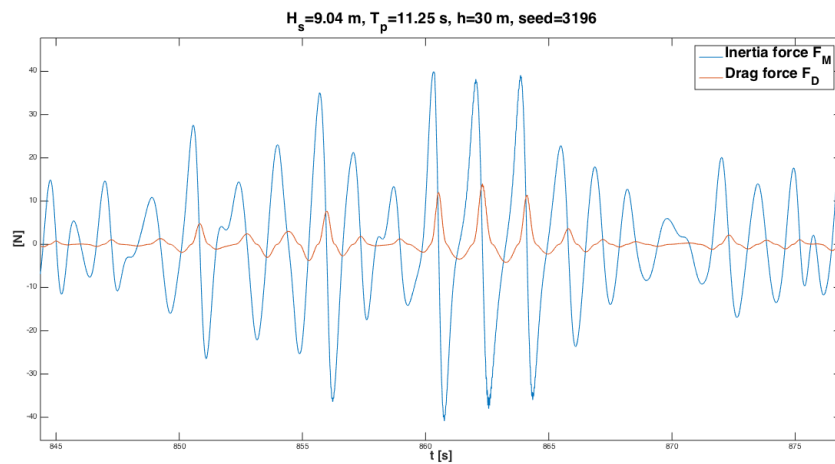


Figure 7.64.: Inertia dominance, with focus on the breaking wave event

Figure 7.65 to some extent illustrates the effect of the self-excitation. The example is from an interval with low response moments, and it shows that in this region the models underestimate the response. This could be caused by the self-excitation mechanism, as the numerical force models use the calibrated wave realizations, i.e. without the radiated waves generated by the structure.

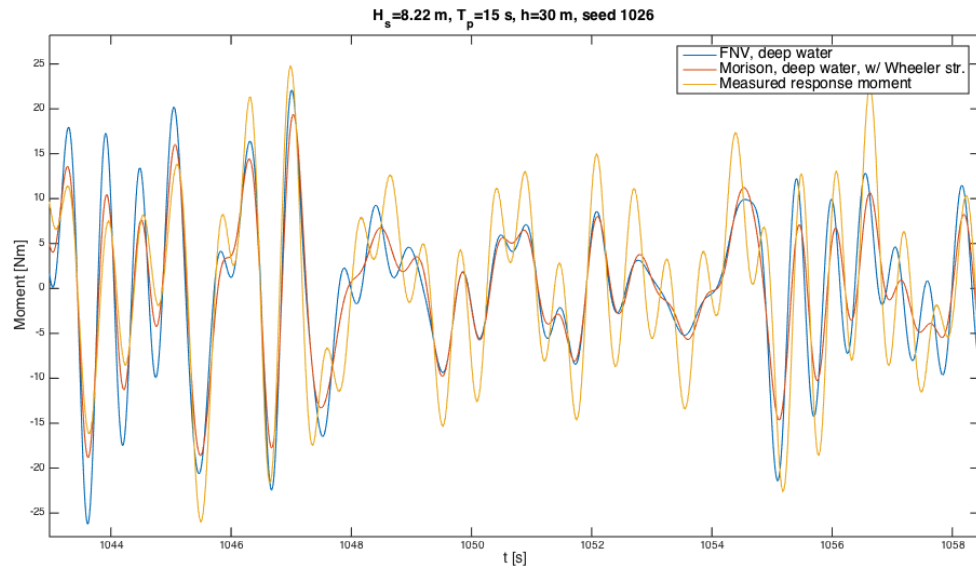


Figure 7.65.: Illustrating the effect of self-excitation

All the maximum moments from each seed of the irregular sea states were plotted with the linear Gumbel regression line. The plots are all attached in appendix C. The general trend is that the deep-water FNV model causes an overestimation of the maximum response moments by approximately 50 % and the finite-depth FNV gives an even larger overestimation of around 60-70 %. Very roughly, the Morison models underestimate the maximum response moments by 25 % for the largest sea states. For the lower sea states of $H_s=6.71$ m, on the other hand, the Morison models seem to give a marginally conservative response. These tendencies are exemplified for one rough and one less rough sea state in figures 7.66 and 7.67.

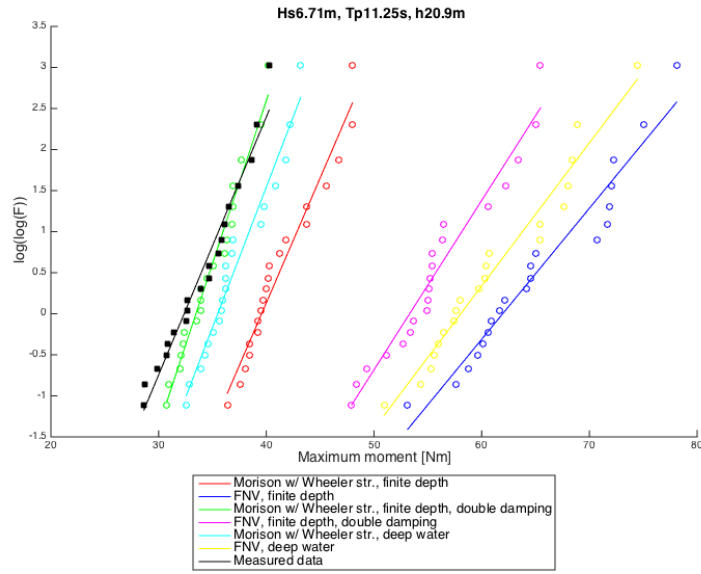


Figure 7.66.: Gumbel plots comparing the response moments from the numerical program with measured data ($H_s=6.71$ m, $T_p=11.25$ s, $h=20.9$ m).

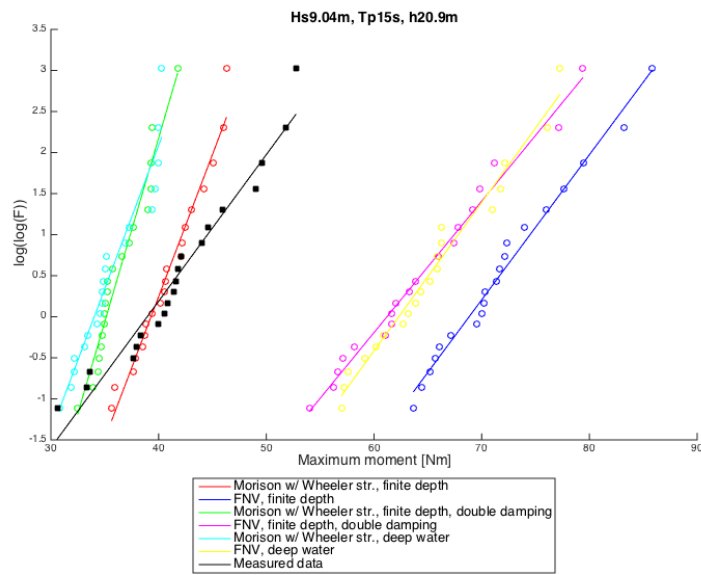


Figure 7.67.: Gumbel plots comparing the response moments from the numerical program with the measured data ($H_s=9.04$ m, $T_p=11.25$ s, $h=30$ m).

For the most severe sea states, the FNV was expected to capture the slope of the Gumbel fit with higher precision than Morison, as the waves are more non-linear. This is illustrated in figure 7.67, where the slope of the FNV Gumbel fits are approximately equal to the measured value slope. The corresponding Morison slopes are too high.

In the industry, these graphs are typically used when dimensioning structures, using the 90 % or 95 % quantiles for clearly non-linear responses, as mentioned previously. It is critical that the numerical model generates realistic loads, in order to correctly evaluate the design load.

To test the hypothesis that the abundant first-mode motion in the experiments linearizes the response, numerical simulations with increased damping ratios were performed. The aim was to test whether the largest simulated moments would change the configuration of the linear trend, i.e. cause a rightward bend-off induced by non-linear effects, as discussed in section 7.7. However, no such trends were observed; the response maxima were still following the linear Gumbel regression. The magenta plots in figures 7.66 and 7.67 are the finite-depth FNV simulations using twice the damping level. A double damping curve using Morison is also plotted as a comparison, since it is not capable of simulating ringing response from 3rd and 4th-order wave components.

Since appendix D illustrates that the implementation of the FNV equations are correct according to [Newman, 1996], the question remains whether the measured wave input is consistent and linear. In figure 7.68, a 0.8 factor was applied on the high cut-off frequency (given in section 6.2) of the finite-depth FNV input wave elevation. The plot shows that the finite-depth FNV response is sensitive to the specified cut-off frequency. However, arranging the cut-offs to fit the measured values without any realistic foundation wouldn't serve any purpose.

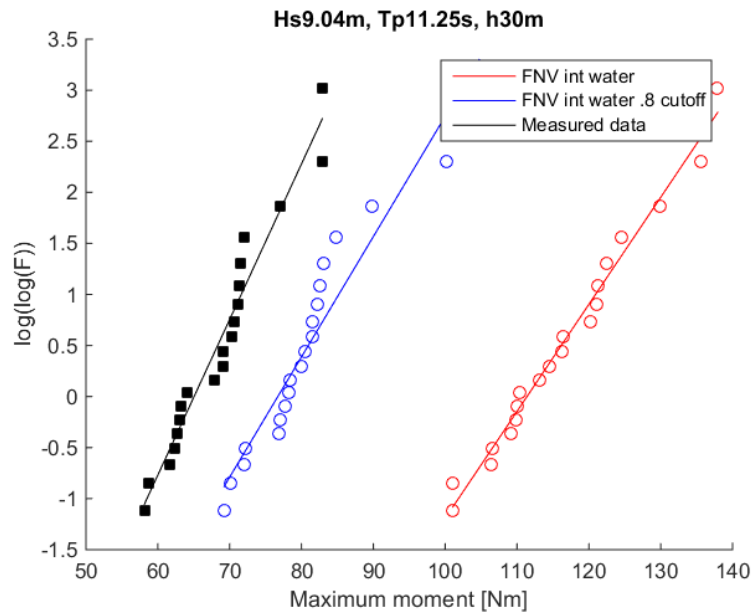


Figure 7.68.: Gumbel plots for the finite-depth version of the FNV, with and without a 0.8 factor applied on the cut-off frequencies.

On the capacity side, structural utilization factors could have been established based on the measured moments and known turbine designs and material compositions. Ringing induced by non-linear components is considered as an amplification of the linear response, usually estimated as a 30-50 % addition, in design. However, since the FNV simulations show such a large discrepancy from measurements for both rough and less rough sea states, the additional load and structural response from non-linearities cannot be determined. If the Morison, FNV and measured values had shown a large degree of compliance for a smaller sea state, and the FNV and measured values were similar, but much larger than the Morison responses for a larger sea state, the amplification from non-linearities could have been discussed. The focus in this thesis has been on the loads, not the structural capacity.

In figure 7.69 the measured shear force and the numerical Morison excitation force with the slamming component, are compared. The high-frequency oscillations of the measured shear force are not present in the numerical excitation force. The numerical impact duration is seen to be considerably shorter relative to the total load cycle duration, than in figure 4.6. The wave steepness-dependent α factor is set to $\alpha = 0.3$ in [Nestegård et al., 2004]. However, as the same source

specifies $\alpha = 1$ for a breaking wave, that value is used in the present work, thus resulting in a much shorter impact. As discussed earlier, the measured impact excitation force is not properly captured, so the magnitudes cannot be compared.

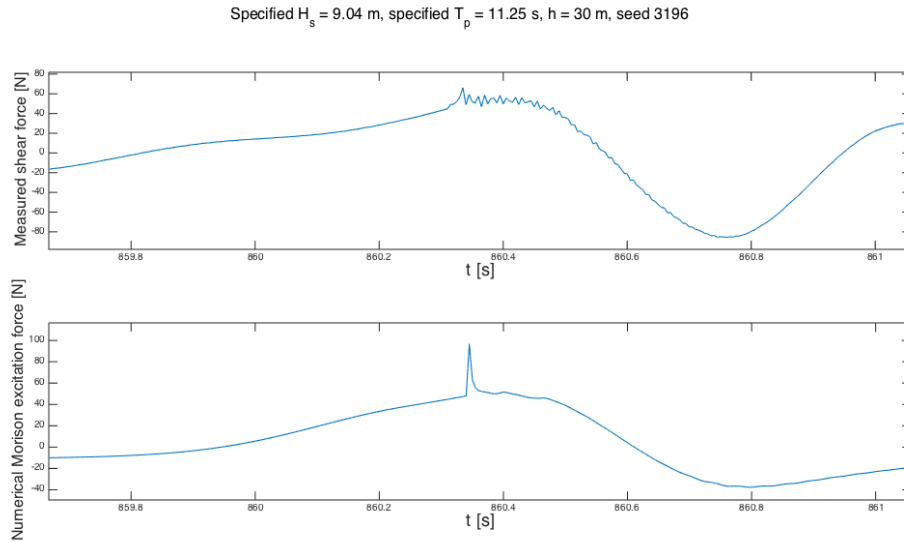


Figure 7.69.: Comparing the measured shear force with the numerical Morison excitation force for the same event as in figure 7.57.

The same breaking wave event is shown in figures 7.56, 7.62 and 7.69. Since the discrepancy in FNV and Morison responses are so large, as seen in the response pattern in figure 7.62, the developed models do not shed light on the excitation mechanism of the breaking wave event. For both models, the pile oscillates at the eigenperiod. The Morison model with slamming greatly underestimates the response after impact, whilst the FNV causes an overestimation, except for the first maximum, where the measured response is larger than for both of the models.

8 | Conclusions

The reflected waves in the decay tests caused a self-excitation of the structure, resulting in response moment oscillations with magnitudes around 5 % of the applied moment. If the excessive first-mode motion does not change the frequency of the non-linear phenomena giving the largest response maxima, then the self-excitation has little significance on the conclusions regarding the stochastic ULS maxima.

The effect of the frequent structural excitation is uncertain. The attempt to trigger ringing artificially was unsuccessful, as discussed in section 7.4.1. Thus, firm conclusions to whether the measured maximum responses are realistic cannot be drawn. The first-mode motion causes a phase problem. When the pile response and the incoming wave are in phase, the response is enhanced, whilst it is reduced when they are in counter-phase. Statistically, the artificial response reinforcement should occur for half of the incoming waves.

The largest measured response moments occurred for breaking wave events. Whether the excitation mechanism was that of ringing induced by non-linear wave components or from the impulse load of the breakers, is unclear. In order to distinguish between the two, the seeds giving the largest responses should be run with a higher measurement sampling frequency and a much stiffer base rotational spring. In that way, the magnitude, shape and duration of the excitation impulse force can be captured, in order to determine whether the response corresponds to that of a slamming-type impact.

The physics of the selected sea states are drawn into question because of the large amounts of breaking. The breakers in question often propagate the length of the flume before breaking at structural impact. In the real Dogger Bank region, the relative distance between breaking zones and the wind parks are often much larger than in the tank, so many of the waves are prone to dissipate much energy before impacting a turbine. In addition, the metocean report for Creyke Beck B locations probably do not accurately take shallow water effects into account, as pointed out by [Engebretsen, 2012]. The largest measured H_s value at $h=20.9$ m for $T_p=11.25$ s is $H_s=7.95$ m, which is lower than the 50-year value of 8.22 m, shown in figure 5.23.

[Det Norske Veritas, 2014] specifies that the most unfavorable water level should be used in the ULS design analysis of an offshore wind turbine. The greatest water depth generally resulted in the largest response loads (see figures 7.29 and

7.30). This implies that the effect of the longer moment arm exceeded that of the shallower depth-increased wave non-linearity. The relative difference in maximum loads were smaller for $T_p=15$ s than for $T_p=11.25$ s, indicating that the increased non-linearity of a longer wave had an amplifying effect on the maximum loads. However, the 30-m depth does not correspond to any realistic quantile in the distribution of the annual maximum water depth. If using the h_{low} and h_{high} values discarded in section 5.6.1.1, due to wave breaking considerations, the conclusion might be reversed. It can be discussed whether the larger degree of breaking at the lower water depth has an impact on measured maxima given in tables 7.9 and 7.10, but using the data for the mean of the largest maxima as a general trend should be reasonable.

There are many uncertainties in the stochastic analyses. They are related to the effect of the excessive first-mode motion on the maximum loads, the degree of realism of the generated sea states and the excitation mechanism for the largest responses. Thus, it is difficult to determine the importance of breaking compared to non-breaking steep waves, in design. At this level of uncertainty it would have been too audacious to draw conclusions contrary to the specifications in the industry standards.

The numerical FNV model gave the largest responses, the intermediate-depth version (inconsistent with FNV assumptions) more so than the one for deep water. It was expected that the finite-depth extension generates greater loads as the kinematics on shallower water are stretched out horizontally. In the asymptotic shallow-water solution there is no contribution in the z -direction, as shown in figure 3.7. As the FNV forces take the horizontal kinematics into account, the resulting loads should be higher. A reason for the large responses using the FNV model compared with the measured values could be non-linearities in the input wave elevations.

The slamming model should be tested for an impulse-type event where the structure is not already excited at the first-mode. With the excessively excited experimental structure, no such measured slamming event could be found. In further work, this could be done as validation. In addition, with a higher sampling frequency and stiffer rotational spring, the impulse load can be measured and compared with the resulting numerical impulse. It should be noted that the slamming model is deemed valid for spilling and surging breakers [Det Norske Veritas, 2014], whereas the breaking wave events that generated the largest responses in the experiments were clearly plunging. This must be considered as there is considerable

scatter in measurements of plunging impulse loads, due to curling factors, impact areas and points of breaking.

9 | Further Work

Recommendations for further work:

- Only one damping level was experimentally tested. In order to determine whether the damping in the numerical program is adjustable, tests with more damping levels should be performed as reference.
- In order to solve the combined problem of excessive first-mode motion, several steps could have been taken. One could have increased the damping and kept the realistic first mode eigenperiods constant, by introducing a larger moment of inertia, i.e. larger distributed mass combined with a higher stiffness. Also, installing wave absorbers along the tank could have contributed to damping out the radiated waves.
- The damping levels in the numerical model are constants based on the decay tests, where the surface is initially flat. As shown in the tests, the damping is a function of the submergence. At a large wave impact the temporary submergence is increased, leading to a higher damping level. This submergence-dependent damping could be included in further development of the model, but the effect is probably limited.
- A frequency-dependent wave-radiation damping should be included in the numerical program.
- A validation of the numerical program against another should be performed.
- To get a better understanding of the effects of the first-mode motion, more bi-chromatic/special wave tests should be performed. The objective would be to successfully generate ringing artificially. If the ringing only occurs either with or without the first mode excited in advance, the effect of the excessive first-mode motion (caused by the self-excitation, conservative mode shape and low damping) on the largest maxima could be evaluated.
- Working pressure gauges could be included to assess the vertical pressure distribution of a slam. Combined with a stiffer base spring the excitation force magnitude, shape and impact duration can be determined. For an impact load duration of a few ms, the measurement sampling frequencies should optimally be a few kHz. This means at least a tenth multiple increase

from the current setup of $f_{sampling} = 200 \text{ Hz}$. The linear excitation loads without dynamic amplification are found in section 6.3. With a stiffer model, the excitation loads for non-linear response could also be determined.

- More force models can be implemented in the numerical program to compare their degree of conservatism with that of the FNV.
- An improvement to the [Nestegård et al., 2004] slamming model could be to redefine how the penetration parameter (s) and local phase velocity are calculated (e.g. by utilizing the Hilbert transform).
- Testing with an added surface roughness should be performed in order to verify that the effect on the maximum loads is small.
- The steepness-dependent α factor in the slamming model is set equal to 1 in the current setup, as it is only used for deterministic analyses for a breaking wave. The model can be improved by considering the local wave steepness, implying a wider scope of usage, valid also for steep but non-breaking waves.
- The slamming model should be tested for an impulse-type event where the structure is not already excited at the first-mode.

Bibliography

- [Arany et al., 2014] Arany, L., Bhattacharya, S., MacDonald, J., and Hogan, S. J. (2014). Simplified critical mudline bending moment spectra of offshore wind turbine support structures. *Wiley Online Library*.
- [Arntsen et al., 2011] Arntsen, O., Ros, X., and Tørum, A. (2011). Impact forces on a vertical pile from plunging breaking waves. In *6th International Conference on Coastal Structures*.
- [Ashuri, 2012] Ashuri, T. (2012). *Beyond Classical Upscaling: Integrated Aeroelastodynamic Design and Optimization of Large Offshore Wind Turbines*. Thesis.
- [Bergdahl, 2009] Bergdahl, L. (2009). Comparison of measured shallow-water wave spectra with theoretical spectra. In *8th European Wave and Tidal Energy Conference*, Chalmers University of Technology.
- [Bishop and Donelan, 1989] Bishop, C. and Donelan, M. (1989). *Wave Prediction Models*. Elsevier, New York.
- [Bredmose et al., 2012] Bredmose, H., Schløer, S., and Paulsen, B. T. (2012). Higher-harmonic response of a slender cantilever beam to fully nonlinear regular wave forcing. In *Proceedings of the ASME 2012 31th International Conference on Ocean, Offshore and Arctic Engineering*.
- [Campbell and Weynberg, 1980] Campbell, I. and Weynberg, P. (1980). *Measurement of Parameters Affecting Slamming*. University of Southampton, Department of Aeronautics and Astronautics.
- [Chakrabarti, 1989] Chakrabarti, S. K. (1989). *Modeling of Offshore Structures*. Elsevier, New York.
- [Chakrabarti, 1994] Chakrabarti, S. K. (1994). *Advanced Series on Ocean Engineering, Volume 9: Offshore Structure Modeling*. World Scientific.
- [Chaplin et al., 1997] Chaplin, J. R., Rainey, R. C. T., and Yemm, R. W. (1997). Ringing of a vertical cylinder in waves. *Journal of Fluid Mechanics*, 350:119–147.
- [Chau and Taylor, 1992] Chau, F. P. and Taylor, R. E. (1992). Second-order wave diffraction by a vertical cylinder. *Journal of Fluid Mechanics*, 240:571–599.

- [Choi, 2014] Choi, S.-J. (2014). *Breaking wave impact forces on an offshore structure: the effect of dynamic amplification due to the structure's vibration on breaking wave impact*. Thesis. Ph.D. - Universitetet i Stavanger.
- [Chopra, 2012] Chopra, A. K. (2012). *Dynamics of Structures: Theory and Applications to Earthquake Engineering*. Pearson Prentice Hall, Upper Saddle River, N.J. 4th ed.
- [Damgaard et al., 2013] Damgaard, M., Ibsen, L. B., Andersen, L. V., and Andersen, J. K. F. (2013). Cross-Wind Modal Properties of Offshore Wind Turbines Identified by Full Scale Testing. *Journal of Wind Engineering and Industrial Aerodynamics*, 116:94–108.
- [Dean and Dalrymple, 1991] Dean, R. G. and Dalrymple, R. A. (1991). *Water wave mechanics for engineers and scientists*. World Scientific, Singapore. 2nd printing with corrections.
- [Det Norske Veritas, 2010] Det Norske Veritas (2010). DNV-RP-C205 Environmental Conditions and Environmental Loads.
- [Det Norske Veritas, 2014] Det Norske Veritas (2014). DNV-OS-J101 Design of Offshore Wind Turbine Structures.
- [Engebretsen, 2012] Engebretsen, E. A. (2012). *Wave Conditions for Offshore Wind Turbine Foundations in Intermediate Water Depths*. Thesis.
- [Faltinsen et al., 1995] Faltinsen, O., Newman, J., and Vinje, T. (1995). Nonlinear Wave Loads on a Slender Vertical Cylinder. *Journal of Fluid Dynamics*, Vol. 289:pp. 179–198.
- [Faltinsen, 1990] Faltinsen, O. M. (1990). *Sea loads on ships and offshore structures*. Cambridge University Press, Cambridge.
- [Faltinsen and Timokha, 2009] Faltinsen, O. M. and Timokha, A. N. (2009). *Sloshing*. Cambridge University Press.
- [Fichaux et al., 2011] Fichaux, N., Frandsen, S., Sørensen, J. D., Eecen, P., Malamatianos, C., Gomez, J. A., Hemmelmann, J., Kuik, G. v., Bulder, B., Rasmussen, F., Janssen, B., Fischer, T., Bossanyi, E., Courtney, M., Giebhardt, J., Barthelmie, R., Holmstrøm, O., Beurskens, J., Jensen, P. H., and Wilkes,

- J. (2011). Design limits and solutions for very large wind turbines. Report, UpWind.
- [Flow Science, 2015] Flow Science (2015). Modeling capabilities | Water & Environmental Models | Waves [Online]. <http://www.flow3d.com/home/resources/modeling-capabilities/water-environmental-models/waves>. [Accessed 20th May 2015].
- [Frimann-Dahl, 2014] Frimann-Dahl, J. F. (2014). *Assessment of Nonlinear Wave Loads on Large-Diameter Monopiles*. Thesis.
- [Gaidai and Krokstad, 2014] Gaidai, O. and Krokstad, J. R. (2014). Extreme Response Statistics of Fixed Offshore Structures Subjected to Ringing Loads. *Journal of Offshore Mechanics and Arctic Engineering*, 136.
- [Goda et al., 1966] Goda, Y., Haranaka, S., and Kitahata, M. (1966). Study of impulsive breaking wave forces on piles. Report, Ministry of Transport, Japan.
- [Greco, 2012] Greco, M. (2012). *TMR 4215: Sea Loads, Lecture Notes*. Dept. of Marine Hydrodynamics, NTNU.
- [Grue and Huseby, 2002] Grue, J. and Huseby, M. (2002). Higher-harmonic wave forces and ringing of vertical cylinders. *Applied Ocean Research*, 24(4):203–214.
- [Hallowell et al., 2015] Hallowell, S., Myers, A. T., and Arwade, S. R. (2015). Variability of breaking wave characteristics and impact loads on offshore wind turbines supported by monopiles. Report.
- [Hansen, 2008] Hansen, M. (2008). *Aerodynamics of Wind Turbines*. Earthscan.
- [Haver, 2007] Haver, S. (2007). Prediction of Characteristics Response for Design Purposes. Report, StatoilHydro.
- [IEC, 2006] IEC (2006). IEC 61400-3, Wind turbines – Part 3: Design requirements for offshore wind turbines.
- [Jonkman et al., 2009] Jonkman, J., Butterfield, S., Musial, W., and Scott, G. (2009). Definition of a 5-MW Reference Wind Turbine for Offshore System Development. Report, NREL.

- [Kleiven and Haver, 2003] Kleiven, G. and Haver, S. (2003). Application of environmental contour lines for predicting design response. Report, Statoil. Report PTT-KU-MA-2002/018, Rev. 2003- 05-05.
- [Kristiansen and Bachynski, 2015] Kristiansen, T. and Bachynski, E. (2015). ULS study of wave loads on WTG monopile support for the Dudgeon Offshore Wind farm. Report, MARINTEK. Confidential report.
- [Krokstad, 2015] Krokstad, J. (2015). Personal communication with Prof. II Jørgen Krokstad.
- [Krokstad et al., 1996] Krokstad, J. R., Stansberg, C. T., Nestegård, A., and Marthinsen, T. (1996). *A New Non-Slender Ringing Load Approach Verified Against Experiments*, volume no 102. Marintek, Trondheim. "Presented at OMAE -96."
- [Kühn, 2001] Kühn, M. (2001). *Dynamics and Design Optimisation of Offshore Wind Energy Conversion Systems*. Phd thesis.
- [Langen and Sigbjörnsson, 1979] Langen, I. and Sigbjörnsson, R. (1979). *Dynamisk analyse av konstruksjoner*. Tapir forlag.
- [Larsen, 2012] Larsen, C. M. (2012). *TMR4182 Marin dynamikk*. Department of Marine Technology, NTNU, Trondheim, Norway.
- [Le Mehaute, 1976] Le Mehaute, B. (1976). *An Introduction to Hydrodynamics and Water Waves*. Springer-Verlag Berlin Heidelberg, 1st ed. edition.
- [Leblanc and Tarp-Johansen, 2010] Leblanc, C. and Tarp-Johansen, N. J. (2010). Monopiles in Sand. Stiffness and Damping. Oral presentation, EWEA 2011, Brussels.
- [Lighthill, 1979] Lighthill, J. (1979). Waves and hydrodynamic loading. Cranfield: BHRA Fluid Engineering.
- [Lugni, 2015] Lugni, C. (2015). Personal communication with Claudio Lugni.
- [Malenica and Molin, 1994] Malenica, S. and Molin, B. (1994). Third order triple frequency wave forces on fixed vertical cylinders.

-
- [Manwell et al., 2009] Manwell, J., McGowan, J., and Rogers, A. (2009). *Wind Energy Explained: Theory, Design and Application*. John Wiley & Sons, Ltd., 2nd ed. edition.
- [Marino et al., 2011] Marino, E., Borri, C., and Peil, U. (2011). A fully nonlinear wave model to account for breaking wave impact loads on offshore wind turbines. *Journal of Wind Engineering and Industrial Aerodynamics*, 99(4):483–490.
- [Marino et al., 2013] Marino, E., Lugni, C., and Borri, C. (2013). A novel numerical strategy for the simulation of irregular nonlinear waves and their effects on the dynamic response of offshore wind turbines. *Computer Methods in Applied Mechanics and Engineering*, 255(0):275–288.
- [Mathiesen et al., 2014] Mathiesen, M., Nygaard, E., and Andersen, O. J. (2014). Dogger Bank Wind Power Sites Metocean Design Basis. Report. Revision 4.
- [Mei et al., 2005] Mei, C., Stiassnie, M., and Yue, D. (2005). *Theory and Applications of Ocean Surface Waves: Part 1: Linear Aspects; Part 2: Nonlinear Aspects*. WORLD SCIENTIFIC Publishing Company.
- [Myrhaug, 2001] Myrhaug, D. (2001). *Oceanography: Wind, Waves*, volume UK-00-78. Marinteknisk senter, Trondheim.
- [Myrhaug, 2007] Myrhaug, D. (2007). *Marin dynamikk: Uregelmessig sjø*, volume UK-2007-77. Marinteknisk senter., Trondheim. Katalogisert etter omslag.
- [Nestegård et al., 2004] Nestegård, A., Hagatun, K., Haver, S., Kalleklev, A. J., Wu, Y. L., and Lehn, E. (2004). Resonant Vibrations of Riser Guide Tubes due to Wave Impact. In *23rd International Conference on Offshore Mechanics and Arctic Engineering*.
- [Newland, 1993] Newland, D. E. (1993). *An introduction to random vibrations, spectral and wavelet analysis*. Longman Scientific & Technical, 3rd edition.
- [Newman, 1977] Newman, J. (1977). *Marine Hydrodynamics*. Wei Cheng Cultural Enterprise Company.
- [Newman, 1996] Newman, J. (1996). *Nonlinear scattering of long waves by a vertical cylinder*. Fluid Mechanics and Its Applications. Springer Netherlands.
- [NORSOK, 2004] NORSOK (2004). N-001 Structural design.

- [NORSOK, 2007] NORSOK (2007). N-003 Actions and Action Effects.
- [Næss and Moan, 2012] Næss, A. and Moan, T. (2012). *Stochastic Dynamics of Marine Structures*. Cambridge University Press.
- [Okan et al., 2002] Okan, B., Downie, M., and Incecik, A. (2002). Investigation of Wave Loads on Wind Turbine Structures in Shallow Waters.
- [Rainey, 1989] Rainey, R. C. T. (1989). A new equation for calculating wave loads on offshore structures. *Journal of Fluid Mechanics*, 204:295–324.
- [Rainey, 1995] Rainey, R. C. T. (1995). The hydrodynamic load at the intersection of a cylinder with the water surface.
- [Rainey, 2007] Rainey, R. C. T. (2007). Weak or strong nonlinearity: the vital issue. *Journal of Engineering Mathematics*.
- [RenewableUK, 2015] RenewableUK (2015). Offshore Wind. <http://www.renewableuk.com/en/renewable-energy/wind-energy/offshore-wind/index.cfm>. [Accessed 23rd May 2015].
- [Rosenlund, 2013] Rosenlund, E. (2013). *Nonlinear Hydrodynamic Effects for Bottom-Fixed Wind Turbines*. Master thesis.
- [Royal HaskoningDHV, 2013] Royal HaskoningDHV (2013). Dogger Bank Creyke Beck Information for Appropriate Assessment Report. Report.
- [Sarpkaya, 1976] Sarpkaya, T. (1976). In-Line and Transverse Forces on Cylinders in Oscillatory Flow at High Reynolds Numbers.
- [Sarpkaya and Isaacson, 1981] Sarpkaya, T. and Isaacson, M. (1981). *Mechanics of Wave Forces on Offshore Structures*. Van Nostrand Reinhold, New York.
- [Sawaragi and Nochino, 1984] Sawaragi, T. and Nochino, M. (1984). Impact forces of nearly breaking waves on a vertical circular cylinder. *Coastal Engineering in Japan*.
- [Schlør, 2013] Schlør, S. (2013). *Fatigue and extreme wave loads on bottom fixed offshore wind turbines: Effects from fully nonlinear wave forcing on the structural dynamics*. Thesis.

-
- [Sieros et al., 2012] Sieros, G., Chaviaropoulos, P., Sørensen, J. D., Bulder, B. H., and Jamieson, P. (2012). Upscaling wind turbines: theoretical and practical aspects and their impact on the cost of energy. *Wind Energy*, 15(1):3–17.
- [Skjelbreia and Hendrickson, 1962] Skjelbreia, L. and Hendrickson, J. (1962). *Fifth Order Gravity Wave Theory with Tables of Functions*. National Engineering Science Company.
- [Stansberg, 2005] Stansberg, C. T. (2005). *Comparing models for kinematics under irregular waves*. Marintek Report. Norwegian Marine Technology Research Institute - Marintek, Trondheim.
- [Steen, 2014] Steen, S. (2014). *Experimental Methods in Marine Hydrodynamics*. Department of Marine Technology, Trondheim.
- [Suja-Thauvin et al., 2014] Suja-Thauvin, L., Eliassen, L., and Krokstad, J. R. (2014). The Scalability of Loads on Large Diameter Monopile Offshore Wind Support Structures.
- [Tanimoto et al., 1986] Tanimoto, K., Takahashi, S., Kaneko, T., and Shiota, K. (1986). Impulsive breaking wave forces on an inclined pile exerted by random waves.
- [Tempel, 2006] Tempel, J. V. d. (2006). *Design of Support Structures for Offshore Wind Turbines*. Thesis.
- [The United Kingdom Hydrographic Office, 2015] The United Kingdom Hydrographic Office (2015). Admiralty Easytide [Online]. <http://www.ukho.gov.uk/Easytide/easytide/Support/faq.aspx>. [Accessed 19th March 2015].
- [Thresher et al., 2008] Thresher, R., Robinson, M., and Veers, P. (2008). Wind Energy Technology: Current Status and R&D Future.
- [Tromans et al., 2006] Tromans, P., Swan, C., and Masterton, S. (2006). Nonlinear potential flow forcing: the ringing of concrete gravity based structures. Report, Ocean Wave Engineering Ltd for the Health & Safety Executive.
- [Twidell and Gaudiosi, 2009] Twidell, J. and Gaudiosi, G. E. (2009). *Offshore Wind Power*. Multi-Science Publishing.
- [USFOS, 2010] USFOS (2010). USFOS Hydrodynamics Manual.

- [Vestas, 2015] Vestas (2015). Vestas | Offshore [Online]. http://www.vestas.com/products_and_services/offshore#!offshore-experience. [Accessed 27th January 2015].
- [Vogt, 2013] Vogt, Y. (2013). Windmills at sea can break like matches [Online]. <http://www.apollon.uio.no/english/articles/2013/windmills.html>. [Accessed 20th February 2015].
- [von Kármán, 1929] von Kármán, T. (1929). *The Impact on Seaplane Floats During Landing*. National Advisory Committee for Aeronautics.
- [Welch et al., 1999] Welch, S., Levi, C., Fontaine, E., and Tulin, M. P. (1999). Experimental Study of the Ringing Response of a Vertical Cylinder in Breaking Wave Groups. *International Journal of Offshore and Polar Engineering*, 9(4).
- [Wheeler, 1970] Wheeler, J. D. (1970). Method for Calculating Forces Produced by Irregular Waves. *Journal of Petroleum Technology*, 22:359–367.
- [Wienke and Oumeraci, 2005] Wienke, J. and Oumeraci, H. (2005). Breaking wave impact force on a vertical and inclined slender pile—theoretical and large-scale model investigations. *Coastal Engineering*, 52(5):435–462.
- [Wienke et al., 2005] Wienke, J., Sparboom, U., and Oumeraci, H. (2005). *Theoretical Formulae for Wave Slamming Loads on Slender Circular Cylinders and Application for Support Structures of Wind Turbines*, pages 4018–4026. World Scientific Publishing Company.

A | Regular Wave Realizations

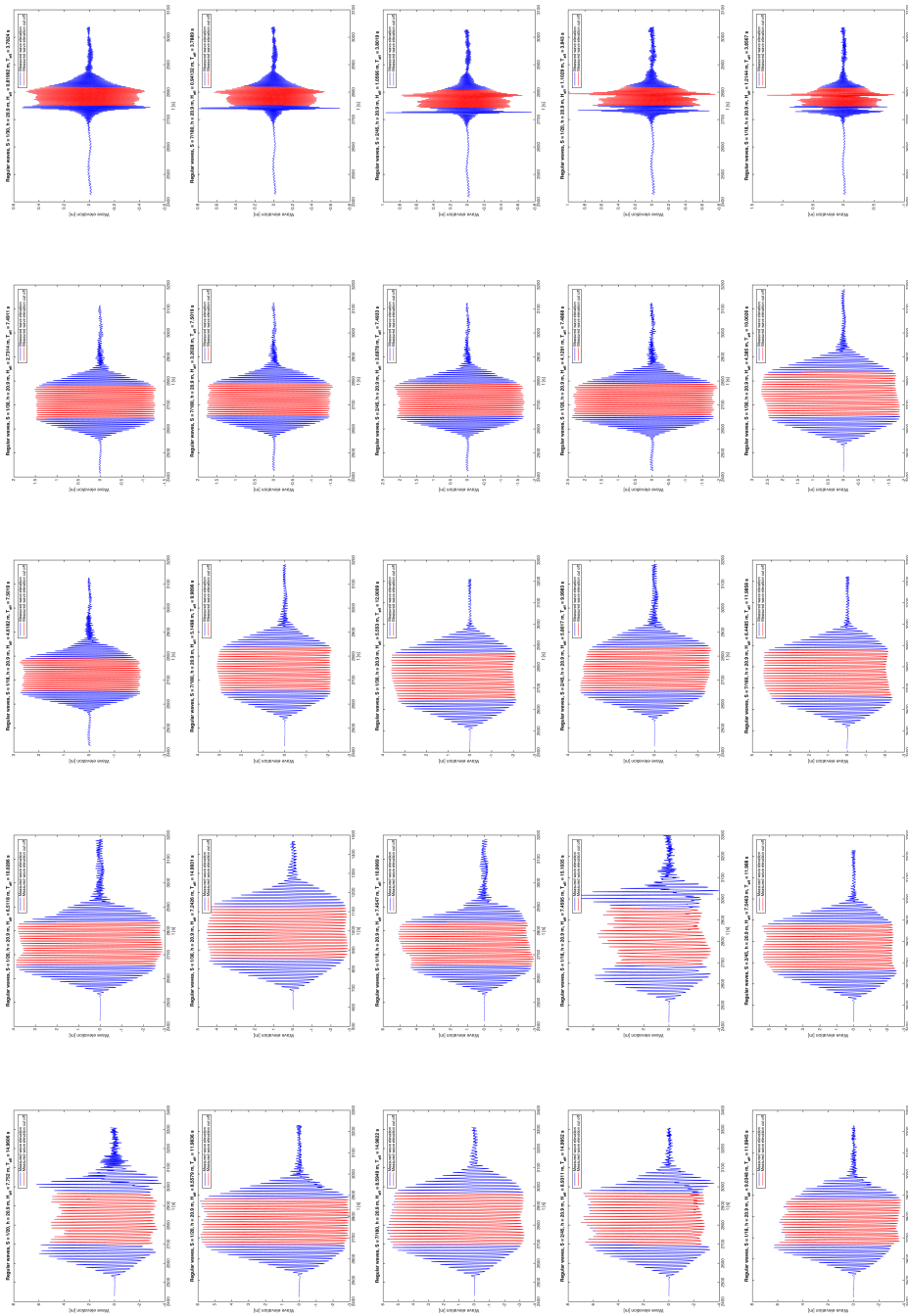


Figure A.1.: Regular wave realizations at $h = 20.9$ m. The figures are ordered according to steepness, from $S = 1/30$ (left) to $S = 1/18$ (right), and specified wave period, from $T = 3.77$ s (top) to $T = 15$ s (bottom).

Appendix A. Regular Wave Realizations

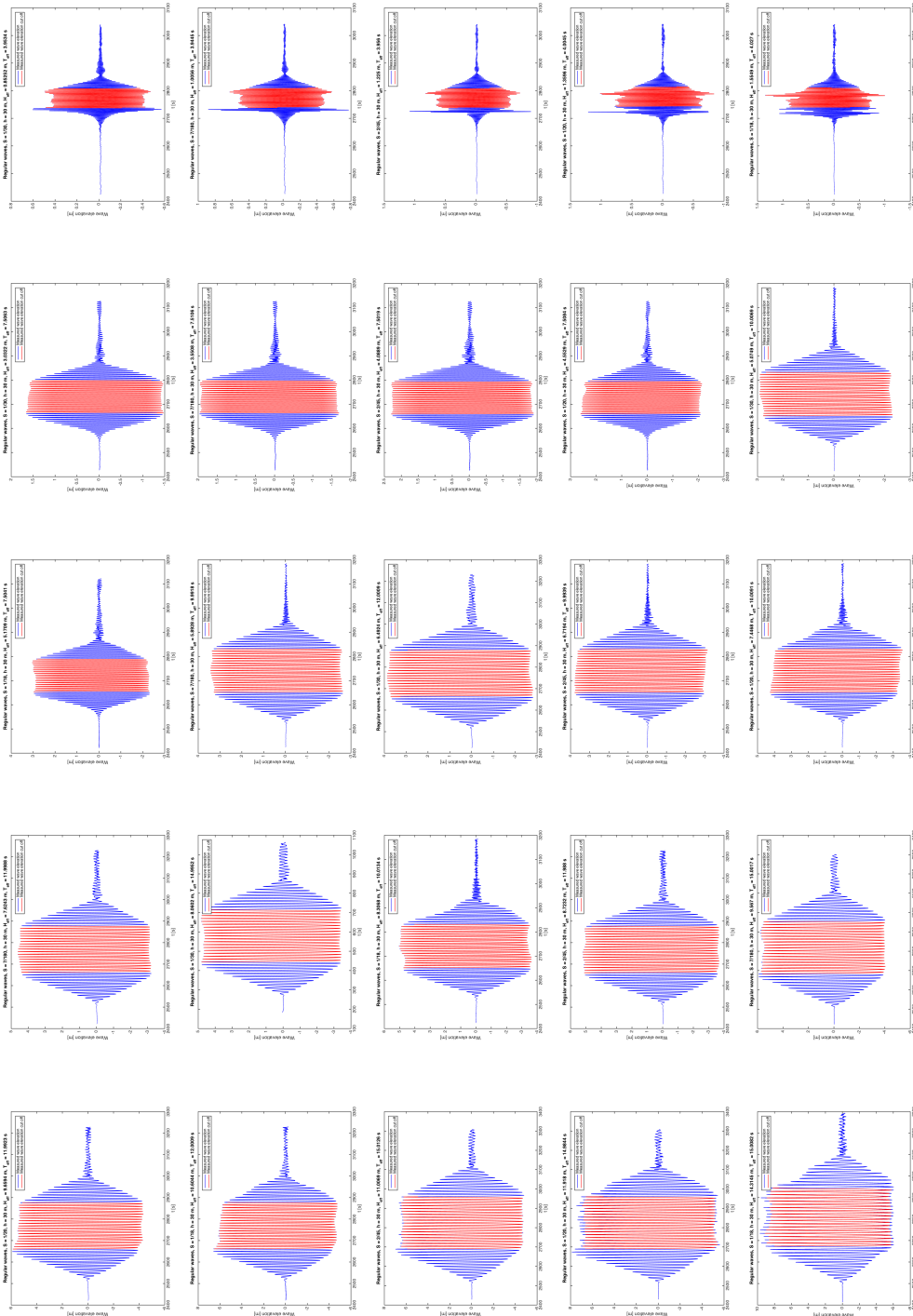


Figure A.2.: Regular wave realizations at $h = 30$ m. The figures are ordered according to stepness, from $S = 1/30$ (left) to $S = 1/18$ (right), and specified wave period, from $T = 3.94$ s (top) to $T = 15$ s (bottom).

B | Moment Gumbel Plots

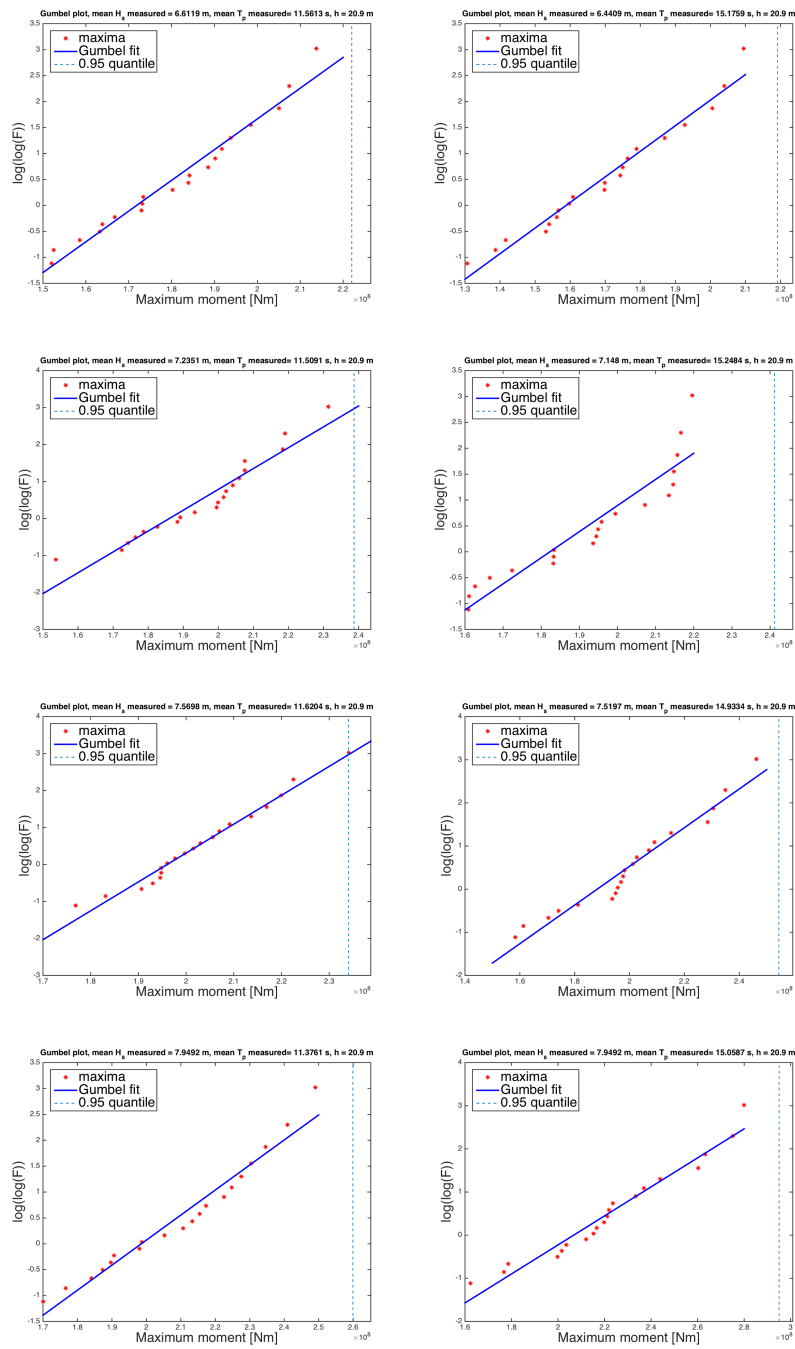


Figure B.1.: Gumbel plots for the maximum response moments in each seed, $h = 20.9$ m. Ordered from $H_s=6.71$ m (top) to $H_s=9.04$ m (bottom) and $T_p=11.25$ s (left) to $T_p=15$ s (right).

Appendix B. Moment Gumbel Plots

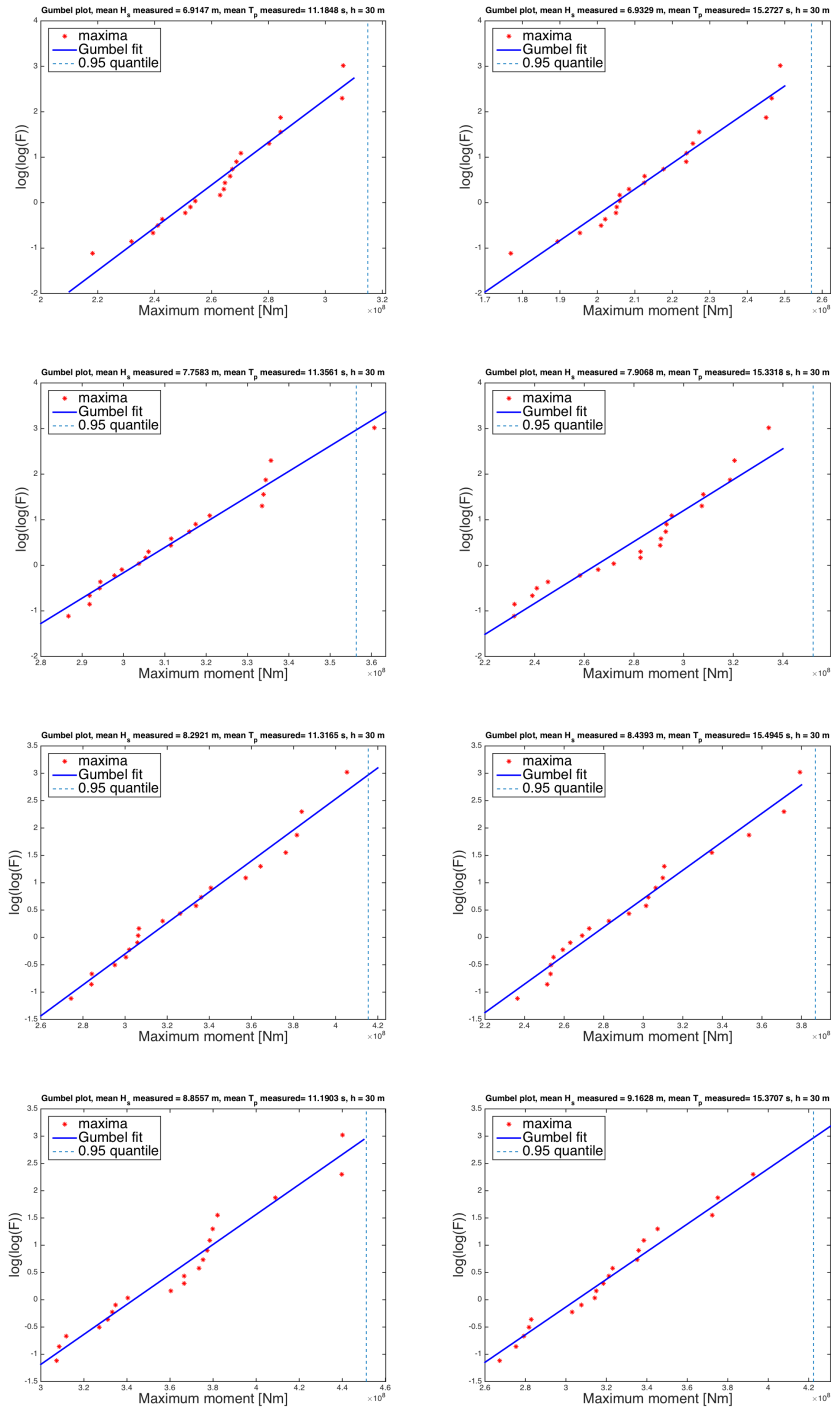


Figure B.2.: Gumbel plots for the maximum response moments in each seed, $h = 30$ m. Ordered from $H_s=6.71$ m (top) to $H_s=9.04$ m (bottom) and $T_p=11.25$ s (left) to $T_p=15$ s (right).

C | Moment Gumbel Plots for the Numerical Program

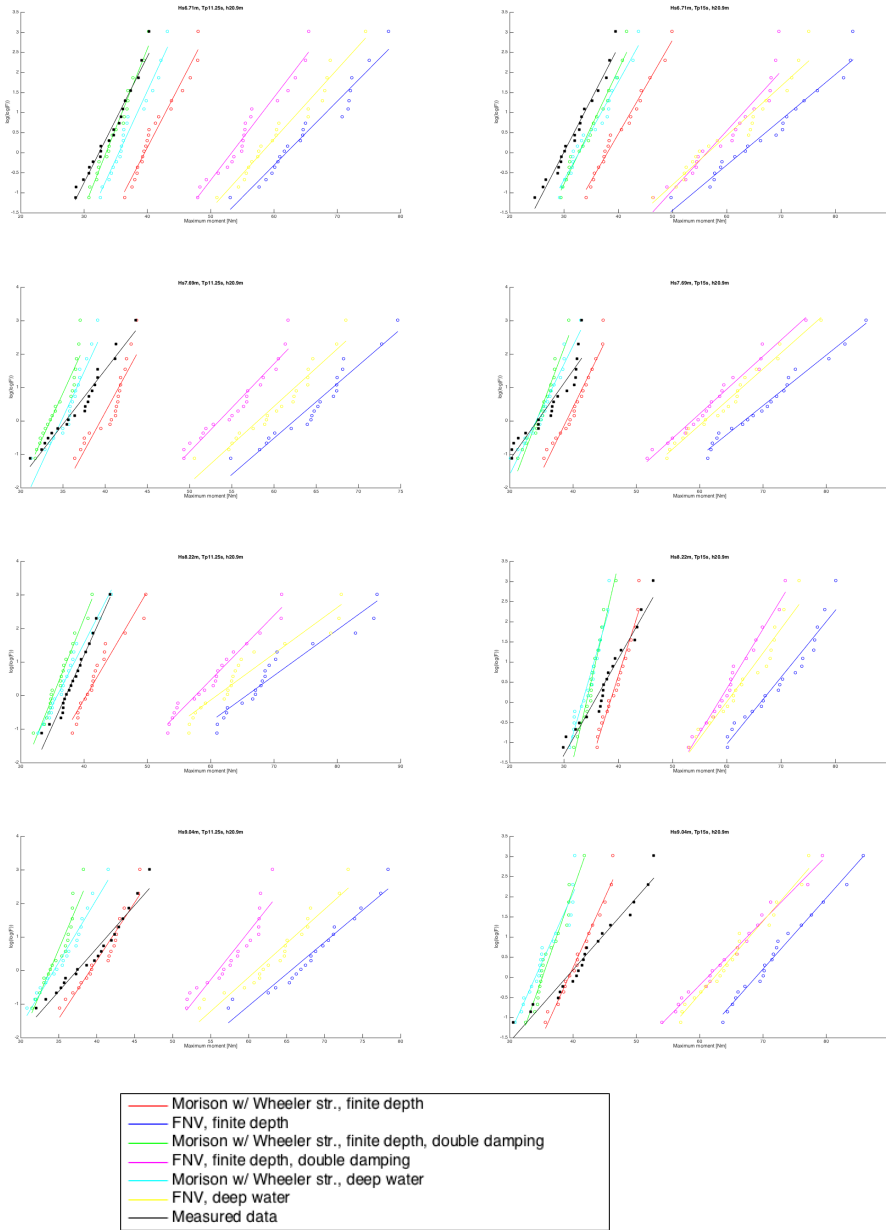


Figure C.1.: Comparing numerical model output with measured data. Gumbel regression lines for the maximum response moments in each seed, $h = 20.9$ m. The plots are ordered with increasing H_s from 6.71 m (top) to 9.04 m (bottom). $T_p = 11.25$ s is on left and $T_p = 15$ s is on the right. x-axes: Maximum moment [Nm], y-axes: $\log(\log(F))$.

Appendix C. Moment Gumbel Plots for the Numerical Program

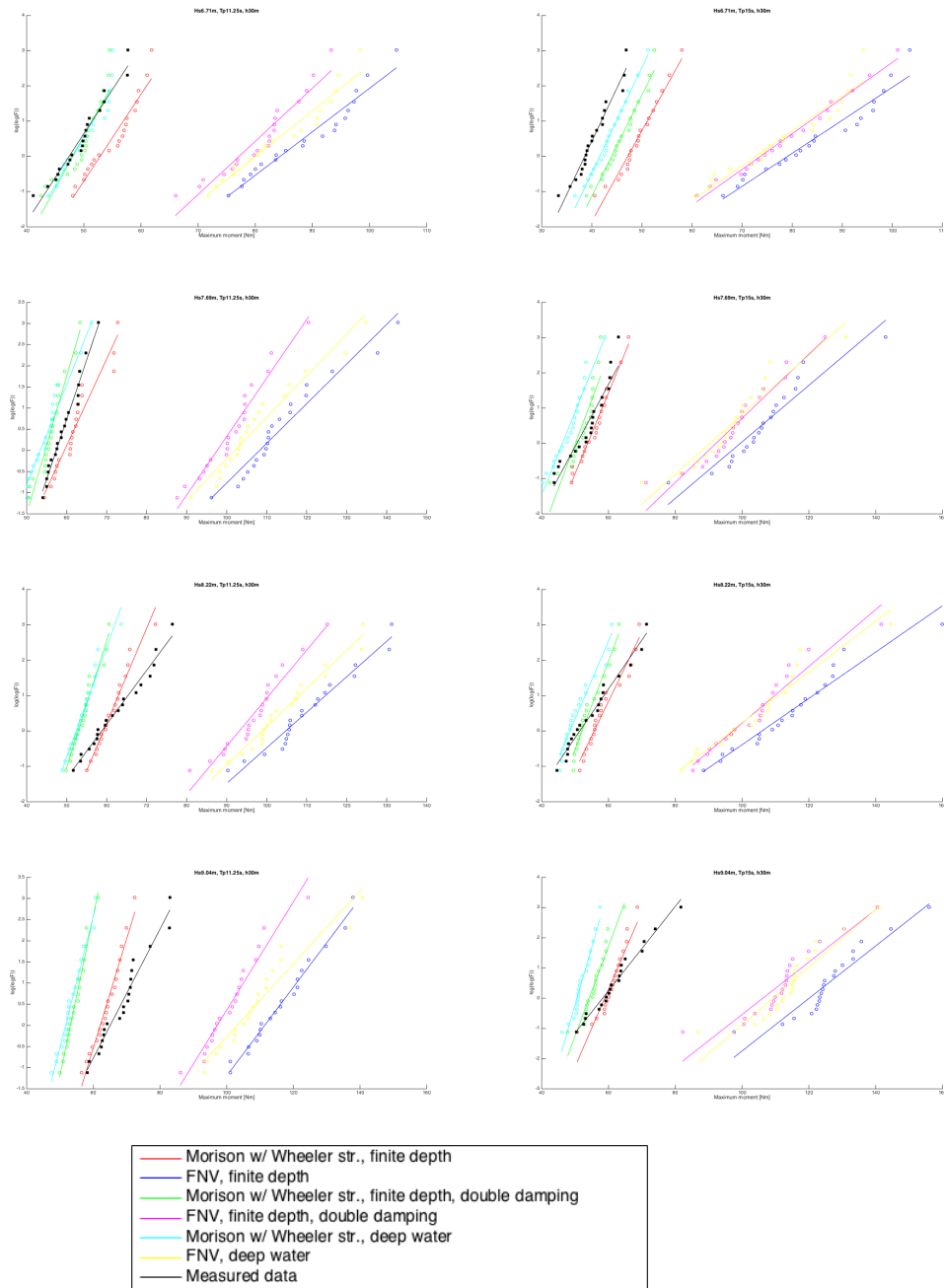


Figure C.2.: Comparing numerical model output with measured data. Gumbel regression lines for the maximum response moments in each seed, $h = 30$ m. The plots are ordered with increasing H_s from 6.71 m (top) to 9.04 m (bottom). $T_p = 11.25$ s is on left and $T_p = 15$ s is on the right. x-axes: Maximum moment [Nm], y-axes: $\log(\log(F))$.

D | Validation of the FNV implementation

In [Newman, 1996], a first-order free-surface elevation is put together by five sinusoidal components

$$\zeta_1 = \sum_{n=1}^5 A_n \sin \omega_n t \quad (\text{D.1})$$

In order to test whether the coded deep-water implementation of the FNV is done correctly, the resulting components of the force are compared to those in [Newman, 1996]. In the following figures, the upper graphs are from [Newman, 1996] and the lower graphs are from the numerical deep-water FNV implementation. The curves show a perfect fit.

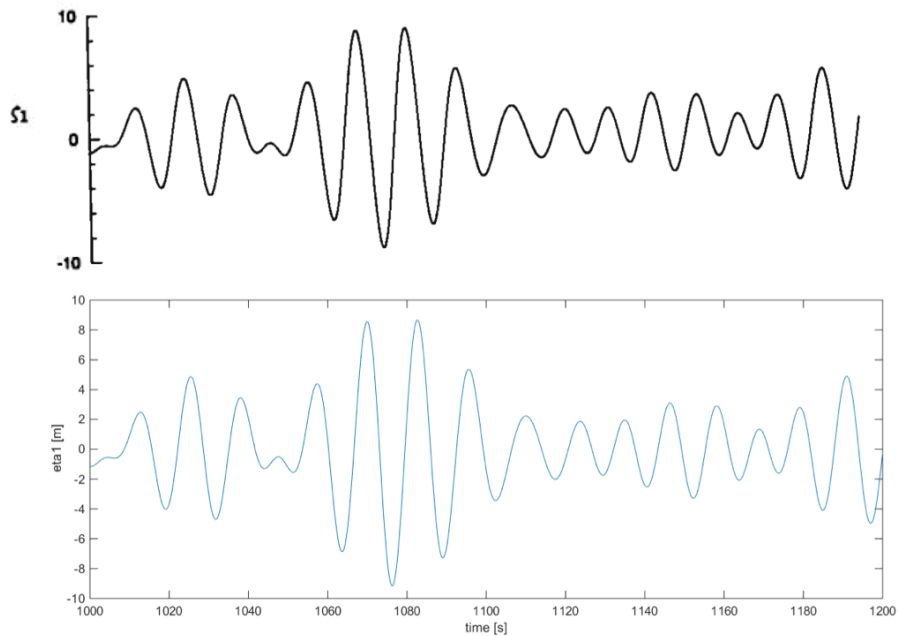


Figure D.1.: First-order free-surface elevation ζ_1

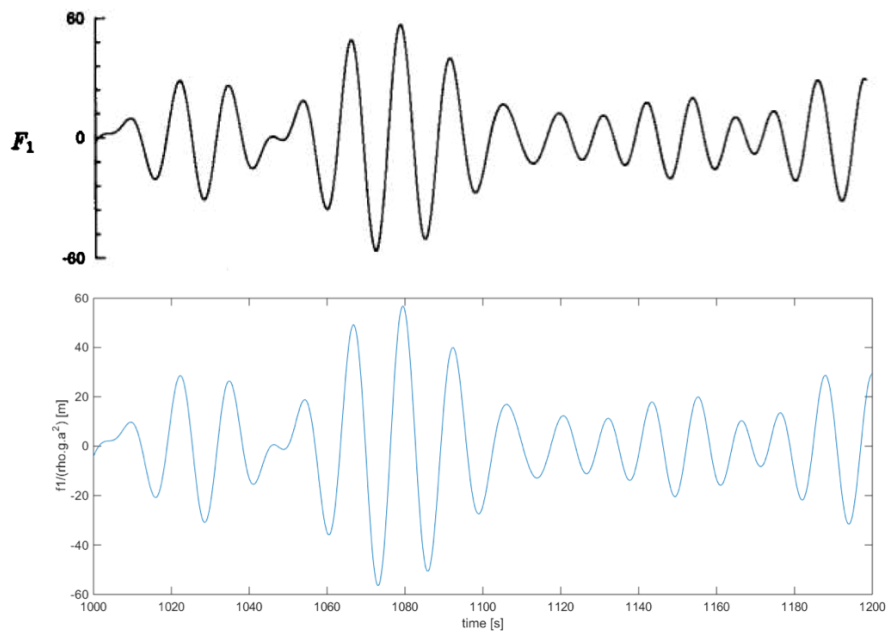


Figure D.2.: F_1

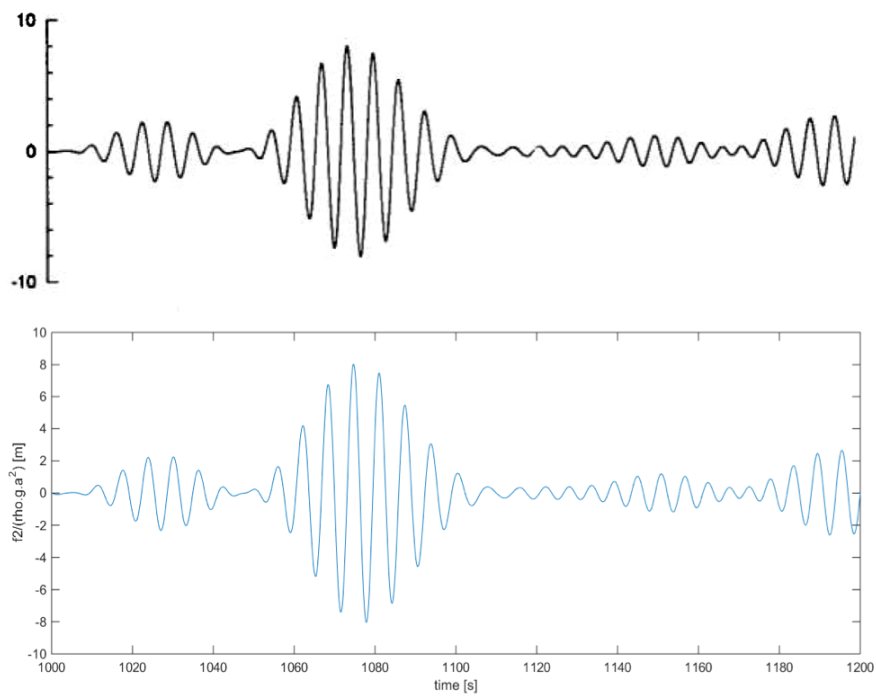


Figure D.3.: F_2

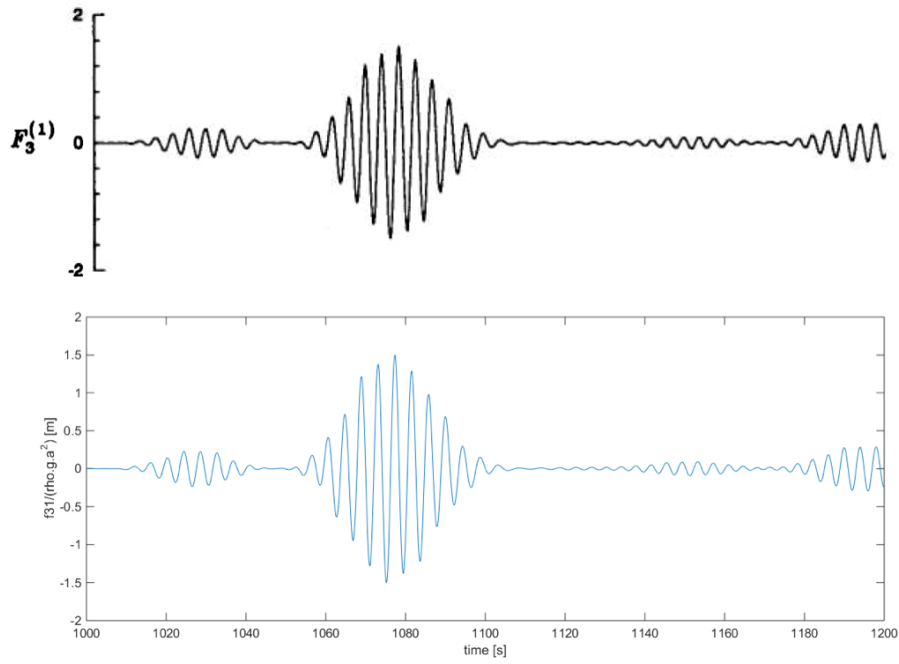


Figure D.4.: $F_3^{(1)}$

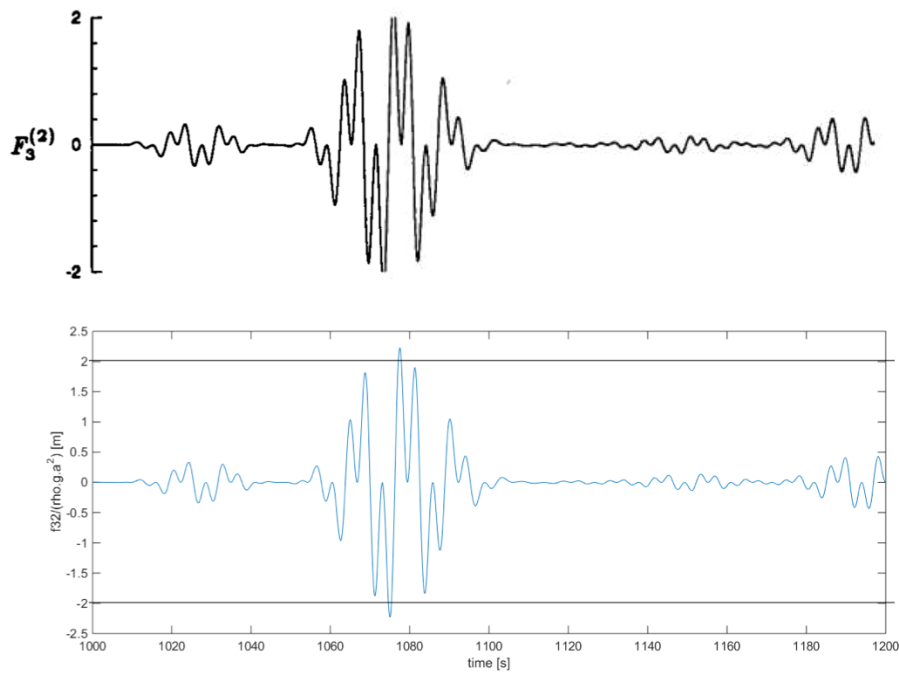


Figure D.5.: $F_3^{(2)}$

E | MATLAB routines

```
%% AnalyzeAllSimulatedData
% Objective: To run AnalyzeSimulatedData.m for all sea states
% Method: For-loop
% Last Modified: 05.2015
% Authors: Loup and Joakim

%% AnalyzeSimulatedData
% Objective: To analyze the output binary files from PileResponse.m
% Method: Gumbel analysis
% Last Modified: 05.2015
% Authors: Loup and Joakim

%% biesel
% Objective: Find the H/S for a piston-type wavemaker
%           H: wave height for a linear wave [m]
%           S: wave maker stroke
% Method: Using the Biesel transfer function
% Last Modified: 03.2015
% Authors: Trygve Kristiansen (MARINTEK)
% Modified by: Loup and Joakim
function [HS_pist]=biesel(omega,h,iwrite)

%% CalcHsTpProbability
% Objective: To establish sea state probabilities for the Dogger Bank,
%           Creyke Beck B, location 2
% Method: Using the values and formulae of [Mathiesen et al., 2014]
% Last Modified: 05.2015
% Authors: Loup and Joakim

%% CheckHsTpFromInput
% Objective: Checking the nominal Hs, Tp values
% Method: Spectral analysis
% Last Modified: 05.2015
% Authors: Loup and Joakim
function [Hs,Tp,F,Y] = CheckHsTpFromInput(filepath,ramp,duration,lambda)

%% CheckHsTpFromMeas
% Objective: Checking the effective Hs, Tp values
% Method: Spectral analysis
% Last Modified: 05.2015
% Authors: Loup and Joakim
function [Hs_meas,Tp_meas,dt] =
CheckHsTpFromMeas(filepath,ramp,duration,trigger_end,lambda)

%% Compare
% Objective: Checking the nominal and effective Hs, Tp values
% Method: Spectral analysis
% Last Modified: 05.2015
% Authors: Loup and Joakim
function [Hs_in,Tp_in,Hs_meas,Tp_meas,dt_out,F_in,Y_in] =
Compare(folderpath,log_path,output_path,ramp,duration,file,trigger_end,lambda)

%% CompareDecay
% Objective: To compare measured decay with the calculated numerical decay
% Method: Solving the rotational equation of motion
% Last Modified: 05.2015
% Authors: Loup and Joakim
function []=CompareDecay()
```

```

%% CompareFiles
% Objective: Post-processing irregular wave data
% Method: Spectral analyses and stochastic Gumbel analyses
% Last Modified: 05.2015
% Authors: Loup and Joakim

%% CompareFMspectra
% Objective: To compare force and moment spectra (smoothed and unsmoothed)
% for each seed of a sea state
% Method: Plotting the nominal and effective wave spectra
% Last Modified: 05.2015
% Authors: Loup and Joakim
function
[]=CompareFMspectra(freq,moment_tot,force_tot,h,files,Tp_vec_meas,Hs_specified,
Tp_specified,lambda)

%% CompareHsTpPlot
% Objective: To compare the Hs, Tp values for each sea state seed
% Method: Plotting the specified nominal and effective Hs, Tp values
% Last Modified: 05.2015
% Authors: Loup and Joakim
function
[]=CompareHsTpPlot(h,files,Hs_specified,Tp_specified,Hs_vec_in,Tp_vec_in,Hs_vec
_meas,Tp_vec_meas)

%% CompareSpectra
% Objective: To compare wave spectra (smoothed and unsmoothed) for each
% seed of a sea state
% Method: Plotting the nominal and effective wave spectra
% Last Modified: 05.2015
% Authors: Loup and Joakim
function
[]=CompareSpectra(h,files,Hs_specified,Tp_specified,F_in_vec,Y_in_vec,freq,wave
_tot)

%% CreateBatch
% Objective: Generating the batch files for irregular waves
% Method: Using the wavemaker transfer functions, reading in the generated
% irregular wave elevation time series
% Last Modified: 04.2015
% Authors: Loup and Joakim

%% CutTime
% Objective: Removing the ramp duration
% Method: Utilizing the ramp duration and seed duration and the specified
% position where the ramp starts
% Last Modified: 05.2015
% Authors: Loup and Joakim
function [out] = CutTime(in,first_step,ramp,duration)

%% damping
% Objective: To find the linear and nonlinear damping coefficients as well as
% the damping ratio using measurements from a decay test
% Method: Using the logarithmic decrement method of [Steen, 2014]
% Last Modified: 05.2015
% Authors: Loup and Joakim

```



```

%% eqmotion
% Objective: Solving the differential equation of motion for Morison
% Method: Using a procedure specified in the TMR4215 Sea loads exercise 8
% Last Modified: 03.2015
% Authors: Loup and Joakim

%% eqmotion_FNV
% Objective: Solving the differential equation of motion for FNV
% Method: Using a procedure specified in the TMR4215 Sea loads exercise 8
% Last Modified: 04.2015
% Authors: Loup and Joakim

%% FilteringButterworth
% Objective: To separate high and low frequency components in a moment time
% series
% Method: Using a 5th-order Butterworth filter
% Last Modified: 05.2015
% Authors: Loup and Joakim
function []=FilteringButterworth(t,M,lambda,Fc)

%% FindingTF_Regular
% Objective: Finding the transfer function TF = theta [rad]/M [rad] for the
% lowest-steepness regular waves in order to test the linear response of
% the numerical program
% Method: Filtering away the frequencies above 1.5*f_1, where f_1 is the
% measured reciprocal to the regular wave frequency
% Last Modified: 05.2015
% Authors: Loup and Joakim
function [meanFiltMMax,meanFiltThetaMax] =
FindingTF_Regular(t,dt,freq,M,accx,Fc,T_meas,ph)

%% findk
% Objective: To find the wave number k using linear wave theory
% Method: Using an iterative procedure to find k on a finite water depth
% Last Modified: 03.2015
% Authors: Loup and Joakim
function [k]=findk(T,h)

%% findk2
% Objective: To find the wave number k for a vector of wave frequencies
% using linear wave theory
% Method: Using an iterative procedure to find k on a finite water depth
% Last Modified: 03.2015
% Authors: Jørgen Krokstad
function [k]=findk2(w,h)

%% ForcesFNV
% Objective: Calculating the 1st, 2nd and 3rd-order FNV
% loads on a cylinder
%Method: Using formulae for irregular waves from [Newman, 1996]
% Last Modified: 03.2015
% Authors: Loup and Joakim
function [f1,f2,f3] = ForcesFNV(
time,h,g,a,wave_elevation,rho,CD,CM,potential_M,potential_FNV)

%% ForcesMorison
% Objective: Calculating the hydrodynamic Morison loads on a cylinder
% Method: Using the Morison equation

```

```

% Last Modified: 05.2015
% Authors: Loup and Joakim
function [Fs,FD,FM] =
ForcesMorison(time,h,g,a,Wave_elevation,rho,CD,CM,potential,wheeler,include_Cs,
output_path_cal,alpha,impulse_pos)

%% FreqDomain
% Objective: Finding the Fourier components for the wave elevation and the
% wave number for a given a circular wave frequency.
% Created: 2015-03-12
% Last Modified:
% Author: Loup and Joakim
function [Y2,W,k,a,b] = FreqDomain(wave_elevation,time,g,h,potential_)

%% Gumbel
% Objective: Gumbel analysis, finding the maximum value for the specified
% quantile
% Method: Using formulae from [Naess and Moan, 2012]
% Last Modified: 05.2015
% Authors: Loup and Joakim
function [x] = Gumbel(vec_max,quantile)

%% GumbelAnalyze
% Objective: Gumbel analysis, finding the maximum value for the specified
% quantile and the p1 and p2 of the regression line  $y=p1*x+p2$ 
% Method: Using formulae from [Naess and Moan, 2012]
% Last Modified: 05.2015
% Authors: Loup and Joakim
function [x,p1,p2] = GumbelAnalyze(vec_max,quantile)

%% GumbelPlot
% Objective: Plotting Gumbel fits, finding the maximum values for the
% specified quantile
% Method: Using formulae from [Naess and Moan, 2012]
% Last Modified: 05.2015
% Authors: Loup and Joakim
function [x] = GumbelPlot(vec_max,quantile,Mean_HsMeas,Mean_TpMeas,Hs,Tp,h,FM)

%% IntegrateAcceleration
% Objective: Finding the pile top position time histories from the
% accelerometer measurements
% Method: Using a highpass filter and integrating twice
% Last Modified: 05.2015
% Authors: Loup and Joakim
function [pos] = IntegrateAcceleration(t,acc,cutoff)

%% IrregWaveSeries
% Objective: Generating the irregular output file which is input for
% CreateBatch.m
% Method: Calculating the JONSWAP peakedness factor gamma and executing
% Realize.m
% Last Modified: 04.2015
% Authors: Loup and Joakim
function [] = IrregWaveSeries()

%% JONSWAP_spectrum
% Objective: Generating a JONSWAP spectrum
% Method: Taking in the peakedness factor gamma to be multiplies with the

```

```

% PM spectrum
% Last Modified: 02.2015
% Authors: Loup and Joakim
function [JSWP] = JONSWAP_spectrum(w,Hs,Tp,gamma)

%% MechTF
% Objective: Specifying the mechanical transfer function
% Method: Linear interpolation between frequency values
% Last Modified: 03.2015
% Authors: Loup and Joakim
function [MTF] = MechTF(omega)

%% Mirror
% Objective: This function mirrors a spectrum wrt. its central value.
% Last Modified: 01.2015
% Authors: Loup and Joakim
function [Xm] = Mirror(X)

%% numToString100
% Objective: Used for the three-digit run numbers that begin with '0' or
% '00'
% Method: If-sentences
% Last Modified: 02.2015
% Authors: Loup and Joakim
function [num_string] = numToString100(num)

%% PiersonMoskowitz_spectrum
% Objective: Generating a Pierson-Moskowitz spectrum
% Method: Using the formula specified in DNV-OS-J101
% Last Modified: 02.2015
% Authors: Loup and Joakim
function [PM] = PiersonMoskowitz_spectrum(w,Hs,Tp)

%% PileResponse
% Objective: To calculate the pile response in the time domain, using
% different excitation force models
% Method: The response is found by solving the equation of motion:
%  $(Imp+Imd+Ima)*ddtheta(t) + Crot*dtheta(t) + Krot*theta(t) = M(t)$ 
% Last Modified: 05.2015
% Authors: Loup and Joakim

%% PlotHsTpGraph
% Objective: To plot the contour lines for the Dogger Bank, Creyke Beck B,
% location 2
% Method: Using the values and formulae of [Mathiesen et al., 2014] through
% CalcHsTpProbability.m.
% Last Modified: 02.2015
% Authors: Loup and Joakim

%% Realize
% Objective: Generating an irregular wave elevation time series
% Method: Utilizing the procedure specified in [Newland, 1993]
% Last Modified: 02.2015
% Authors: Loup and Joakim
function [t,x] = Realize(Tmax,dt,Hs,Tp,gamma,h,g,seed)

%% RegWaveSeries
% Objective: Generating the batch files for regular waves

```

```
% Method: Using the wavemaker transfer functions and linear wave theory
% Last Modified: 04.2015
% Authors: Loup and Joakim
function [] = RegWaveSeries()

%% slamcoeff
% Objective: Calculating the slamming coefficient to go with the impulse
% force included in the Morison load
% Method: Using the procedure from [Nestegaard, 2004]
% Last Modified: 05.2015
% Authors: Loup and Joakim
function [Cs]=slamcoeff(h,g,R,rho,output_path_cal,alpha,impulse_pos)
```